THE UNIVERSITY
of EDINBURGH

This thesis has been submitted in fulfilment of the requirements for a postgraduate degree (e.g. PhD, MPhil, DClinPsychol) at the University of Edinburgh. Please note the following terms and conditions of use:

This work is protected by copyright and other intellectual property rights, which are retained by the thesis author, unless otherwise stated.
A copy can be downloaded for personal non-commercial research or study, without prior permission or charge.
This thesis cannot be reproduced or quoted extensively from without first obtaining permission in writing from the author.
The content must not be changed in any way or sold commercially in any format or medium without the formal permission of the author.
When referring to this work, full bibliographic details including the author, title, awarding institution and date of the thesis must be given.

Squeezing the Sponge: the Role of Serpentinites in Subduction Zones

Eleri Clarke

Submitted for the degree of Doctor of Philosophy

The University of Edinburgh

2019

0.1 Abstract

Subduction zones are the main drivers of global volatile recycling through the supply of water to the mantle wedge which, in turn, triggers arc volcanism. Serpentinites may contribute greatly to this process due to their high water content and widespread presence in oceanic lithosphere. B isotopes are a powerful tracer of serpentinites due to their distinct signature (δ^{11}B = +5 to +40‰) and the signature of their expelled fluids (δ^{11}B up to +15‰), compared to the mantle which has a low δ^{11}B (-7.1‰). However, despite its fluid mobile nature, B-rich metamorphic olivine has been found in dehydrated serpentinites in the field as well as in experiments. This retention of B in olivine potentially fractionates B isotopes during serpentinite dehydration, but details of this process remain largely unconstrained. The aim of this thesis is to analyse the B and δ^{11}B distribution between phases in dehydrated serpentinites from two different geological settings: a subduction zone and a contact aureole, in order to constrain B isotope behaviour during deserpentinization. In addition we ran olivine-fluid B partitioning experiments to quantitatively constrain the partitioning behaviour of isotopes between olivine and fluid. This project provides an insight into serpentinite-associated fluid movements during subduction and contact metamorphism and the partitioning of B and its isotopes between olivine and fluid. We find that open system dehydration significantly effects the B isotope signature of dehydrated serpentinites and ^{11}B partitioning preferences are fluid>olivine>serpentine.

0.2 Lay Summary

This thesis contributes to the overall understanding of how to build a habitable planet. Our planet is split into 3 main layers: the crust, the mantle and the core. The crust is very thin compared to the rest of a planet, yet has supported the evolution of life for the last 3.5 billion years. Its success is down to dry land and breathable air. Dry land exists upon thicker continental crust and Earth's breathable atmosphere is continuously maintained by the release of water and other gases from volcanic eruptions. Both the formation of the continental crust and volcanoes relies on a supply of molten rock from the mantle. The crust is split into sections called tectonic plates, which are made of the crust and part of the upper mantle. Water is added to the mantle where two tectonic plates collide and the denser plate (slab) sinks below the other (a.k.a Subduction Zone). Water is transported inside hydrous minerals in the slab and is released into the mantle as the slab descends. Water reduces the melting point of the mantle, forming the molten rock needed for continental crust and volcanoes. As important as this process is, we are still unsure which layer of the slab carries the most water. The layers all have a very similar chemical composition, apart from the ratio of two isotopes of boron (B). Isotopes are the same element but with slightly different weights. The different layers of the slab: sediments, crust and hydrated mantle (serpentinite) have very different ratios of heavy and light B. Think of it like the ratio of blue and red balls, one layer might have a ratio of 2:5, another may have a ratio of 2:9. Both layers might have the same overall number of balls, however, using the ratios of blue to red we can now tell them apart. This thesis outlines a study into the behaviour of B isotopes in serpentinites to find out whether serpentinites could be responsible for contributing water to the mantle. What we find is that we most likely owe a debt of gratitude to the ugly green/grey serpentinites for playing a dominant role in the delivery of water to the mantle and likely the development of life on Earth.

0.3 Declaration

I declare that this thesis has been composed solely by myself and that it has not been submitted, in whole or in part, in any previous application for a degree. Except where states otherwise by reference or acknowledgement, the work presented is entirely my own.

Signed

Name

Date

0.4 Acknowledgments

"We are like dwarfs sitting on the shoulders of giants. We see more, and things that are more distant, than they did, not because our sight is superior or because we are taller than they, but because they raise us up, and by their great stature add to ours." - John of Salisbury

During the course of my PhD I have relied heavily on the support and guidance of many people to whom I am incredibly grateful. The first and foremost acknowledgment goes to my husband, Ben Clarke, who despite having his own thesis to write never failed in his support of me. I thank him for all of dinners he cooked, drives he made, time he committed, pep talks he gave, endless python help and most importantly his unconditional love and forgiveness for me when I have been grumpy and difficult. Secondly I want to thank my family: Mum, Dad, my sister Cerys and her husband Jonathan, for always understanding what I'm going through and their incredible ability to stay interested in my PhD! Thank you for all the board game fun, the sunny outings, the long phone calls and your support throughout this journey. Special thanks to my parents for taking us away to a cottage in the middle of nowhere, which was just what I needed to focus and churn out my thesis. Thirdly, my closest friends in Edinburgh and afar, thank you for always believing in me saying the right things at the right time, special thanks to Roseanne and Lauren for pep talks at girly nights and Keya for always ringing to check up on me.

The biggest academic acknowledgment goes to my supervisor Cees-Jan de Hoog without whom this work would not have been possible, and many of his great ideas lie within these pages. Thank you for always having time for me, your generous helpings of constructive criticism (significantly improving my work every time!), speedily returning my work and e-mails, and your efforts to develop me as a scientist by getting me experience in many labs across

the world. You have taught me so much that I will take with me into my future career and beyond. My secondary supervisors: Linda Kirstein, thank you for your helpful discussions, useful feedback and always checking up on me, Geoff Bromiley, thank you for your endless help in the lab and expertise on my experimental setup and Jason Harvey for always being quick to answer e-mails, supplying me with Almirez samples and NIST951 powder, and teaching me the ropes of Sr isotope column chemistry. I have been blessed with this supervisory team and am eternally grateful for the time and effort each of them has put in to helping me complete this thesis.

My final acknowledgements go to the large array of incredible scientists who have supported this work through guidance, discussion and samples. Firstly, I would like to thank Baptiste Debret for giving me my first samples (Incl. Vis5b of the main sample set) and keeping a strong interest in this work and providing excellent discussion. Romain Lafay for giving me the entire suite of samples from Valmalenco and again has providing excellent discussion and ideas towards interpreting the data. Prof. Ray Burgess for kindly donating samples DC47 and DC84 of the main sample set. Lukas Baumgartner for leading the field work for sample collection of the 'ZS17' samples. Marco Scambelluri for insightful discussions about the data. Samuele Agostini for assisting me with the collection of whole rock B isotopes in Pisa. Ivan Savov for his unfailing interest and keen discussion, and for looking after me in Pisa. Kristina Walowski for giving me that much needed pep talk at the start of my PhD and encouraging me to take my project by the horns! John Craven for his sarcasm and dry humour, and the great effort he put into helping me in the prep lab and with the oxygen isotopes project. Mike Hall for being the best thin section technician and polishing endless difficult to polish serpentinites and serpentine grains (and not complaining once!). Nicci Potts for her invaluable support and guidance in my early days of working in the experimental lab. The Deep

Volatiles consortium and NERC E3 DTP for providing funding for this research. Finally, I wish to thank every single member of the grant attic during my stay. It has been my honour to be surrounded by smart, incredible people who like to talk about the difference between raisins and sultanas at lunch time. Thank you for believing in me, entertaining me and of course cake fridays and Kirsty with her motivational oranges!

One final acknowledgement, to the One through whom all this was possible. Thank you for all you have done in my life, I am blessed beyond words.
'For from him and through him and for him are all things. To him be the glory forever! Amen.' - Romans 11:36.

Contents

0.1 Abstract i
0.2 Lay Summary ii
0.3 Declaration iii
0.4 Acknowledgments iv

1 Introduction **1**
1.1 Subduction zones 2
1.1.1 Subduction zone structure 2
1.1.2 Subduction interface and exhumation 7
1.2 Mantle-metasomatising fluids 9
1.2.1 Boron as a fluid tracer 10
1.3 Serpentinites 13
1.3.1 Serpentinization reaction 13
1.3.2 Prograde metamorphism of antigorite serpentinites 15
1.4 Subducted Serpentinites 16
1.4.1 Oceanic crust serpentinites 17
1.4.2 Mantle wedge serpentinites 17
1.5 Water transport mechanisms 18
1.6 The knowledge gap 20
1.7 Thesis overview 21
1.7.1 Chapter outline 22

2 Analytical Methods **25**

2.1 Foreword 25
2.2 Major element analyses 25
2.3 Fluid-mobile element concentration analyses 31
2.4 *In situ* B isotope analyses 31
2.5 External fluid composition model 37
2.6 Error propagation 39

3 Subduction Zone Serpentinites: *Alps and Spain* 41
3.1 Abstract 41
3.2 Introduction 42
3.3 Samples and their geological setting 43
3.4 Results 47
3.4.1 Major elements 49
3.4.2 Fluid-mobile Elements (FME) 49
3.4.3 B isotope compositions of olivine and antigorite 50
3.5 Summary Data 53
3.6 Discussion 56
3.6.1 Boron isotope fractionation during serpentine dehydration 56
3.6.2 Implications for the subduction interface 59
3.6.3 Implications for deep recycling of heavy δ^{11}B 63
3.6.4 Ocean floor serpentine: a discussion on the serpentinite starting value 64
3.7 Oxygen Isotopes 68
3.7.1 Introduction 68
3.7.2 Standard characterisation 69
3.8 Conclusion 72

4 Contact Aureole Serpentinites: *Valmalenco* 73
4.1 Foreword 73
4.2 Introduction 74

4.2.1 Geological background 74
4.2.2 Sample descriptions 82
4.2.3 Contact aureoles 86
4.3 Results 88
4.3.1 Major elements 88
4.3.2 Fluid mobile elements and Boron isotopes 90
4.4 Summary Data 95
4.5 Discussion 99
4.5.1 Jack-straw-textured-olivine 99
4.5.2 F in AZO samples. 99
4.5.3 The differences between PR and AZO olivines 99
4.5.4 The differences between Preda Rossa and Alpe Zocca localities 102
4.6 Conclusion 109

5 Olivine growth experiments 111
5.1 Introduction 111
5.1.1 Previous work 112
5.2 Methods 114
5.2.1 Analytical 114
5.2.2 End-loaded piston cylinder set up 114
5.2.3 Haplogranite capture method 116
5.2.4 Olivine growth method 116
5.3 Results 119
5.3.1 Sample description 119
5.3.2 Major Elements 119
5.3.3 B concentration 122
5.3.4 B isotopes 123
5.4 B diffusion 125
5.5 Discussion 125

5.5.1 The effect of pH and temperature on B isotope fractionation 128
5.5.2 Implications for use in geosciences 131
5.5.3 Contribution of serpentinites to subduction zone fluids . . 132
5.5.4 Pyroxene 136
5.5.5 Temperature effect with the addition of NaOH 136
5.6 Limitations 137
5.7 Conclusion 137

6 Conclusions and Further Work Recommendations 139
6.1 Conclusions 139
6.1.1 Chapter 3: Subduction Zone Serpentinites 140
6.1.2 Chapter 4: Contact Aureole Serpentinites 140
6.1.3 Chapter 5: Experiments 141
6.1.4 Final words 141
6.2 Recommendations for Further Work 142

Appendix A Equations used in handling data 145
A.1 Calculating $[B]_{ol-srp}$ and $\Delta^{11}B_{ol-srp}$ 145
A.2 Calculating 'best guess' equilibrium $D_B^{ol/srp}$ 146

Appendix B Data 147
B.1 Data for Chapter 3: Alps and Betic Cordillera 147
B.1.1 Major elements data tables 148
B.1.2 Trace elements and Boron isotopes data tables 161
B.1.3 Combined 176
B.2 Data for Chapter 4: Valmalenco 178
B.2.1 Major elements 179
B.2.2 Trace elements and Boron isotopes 197
B.2.3 Combined 218
B.3 Data for Chapter 5: Experimental 228
B.3.1 Graphs 228

B.3.2 Data 231
B.3.3 Combined 239
B.3.4 Run conditions 241

Appendix C Images **249**

C.1 Sample images for Chapter 3: Alps and Baetic Cordillera 249
C.1.1 Main samples 249
C.1.2 Extra samples 268
C.2 Sample images for Chapter 4: Serpentinites of Valmalenco . . . 283
C.3 Sample images for Chapter 5: Experiments 301

Figure Index

1.1 Subduction zone schematic with hydrous phase stability 3
1.2 PT paths for slab Moho 5
1.3 Slab-mantle interface 8
1.4 B isotopes of subduction zone fluid sources 10
1.5 Serpentine phase diagram 14
1.6 Porosity waves explanation 19

2.1 Sample prep slow chart 26
2.2 SIMS Calibration line 32
2.3 IMF for standards on 1270 33

3.1 Geological locality maps Alps and Spain 44
3.2 Olivine textures: Alps and Spain 47
3.3 δ^{11}B Alps and Spain vs literature 51
3.4 Discrimination plot 52
3.5 External fluid proportions: Alps and Spain 58
3.6 Serpentine dehydration cartoon 60
3.7 Tectonic setting for serpentinites 62
3.8 Geothermometers 71
3.9 Temperature vs Error for O Isotopes 71

4.1 T-time plot 75
4.2 Geological map: Valmalenco 76

4.3 X_{CO_2} 78
4.4 Bergell cross section 80
4.5 Sample textures: Valmalenco 81
4.6 Sample textures: Valmalenco Jack Straw texture 82
4.7 T-Distance for Bergell aureole 87
4.8 Mg# vs MnO - Valmalenco 89
4.9 δ^{11}B vs F: Valmalenco 91
4.10 δ^{11}B vs B: Valmalenco 100
4.11 Discriminate: Valmalenco 101
4.12 PT conditions: Valmalenco 103
4.13 Dehydration models 105
4.14 External fluid compositions: Valmalenco 107

5.1 Structure of the experimental cell 115
5.2 Inflated capsule photograph 120
5.3 Inflated vs deflated capsule: SEM images 121
5.4 B concentration vs temperature of only olivines in each successful experiment. There is no correlation with B content. 126
5.5 $\Delta^{11}B_{ol-fl}$ vs 1000/Temperature (Kelvin) 127
5.6 Distribution of boric acid and borate in seawater 129
5.7 3-way mixing diagram 133
5.8 3-way mixing diagram 134

B.1 NiO vs MnO for aureole phases - Valmalenco 179
B.2 Mg# vs Al_2O_3 - Valmalenco 180
B.3 Mg# vs MnO - Valmalenco 181
B.4 Mg# vs NiO - Valmalenco 182
B.5 Mg# vs Al_2O_3 all phases - Valmalenco 183
B.6 Mg# vs MnO all phases - Valmalenco 184
B.7 Mg# vs NiO all phases - Valmalenco 185
B.8 F vs Cl for serpentinite phases - Valmalenco 197

B.9 Li vs B for aureole phases - Valmalenco 198
B.10 δ^{11}B vs B - Valmalenco 199
B.11 δ^{11}B vs B all phases - Valmalenco 200
B.12 B vs Li all phases - Valmalenco 201
B.13 B vs F all phases - Valmalenco 202
B.14 B vs Cl all phases - Valmalenco 203
B.15 F vs Cl all phases - Valmalenco 204
B.16 Li vs F all phases - Valmalenco 205
B.17 Li vs Cl all phases - Valmalenco 206
B.18 δ^{11}B vs Cl all phases - Valmalenco 207
B.19 δ^{11}B vs F all phases - Valmalenco 208
B.20 δ^{11}B vs Li all phases - Valmalenco 209
B.21 Mg# vs B - Valmalenco 222
B.22 Mg# vs δ^{11}B - Valmalenco 223
B.23 Mg# vs Li - Valmalenco 224
B.24 Mg# vs B all phases - Valmalenco 225
B.25 Mg# vs Li all phases - Valmalenco 226
B.26 Mg# vs δ^{11}B all phases - Valmalenco 227
B.27 Al_2O_3 and SiO_2 vs MgO - Experiments 229
B.28 Al_2O_3 and MgO vs B - Experiments 230

C.1 Valmalenco samples images 283
C.15 Whole image of sample PR02 with pit locations. 297

Table Index

1.1 Hydrous phases in subduction zones 4

2.1 EMPA conditions 27
2.2 B isotope and FME composition of SIMS standards 34
2.3 Majors B mineral standards 35

3.1 Sample descriptions: Alps and Spain 48
3.2 The average B isotope and FME compositions of each phase in every sample. 53
3.3 The average Major compositions of each phase in every sample, data for samples VT8-3 and AL98-4 are published in De Hoog et al. (2014) and Harvey et al. (2019). 55
3.4 ODP FME 66
3.5 ODP Majors 67
3.6 Whole rock O isotopes 69
3.7 In-situ O isotopes 70

4.1 Location and phase compositions of Valmalenco samples 83
4.2 Average B compositions: Valmalenco 94
4.3 The average FME compositions of each phase in every sample. 95
4.4 The average Major compositions of each phase in every sample. 97

5.1 Starting mix composition 117
5.2 Capsule compositions for each experiment 118

5.3 B vs δ^{11}B: Experiments 124

B.1 Major elements - subduction zone samples 148
B.2 Major elements - extra subduction zone samples 153
B.3 FME - subduction zone samples 161
B.4 FME - extra subduction zone samples 167
B.5 Linked analysis pit numbers subduction zone samples 176
B.6 Valmalenco Major Data 186
B.7 Valmalenco trace and boron isotope data 210
B.8 Linked analysis pit numbers Valmalenco 218
B.9 FME and isotope data - Experiments 231
B.10 Major data - Experiments 235
B.11 Linked analysis pit numbers Experiments 239
B.12 Run conditions for experiments 241

Chapter 1

Introduction

"It's a dangerous business, Frodo, going out your door. You step onto the road, and if you don't keep your feet, there's no knowing where you might be swept off to."
J.R.R. Tolkien, The Lord of the Rings

Subduction zones are thought to play a big part in the evolution of life on our planet. This is because they are unique in their supply of hydrated lithologies to the mantle. The transfer of volatiles to the mantle is in part responsible for magma generation in the mantle wedge. This, in turn, supports the creation of continental crust and the maintenance of Earth's atmosphere. But the processes involved in volatile transfer at depth remain elusive. There are many theories at large to explain and account for the formation of arc magma, but it is well accepted that the mantle wedge below the over-riding plate is hydrated by metamorphic fluid. This lowers the mantle's melting point and produces partial melt which rises to the surface to form evolved crust (by fractional crystallisation during ascent) and arc volcanoes. However the nature and source of this fluid is still widely debated (see section 1.2. Mantle-metasomatising fluids, for more in-depth discussion). One can shed light on the source of these fluids and the processes of volatile transfer by studying rocks that have been exhumed from sub-arc depths. In particular the role of serpentinites in volatile transfer has recently gained more and more attention, due to their prevalence in oceanic lithosphere and high water contents (up to 13 wt% in hydrous phases). Therefore, this thesis aims to better

constrain the role and environment of serpentinite dehydration in subduction zones using boron isotopes. This approach gives insight into the composition of serpentinite dehydration fluids and sheds light on the fluid processes occurring at sub-arc depths. The following is a brief review of the literature on subduction zones, serpentinites and using boron isotopes as a tracer.

1.1 Subduction zones

1.1.1 Subduction zone structure

A subduction zone occurs where two tectonic plates collide (oceanic vs oceanic, oceanic vs continental and continental vs continental) and one plate, driven by higher density, sinks below the other into the mantle. The general conditions for subduction include mechanical detachment between the upper and lower plate, presence of sufficient slab-pull and slab-push forces and enough mechanical strength in the lower plate to maintain its integrity as it subducts. Subduction of oceanic lithosphere is more common due to the negative buoyancy of the oceanic lithosphere, high bulk plate strength, its ability to yield to plastic hinging and serpentinitization of the crust and mantle, which provides lubrication (Burov et al., 2014).

Subduction zones incorporate 3 major lithologies: sediments, mafic igneous crust and ultramafic mantle (Fig. 1.1). After sea water alteration, all lithologies contain hydrous minerals as vectors for water transport into the mantle. One of the most important depths for the volatile cycle is the sub-arc depth ($\sim$120 km) because fluids released here trigger mantle melting which ultimately feeds arc volcanoes. Volatiles released at this depth will be recycled to the surface and volatiles retained at this depth will be further subducted into the mantle and have little effect on the composition of arc lavas. There are many different hydrous phases that are subducted into the mantle (see Table 1.1), but they have different PT stabilities and therefore release their volatiles at different depths and temperatures. However, the depths at which certain PT conditions are met changes depending on the PT path that the subducting

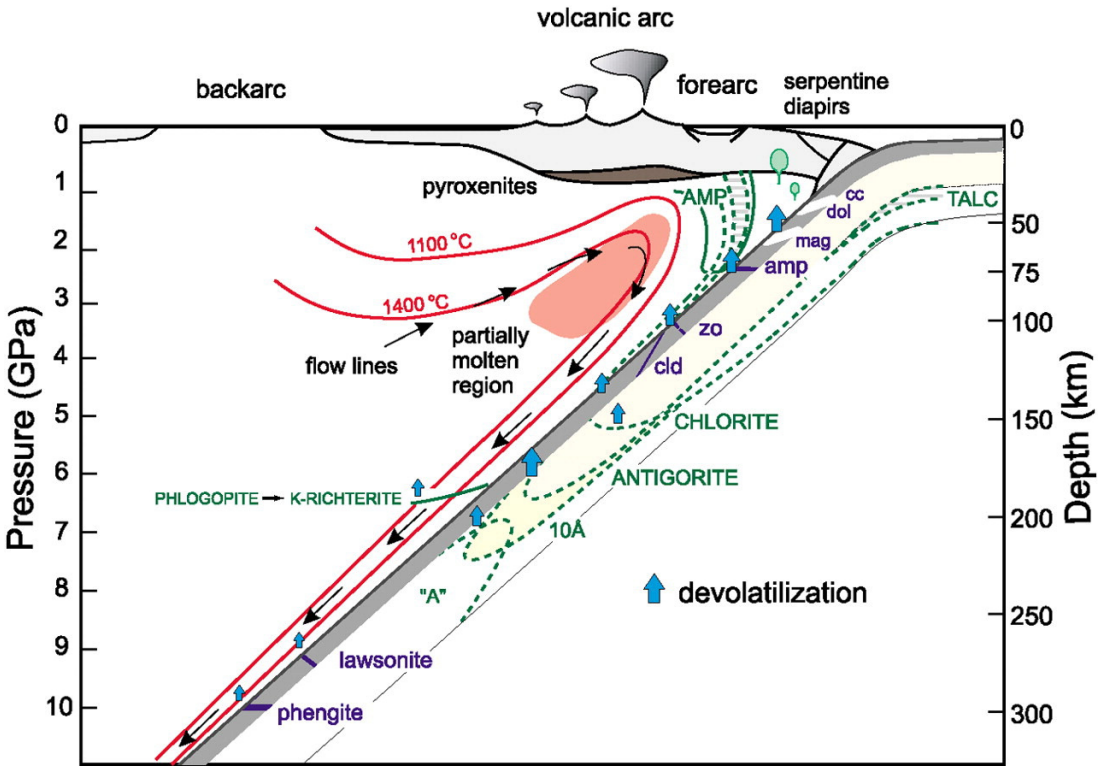

Figure 1.1: Schematic of a subduction zone from Poli and Schmidt (2002). Showing potential hydrous phase stability with depth of subducted slab.

slab takes. The thermal structure of a subduction zone varies considerably across the globe and is mainly controlled by: age of the crust, collision velocity, geometry of the subducting slab and plate structure (Syracuse et al., 2010). This results in a wide range of PT paths that can be taken (as modelled in Fig. 1.2 by Syracuse et al., 2010).

In any thermal regime, sediments are often compacted and dehydrated early on in subduction, with only phengite-rich sedimentary layers retaining any water to significant depths (∼300 km, Schmidt and Poli, 1998). In fact, phengite is stable to such significant depths (5.5 to 11 GPa at 900°C, Domanik and Holloway, 1996) that it will not release its volatiles at sub-arc depths. Hydrous phases in mafic and ultramafic rocks tend to retain their volatiles deeper, but depending on the PT path of the slab, dehydrate at varying depths below the arc. Fig.1.2 shows computationally modelled PT paths for the slab moho by Syracuse et al. (2010). Dehydration of any phase on this diagram occurs to the left of/above the black phase lines. Though this diagram

implies that dehydration is instantaneous, breakdown and release of volatiles is an ongoing process and can be considered to keep occurring for many 10s of degrees above the initial breakdown temperature.

Any phases that breakdown in and around the blue box in Fig.1.2, may provide fluids at the right depths for melt triggering and arc magma supply (this is roughly 120 km depth and before the slab has melted). Zoisite may be an important deliverer of volatiles, however, at lower temperatures it forms lawsonite which will retain much of the zoisite volatile budget. Only the very hottest PT paths will encounter lawsonite destabilisation at the right depth. Amphibole starts dehydrating at lower pressures, but it may have already lost a great deal of its volatiles before reaching sub-arc depths, especially since it contains only 2 wt% H_2O. Serpentine (in the form of the antigorite polymorph) goes through two breakdowns depending on whether brucite (MgOH) is present, both of which occur around the right depth.

Name	**wt% H_2O**
Basalt and sediment systems	
Amphibole	2.1 - 2.3
Zoisite	2
Staurolite	2
Apatite	1.8
Sphene	1.5
Phlogopite	4.8
Lawsonite	11.5
Chloritoid	8
Phengite	4.6
Peridotite system	
Chlorite	13
Talc	4.8
Antigorite	12.5
Clinohumite	1.4-2.9
Brucite	30.9
Phase A	11.8

Table 1.1: From Kawamoto (2006), summary of hydrous phases in subduction zone lithologies accompanied by their average water contents.

Of all contenders serpentine breakdown dominates at sub-arc depths, particularly for colder PT paths, due to its wide range of temperatures at which it is releasing volatiles. This may make it the stronger contender for volatile transport to sub-arc

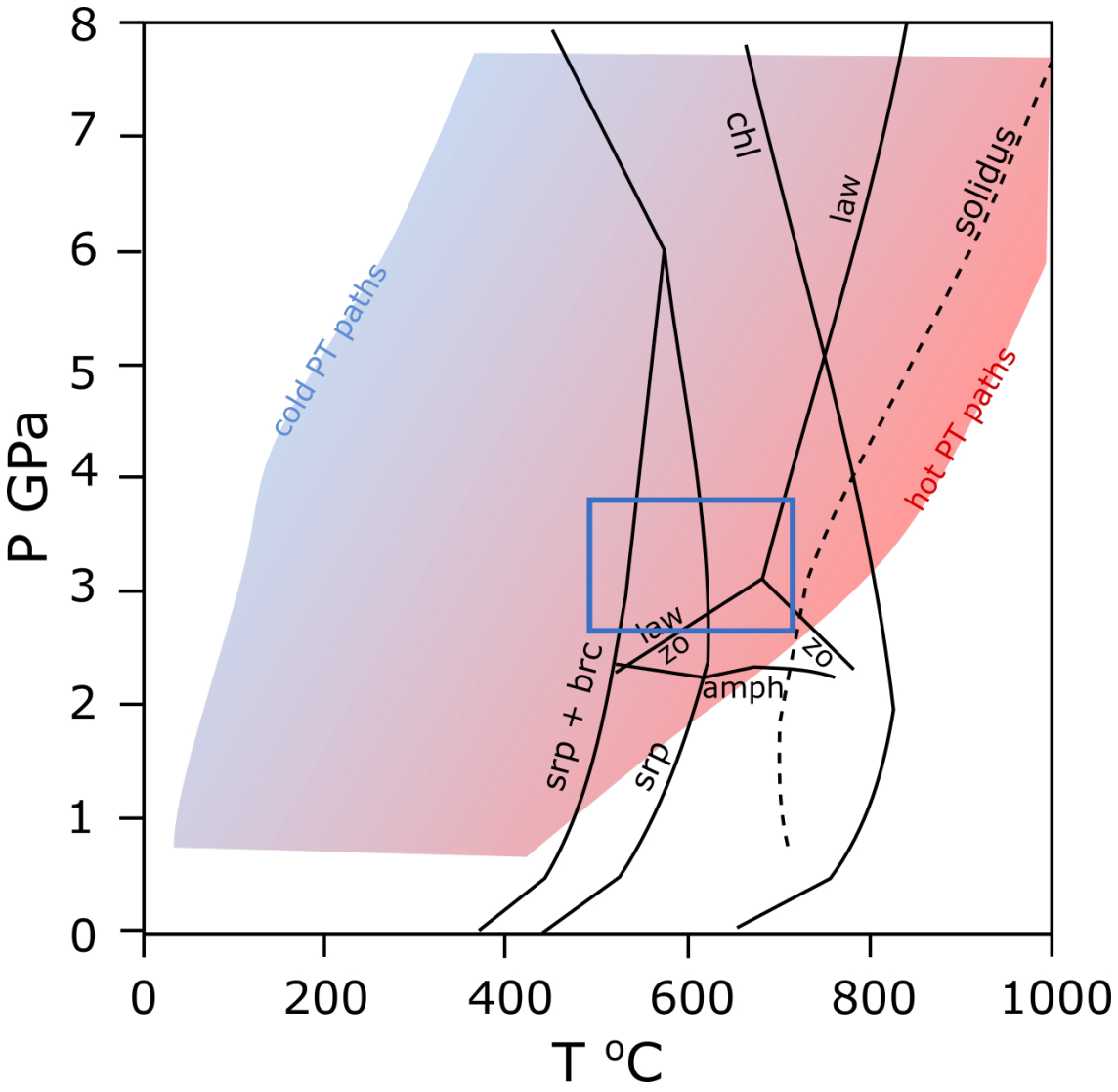

Figure 1.2: Stability of common hydrous minerals in harzburgite: srp = serpentine, brc = brucite and chl = chlorite (Hacker et al., 2003) and in metabasites: law = lawsonite, zo = zoisite and amph = amphibole (Schmidt and Poli, 1998). The red/blue shaded region is taken from Syracuse et al. (2010) and it represents the range of perturbed geotherms for the slab Moho (7km beneath surface). PT paths run from the bottom of the shaded region to the top and generally mimic the shape of the right or left edge. If the PT path runs through a black phase stability line the mineral will breakdown and, in all cases shown here, dehydrate. The blue box highlights all of the dehydration reactions taking place at the slab Moho when it reaches sub-arc depths ($\sim$120 km). Only the warmer PT paths run through the blue box.

depths, though in truth all phases will contribute. Despite this, over half of the PT paths do not encounter any phase-out lines at sub-arc depths and many cold paths do not encounter even serpentine dehydration on this diagram. But it is worth noting that these PT paths have been modelled for the slab moho, which may be a few hundred degrees colder than the slab/mantle wedge interface. Theses phases are still likely to be present at this interface due to crustal lithologies being closer to the slab top and mantle wedge serpentinites being dragged down by the descending slab. This effect of this would shift the PT paths to the left by a few hundred degrees, meaning that many more PT paths would cross phase dehydration lines. In conclusion, the fact still remains that serpentine dehydration not only occurs at the right depth but may also dominate the delivery of volatiles from slabs descending on a cold PT path and play an important role in slabs descending on hotter PT paths.

1.1.2 Subduction interface and exhumation

The subduction interface and exhumation of the subducted slab are intrinsically linked. The structure of the subduction interface depends heavily on subduction zone temperature (see Fig. 1.3). In cold subduction zones, serpentinites are mainly constrained to the oceanic lithosphere which enhances the formation of large ophiolite 'slices', a proposed method for exhumation. In hot subduction zones, serpentinites have significant presence in the mantle wedge which favours the formation of a subduction melange which throws sediments, crust and serpentinites next to and intertwined with one another (Guillot et al., 2015).

Exhumation is a crucial process whereby rocks that have been deeply subducted (to a variety of depths) are brought back to the surface. This is incredibly important as it has allowed us to study rocks from subduction depths. Exhumation is not present in every subduction zone, as strict conditions need to be met for the process to occur. Modelling has shown that for the exhumation of Ultra-High-Pressure (UHP) rocks they must be under a low compression subduction regime, however, this regime is incompatible with the formation of UHP rocks and therefore a switch from high to low compression must occur (Boutelier and Chemenda, 2008). One possible cause is the deceleration of plate convergence. In addition, exhumation is often aided by association with low-density continental rocks (e.g. Burov et al., 2014) or low-density serpentinized mantle (e.g. Luffi et al., 2009; Hermann et al., 2000), channel flow along a weak subduction interface (e.g. serpentinite channel) and underplating of slabs (Guillot et al., 2009). Interestingly, the return flow within a serpentinite channel is enhanced by serpentinite dehydration at sub-arc depths at temperatures of 650 to 700 °C (Guillot et al., 2009). Therefore, Guillot et al. (2009) suggests that the exhumation of HP and UHP subduction zone rocks is perhaps an integral part of the subduction process. Exhumed subduction zone rocks are likely to be representative of normal subduction processes that have been interrupted by a shift in subduction regime.

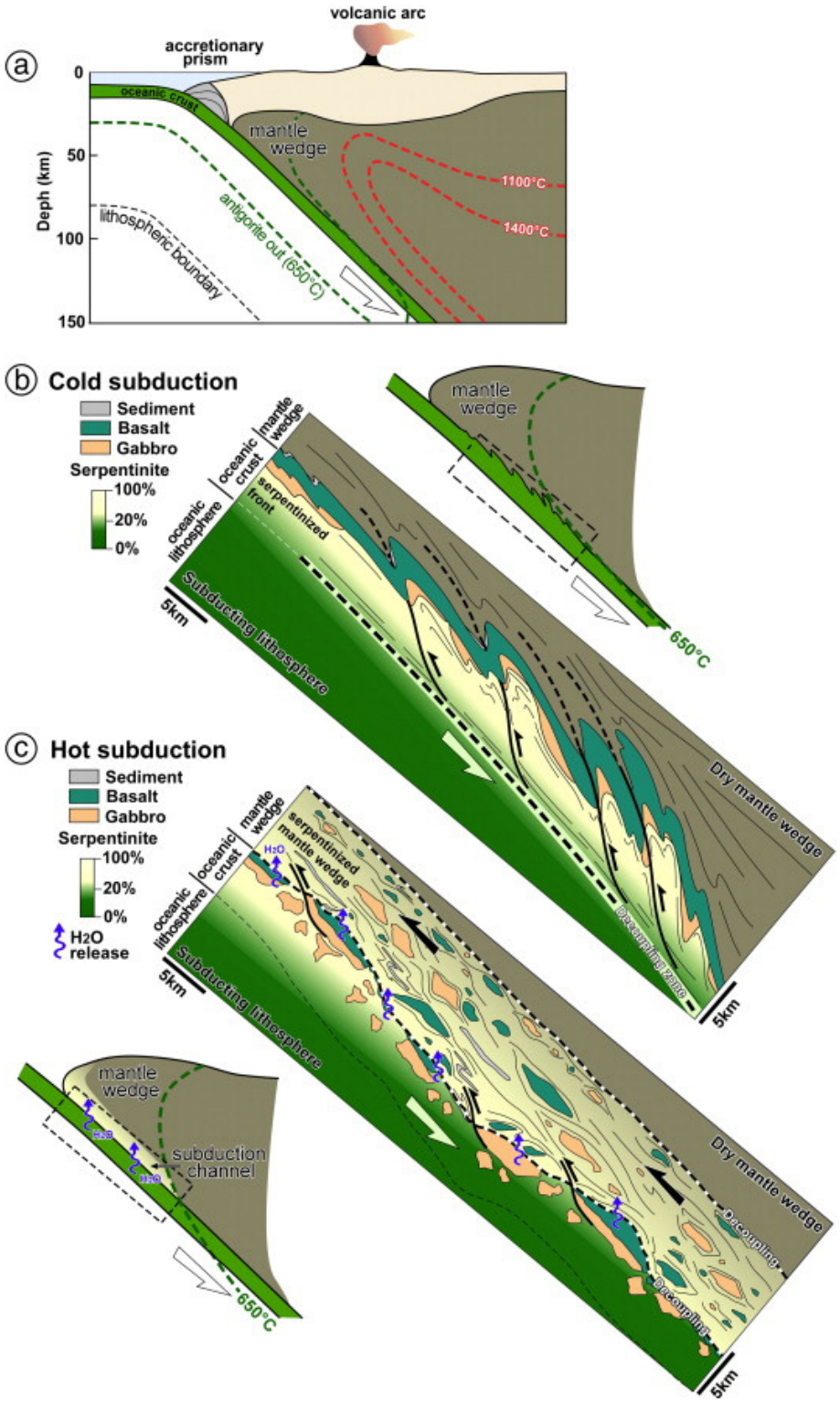

Figure 1.3: Schematic of the interface between the subducted slab and the mantle wedge in both cold and hot subduction settings (Guillot et al., 2015). This diagram is a culmination of: field observations of HP subduction zone rocks in the western Alps, Cuba and western Himalaya, and thermo-mechanical numerical modelling.

1.2 Mantle-metasomatising fluids

The source of the mantle-metasomatising fluid is the centre of wide debate. Since we cannot directly sample these deep fluids, the best method for identifying the fluid's source is to compare the inputs (sediments, crust and upper mantle) with the outputs (arc lavas) of a subduction zone. Whichever input's chemistry matches the best with the output must be the most prevalent source of fluids at sub-arc depths. Early models accounted for the source of these fluids by the decomposition of amphibole or chlorite. The fluid then travels into the sub-arc mantle and triggers melting. Other hydrous phases such as serpentine were originally discounted based on phase stability and projected geotherms for subducting slabs (Tatsumi, 1986). In addition, researchers found evidence for large amounts of H_2O released by the blueschist-eclogite transition, of which amphibole is a prominent phase, in oceanic crust which may play a role in generating arc magmas (Peacock, 1993). This is further supported by oxygen isotopes where δ^{18}O values present in melt inclusions from island arcs are elevated above mantle values (Eiler et al., 1998), which suggests that arc magma was produced by melting mantle that was metasomatised by ocean crust-derived fluids. Subsequent models invoked the role of sediments as the main source of fluid. Arguments centered around geochemical similarities between sediments and arc lavas, such as those in Plank and Langmuir (1993) who found correlations between increased K, Ba, Sr and Th enrichment in arc basalts with increased subduction of sediments.

With the more recent re-evaluation of serpentine stability (Ulmer and Trommsdorff, 1995) and subduction geotherms (Syracuse et al., 2010), serpentinites were also re-evaluated as a potential fluid source. Enrichment in trace elements, particularly Li, B, Large Ion Lithophiles (LILE), Light Rare Earth Elements (LREE) and U can be explained by serpentinite dehydration (Spandler et al., 2014). The truth is that with only this data, there is no reliable way to determine the source of the mantle-metasomatising fluids; each of the possible sources (metabasites, sediments or serpentinites) have too similar compositions of LILEs and Fluid-mobile elements (FME) and all are reflected in the composition of arc lavas. This is why B and its isotopes have been increasingly used to study subduction zone fluid behaviour.

1.2.1 Boron as a fluid tracer

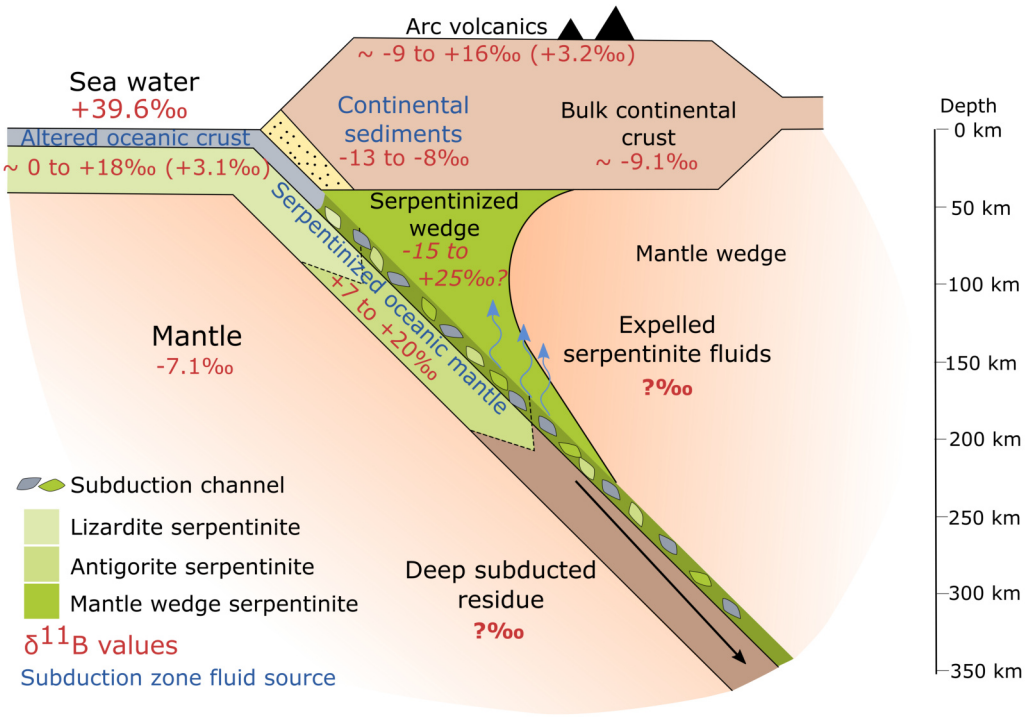

Figure 1.4: Schematic of the fluid sources in a subduction zone and their whole-rock B isotope ratios. Data from De Hoog and Savov (2018) and Marschall et al. (2017). Polymorph of serpentine switches from lizardite to antigorite around 300°C to 390°C, which is shown by the dashed boundary between the light and dark green patches on the downgoing slab. Mantle wedge serpentinite (the darkest green) is formed by dehydration of crust and sediments early on in subduction.

B will dissolve in aqueous fluids and is considered fluid mobile. It has an ionic radius of 0.2 A and likely substitutes for Si $^{4+}$ or Al $^{3+}$ in silicate structures in tetrahedral coordination (Leeman and Sisson, 2002), with tourmaline being a notable exception. In fluids, B commonly forms one of two structures: Boric Acid ($B(OH)_3$) or Borate ($B(OH)_4^-$) (Kakihana et al., 1977; Leeman and Sisson, 2002). With a pKa of 9.24, Boric acid dominates in fluids with neutral and low pH and Borate dominates at high pH. ^{11}B preferentially resides in trigonal coordination and ^{10}B in tetrahedral coordination and it is this characteristic of B that enhances the fractionation of its two isotopes. The isotopes will be fractionated in fluids at low and high pH or between phases that

have different co-ordinations for B.

Fig.1.4 shows the current estimates of the δ^{11}B of each subduction zone lithology. The fractionation of B isotopes between these reservoirs is large (Fig. 1.4): seawater (δ^{11}B +39.6‰, Foster et al., 2010) mantle (δ^{11}B -7.1 ‰) (Marschall et al., 2017), altered oceanic crust (δ^{11}B +0 to +18 ‰: average δ^{11}B +3.4 ‰), continental sediments (δ^{11}B -13 to -8 ‰), marine sediments (δ^{11}B +2 to +26 ‰) and serpentinized peridotitic mantle (δ^{11}B +7 to +20 ‰) De Hoog and Savov (2018) (and references therein) all show distinctive values. The value of the mantle is more or less homogeneous and the most recent value (δ^{11}B -7.1 ‰) is derived from 56 MORB samples from the Mid-Atlantic ridge. Although the value has varied over the years, with the highest MORB values around 0 ‰ and the lowest around -12.5 ‰ (Marschall et al., 2017), which have all been measured in unaltered MORB glasses. OIB samples have also shown light δ^{11}B values: -7.9 ‰ in La Réunion and -10.5 ‰ in La Palma (Walowski et al., 2019). This suggests that the B isotope signature of the mantle is both relatively homogeneous and light. This is in stark contrast to serpentinites and altered oceanic crust (AOC) which have much heavier signatures. There is still some debate over the B isotope signature of mantle wedge serpentinites, hence the wide range on Fig 1.4. Mantle wedge serpentinites form early on in subduction by the inundation of the mantle wedge by slab fluids. Benton et al. (2001) suggest that slab fluids at these depths are more highly enriched in ^{11}B, which would imply a heavier B isotope signature for mantle wedge serpentinites ($\sim$ the +15‰ found in serpentine mud volcanoes). However, studies of natural mantle wedge serpentinites and their B isotopes are rare, yet one (Martin et al., 2016) find quite light isotopic signatures for mantle wedge serpentinite from the Guatemala suture zone (–14.4‰ to +9.7‰).

The literature is even less sure on the δ^{11}B signature of expelled slab fluids and the deep subducted residue. Recent studies have found blue boron-bearing diamonds from subduction zone settings (Smith et al., 2018), implying that B is subducted to depths below 300 km. However, they did not measure the B isotope signature of the diamonds. So, we know that B is deeply subducted, but we don't know its B isotope

signature and thus we don't know where it is from. Expelled fluids have been measured for FME (Tenthorey and Herman, 2004; Spandler et al., 2014) and even Li isotopes (Wunder et al., 2009), but never for B isotopes meaning that we do not know for sure the B isotope composition of sub-arc fluids. This is incredibly important for tracing this fluid, understanding its origins and identifying the various contributions of different fluid sources in a subduction zone. Many models currently assume (e.g. Scambelluri and Tonarini, 2012) that all B escapes during dehydration and that there is therefore no fractionation of the isotopes. But the discovery of B retention in secondary olivine both experimentally (Tenthorey and Herman, 2004) and naturally (De Hoog et al., 2014) could indicate that fractionation does occur during dehydration but there are currently no studies into this issue at this time.

Our best guess for the source of volatiles in subduction zones is well discussed in the literature. In addition to the earlier discussion of mineral stability around Fig. 1.2, matching up the B isotopic signature of the subduction inputs and outputs further supports serpentine as the prominent volatile deliverer. Early work on the B composition of arc lavas reported high δ^{11}B values (-2.3 to +7.3 ‰) (Palmer, 1991; Ishikawa and Nakamura, 1994) which they put down to a mixture of fluids from altered ocean crust and sediments. However, others argue that in order to create the δ^{11}B signature of arc lavas, the mantle must be mixed with a heavy B source (Scambelluri and Tonarini, 2012). This heavy δ^{11}B source could be marine sediments (δ^{11}B +2 to +26 ‰), but sediments experience higher temperature owing to their position on top of the slab and therefore dehydrate often below the forearc (Van Keken et al., 2011). The source could be oceanic crust, but ongoing dehydration of amphiboles releases ^{11}B into the fluids, leaving a much lighter residue at sub-arc depths. Therefore, the source is most likely serpentinite (e.g.Tonarini et al., 2007, 2011; Scambelluri and Tonarini, 2012; Leeman et al., 2017; De Hoog and Savov, 2018).

Serpentinites are a good candidate for volatile transport to sub-arc depths due to the stability of their hydrous phases to higher pressures and temperatures (antigorite is stable up to 600 to 750°C and 5.8 GPa and chlorite up to 750 to 800°C, Ulmer

and Trommsdorff, 1999; Bromiley and Pawley, 2003; Fumagalli and Poli, 2005), their widespread presence in hydrated forearc mantle wedge and subducted lithosphere (up to 30% of the upper 2 km oceanic lithosphere e.g. Contreras-Reyes et al., 2007; Ranero et al., 2003) and high water content (in excess of 13 wt % H_2O in hydrous phases, Ulmer and Trommsdorff, 1999). But before we delve into the involvement of serpentinites in the delivery of volatiles to the mantle, we must first discuss their formation and prograde pathway during subduction.

1.3 Serpentinites

1.3.1 Serpentinization reaction

The generalised serpentinization reaction occurs as follows:

$$Olivine + H_2O = serpentine + brucite + magnetite + H_2(aq) \tag{1.1}$$

(Evans, 2010)

Serpentinization is a hydrating metamorphic reaction that occurs when water comes into contact with ultramafic olivine-rich rocks. Serpentinites are ultramafic, low-silica rocks and therefore will only form from ultramafic, olivine bearing lithologies. Mantle olivine and pyroxene break down in the presence of water and predominantly form serpentine. There are three polymorphs of serpentine; lizardite, chrysotile and antigorite. Lizardite and chrysotile are the low temperature polymorphs and are the dominant serpentine species up to 300 °C (Schwartz et al., 2013) (see Fig 1.5). Lizardite and chrysotile differ structurally: chrysotile forms pale fibrous strands and accounts for the majority of commercial asbestos. Lizardite forms tabular shards and is by far the most common type of serpentine and makes up the bulk of low Pressure-Temperature (PT) serpentinites.

Many studies into the serpentinization processes document a similar process of lizardite formation (e.g. Rouméjon et al., 2018; Viti and Mellini, 1998; Rouméjon and Cannat, 2014). These studies are based on observations of serpentine texture. Mesh

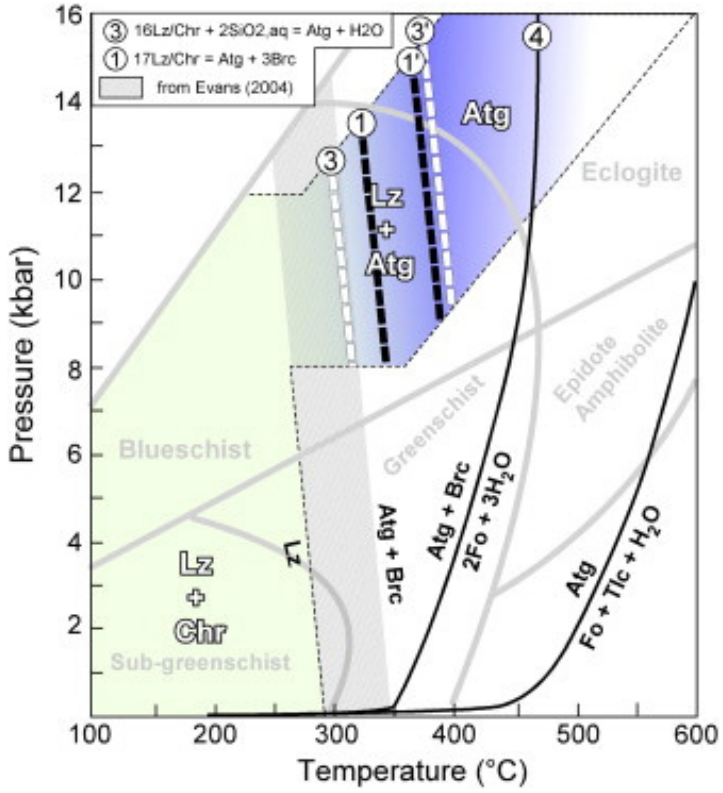

Figure 1.5: Phase diagram from Schwartz et al. (2013). 1 and 3 refer to the onset of reactions 1 and 3 and 1' and 3' refer to the end of these reactions. Lizardite (lzd) and antigorite (atg) coexist between 320°C and 390°C above which lzd is completely replaced by atg. Above 460°C (reaction 4) secondary olivine is stable.

texture and bastite form after olivine and pyroxene respectively. An interconnected network of microfractures develops around the olivines and defines the mesh cells (Rouméjon et al., 2018; Rouméjon and Cannat, 2014). This provides a pathway for serpentinization fluids. Olivine is less stable than pyroxene and therefore reacts with infiltrating fluids first. Lizardite nucleates as flakes along the edge of the olivine and gradually layers grow upon layers as more olivine is metamorphosed. After this, the mesh cores are serpentinized to form lizardite and pyroxenes to form Al-rich bastite (Viti and Mellini, 1998). During lizardite serpentinization the low temperatures cause the olivine to dissolve incrementally, which fuels the Mg-rich lizardite formation but does not allow the olivine to adjust its own composition, i.e. the residual olivine does not become enriched in Fe as a consequence (Evans, 2010). Therefore, to satisfy mass balance, Fe minerals such as magnetite or awarite form from the excess Fe (Evans, 2010, 2008). Initially, much of this Fe can be taken into the forming serpentine (up to 80%) during the first 75% of the reaction (Andreani et al., 2013), beyond which the formation of magnetite spikes.

Antigorite is the high temperature polymorph and either forms at a higher temperature directly from olivine or during prograde metamorphism of lizardite (and chrysotile) (Moody, 1976). Antigorite starts to replace lizardite from 300°C and over temperatures of 390°C lizardite is no longer present and antigorite is dominant (Schwartz et al., 2013). The transition from lizardite to antigorite occurs as either water conserving when brucite is involved or water producing when brucite is absent, see equations 1.2,1.3 and 1.4 (Evans, 2004):

$$17Liz/Chr = Atg + 3Brc \tag{1.2}$$

$$16Liz/Chr + 2SiO_2(aq) = Atg + H_2O \tag{1.3}$$

$$20Liz/Chr = Atg + 6Fo + 9H_2O \tag{1.4}$$

Lzd/Chr = Lizardite/Chrysotile $Mg_3Si_2O_5(OH)_4$

Atg = Antigorite $Mg_{48}Si_{34}O_{85}(OH)_{62}$

Fo = Forsterite Mg_2SiO_4

Brc = Brucite $Mg(OH)_2$

Antigorite serpentinization directly from olivine occurs at higher temperatures than lizardite serpentinization. The higher temperatures allow Fe enrichment of the olivine and causes little to no formation of magnetite. Therefore, the presence of large amounts of magnetite in antigorite serpentinite indicates that original lizardite serpentinization underwent prograde metamorphism (Evans, 2010).

1.3.2 Prograde metamorphism of antigorite serpentinites

The most important reaction for volatile cycling is the breakdown of antigorite. This expels fluids at sub-arc depths (∼120 km) through a series of metamorphic reactions (Scambelluri et al., 2004):

$$Atg + Brc = Fo + fluid\ at\ \ 450^oC\ and\ 1.4\ GPa \tag{1.5}$$

$$Atg = Fo + Tlc + fluid\ at\ \ 625^oC\ and\ 1.2\ GPa \tag{1.6}$$

$$Atg = Fo + Opx + fluid\ at\ \ 625^{o}C\ and\ 3\ GPa \tag{1.7}$$

Atg = Antigorite $Mg_{48}Si_{34}O_{85}(OH)_{62}$

Fo = Forsterite Mg_2SiO_4

Brc = Brucite $Mg(OH)_2$

Tlc = Talc $Mg_3Si_4O_{10}(OH)_2$

Opx = Orthopyroxene $(Mg, Fe^{2+})_2Si_2O_6$

Metamorphic olivines can be distinguished from primary (relict) olivine both texturally and chemically. Metamorphic olivines tend to have higher Mg# (88.7 to 96.5) due to Fe sequestration in magnetite during serpentinization, higher MnO (0.2 to 0.5 wt %), and higher B most likely due to their formation by brucite and/or antigorite breakdown. Texturally, metamorphic olivines in this study form veins or elongate clusters (see Fig 3.2), and such veins are often associated with dehydration reactions (López Sánchez-Vizcaíno et al., 2009; Healy et al., 2009), whereas relict olivines are often preserved in the cores of serpentine mesh texture (e.g. Rouméjon and Cannat, 2014). It is worth noting here, that, using this definition, the olivines presented in this thesis are metamorphic in origin and, by association with antigorite, formed from serpentine, not brucite, break down.

1.4 Subducted Serpentinites

Geophysical evidence indicates widespread presence of serpentinites in subduction zones. This is inferred by the combination of lower seismic wave velocities and an increase in the ratio between P-wave and S-wave velocity (Vp/Vs) (Reynard, 2013). There are two types of serpentinite that may contribute to the volatile cycle. They are categorized by their location in the subduction stratigraphy and method of formation: Abyssal and Mantle wedge serpentinites.

1.4.1 Oceanic crust serpentinites

Abyssal serpentinites are predominantly formed at slow or ultraslow spreading ridges where longer timescales and numerous faults allow the exhumation of peridotite to the ocean floor and the deep circulation of hydrothermal fluids, as evidenced by ODP drill cores (e.g. Skelton and Valley, 2000). O and H isotopes reveal that the serpentinizing fluid is sea-water (Fruh-Green et al., 1996; Agrinier and Cannat, 1997). These exhumed peridotite terrains can be tens of km wide and estimated 95-100% serpentinized to a depth of 2-3 km (Skelton and Valley, 2000). However, these serpentinites are thought to be scarce or absent from fast spreading plates, except where uplift of peridotite has occurred or pathways between the ocean and mantle have been opened by earthquakes or possibly slab bend faults (Ranero et al., 2003). Addition of water and B to oceanic mantle is likely decoupled due to large differences between the necessary water/rock ratios required to fully serpentinize olivine (0.13) and required to add the observed B to serpentine (10-50) (McCaig et al., 2018). Such high water/rock ratios can only be achieved in 'multipass' circulation, something that is unlikely in fast spreading plates (McCaig et al., 2018).

1.4.2 Mantle wedge serpentinites

Mantle wedge serpentinites form at T < 700 °C when the mantle is inundated and serpentinized by slab fluids. These serpentinites are down-dragged by the subducted slab deeper into the upper mantle (e.g. Deschamps et al. 2010; Hyndman and Peacock 2003). Mantle wedge serpentinites may contribute significantly to the generation of arc magma (Hattori and Guillot, 2003). It is commonly observed that δ^{11}B decreases in arc volcanoes with increasing distance from the subducted slab below (Benton et al., 2001). This implies that shallow dehydration fluids have δ^{11}B that is more positive than deeper ones. Despite not being deep enough to account for arc lava genesis, this B isotopic signature from shallow dehydration can be captured in mantle wedge serpentinites and dragged down to sub-arc depths. Percentage serpentinization of the mantle wedge increases with increasing temperature of subduction due to increased dehy-

dration of the shallow slab (Reynard, 2013; Van Keken et al., 2011). Down-dragged mantle wedge serpentinites are implied to account for high δ^{11}B values in the South Sandwich Islands lavas (Tonarini et al., 2011) and Cerro del Almirez (De Hoog and Savov, 2018) which range from +7 to +23‰. Contrary to this, mantle wedge serpentinites along the Guatemala Suture Zone are predominantly negative (-14.4 to +9.3‰, Martin et al., 2016), which is explained by the addition of negative fluids from altered oceanic crust at 50-70km depth. This may help to explain the range in arc lava compositions seen in Fig. 1.4.

1.5 Water transport mechanisms

Deformation has a key role in the breakdown of serpentine and the release of volatiles into the mantle wedge. Fluid channelisation has been observed in ophiolites (e.g. Prigent et al., 2018; Angiboust et al., 2014), where fluid transport is concentrated along shear zones. However, fluid transport may also occur on the micro scale. Antigorite breakdown is concentrated at crystal boundaries or kink axial planes. These planes are sites of enhanced reactivity, resulting in enhanced breakdown and formation of dehydration products (Viti and Hirose, 2008). Dehydration experiments by Tenthorey and Cox (2003), show that during the dehydration of serpentine there is an early rapid increase in porosity and permeability allowing the fluid to drain from the rock. This increase in porosity accompanies the growth of secondary phases: olivine and talc (and fluids). Plümper et al. (2017) report a similar notion; that dehydration is localised at specific microsites which generate porosity and vein networks. This channelizes fluids and results in large-scale fluid escape and transfer from the serpentinite to the mantle wedge without the need for brittle failures and opening of fault pathways. However, this high permeability is short lived owing to high pressures, therefore, as soon as enough fluid has evacuated the system, the pore structures would collapse due to brittle failure or creep (Tenthorey and Cox, 2003).

Local generation of porosity may induce the phenomena known as 'porosity waves' (Connolly, 2010). The dehydration reaction locally induces interconnected porosity

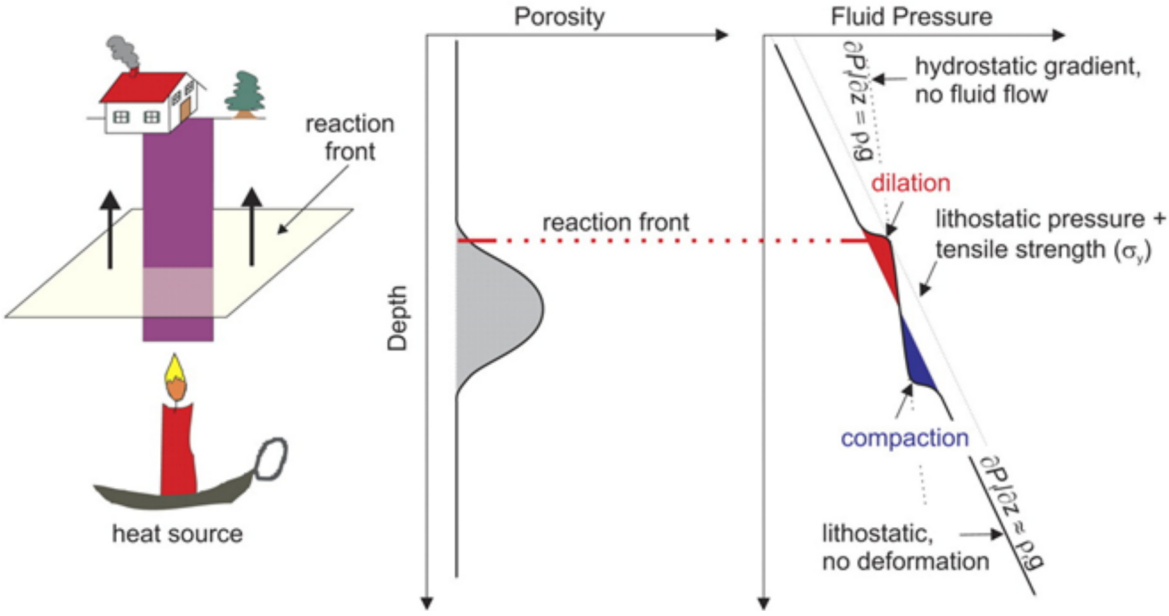

Figure 1.6: Diagram and caption taken directly from Connolly (2010): '*Conceptual model of metamorphic devolatilization. The reaction leaves a region of elevated porosity and permeability in its wake. Fluid flux is proportional to the permeability and the difference between the fluid pressure gradient and the hydrostatic gradient. In the absence of deformation, conservation of mass requires that this drainage flux must also be the flux within the reacted horizon with permeability k » k0; this is possible only if the difference between the fluid pressure gradient and the hydrostatic gradient is small. However, this near-hydrostatic fluid-pressure gradient within the reacted rocks gives rise to an effective pressure, P - Pf, gradient of* $\sim \Delta\rho g$*, so that pore fluids become increasingly underpressured relative to the lithostat with depth within the high-porosity zone and, conversely, increasingly overpressured toward the reaction front. The resultant effective pressures are the driving force for deformation and fluid expulsion*'.

which increases fluid pressure. This pushes the local hydrostatic gradient beyond the lithostatic gradient which results in a region of dilation and a region of compaction at this porosity 'wave'. This local dilation creates permeable fluid pathways (see Fig.1.6). Compaction works to squeeze fluids towards the dilation which maintains the high fluid pressure and ultimately propagates the porosity wave further (Richter and McKenzie, 1984). This local deformation and formation of micro-networks may aid in the transport of fluids from dehydrating serpentinites to the mantle wedge. However, porosity waves create instantaneous porosity that is not long lasting and suggests that any fluids present would be driven off immediately, without time for equilibration. So this is not a phenomenon responsible for driving fluids away in a system that displays any level of equilibrium. In this case, grain boundary fluid migration (as observed in experiments by Schenk and Urai, 2005), whereby fluid forms along the crystal edges and as more crystals breakdown the edges join up to form connected grain boundary networks along which fluid can move. This method does not require immediate removal of fluids thereby allowing time for equilibration.

Local heterogeneities in reaction kinetics are thought to be responsible for rare formation of spinifex-like or Jackstraw textured olivines in partially dehydrated serpentinites (Padrón-Navarta et al., 2011). They suggest that jackstraw olivines grow where reaction affinities (the 'driving force' of the reaction) are high. The presence of these olivine textures in serpentinites from Cerro del Almirez and Val Malenco (Lafay et al., 2019) suggests that these dehydration reactions are to some extent controlled by localised heterogeneities.

1.6 The knowledge gap

Boron is a highly valuable tool in understanding subduction zone fluid fluxes and sources. However the global database of B compositions of serpentinite is lacking, leaving many interpretations up to guess work. This leaves the contribution of serpentinites to arc magmas relatively unconstrained (point 3 of outstanding work in De Hoog and Savov, 2018). In addition this lack of data hinders our understanding of B supply

to the deeper mantle by transport in metamorphic olivine (point 4 of outstanding work in De Hoog and Savov, 2018). In general there is also a lack of understanding of B isotope behaviour during serpentinite dehydration with experimental studies focusing on B concentrations only, in fact Marschall (2018) states that there is a noticeable lack in fluid-mineral B isotope fractionation data in serpentinites.

This thesis aims to fill these knowledge gaps by studying the B isotopic composition of natural oceanic and mantle wedge serpentinites, contact aureole serpentinites and experimentally grown olivines. This is the first study of *In situ* δ^{11}B and B in serpentine and metamorphic olivine in partially dehydrated serpentinites and is the first study that can comment on the behaviour of B and its isotopes during antigorite breakdown. As a result this thesis provides an insight to the δ^{11}B and B of serpentinite dehydration fluids and the dehydrated residue. In addition, this data allows us to discriminate oceanic serpentinites from fore-arc serpentinites and provides direct evidence for large scale fluid flow and inter-connectivity of lithologies at the slab-mantle interface. These data will also contribute to a database of metamorphic olivine B isotopic compositions, allowing characterisation of the mantle-headed downgoing slab. For the first time, B isotope data from serpentinites in contact aureole settings is presented and describes fluid movement during contact metamorphism. The current lack of fluid-mineral B isotope fractionation data in serpentinites is partly addressed by experiments described in Chapter 5. These are the first of their kind to look at the partitioning of B isotopes between olivine and fluid at different temperatures and pH. In summary I believe that this thesis builds upon and adds significantly to current cutting edge research into the role of serpentinites in subduction zones.

1.7 Thesis overview

The overall aim of this thesis is to better constrain the role and environment of serpentinite dehydration in subduction zones. Primarily I have used Boron isotopes to gain a better picture of serpentinite dehydration. This has been a 3-pronged approach: firstly studying partially-dehydrated, natural, subduction-zone serpentinites, secondly study-

ing partially-dehydrated, natural, contact-aureole serpentinites and lastly conducting olivine-fluid B partitioning experiments. These 3 prongs form the 3 main discussion chapters. The following section briefly describes all chapters in this thesis and their aims.

1.7.1 Chapter outline

Methods

The aim of this section is to describe all methods undertaken for the collection of data presented in Chapter 3 and Chapter 4. This is consolidated here because many of the analytical methods are shared between these 2 discussion chapters.

Subduction-zone serpentinites from Alps and Betic Cordillera

The aim of this section is to explore the B concentration and isotopic data collected from partially-dehydrated Alpine and Spanish ophiolitic serpentinites. I sourced samples from these particular areas because they are well studied and characterised which allowed us to focus purely on the B isotopes. The sites are well understood and have many years of solid research into their geological history, which is detailed in the chapter. This study provides a new insight into fluid processes and pathways, and the composition and volume of fluids moving through subduction zones. Its also explores the potential implications this has for the contribution of serpentinites to mantle-metasomatising fluids and the consequent formation of arc magma.

Contact-aureole serpentinites from Valmalenco, Italy

The aim of this section is to explore B concentration and isotopic data collected from contact-aureole serpentinites from Valmalenco, Italy. I chose these samples to study because I hypothesized that they would form an interesting comparison to the serpentinites in subduction zones. In addition they are well studied and their geological history is reasonably well constrained. I find that the behaviour recorded in these serpentinites is very similar to the behaviour recorded in subduction zone serpentinites, both settings recording infiltration of external fluids during olivine growth.

Experimental metamorphic olivine growth

The aim of this chapter is to discuss the data from the olivine growth experiments. It also discusses in detail the experimental approaches, both what worked and what didn't and lessons learned. I find interesting B isotope fractionation between olivine and fluid during the experiments in all conditions

Conclusions/Further work

An itemized list of the conclusions of each chapter and a list of suggested further work to expand on the conclusions of this thesis.

Chapter 2

Analytical Methods

"It's the job that's never started that takes the longest to finish."
J.R.R. Tolkien, The Lord of the Rings

2.1 Foreword

Fig.2.1 shows the step by step process for sample preparation and analysis taken by every sample in this thesis. Here follows a detailed description of the different analytical and data collection methods employed.

2.2 Major element analyses

Major element analyses were conducted by electron microprobe analysis (EMPA) at the University of Edinburgh. Samples were carbon coated before analysis. Set-up was tailored to each phase individually, see Table 2.1. Spot size varied from 2 to 8, depending on the phase, and Kv was set at 15. Current (nA) varied from 2 to 100 depending on phase and element. Peak counting times varied from 20 to 120s and background times varied from 10 to 100s. Data was calibrated using in house mineral standards.

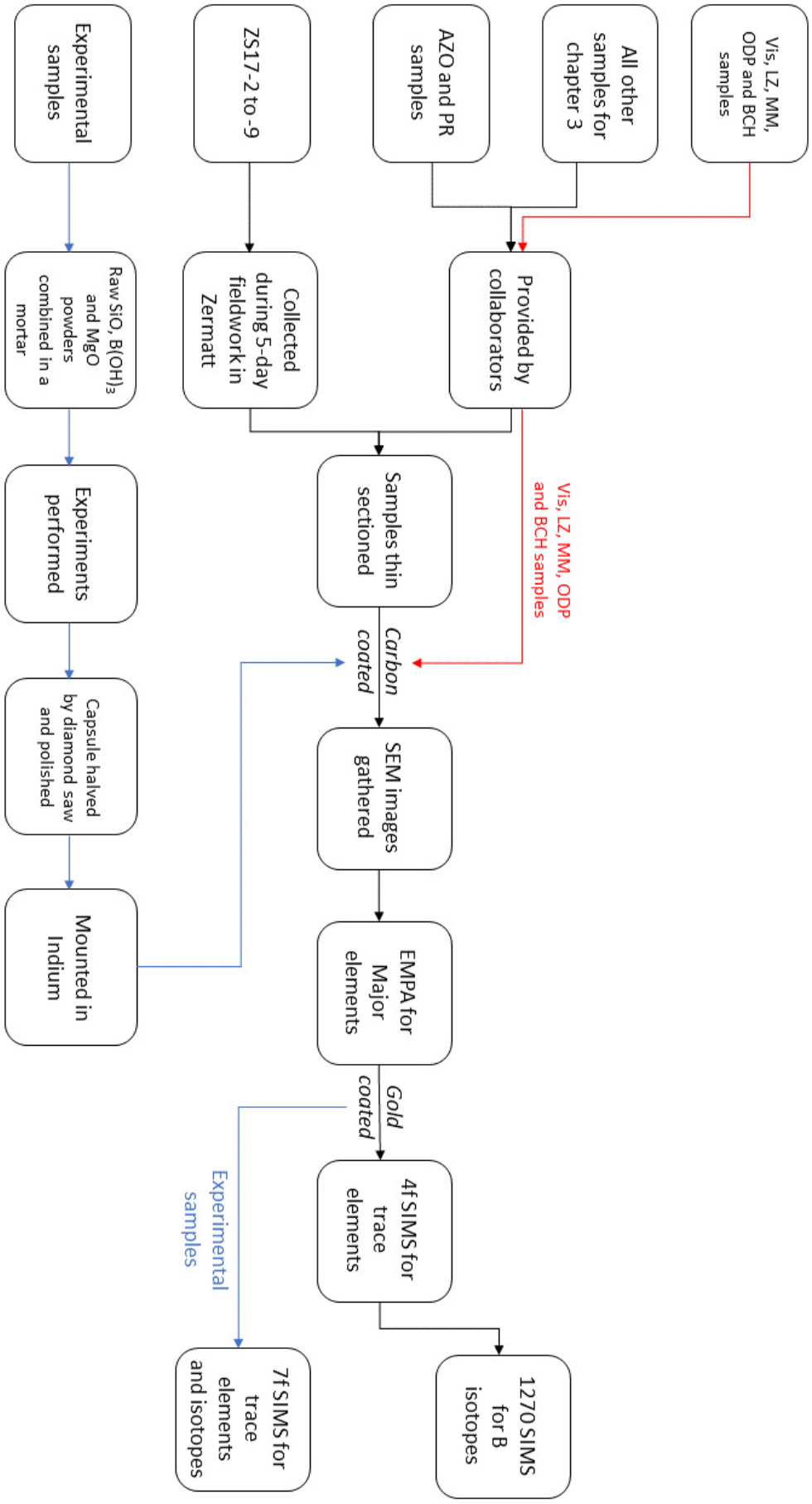

Figure 2.1: Sample analysis and preparation step by step guide for all samples in this thesis.

Table 2.1: EMPA beam conditions for all analytes. HV(kv) 15 for all analyses. Cond. = if different elements being measured for the same phase require a different current (I), a new condition would be made.

Mineral	Size (μm)	Cond.	I (nA)	Element	Pk time (s)	Bg time	Calibration
Ol	2	1	2	Mg	20	10	Forsterite_MgSp5_SiSp4
				Si	20	10	
				Fe	20	10	Fayalite_FeSp2
		2	100	Na	60	30	Jadeite-BL7_NaSp5
				Al	100	80	Spinel-BL8_MgSp5_AlSp4
				Ca	20	10	Wollastonite-BL7_SiSp4_CaSp1_CaSp3
				Mn	60	50	PuMn -BL8_MnSp2
				Ni	60	40	PuNi -BL8_NiSp2
				Ti	40	20	Rutile-BL8_TiSp1_TiSp3
Cpx	2	1	2	Mg	20	10	Forsterite_MgSp5_SiSp4
				Si	20	10	
				Al	20	10	Spinel-BL8_MgSp5_ AlSp4
				Ca	20	10	Wollastonite-BL7_SiSp4_CaSp1_CaSp3
				Fe	20	10	Fayalite_FeSp2
		2	100	Na	50	25	Jadeite-BL7_NaSp5
				K	20	10	Orthoclase-BL7_K Sp1_K Sp3

Mineral	Size (μm)	Cond.	I (nA)	Element	Pk time (s)	Bg time	Calibration
				Mn	60	50	PuMn -BL8_MnSp2
				Ni	60	40	PuNi -BL8_NiSp2
				Ti	50	25	Rutile-BL8_TiSp1_TiSp3
Srp	8	1	2	Mg	20	10	Forsterite_MgSp5_SiSp4
				Si	20	10	
				Fe	20	10	Fayalite_FeSp2
		2	60	Na	60	30	Jadeite-BL7_NaSp5
				Al	100	80	Spinel-BL8_MgSp5_AlSp4
				Ca	40	20	Wollastonite-BL7_SiSp4_CaSp1_CaSp3
				Mn	60	50	PuMn -BL8_MnSp2
				Ni	60	40	PuNi -BL8_NiSp2
				Cr	60	30	PuCr -BL8_CrSp2_123
Chl	8	1	2	Mg	40	20	Forsterite_MgSp5_SiSp4
				Si	20	10	
				Al	20	10	Spinel-BL8_MgSp5_ AlSp4
				Fe	40	20	Fayalite_FeSp2
		2	60	Na	60	30	Jadeite-BL7_NaSp5
				Al	100	80	Spinel-BL8_MgSp5_AlSp4

Mineral	Size (μm)	Cond.	I (nA)	Element	Pk time (s)	Bg time	Calibration
				Ca	40	20	Wollastonite-BL7_SiSp4_CaSp1_CaSp3
				Mn	60	50	PuMn -BL8_MnSp2
				Ni	60	40	PuNi -BL8_NiSp2
				Ti	20	10	Rutile-BL8_TiSp1_TiSp3
Talc	8	1	2	Mg	20	10	Forsterite_MgSp5_SiSp4
				Si	20	10	
		2	60	Na	60	30	Jadeite-BL7_NaSp5
				Al	100	80	Spinel-BL8_MgSp5_AlSp4
				Ca	40	20	Wollastonite-BL7_SiSp4_CaSp1_CaSp3
				Mn	60	50	PuMn -BL8_MnSp2
				Ni	60	40	PuNi -BL8_NiSp2
Spinel	2	1	2	Ti	30	15	Rutile-BL8_TiSp1_TiSp3
				Fe	20	10	Fayalite_FeSp2
		2	60	Al	60	40	Spinel-BL8_MgSp5_AlSp4
				Si	20	10	Wollastonite-BL7_SiSp4_CaSp1_CaSp3
				Ca	120	100	Wollastonite-BL7_SiSp4_CaSp1_CaSp3
				Mn	60	50	PuMn -BL8_MnSp2
				Ni	60	40	PuNi -BL8_NiSp2
				Cr	60	30	PuCr -BL8_CrSp2

Mineral	Size (μm)	Cond.	I (nA)	Element	Pk time (s)	Bg time	Calibration
				Zn	50	30	PuZn -BL8_ZnSp2
				Mg	120	100	Spinel-BL8_MgSp5_AlSp4

2.3 Fluid-mobile element concentration analyses

B, Li, F, Cl and H_2O data were obtained using the Cameca ims-4f instrument at the NERC ion microprobe facility at the University of Edinburgh. Thin sections were gold coated before analysis. For all phases, a 5-nA primary beam of ^{16}O ions accelerated to 14.5 kV was used with an energy offset of 75kV. The spot size was $\sim$15μm and depth <2 μm. Total counting times were 30s per isotope per analysis. Analyses were calibrated using an in-house basaltic glass standard (St81-A9; Lesne et al., 2011), an olivine standard (Esquel: pallasite), and GSD1-G and BCR-2G (basalt glasses) [U.S. Geological Survey, Box 25046, MS 963, Denver, CO 80225, USA]. Full list of standards used and their compositions can be found in Table.2.2.

2.4 *In situ* B isotope analyses

Boron isotope ratios were measured using the Cameca IMS 1270 by secondary ion mass spectrometry (SIMS) at the NERC Edinburgh Ion Microprobe Facility (EIMF). Matrix-matched standards including several serpentines and a single olivine were used for calibration data can be found in Table 2.2. Thin sections were gold coated before analysis. A primary ion beam of $^{16}O_2^-$ accelerated to 22.5 kV with a beam current of 25-30 nA (pyroxene, olivine, chlorite, serpentine). Analysis time, including pre-sputtering, was around 10 minutes per spot and resulted in a spot size of $\sim$20 μm. Instrument drift was corrected for by measuring standard GSD1-G periodically throughout each session. Data was calibrated using 3 other standards: BCR-2G, and GOR128-G and StHs6/80-G, using the equation of the slope (as seen in Fig. 2.2). The calibration correction coefficient (y) does not vary greatly between the sessions (see caption for details) now between instruments. Boron isotope ratios are presented as delta values in ‰ relative to standard (SRM951 $^{11}B/^{10}B$ ratio of 4.0437, Catanzaro et al., 1970) using the equation:

$$\delta^{11}B_{sample} = 1000 * [(\frac{R_{sample}}{R_{SRM951}}) - 1] \quad (2.1)$$

where R = $^{11}B/^{10}B$ ratio. It is important to use standards with similar major element

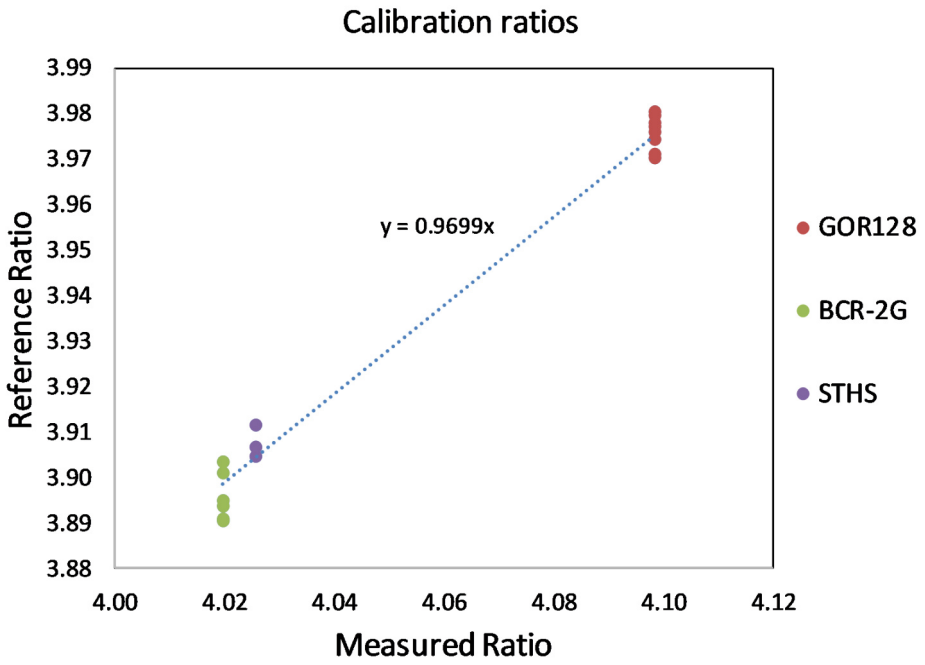

Figure 2.2: Calibration line used in April 2016 SIMS collection as an example of how standards are used to calibrate the data. The equation of this line is applied to the data set to calibrate offset. The calibration for the June 2017 1270 session was 0.95561, Oct 2017 1270 session was 0.9735 and August 2019 7f session was 0.9584. Ratio = $^{11}B/^{10}B$

composition, so these data were collected for all of the B mineral standards, see Table 2.3. Mineral and glass standards were collected at the beginning and end of each day of the session, where a session typically lasted for 5 days. Analysis of serpentine and amphibole standards revealed instrumental mass fractionation (IMF) of ∼6-8 ‰ and ∼2-3 ‰, respectively. Fig.2.3 shows the IMF on each standard across the 3 1270 sessions. In general the mass fractionation is consistent across sessions, but owing to the slight spread of results, IMF corrections were applied in each session separately. Olivine measurements over all 1270 sessions were corrected using the offset shown by the GSD glass which was ∼ 1.6‰. The olivine mineral standard KoH was not fully prepared until the end of the PhD and was later measured on the 7f with an IMF of 1.7‰. This was deemed close enough to the GSD offset that all data corrections from previous 1270 sessions are still valid.

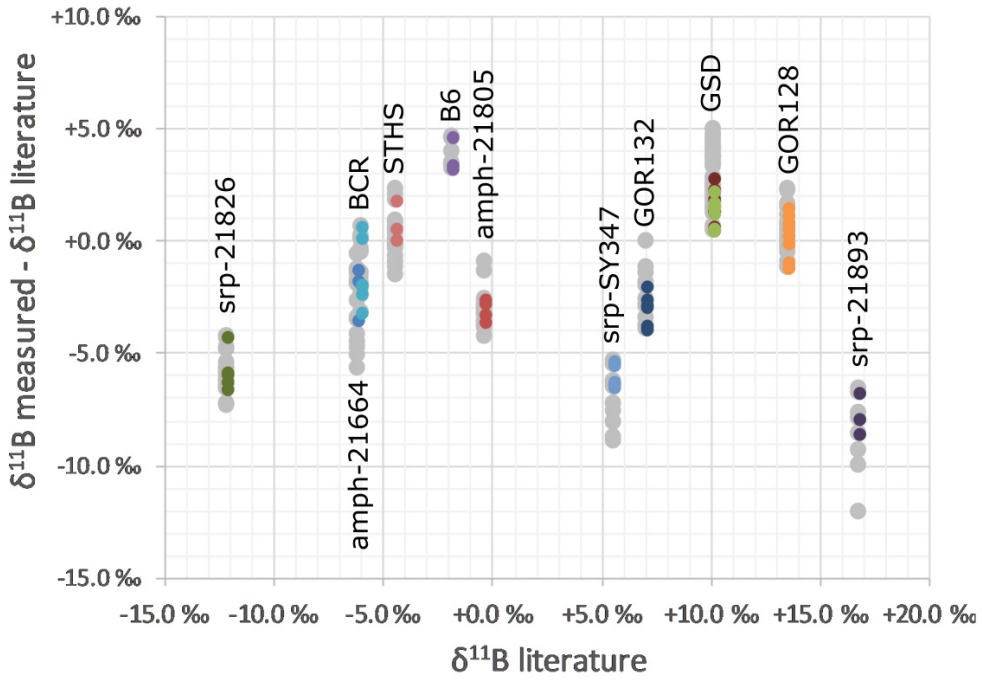

Figure 2.3: Instrumental mass fractionation (IMF) plotted for all standards used in the 3 1270 sessions. Coloured dots are standards from April 2016 session (first session for PhD) and the grey dots are from June and October sessions 2017. The y-axis plots the mass fractionation which is defined as the difference between the reference literature data and the data collected by the 1270. If points plot at y=0.0 there is no IMF.

Table 2.2: B isotope and FME concentrations of all standards used with SIMS. Check marks indicate instrument used.

Standard	**Phase**	δ^{11}**B**	2σ	**B**	**F**	**Cl**	**Li**	**4f**	**1270**	**7f**	***Reference***
GOR128	Glass	+13.6‰	*+0.2‰*	22.7					✓	✓	*Rosner and Meixner (2004)*
STHS	Glass	-4.4‰	*+0.3‰*	11.6					✓	✓	*Rosner et al. (2008)*
B6	Glass	-1.8‰		203.8					✓	✓	*Marschall and Monteleone (2014)*
GOR132	Glass	+7.1‰	*+1.0‰*	15.6					✓	✓	*Rosner and Meixner (2004)*
Ebay Fo	Olivine	-13.6‰								✓	*in house*
GSD	Glass	+10.2‰	*+0.5‰*	50				✓	✓	✓	*Jochum et al. (2010)*
Koh	Olivine	-4.7‰								✓	*in house*
St81-A9	Glass			48.8	225	2000	56	✓			*Lesne et al. (2011)*
Esquel	Olivine			0.1-0.3				✓			*in house*
BCR-2G	Glass	-5.9‰		4.2	359		9	✓	✓		
srp-21826	Srp	-12.1‰		17					✓		*in house*
SY347	Srp	+5.6‰		5.5					✓		*in house*
srp-21893	Srp	+16.8‰		35-100					✓		*in house*
srp-1	Srp	-8.1‰		6.4					✓		*in house*
amph-21805	Amph	-0.3‰		14					✓		*in house*
amph-21664	Amph	-6.1‰		2.5					✓		*in house*

Table 2.3: Major element data of mineral standards.

Sample	Phase	MgO	SiO_2	FeO	Na_2O	Al_2O_3	CaO	MnO	NiO	Cr_2O_3	K_2O	TiO_2	Total
AMPH-21664	**AMPH**	22.2	58.9	3.4	0.03	0.3	13.3	0.11	0.20	0.17	0.01	0.01	98.5
AMPH-21664	**AMPH**	22.7	57.9	3.3	0.03	0.1	13.5	0.10	0.17	0.18	0.01	0.00	98.1
AMPH-21664	**AMPH**	22.1	57.2	4.1	0.04	0.5	13.0	0.12	0.21	0.21	0.01	0.01	97.4
SRP-21826	**PX**	26.0	56.5	3.2	0.25	0.5	10.9	0.17	0.14	0.07	0.05	0.01	97.7
SRP-21826	**SRP**	35.8	42.0	6.6	0.00	2.9	0.02	0.11	0.25	0.34			88.1
SRP-21826	**SRP**	35.9	42.8	6.3	0.00	2.9	0.02	0.12	0.26	0.34			88.7
SRP-21826	**SRP**	36.6	41.9	6.4	0.00	2.8	0.02	0.11	0.26	0.35			88.4
SRP-PF1	**SRP**	37.9	43.9	3.5	0.01	2.0	0.01	0.04	0.13	0.15			87.7
SRP-PF1	**SRP**	37.5	43.1	3.6	0.01	2.4	0.02	0.03	0.14	0.15			86.9
SRP-PF1	**SRP**	38.0	43.7	3.7	0.01	2.2	0.01	0.04	0.13	0.15			88.0
SRP-SY347	**SRP**	34.8	41.8	7.8	0.00	2.5	0.03	0.10	0.23	0.35			87.6
SRP-SY347	**SRP**	34.9	42.4	7.7	0.00	2.5	0.03	0.10	0.25	0.34			88.2
SRP-SY347	**SRP**	34.8	42.4	7.7	0.00	2.5	0.03	0.10	0.24	0.34			88.1
SRP-GEISS1	**SRP**	36.6	43.5	5.0	0.00	2.3	0.10	0.10	0.19	0.14			87.9
SRP-GEISS1	**SRP**	36.0	43.6	5.0	0.00	2.5	0.11	0.10	0.20	0.16			87.8
SRP-GEISS1	**SRP**	34.0	53.6	3.0	0.01	0.9	0.04	0.05	0.18	0.06			91.9
OL-DC0212	**OL**	49.8	40.0	9.5	0.00	0.0	0.08	0.14	0.40	0.02			100.0

Sample	Phase	MgO	SiO_2	FeO	Na_2O	Al_2O_3	CaO	MnO	NiO	Cr_2O_3	K_2O	TiO_2	Total
AMPH-21879	**AMPH**	20.4	56.2	8.6	0.12	1.5	12.7	0.16	-0.01	0.00	0.03	0.01	99.7
AMPH-21879	**AMPH**	27.2	59.0	3.0	0.20	0.7	2.3	0.26	0.00	0.00	0.06	0.02	92.7
AMPH-21879	**AMPH**	25.2	59.2	5.0	0.08	0.7	6.3	0.15	0.00	0.01	0.02	0.01	96.7
AMPH-21805	**AMPH**	21.2	57.0	6.2	0.04	0.2	13.0	0.20	0.03	0.00	0.04	0.01	97.8
AMPH-21805	**AMPH**	21.7	57.6	5.8	0.05	0.1	12.8	0.18	0.03	0.01	0.04	0.01	98.4
AMPH-21805	**AMPH**	21.2	57.9	6.1	0.05	0.2	12.9	0.18	0.03	-0.01	0.05	0.00	98.7

2.5 External fluid composition model

This model is used twice in this thesis to back calculate potential composition for mystery external fluids that have caused the δ^{11}B of a metamorphic olivine to deviate from its equilibrium composition. This is identified in rocks where B_{ol}>B_{srp}. For this model we assume the following dehydration environment: as the serpentine breaks down it releases a fluid that is held in the deserpentinization-induced pore spaces and remains in equilibrium with the growing secondary olivine. As the pore space increases so does the overall rock permeability which allows externally derived fluids to infiltrate the pore spaces, mix with the serpentine breakdown fluid and remain in equilibrium with the growing olivine. Therefore, this model simulates this mixing process and calculates the composition of the externally derived fluid. We can calculate the serpentine fluid and the mixed fluid using the following equations, $DB^{fl/ol}$ = 4 Tenthorey and Herman (2004):

Internal (serpentine-produced) fluid

$$B_{int} = \Delta B_{fl/ol} \times B_{ol} \tag{2.2}$$

$$\delta^{11}B_{int} = Average\ \delta^{11}B_{srp} + \delta^{11}B_{srp-fluid} \tag{2.3}$$

Where:
$B_{ol} = \frac{Average\ B_{srp}}{(D^{B}_{fl/ol} \times 0.13) + 0.87)}$ olivine in equilibrium/closed system
$\delta^{11}B_{srp-fluid}$ = 9.8‰ in acidic to neutral pH conditions

B_{srp} and $\delta^{11}B_{srp}$ are the measured serpentine composition in one sample. Averages are taken from all serpentine measurements in the same sample and the 1σ error on the average is propagated through. $\Delta^{11}B_{srp-fluid}$ is based upon the isotopic fractionation of B between IV-coordinated B in silicates and III-coordinated B in acidic fluids, from Williams et al. (2001).

Predicted mixed olivine fluid

$$B_{mix} = D^{B}_{fl/ol} \times Average\ B_{ol} \tag{2.4}$$

$$\delta^{11}B_{mix} = Average\ \delta^{11}B_{ol} + \delta^{11}B_{ol-fluid} \tag{2.5}$$

Where:

B_{ol} = measured olivine

$\delta^{11}B_{ol-fluid}$ = 0.0‰ in acidic conditions

$\Delta^{11}B_{ol-fluid}$ is based upon the isotopic fractionation of B between III-coordinated B in olivine and III-coordinated B in acidic fluids. It is based on the theory that there will be little to no fractionation between III sites in silicates and III sites in fluids.
The model was written in Python and has several loops whereby it cycles through possible external fluid compositions and fractions (with steps of 1 ppm B_{ext} 0.1‰ $\delta^{11}B_{ext}$ and 1% Fraction). The external fluid is mixed at each step with the internal serpentine fluid using the following calculations:

External fluid

$$^{10}B_{ext} = \frac{B_{ext}}{SRM \times (\frac{1+\delta^{11}B_{ext}}{1000+1})} \tag{2.6}$$

$$^{11}B_{ext} = B_{ext} - ^{10}B_{ext} \tag{2.7}$$

Calculated mixed fluid

$$^{10}B_{mix} = ^{10}B_{int} \times Fr + ^{10}B_{ext} \times (1 - Fr) \tag{2.8}$$

$$^{11}B_{mix} = ^{11}B_{int} \times Fr + ^{11}B_{ext} \times (1 - Fr) \tag{2.9}$$

$$B_{mix} = ^{11}B_{mix} + ^{10}B_{mix} \tag{2.10}$$

$$\delta^{11}B_{mix} = \frac{\frac{^{11}B_{mix}}{^{10}B_{mix}}}{(SRM - 1) \times 1000} \tag{2.11}$$

Where:

SRM = SRM951 $\frac{^{11}B}{^{10}B}$ ratio of 4.04367 (Catanzaro et al., 1970)

Fr = Fraction (%) of internal fluid added

If the calculated mixed fluid is within error (standard error of the mean/average = percentage error) of the predicted mixed fluid then the external end member composition is stored to a list. This list was used to plot Figs.3.5 and 4.14, with the fraction inverted (1-Fr) for plotting fraction of external fluid added.

2.6 Error propagation

The following theory has been used to propagate errors throughout this thesis. This method has been used for errors on both the natural and experimental data.

Adding or subtracting numbers that have errors

$$Q = a + b \; or \; a - b \tag{2.12}$$

$$errQ = \sqrt{(erra)^2 + (errb)^2 + ...} \tag{2.13}$$

If a or b is a constant with no error then the error from the other item carries over. I.e. if a = 1$\pm$0.5 and b=10 then Q=11$\pm$0.5.

Multiplying or dividing numbers that have errors

$$Q = a \times b \; or \; \frac{a}{b} \tag{2.14}$$

$$errQ = Q \times \sqrt{(\frac{a}{erra})^2 + (\frac{b}{errb})^2} \tag{2.15}$$

If a or b is a constant with no error then error is propagated as a percentage. I.e. if a = 2$\pm$0.5 and b=10 then Q=20$\pm$5.

Averaging numbers that have errors

This issue arose when calculating the average isotopic value of a population of the same phase in a sample. Each isotope measurement was accompanied by instrumental error and IMF error. This was solved by using standard error of the mean on

the raw concentration (the instrumental error is naturally reflected in the spread of the data anyway so it can be discarded), then using the addition error propagation method (above) to add the IMF error onto the average.

$$SEM\ or\ (1\sigma) = \frac{Std}{\sqrt{N}} \tag{2.16}$$

Where:

SEM = Standard error of the mean

Std = Standard deviation

N = Count of the population

Chapter 3

Subduction Zone Serpentinites

Alps and Spain

"Then something Tookish woke up inside him, and he wished to go and see the great mountains, and hear the pine-trees and the waterfalls, and explore the caves, and wear a sword instead of a walking-stick."

J.R.R. Tolkien, The Hobbit

*NB: most of the following chapter has been submitted to Geology for publication. The submission is entitled '**Boron isotopes in metamorphic olivine record external fluid infiltration during serpentinite dehydration in subduction zones**'.*

3.1 Abstract

Fluid sources, pathways and migration through the slab/mantle wedge interface is key to understanding chemical exchanges in subduction zones. This interface is sometimes exposed in exhumed subducted terranes, which include partially to fully dehydrated serpentinite bodies. Metamorphic olivines produced by serpentine dehydration at sub-arc conditions from the Western Alps and Spain contain significant concentrations of B (2-30 μg g^{-1}) with a heavy δ^{11}B signature (+9 to +28 ‰), whereas co-

existing serpentines have 2-50 μg g^{-1} B with δ^{11}B= -5 to +24 ‰. Differences between $\delta^{11}B_{ol}$ and $\delta^{11}B_{srp}$ ($\Delta^{11}B_{ol-srp}$) in single samples are highly variable and indicate significant isotopic disequilibrium. Importantly, there is an inverse correlation between $[B]_{ol/srp}$ and $\Delta^{11}B_{ol-srp}$: samples with high $[B]_{ol/srp}$ have low $\Delta^{11}B_{ol-srp}$ (down to -10 ‰) whereas samples with low $[B]_{ol/srp}$ have high $\Delta^{11}B_{ol-srp}$ (up to +15 ‰). This suggests that B-depleted olivines which record positive $\Delta^{11}B_{ol-srp}$ represent equilibrium fractionation of boron isotopes between olivine and serpentine. In contrast, B-enriched olivines with lower $\Delta^{11}B_{ol-srp}$ grew in the presence of externally-derived fluids most likely derived from subducting sediments and crust. Localities with serpentinites that show influx of external fluids (Monviso, Voltri and Almirez) were close to the original subduction interface, where an influx of externally derived fluid is more likely. Our results indicate that serpentinite dehydration is generally associated with influx of external fluids, that metamorphic olivine is a sensitive recorder of this process, and that olivine may be an effective host for transporting heavy B into the deep mantle.

3.2 Introduction

The recycling of lithosphere-hosted volatile elements (e.g. H_2O, CO_2, B, Li) back into the convecting mantle via subduction has been crucial for Earth's evolution. The role of deep slab dehydration in mantle melting at convergent margins (e.g., Plank and Langmuir, 1993) has recently been challenged by studies invoking a role for hydrated (up to 13 wt.% H_2O), down-dragged mantle wedge serpentinites (Scambelluri and Tonarini, 2012; Pagé et al., 2018) as a source of water and fluid-mobile elements (FME).
Evidence for serpentinite involvement comes from boron isotopes, with arc lavas recording a δ^{11}B signal dominated by slab-derived components (+3$\pm$ 6 ‰; De Hoog and Savov, 2018) compared to MORB (δ^{11}B = -7$\pm$ 1 ‰; Marschall et al., 2017), which requires a significant serpentinite contribution (δ^{11}B = +7 to +20 ‰; De Hoog and Savov, 2018, and refs therein). However, many details of serpentinite dehydration in subduction zones are still poorly understood, including the relative roles of mantle wedge vs. ocean floor serpentinites (e.g., Martin et al., 2016) and B isotope fractionation dur-

ing serpentine breakdown (De Hoog et al., 2014). Previous work on deserpentinization processes in subduction settings have focussed on whole-rock geochemistry (e.g. Cannaó et al., 2015; Harvey et al., 2014) which obscures the detailed record of fluid-rock interaction preserved in individual mineral phases.

Metamorphic olivine is formed during brucite and antigorite (high-pressure serpentine) breakdown at $\sim$400°C and $\sim$650°C, respectively (Scambelluri et al., 2004), and is often B-rich (up to 100 μg g^{-1}; (De Hoog et al., 2014; Tenthorey and Herman, 2004; Scambelluri et al., 2004) compared to primary mantle olivine (<0.015 μg g^{-1} ; Chaussidon and Marty, 1995). The incorporation of B in metamorphic olivine uniquely records fluid processes during serpentinite dehydration and allows insight into the source of these fluids.

Here we present in situ δ^{11}B data of serpentine and its metamorphic breakdown product olivine from high-pressure serpentinites, which shows significant isotopic disequilibrium between the two minerals in many partially dehydrated serpentinites. This is evidence of pervasive externally (crustal) derived fluid flux near the slab-wedge interface during serpentinite dehydration. Boron sequestered in metamorphic olivine may be subducted beyond the arc and bypass arc magma fluid source regions and may serve as a robust container to transport a heavy δ^{11}B signature into the deep mantle.

3.3 Samples and their geological setting

To capture the dehydration process we have studied samples with phase assemblages between the brucite-out and antigorite-out phase transitions from the Western Alps and southern Spain (Fig. 3.1). 8 serpentinite samples from four ophiolites were investigated. They contain 20-40 modal% olivine. Sample descriptions are in Table.3.1.

The Monviso Lago Superiore Unit (LSU) is a shear zone comprising meta-basalts, meta-gabbros, metamorphosed pillow basalts, calschists and serpentinites, which underlies the Monviso Unit and overlies the Dora Maira metasediments. The Monviso ophiolite was subducted to a depth of $\sim$ 80 km (Groppo and Castelli, 2010), reaching lawsonite-eclogite facies metamorphism about 45 Ma during the alpine orogeny

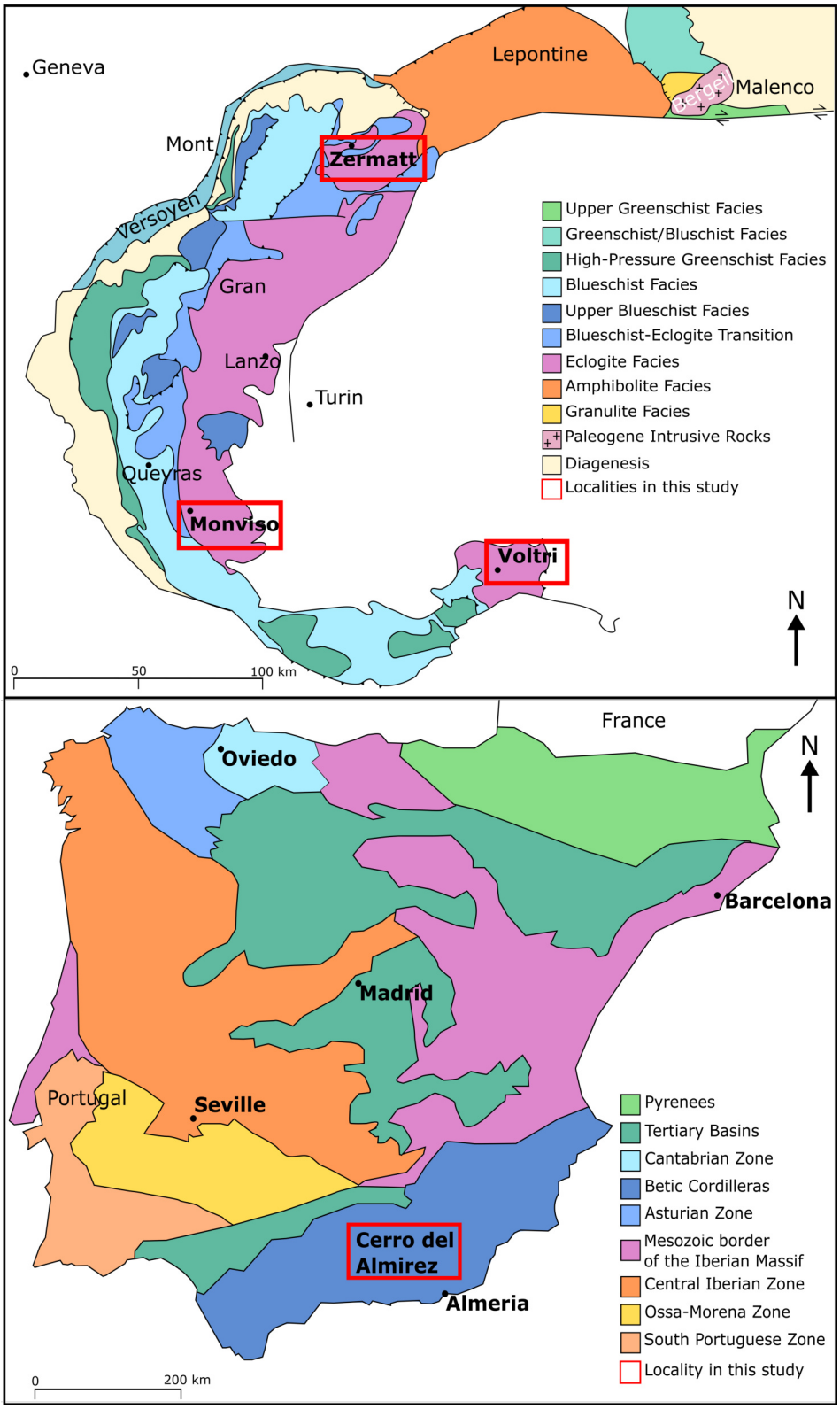

Figure 3.1: Geological maps highlighting the study areas. Alpine map adapted from Bousquet et al. (2012) and Spanish map adapted from Weijermars (1991).

(Rubatto and Herman, 2003). The ophiolite is widely considered to represent ancient Tethyan ocean floor (e.g. Rubatto and Angiboust, 2015) either purely oceanic or ocean-continent transition. It is interpreted as complete ophiolite with well-preserved mantle contacts (Angiboust et al., 2009) or a serpentinite channel on the interface between the subducting plate and overlying mantle (Guillot et al., 2004). There were two retrograde metamorphic phases, with equilibration occuring during blueschist and greenschist facies (Rubatto and Herman, 2003). The presence of the shear zone provides many pathways for fluid flow throughout the ophiolite (Angiboust et al., 2014) leaving the serpentinites exposed to potential extensive interaction with external fluids. Samples Vis5B and DC84 preserve metamorphic olivine veins amongst patches of antigorite, relict pyroxene and rare brucite (see section B.1.1). The former was collected from serpentinites in the lower shear zone of the LSU and has been previously discussed by Debret et al. (2013). The latter was kindly donated by Prof. Ray Burgess, University of Manchester.

The Zermatt-Saas ophiolite comprises antigorite schists, metagabbros, meta-basalts and sheeted dyke complexes, and is thought to represent relict oceanic lithosphere of the Mesozoic Tethys ocean (e.g. Li et al., 2004; Angiboust et al., 2009). Jurassic and Cretaceous metasediments are locally preserved (Angiboust et al., 2009). Metamorphism occurred during subduction to $\sim$60-70 km depth followed by exhumation during the Alpine orogeny (Barnicoat and Fry, 1986) between 34 to 14 Ma (Amato et al., 1999). At this locality, however, there is little to no evidence of external fluids, indicating that the serpentinites have remained relatively isolated from other lithologies during their metamorphic history (Gilio et al., 2019), which is notably different to the geological history of the Monviso ophiolite. Most 'ZS' samples contain metamorphic olivine veins in an antigorite matrix associated with occasional clinohumite, pyroxene and magnetite. Metamorphic olivines are always associated with antigorite shards (see section B.1.1, samples ZS1, ZS17-8 and -9). They were collected from a $\sim$2km thick serpentinite unit in the Zermatt-Saas Ophiolite (most collected just east of Trockener Steg). Zermatt sample DC47 was collected from a different location to the other zermatt samples (Servette Mine, Valle d'Aosta) where the serpentinite is thinner (0.5

km) and surrounded by crustal lithologies (meta-sediments and meta-basalts).

The Voltri massif comprises meta-sediments, metagabbros and serpentinites (Capponi and Crispini, 2002). The Erro-Tobbio metaperidotite is a lherzolitic unit in the Voltri massif, thought to be a slice of subcontinental mantle (Scambelluri et al., 1995). It underwent serpentinization and was subducted to 2-2.5 GPa and 550-600°C during the Cretaceous (145-66 Ma) (Scambelluri et al., 1991, 1995). This unit may represent a slab-mantle interface which has been inundated by slab fluids (Scambelluri and Tonarini, 2012). Due to high As, Sb and δ^{11}B, the wider Voltri massif likely endured fluid-rock interactions taking place within subduction channel domains (Cannaò et al., 2016). Erro-Tobbio serpentinites have a strong foliation defined by antigorite and chlorite, with parallel veins of metamorphic olivine and clinohumite (see section B.1.1). Sample VT8-3 (as in De Hoog et al., 2014) was collected from one of these veins.

Finally, the Cerro del Almirez massif in Southern Spain is in the upper-sequence of the Nevado-Filábride Complex, Betic Cordillera (BC). The BC underwent sea water metasomatism and then subduction during the Alpine orogeny to Albite-Epidote amphibolite facies (Puga et al., 1999). The Almirez serpentinites represent a unique preservation of the antigorite-out isograd dehydrating between 680 to 710°C and 1.6 to 1.9 GPa (Padrón-Navarta et al., 2011; Trommsdorff et al., 1998), conditions which would place it near or within the mantle wedge. The massif comprises 4 zones: antigorite-serpentinite, chlorite-serpentinite (transitional atg-out boundary), granofels harzburgite and spinifex-like olivine harzburgite (Padrón-Navarta et al., 2011). Sample AL98-4 (Harvey et al., 2019) is from the antigorite-serpentinite unit and comprises elongate and orientated patches of metamorphic olivine in an antigorite matrix (analogous to the atg-serpentinite in Harvey et al., 2014). Based on stable isotope compositions, C and S contents the serpentinization likely occurred on the seafloor in oceanic lithosphere (Alt et al., 2013). By comparing the elevated B and Sr concentrations of the prograde units to their less enriched parental units, it is clear that antigorite dehydration in Cerro del Almirez occurred in an open system (Harvey et al., 2014).The sample used in this study is antigorite serpentinite from below the Atg-out isograd with

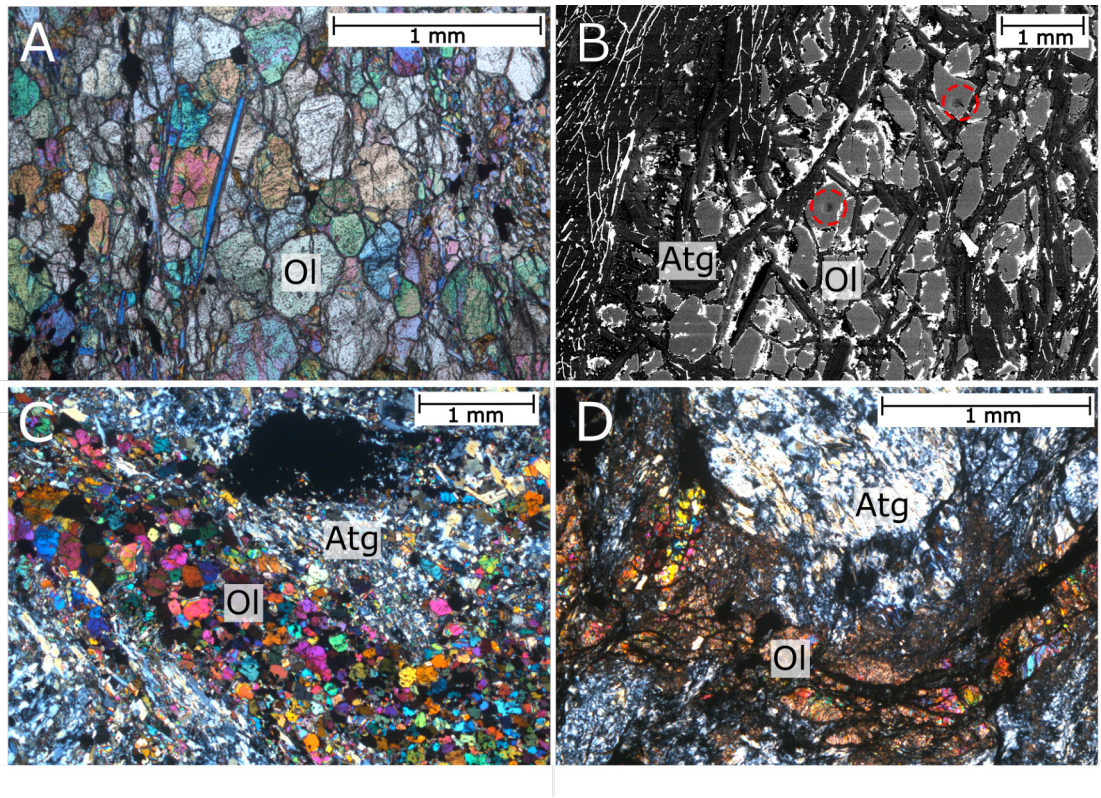

Figure 3.2: Size and texture of metamorphic olivine in thin section. (A) & (C) Zermatt: Thin section XP images of metamorphic olivine veins in a matrix of antigorite. (B) Almirez: SEM backscatter image of metamorphic olivine (light grey) intergrown with laths of antigorite (dark grey). Red dashed circles surround ion probe analysis pits. (D) Monviso: Thin section XP image of metamorphic olivine vein in matrix of antigorite.

B isotope data from (Harvey et al., 2019) (see section B.1.1 for sample images).

3.4 Results

Sample textures

Sample textures are summarised in table 3.1. Fig. 3.2 shows examples of serpentinite textures found in these samples. Full sample images can be found in Appendix B.1.

Location	**Sample ID**	**Phases**	**Textures**
Zermatt-Saas	ZS1	ol2 + srp + chu + mag	Foliated with two distinct types: interlocking ol2 and atg. Ol2 included by atg shards
Zermatt *45°58'04"N 07°44'04"E*	ZS17-8	srp + chu + ol2 + mag + di	Ol and chu form veins around atg patches with px cores. Atg shards included in Ol2 or on grain boundaries
Zermatt *45°58'06"N 07° 43'58"E*	ZS17-9	srp + ol2 + mag + chl	Thick (2mm) veins of ol2 in atg matrix
Zermatt *45°42'11"N 07°27'19"E*	DC47	srp + ol2 + mag	Elongate patches of ol2 in atg matrix
Monviso *see DC84*	Vis5b	srp + brc + ol2	Ol2 in veins amongst patches of atg + brc
Monviso *44°41'52"N 07°05'35"E*	DC84	srp + ol2 + px + mag	Veins of atg+ol2 around relict px
Erro-Tobbio *44°33.677'N 08°48.907'E*	VT8-3	srp + chl + ol2 + chu	Foliation forming atg+chl with veins of ol+chu. Ol2 contain low-Ti mag
Almirez *37°05'05"N 02°54'54'W*	AL98-4	srp + ol2	Elongate patches of ol2 in atg matrix

Table 3.1: Samples descriptions and locations. ol2= metamorphic olivine. Mineral abbreviations as in Kretz (1983): srp= serpentine, chu= clinohumite, mag= magnetite, di= diopside, chl= chlorite, brc= brucite, px= pyroxene. Sample VT8-3 from De Hoog et al. (2014), Vis5b from Debret et al. (2013) and AL98-4 from Harvey et al. (2019).

3.4.1 Major elements

Samples from the Zermatt-Saas ophiolite make up the majority of the samples in this study. They contain Fo_{87-95} olivines, (except one sample, DC47, with Fo_{76}), all have MnO 0.2-0.4 wt % and NiO 0.09-0.27 wt %. Antigorites have Mg# 89-95 and Al_2O_3 1.2-2.9 wt %. Pyroxenes are diopside, with a Mg# 95.7-96.2 and CaO 26.0-26.3 wt%. Clinohumites are Ti-rich TiO_2 $\sim$3.7 wt%, Mg# $\sim$91.7, MnO $\sim$0.33 wt% and NiO $\sim$0.18 wt%. Amphibole compositions are tremolite, Mg# $\sim$95.0 and CaO $\sim$25.4 wt%.
Sample from Voltri (Erro-Tobbio) VT8-3 is described by De Hoog et al. (2014); olivines have lower Fo contents ($\sim Fo_{87}$) than Zermatt olivines but similar MnO $\sim$0.3 wt % and NiO $\sim$0.3 wt % and low TiO 0-0.9 wt %. Clinohumites are also Ti-rich ($\sim$4.7 wt %) and have lower Mg# ($\sim$86) than Zermatt clinohumites with similar MnO $\sim$0.44 wt% and NiO $\sim$0.2 wt%. Antigorites are similar to those from Zermatt with high Mg# ($\sim$95) and Al_2O_3 $\sim$2.6 wt %. Clinopyroxenes are Ca-rich (22.9-25.6 wt%) and have variable Al_2O_3 (0.05 and 5.5 wt%).
Samples from the Monviso ophiolite (Vis5B Debret et al., 2013 and DC84) contain lower Fo olivines (Fo_{74-78}) than the rest of the samples but contain similar MnO 0.3-0.4 wt % and NiO 0.05-0.34 wt %. Monviso antigorites have high Mg# $\sim$91 and Al_2O_3 1.77-1.85 wt %. Full data tables can be found in Appendix A.1.1.

3.4.2 Fluid-mobile Elements (FME)

Throughout the whole suite, B contents are variable (1 to 30 ppm in serpentine and secondary olivine). Secondary olivines also contain high concentrations of other FMEs (F: 5-50 ppm, Cl: 0-40 ppm and Li: 0.1-11.5 ppm) and contain more Li than co-existing serpentine. Minor serpentinite phases: chlorite, clinohumite and pyroxene also contain notable amounts of FMEs, including B (up to 11.9 ppm).
Monviso secondary olivines show higher Li (0.11-0.19 ppm) and B (12.3-16.9 ppm) compared to serpentine Li (0.01-0.02 ppm and B 4.3-5.2 ppm). F and Cl concentrations are more similar between secondary olivines (F $\sim$18.5 ppm and Cl $\sim$19.8 ppm) and serpentines (F $\sim$15.2 ppm and Cl $\sim$18.5 ppm). Pyroxenes have very low B (0.5

ppm), moderate F (10.2 ppm) and Cl (12.7 ppm), and higher Li (1.3 ppm) than secondary olivines.

Zermatt secondary olivines show higher Li (0.11-1.7 ppm) and B (2.2-19.5 ppm) overall compared to serpentine (Li 0.01-0.03 ppm and B $\sim$ 3.0-11.2 ppm), but lower F (7.9-11.6 ppm) and Cl (2.8-10.7 ppm) concentrations compared to serpentines (F 18.0-21.4 ppm and Cl 6.0-31.2 ppm). Other phases are rich in FMEs: Chlorite (where present) has lower B ($\sim$1.6 ppm) but similar Li ($\sim$0.06 ppm), F ($\sim$17.3 ppm) and Cl ($\sim$32.7 ppm) to serpentine. Clinohumite shows similar Li (0.3-0.4 ppm), B (5.4-11.9 ppm) and Cl (5.8-9.8 ppm) to secondary olivine but much higher concentrations of F (111.3-657.5ppm). Diopside contains similar Li ($\sim$0.6 ppm), F ($\sim$8.0 ppm) and Cl ($\sim$7.0 ppm) to olivine but less B ($\sim$2.5 ppm).

Erro-Tobbio (Voltri) secondary olivines contain high B (9-23 ppm) and Li (4-47 ppm) and higher F than other secondary olivines (5-137 ppm).

Almirez secondary olivines and co-existing serpentines have very similar B ($\sim$7.1 ppm and $\sim$6.8 ppm respectively) whereas the olivines show higher Li ($\sim$3.0 ppm) then serpentine ($\sim$0.3 ppm) but lower F ($\sim$37.3 ppm) and Cl ($\sim$16.9 ppm) than serpentine (F $\sim$139.9 ppm and Cl $\sim$ 117.6 ppm). Full data tables can be found in Appendix A.1.2

There is no clear correlation between B and any other FME measured (Cl, F and Li), though serpentine generally contains higher F and Cl and lower Li than metamorphic olivine.

3.4.3 B isotope compositions of olivine and antigorite

Olivine and serpentine are present in all samples and have high δ^{11}B (+10 to +30 ‰) (Fig 3.3), except for antigorite in Zermatt samples (>-5 ‰). On average, Monviso metamorphic olivines show lower δ^{11}B and higher B (δ^{11}B = +9.5 to +12.9 ‰, B $\sim$ 12 μg g^{-1}) than co-existing serpentines (δ^{11}B = +19.1 to +21.3 ‰, B $\sim$ 4.8 μg g^{-1}). Almirez metamorphic olivines have similar δ^{11}B and B to serpentine (δ^{11}B = + 19.1 to +26.9 ‰, B $\sim$ 6.5 μg g^{-1} compared to δ^{11}B +22.6 to +24.4 ‰, B $\sim$ 5.6 μg g^{-1} in serpentine).

Erro-Tobbio metamorphic olivines have slightly higher δ^{11}B and higher B(δ^{11}B +19.1

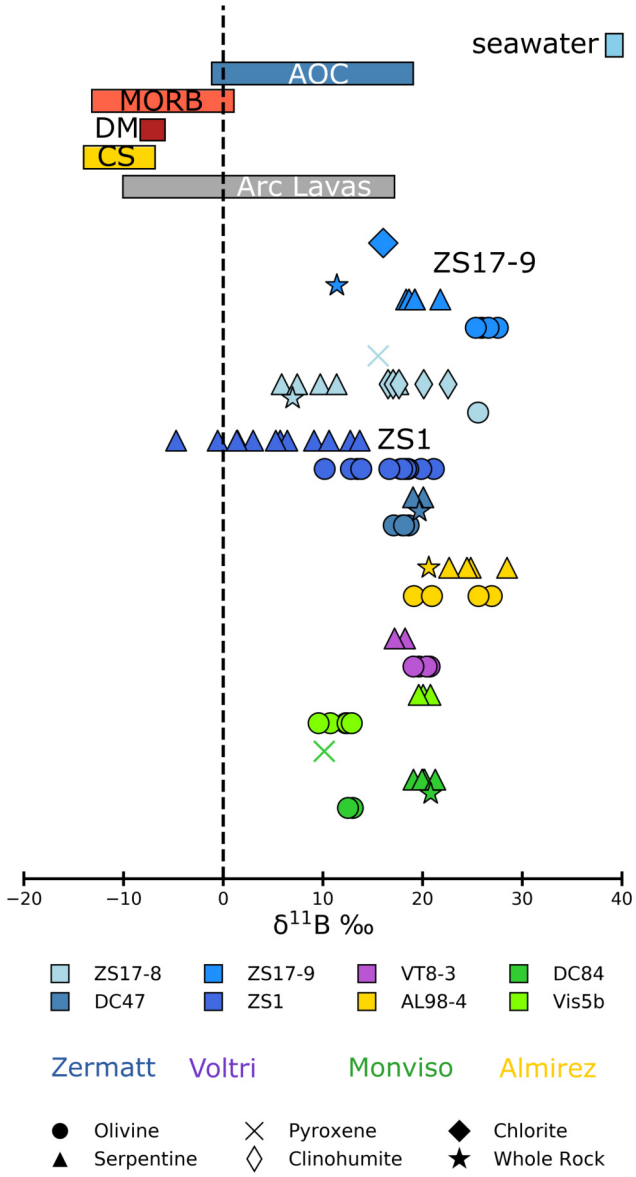

Figure 3.3: Figure comparing δ^{11}B of all samples with literature ranges for subduction zone rocks. Literature ranges from De Hoog and Savov (2018). AOC: altered oceanic crust, CS: continental sediments, DM: depleted mantle, MORB: mid-ocean ridge basalt.

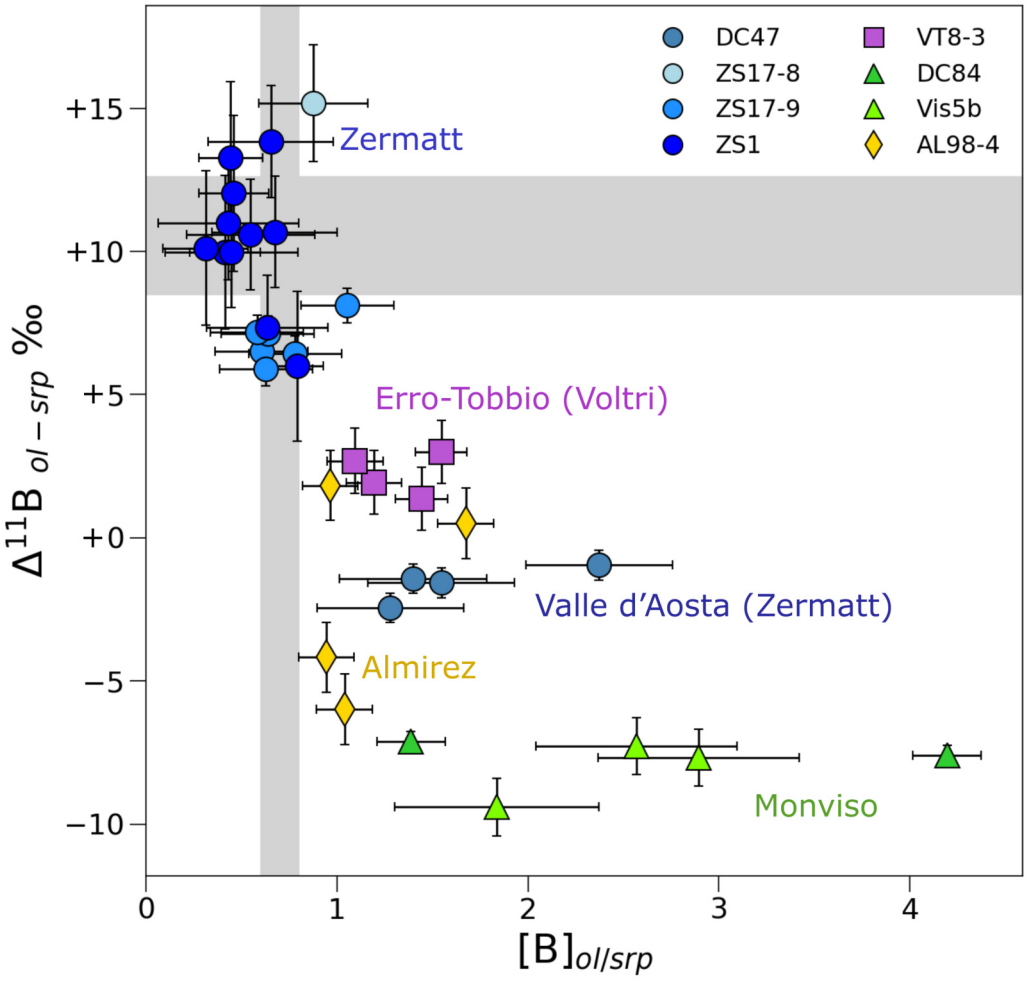

Figure 3.4: Diagram comparing metamorphic olivine compositions with the average serpentine composition in the same sample, where $[B]_{ol/srp}$ and $\Delta^{11}B_{ol-srp}$ calculations can be found in appendix A.1. A broadly negative correlation between $[B]_{ol/srp}$ and $\Delta^{11}B_{ol-srp}$ is observed. Grey bars indicate equilibrium fractionation from Tenthorey and Herman (2004); Williams et al. (2001). Errors are a combination of 1σ on the serpentine average, 1σ on the serpentine standard IMF (which is roughly +6‰) and analytical uncertainty (1σ) on the olivine.

to 20.7 ‰, B ∼15.9 μg g^{-1}) than co-existing serpentines (δ^{11}B +17.2 to +18.2 ‰, B ∼12.0 μg g^{-1}). Zermatt metamorphic olivines have a wider range of δ^{11}B (+10.2 to +27.5 ‰, and higher B ∼8.2 μg g^{-1}) compared to serpentine (δ^{11}B -4.7 to +21.8 ‰, B ∼12.5 μg g^{-1}). Minor phases not present in all samples include pyroxene, chlorite and clinohumite. In general, these minor phases have positive δ^{11}B (where B concentrations are high enough to measure). Monviso pyroxenes show δ^{11}B ∼ +10.1 ‰, Zermatt clinohumites δ^{11}B ∼ +16.5 to +27.3 ‰and Zermatt pyroxenes δ^{11}B ∼ +15.5 to +19.0 ‰.

3.5 Summary Data

Table 3.2: The average B isotope and FME compositions of each phase in every sample.

Sample	Phase	δ^{11}B ‰	±‰	B	H_2O wt%	Li	F	Cl
DC47	OL	+17.9	*0.3*	19.9	0	0.3	11.6	10.7
DC47	SRP	+19.5	*1.0*	12	13.1	0	22.2	28.1
DC47	BAS	+20.6	*1.0*	10.4	12.7	0	20.5	35.7
ZS17-8	CLH	+18.8	*0.8*	5.5	1.7	0.4	115.4	7.1
ZS17-8	OL	+25.5	*0.9*	5.1	0	2.4	28.6	5.2
ZS17-8	PX	+15.5	*1.3*	1.7	0	0.2	3.7	5.9
ZS17-8	SRP	+10.4	*1.2*	5.5	14	0	19.2	8
ZS17-9	CHL	+16.0	*1.3*	1.6	13.1	0.1	17.3	32.7
ZS17-9	OL	+26.3	*1.0*	2.1	0	0.9	7.9	2.8
ZS17-9	SRP	+19.4	*1.3*	3	14	0	18	6
ZS1	OL	+16.1	*1.0*	8	0	0.8	7.1	5.7
ZS1	SRP	+5.7	*1.0*	19.5	13.5	0	148.1	67.1
VT8-3	OL	+19.9	*1.0*	15.9	0	17.3	14.4	91.6
VT8-3	SRP	+17.7	*1.1*	12.1	14.1	0.1	393.2	45.6
DC84	OL	+12.7	*0.3*	14.4	0	0.1	18.8	9.4

Sample	**Phase**	δ^{11}**B ‰**	$\pm$‰	**B**	**H_2O wt%**	**Li**	**F**	**Cl**
DC84	PX	+10.1	*1.8*	0.5	0.1	1.3	10.2	12.7
DC84	SRP	+20.1	*1.0*	5.2	12.7	0	15.2	18.5
Vis5b	SRP	+20.1	*1.3*	4.4	13	0	38.1	38.7
Vis5b	OL	+11.6	*0.9*	10.6	0	0.2	6.6	6.6
AL98-4	SRP	+23.5	*1.2*	5.6		0.2	116.4	121.7
AL98-4	OL	23.1	*1.1*	6.5		3.6	30	15.1

Table 3.3: The average Major compositions of each phase in every sample, data for samples VT8-3 and AL98-4 are published in De Hoog et al. (2014) and Harvey et al. (2019).

Sample	Phase	FeO	MgO	SiO_2	Na_2O	Al_2O_3	P_2O_5	CaO	MnO	NiO	Cr_2O_3	TiO	Mg#
DC47	OL	8.09	51.35	41.41	0	0	0	0	0.38	0.34	0	0	91.88
DC47	SRP	2.72	39.46	43.81	0	1.64	0	0	0.06	0.12	0.26	0	96.28
DC47	BAS	2.58	39.68	43.45	0	1.85	0	0	0.04	0.09	0.24	0	96.48
ZS17-8	CLH	3.88	52.94	37.41	0	0	0	0	0.33	0.18	0.01	3.65	96.05
ZS17-8	OL	3.61	55.06	41.4	0	0	0	0	0.31	0.24	0	0.01	96.45
ZS17-8	PX	0.66	18.42	55.17	0	0.01	0.01	25.54	0.06	0.01	0.01	0	98.03
ZS17-8	SRP	2.03	40.54	43.11	0	2	0	0	0.04	0.08	0.26	0	97.26
ZS17-9	CHL	3.34	35.81	33.99	0	11.65	0	0	0.02	0.09	0	0.01	95.03
ZS17-9	OL	4.36	54.29	41.54	0	0	0	0	0.24	0.24	0	0	95.69
ZS17-9	SRP	2.19	39.62	42.72	0	1.89	0	0	0.03	0.1	0.41	0	97
ZS1	OL	5.97	52.79	41.45	0	0	0	0	0.28	0.27	0	0.01	94.04
ZS1	SRP	1.95	39.83	43.06	0	1.74	0	0	0.04	0.06	0.38	0	97.33
DC84	OL	10.8	48.6	39.8	0	0	0	0	0.3	0	0	0	88.9
DC84	SRP	3	38.6	42.3	0.1	1.8	0	0.1	0	0.1	0.6	0	95.8
Vis5b	SRP	2.9	39	43	0	1.8	0	0	0	0.2	0.5	0	95.9
Vis5b	OL	10.8	48.1	39.8	0	0	0	0	0.4	0.3	0	0	88.8

Our dataset shows a clear covariation between $[B]_{ol/srp}$ and $\Delta^{11}B_{ol-srp}$ (Fig. 3.4). Zermatt metamorphic olivines are depleted in B compared to co-existing serpentine but have heavier δ^{11}B. Monviso olivines, however, are enriched in B compared to the co-existing serpentine but have lighter δ^{11}B. Almirez, Valle D'Aosta and Erro-Tobbio olivines lie between these two end members with roughly similar B and δ^{11}B in olivine and serpentine.

3.6 Discussion

3.6.1 Boron isotope fractionation during serpentine dehydration

No partitioning coefficient of B between serpentine and olivine ($D_B^{ol/srp}$) is available, but a $D_B^{fluid/residue}$ value of ∼3-5 was obtained in serpentinite dehydration experiments (Tenthorey and Herman, 2004). As metamorphic olivine was the main B-bearing phase in the residue, mass balance dictates that $D_B^{ol/srp}$ = ∼ 0.66 to 0.79. Metamorphic olivine with $[B]_{ol/srp}$ ∼0.8 is abundant in Zermatt, see Fig.3.4; these samples show $\Delta^{11}B_{ol-srp}$ ($\delta^{11}B_{ol}$ - $\delta^{11}B_{srp}$ of co-existing olivine and serpentine) of +5.6 to +15.2 ‰. In most silicates, including serpentine, B^{3+} substitutes for Si^{4+} or Al^{3+} in tetrahedral (IV) coordination (Leeman and Sisson, 2002), but in olivine, B has been found to occur in trigonal (III) coordination (Ingrin et al., 2014). ^{11}B preferentially resides in trigonal and ^{10}B in tetrahedral coordination (Kakihana et al., 1977), so if olivine incorporates III B, it should show a heavier B isotope signature than the co-existing serpentine (which incorporates IV B). This pattern is observed in the Zermatt samples, suggesting two things about these Zermatt samples: firstly, olivine likely incorporates III B in and secondly, these samples could show isotopic equilibrium. The average $\Delta^{11}B_{ol-srp}$ of +9.5 ± 0.6‰(1σ) is close to that predicted by experimentally determined B isotope fractionation between IV and III coordination, which decreases from $\Delta^{11}B_{ol-srp}$ = +12.6 to +8.5‰ at 450 to 650°C, respectively (Williams et al., 2001). As Zermatt metamorphic olivines show near-equilibrium $[B]_{ol/srp}$ and $\Delta^{11}B_{ol-srp}$, we conclude that they grew in equilibrium with internal fluids released during serpentinite dehydration with no evi-

dence for external fluid contamination. This is supported by REE and Sr-isotope data (Gilio et al., 2019) and consistent with the geological setting of the Zermatt samples, which come from a thick ($\sim$2 km) serpentinite unit that is part of a coherent section of subducted ocean lithosphere, far from other lithologies.

The majority of metamorphic olivines from localities other than Zermatt show $[B]_{ol/srp}$ >0.8 and $\Delta^{11}B_{ol-srp}$< +5‰, i.e., have more B and ^{10}B than is expected for equilibrium dehydration. The most likely source of the excess B is external fluids, as there are no other B-rich phases in the serpentinite that are dehydrating at 450 to 650°C. Mass balance calculations (for detailed calculation see methods section 2.4) indicate the percentage of external fluid needed to increase B above equilibrium levels (as in Fig.3.4), which varies between the localities (see Fig.3.5). B in fluid at antigorite breakdown depths is $\sim$ 100-200 μg^{-1} (Konrad-Schmolke et al., 2016) meaning that the amount of fluid needed is $\sim$15 to 60%, with $\delta^{11}B$ of +5 to +12 ‰ (Monviso) and +14 to +18 ‰ (Erro-Tobbio), and $\sim$5 to 15% external fluid with $\delta^{11}B$ of +2 to +14 ‰ (Almirez). The fluid rock-sources will be $\sim$10 ‰ lower (-8 to +8 ‰), assuming IV coordination in silicate rocks (Fractionation of B between IV silicates and fluids is around 10‰, Williams et al., 2001). These percentages do not equate to the volume of fluid, simply the percentage of the fluid present that is sourced externally.

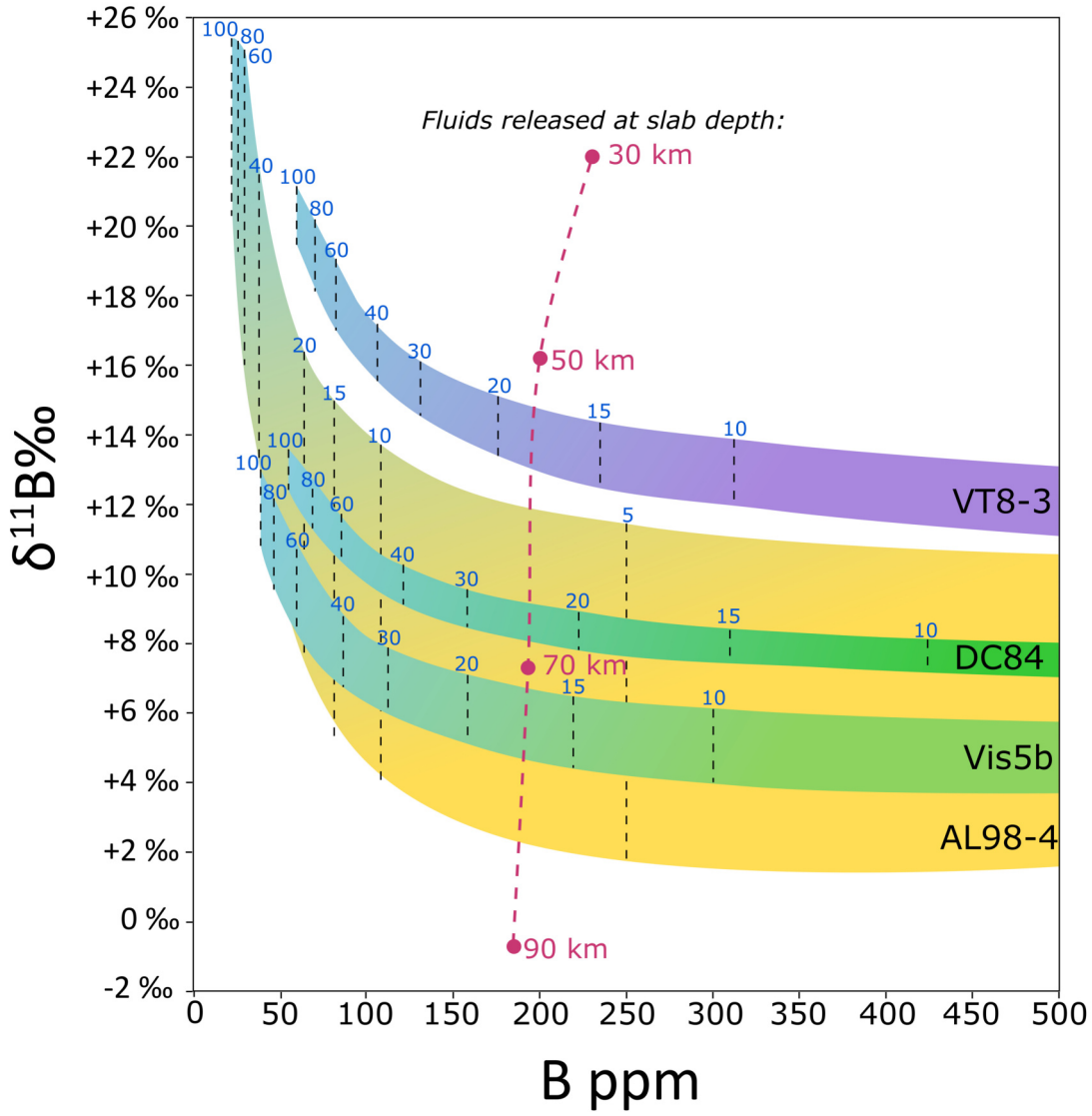

Figure 3.5: Plot of δ^{11}B vs. B concentration of fluids. This diagram highlights the possible range of proportions and compositions of external fluid needed to produce the olivine compositions in the labelled localities (purple = Voltri, yellow = Almirez and the green = Monviso). Blue numbers indicate the percentage of external fluid mixing with serpentine fluid. External fluids are predicted to have exclusively positive δ^{11}B. Also indicated are model compositions of slab-derived fluids (90% AOC + 10% sediment) at various depths of the slab (Tonarini et al., 2011). $D_{fl/ol}$ = 4 in this case.

However, we can estimate the fluid/rock ratio based on a release of 13 wt% fluid from serpentinites. If we take the density of water at these conditions as 1 kg/cm^3 and the density of the serpentinite rock is somewhere between 3.3 and 2.7 kg/cm^3 (we'll take the average of 3 kg/cm^3, since samples vary in their % dehydration), we get a maximum fluid/rock ratio of 0.45, if all fluid was released at once. So if we add the maximum of 60% external fluid needed to alter the olivine composition in this instance, the fluid/rock ratio is 1.05. Given that the rock volume is only decreasing by 13%, it seems unlikely that there would be the space needed for 105 vol% fluid, therefore I would suggest that in this scenario, fluid is produced in small volumes (<6 vol%) at a time, infiltrated by external fluids (potentially as much as a further $\sim$7 vol%) and then drains away as more fluid is produced in its wake. This implies both that there is movement of fluid in and out of the serpentinite body during dehydration and that the fractionation of B isotopes between the olivine and the fluid likely takes place over a long time.

Potential sources of the external fluid in subduction zones are altered oceanic crust (average δ^{11}B +3.4 ‰), meta-sediments (δ^{11}B -13 to -8) and serpentinized lithospheric mantle (δ^{11}B +7 to +20 ‰) (De Hoog and Savov, 2018 and references therein). Any of these fluid sources could supply sufficient light B to produce the co-variance seen in Fig. 3.4, but sediments or crustal-derived fluids would be most effective due to their high B and low δ^{11}B. We suggest that this is direct evidence of fluid fluxes across the slab-mantle interface, with positive δ^{11}B fluid moving through dehydrating serpentinite bodies.

3.6.2 Implications for the subduction interface

Because serpentine dehydration releases water, olivine formed during this reaction grows in the presence of fluid. This fluid is a mixture of internal fluid generated by serpentine breakdown and external fluid infiltrating the rock (see Fig.3.6). This micro-scale process may not be detected using whole-rock δ^{11}B data, as all serpentinites in this study have positive whole-rock δ^{11}B whilst being variably affected by external fluid

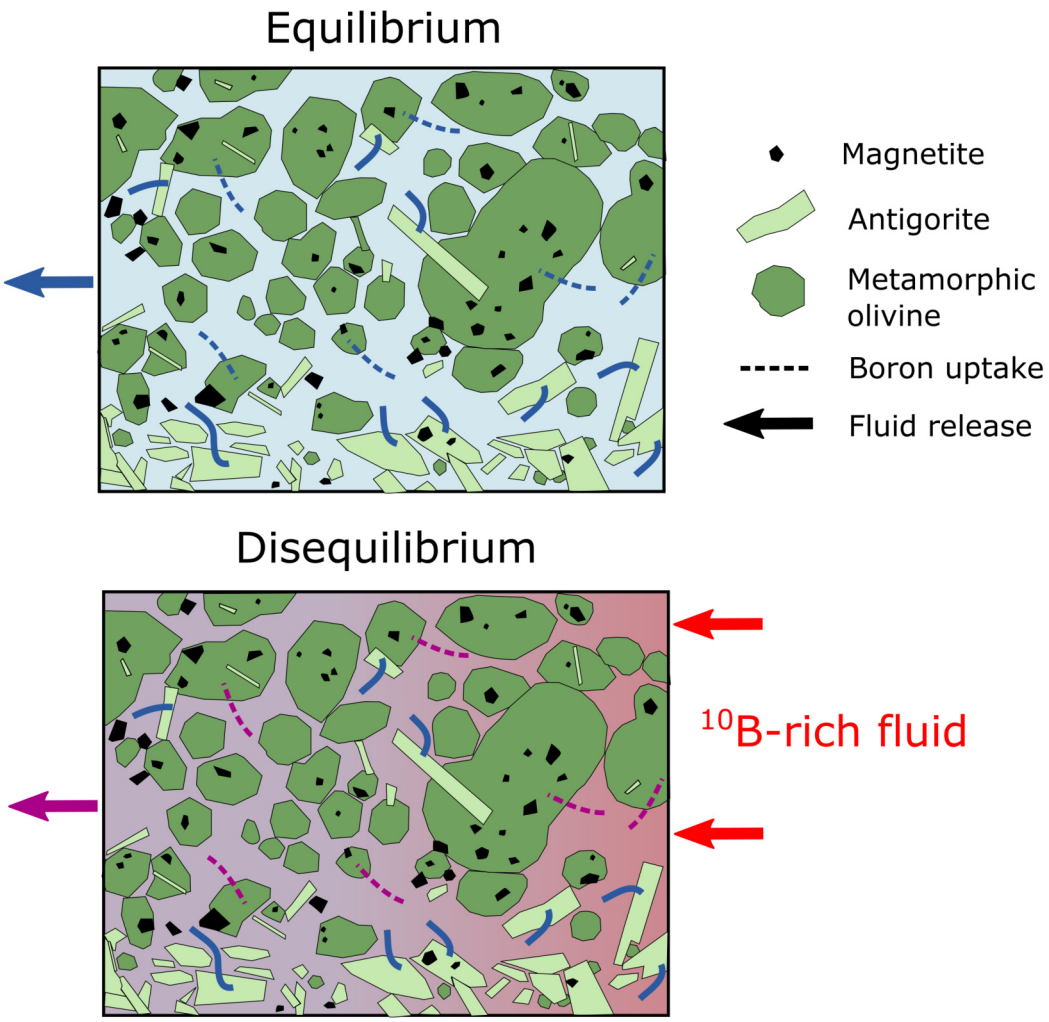

Figure 3.6: Schematic diagrams depicting two different scenarios of serpentine dehydration. (Top) Breakdown of serpentine releases fluid and creates metamorphic olivine. The volume change of the solid components creates porosity. As all fluid is produced internally, olivine and serpentine will be in B isotopic equilibrium; (Bottom) If B-bearing external fluids infiltrate during serpentine dehydration and mix with the serpentine breakdown fluids, metamorphic olivine will be not be in isotope equilibrium with serpentine. Serpentine compositions are unlikely to be affected by the external fluid, as exchange of B between serpentine and fluid is limited by slow diffusion at the low temperatures involved (<650°C).

infiltration. In contrast, subduction mélange serpentinites show negative δ^{11}B (Martin et al., 2016; Cannaó et al., 2015) likely due to the extent of contamination (where lighter δ^{11}B is the result of extreme over-printing), different infiltrating fluid compositions or different starting compositions. This is consistent with the close proximity of serpentinites to large proportions of crustal rocks and sediments in these subduction mélanges. External fluids may permeate dehydrating serpentinites without the need for large-scale faults (Fig.3.6), as seen in Almirez and Erro-Tobbio, which instead only show meter-scale vein networks and deformation. During dehydration reactions there is a rapid increase in porosity and rock permeability allowing the fluid to drain from the rock (Tenthorey and Cox, 2003). Dehydration is localised at specific microsites, such as crystal boundaries or kink axial planes, which generate porosity and vein networks (Plümper et al., 2017; Viti and Hirose, 2008). This channelizes fluids and results in large-scale fluid escape and transfer from the serpentinite to the mantle wedge without the need for brittle failures and opening of fault pathways (Plümper et al., 2017). It is plausible that if the early onset of porosity through micro-fracture networks provides pathways for escaping fluids, it also provides pathways for infiltrating fluids. This process would explain how any external fluid can move through dehydrating serpentinites without large-scale fracture networks.

The trend towards higher [B]$_{ol-srp}$ with lower δ^{11}B$_{ol-srp}$ indicates an increasing influence of B-rich external fluids from Zermatt to Almirez/Voltri to Monviso. This trend correlates with the position of the serpentinite bodies relative to the slab-mantle interface during peak metamorphic conditions (Fig. 3.7). The Monviso ophiolite and Erro-Tobbio unit are thought to represent 'subduction channels' in-between the subducting slab and the mantle wedge (i.e. Guillot et al., 2004; Cannaò et al., 2016). A subduction channel is a domain of intense and focussed deformation where slabs of oceanic crust, sediments and serpentinites are accreted to the slab-mantle interface. This process is aided by the physical properties of serpentinites (density and rheology) and is a prime location to be infiltrated by fluids derived from the subducting slab beneath (Cannaò et al., 2016). These external fluids could be derived from deeper sections of the Monviso and Voltri massifs, as they percolated up along the slab inter-

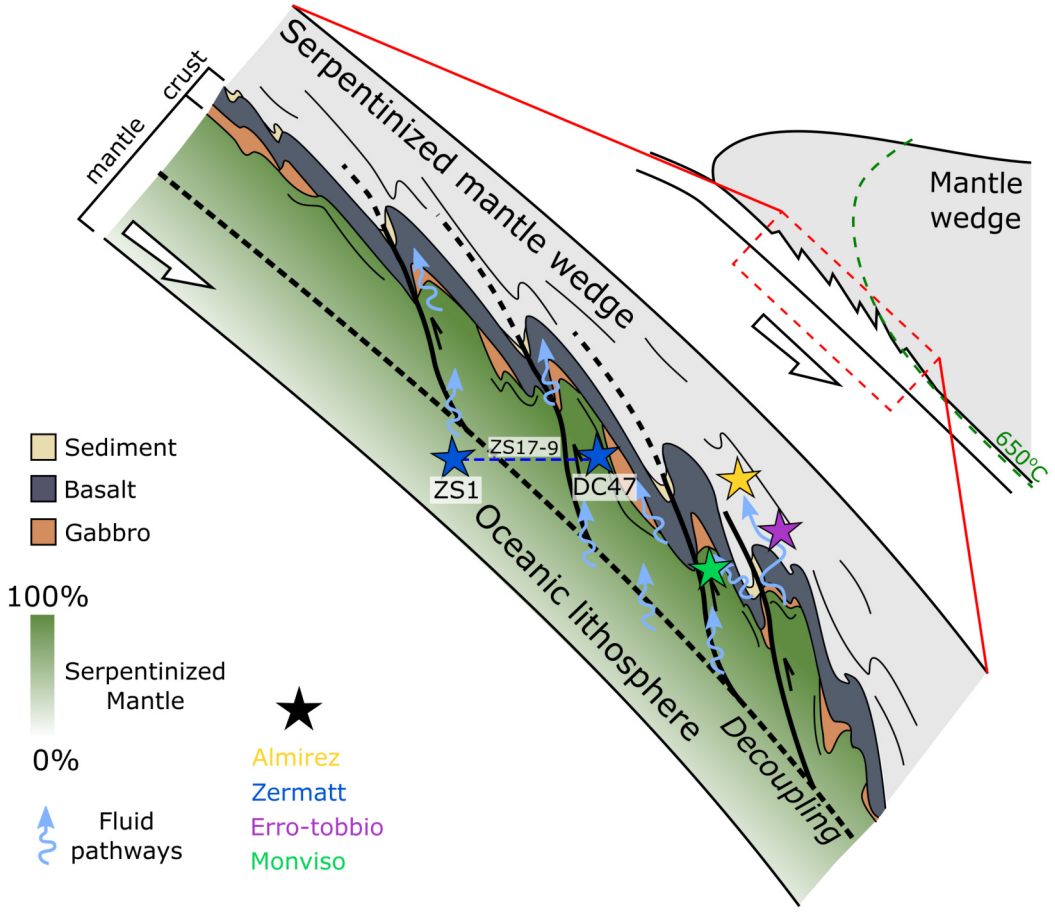

Figure 3.7: Block diagram depicting proposed fluid pathways and tectonic setting for serpentinite localities in this study (base diagram after Guillot et al., 2015). See text for details.

face and into the overlying mantle (Fig. 3.7). Shear zone associated faulting provides many additional pathways for fluid flow throughout the Monviso ophiolite (Angiboust et al., 2014) leaving the serpentinites exposed to extensive interaction with external fluids. Deserpentinization in the Cerro del Almirez massif certainly occurred during subduction (Puga et al., 1999), but the proximity of the ophiolite to the slab-mantle interface is uncertain. The high P-T gradient suggests it was situated near or in the mantle wedge. Infiltration of external fluids into the serpentinite documented here occurred before more pervasive overprint recorded in the chlorite harzburgite residue after the Atg-out reaction (Harvey et al., 2014, 2019). Zermatt sample DC47 was collected in a distal location (Valle d'Aosta) where the serpentinite is thinner ($\sim$0.5 km) and surrounded by crustal lithologies (meta-sediments and meta-basalts). Olivines from this sample show elevated $[B]_{ol-srp}$ and lower $\delta^{11}B_{ol-srp}$ compared to the other Zermatt olivines, likely related to their proximity to other lithologies and increased exposure to dehydration fluids, hence the separation from the other Zermatt samples in Fig.3.7.

3.6.3 Implications for deep recycling of heavy δ^{11}B

Metamorphic olivine in serpentinite contains significant amounts of B with a heavy δ^{11}B signature, as well as other FME (De Hoog et al., 2014; Scambelluri et al., 2004). Boron trapped in metamorphic olivine is not likely to affect the δ^{11}B of arc volcanics as it is locked away and perhaps only released when olivine inverts to a higher-pressure phase. Thus, considerably larger amounts of serpentinite may be needed to supply the B isotope signature of arc lavas (De Hoog and Savov, 2018) than estimates based on loss of all B to the fluid during dehydration. This is modelled in section 5.5.3.

High-pressure polymorphs of olivine (wadsleyite, ringwoodite) may act as sinks for H_2O (Pearson et al., 2014) and therefore probably FME. Thus, the heavy δ^{11}B signature is potentially transported with the descending slab into the deep mantle, together with other FME such as F and N (Pagé et al., 2018). Indeed, deep subduction of serpentinites was implicated by the discovery of B-bearing blue diamonds from the lower mantle (Smith et al., 2018). Our study shows that metamorphic olivine may be the host to transport B, and therefore, deep recycling of B may not be restricted to geotherms

cold enough to stabilise dense hydrous magnesium silicates (Smith et al., 2018). In addition, olivine transports a heavy δ^{11}B signature, which could allow tracking of the deeply subducted residue. However, Walowski et al. (2019) recently studied the δ^{11}B signature of ocean island basalts (OIBs), that form from magma that is thought to sample the core-mantle boundary (CMB). These OIBs have notably light δ^{11}B which would imply that they are not sampling any material sourced from subducted slabs. However, we do not yet know if the heavy B signature survives the olivine-ringwoodite transition, and even less about higher PT phase transitions. If it does survive to the CMB, why is the signature not reflected in OIBs? One suggestion is that the mantle, although low in B, is vast and there is simply not enough slab being subducted that could change the overall δ^{11}B signature of the CMB to a great extent.

3.6.4 Ocean floor serpentine: a discussion on the serpentinite starting value

As part of the initial data collection, we had the opportunity to measure ODP sea floor lizardite on the 4f and 1270 SIMS. We were given the samples by Baptiste Debret and unfortunately do not know their context other than that they are sea floor serpentinites collected on an IODP excursion. ODP6 comprises mostly bastite (lizardite after serpentinization of pyroxene) and ODP7 comprises mostly mesh (lizardite after serpentinization of olivine). Bastite has higher FeO (2 to 2.7 wt%), Al_2O_3 (1.7 to 2.7 wt%) and Cr_2O_3 (1.2 to 2 wt%) than the mesh serpentine, which has FeO (1.3 to 1.6 wt%), Al_2O_3 (0.9 to 1 wt%) and Cr_2O_3 (negligable). Full data in Table.3.5.

In terms of trace elements, bastite from ODP6 has 7.2 to 53.2 ppm B, 193.5 to 894 ppm F and 1240 to 1550 ppm Cl. Mesh from ODP7 has in general lower concentrations of FME; 10.7 to 19 ppm B, 183.9 to 198.2 ppm F and 165.8 to 394.6 ppm Cl. Full data in Table.3.4.

The most interesting part of this data set is the δ^{11}B. Bastite records +3 to +4.8 ‰ and mesh records -1.1 to -1.6 ‰. Sea floor serpentinites are usually presumed to inherit the heavy B isotope signature of sea water. For example, the Lost City serpen-

tinites have δ^{11}B +11.4 to +15.2‰ and B ppm of 14.3 to 90.6 (Boschi et al., 2008). However, these ODP serpentines record much lighter δ^{11}B. This data indicates high δ^{11}B variability in ocean floor serpentinites. This will have a significant effect on the δ^{11}B signature being fed into subduction zones and ultimately into arc magma or the deeper mantle. It may help to explain particularly negative δ^{11}B in subduction zones such as those from the Guatemala Suture Zone (Martin et al., 2016) that show δ^{11}B of -14 to +9.7‰, as fluids lost from these lighter serpentinites will result in lighter fluids serpentinizing the mantle wedge. It could also help explain the large range of arc lavas δ^{11}B values.

This discovery of particularly negative sea floor serpentinites will not affect the models presented in this thesis. Particuarly in figure 5.7, the value used as the serpentinite end member is calculated from the Zermatt serpentine and is an example of the percentage contribution serpentinites of a similar composition could have.

Sample	Phase	δ^{11}B	error	B ppm	F	Cl	Rb	Sr	Cs	Ba	Li
ODP6	Bastite	+3.0 ‰	±0.3 ‰	50.9	806.6	1358.6	0.1	1.5	0.5	0.9	0.4
ODP6	Bastite	+3.2 ‰	±0.2 ‰	53.2	894.0	1240.5	0.8	1.2	0.3	0.9	0.3
ODP6	Bastite	+3.2 ‰	±0.6 ‰	7.2	193.5	1353.3	0.1	0.4	0.0	0.0	0.1
ODP6	Bastite	+4.8 ‰	±0.5 ‰	12.6							
ODP6	Bastite			13.5	261.0	1548.6	0.4	0.4	0.1	0.2	0.1
ODP7	Mesh	-1.1 ‰	±0.4 ‰	16.8	198.2	394.6	0.3	0.4	0.1	0.0	0.1
ODP7	Mesh	-1.6 ‰	±0.4 ‰	16.7	195.2	442.7	0.1	0.5	0.5	0.3	0.1
ODP7	Mesh	-1.5 ‰	±0.4 ‰	19.0							
ODP7	Mesh			10.7	183.9	165.8	-0.2	0.4	0.1	0.4	0.1

Table 3.4: FME and B isotope data for the ODP serpentines

Sample	Phase	FeO	MgO	SiO_2	Na_2O	Al_2O_3	CaO	Cr_2O_3	MnO	NiO	Total
ODP6	Bastite	2.7	36.4	38.2	0.1	2.7	0.0	1.2	0.1	0.3	81.9
ODP6	Bastite	2.6	36.1	37.3	0.2	2.5	0.1	1.2	0.1	0.3	80.3
ODP6	Bastite	2.0	39.4	39.4	0.0	1.7	0.0	2.0	0.1	0.1	84.7
ODP6	Mesh	1.6	38.8	41.0	0.2	0.9	0.0	0.0	0.0	0.2	82.8
ODP7	Mesh	1.3	39.2	40.9	0.1	1.0	0.0	0.0	0.1	0.1	82.8
ODP7	Mesh	1.4	39.5	40.7	0.1	1.0	0.0	0.0	0.1	0.1	83.0
ODP7	Mesh	1.5	39.2	40.5	0.1	0.9	0.0	0.0	0.1	0.1	82.3

Table 3.5: Major element data for the ODP serpentines

3.7 Oxygen Isotopes: characterising a high-Fe, high-Al serpentine standard

3.7.1 Introduction

Oxygen isotopes are commonly used in the measurement of equilibrium temperatures of a mineral pair. The calculation is as follows Chiba et al. (1989):

$$1000ln\alpha = A10^6T^{-2} \tag{3.1}$$

Where α = $^{18}O/^{16}O_{mineral1}$/ $^{18}O/^{16}O_{mineral2}$

A is a constant calculated from the value of α at equilibrium

Unfortunately, no serpentine-olivine geothermometer exists in the literature, however, the constant A has been calculated for both serpentine-magnetite (1000lnα = 1.81$10^6T^{-2}$+ 1.41, Agrinier and Cannat, 1997) and olivine-magnetite (1000lnα = 2.62 10^6T^{-2}, Chiba et al., 1989). Using these equations, the A constant for the serpentine-olivine pair has been calculated as 0.81 (see Fig.3.8). Using the serpentine-olivine geothermometer, a closure temperature of each sample can be calculated. If this temperature agrees with the estimated temperature of formation ($\sim$600-700°C depending on mineralogy) then it can be assumed that the system is in isotopic equilibrium.

The precision of temperature calculations significantly decreases with increasing equilibration temperature (Fig.3.9), due to the maximum precision of $\pm$0.3 ‰ attainable on the SIMS 1270. Expected equilibrium temperatures are between 400-700°C which will attain errors of <200°C. If temperature calculations read >900°C ($\Delta^{18}O_{ol-srp}$ $\sim$+0.6‰) we can safely assume that the system is in disequilibrium. However, if temperatures read between 200 to 900°C the mineral pair are likely to be in equilibrium, since disequilibrium processes are likely to change the δ^{18}O of olivine or serpentine by more than 0.3‰. Despite not being able to aquire an accurate temperature, this method would still decipher whether or not samples from Zermatt, Voltri, Almirez and Monviso preserve *in-equilibrium* olivine-serpentine pairs. However, unfortunately, due to time constraints, the data was not collected for this thesis.

	Run A	**Run B**
Sample	$\delta^{18}O_{vsmow}$	$\delta^{18}O_{vsmow}$
Srp1	6.5‰	6.5‰
Srp1	6.1‰	6.1‰
Srp2	6.5‰	6.2‰
Srp2	5.9‰	6.3‰
Srp3	6.6‰	6.4‰
Srp3	6.8‰	
Srp4	6.4‰	6.2‰
Srp4	6.8‰	6.1‰
Mean	**6.5‰**	**6.3‰**
***1*σ**	*0.11*	*0.06*

Table 3.6: Whole rock O isotope analysis completed by Adrian Boyce at Scottish Universities Environmental Research Centre (SUERC), University of Glasgow. 4 aliquots of ZS17-DS were taken and each aliquot was split in four to be analysed by laser fluorination. A=Laser fluorination runs with <1hr pre-fluorination, B=Laser fluorination run, preceded by degas at 200°C in vacuo, and then with <1hr pre-fluorination.

3.7.2 Standard characterisation

When conducting SIMS measurements it is vital to have standards of a similar composition to the samples. Fe especially can greatly affect the instrument mass fractionation (IMF) of oxygen isotopes (Craven, 2017, *personal comm.*) The Fe composition of the serpentine in this chapter is 1.8 to 3.1 wt%, and Al_2O_3 is 1.2 to 2.3 wt%, and they require a standard of similar major element composition. We collected a dark coloured serpentine from 46°01'01"N and 7°50'32"E not far from Pfulwe, Swiss Alps. The piece (ZS17-DS) was not *in-situ*, but that is not necessary for a standard. ZS17-DS was analysed semi-quantitatively on the SEM at University of Edinburgh and has the same Al_2O_3 at 2.3 wt% and $\sim$5wt% FeO, which is higher than the serpentines in this study. But IMF can be characterised for the correct FeO contents using this stan-

dard and other low-Fe serpentine standards already available at EMMAC. Whole-rock measurements (Table.3.6) and *in-situ* measurements (Table.3.7) demonstrate homogeneity.

Table 3.7: In-situ SIMS data collected on the 1270. 4 other aliquots of ZS17-DS were taken and mounted in different orientations. Serp-D did not polish well, possibly due to the orientation and therefore produced slightly anomalous results. The other aliquots polished well and produced results in agreement with the WR data.

	Serp-A	**Serp-C**	**Serp-D**	**Serp-E**
Average	**6.4‰**	**6.8‰**	**7.8‰**	**6.3‰**
St.Dev	*0.52*	*0.34*	*0.36*	*0.38*
1σ	*0.05*	*0.05*	*0.11*	*0.05*

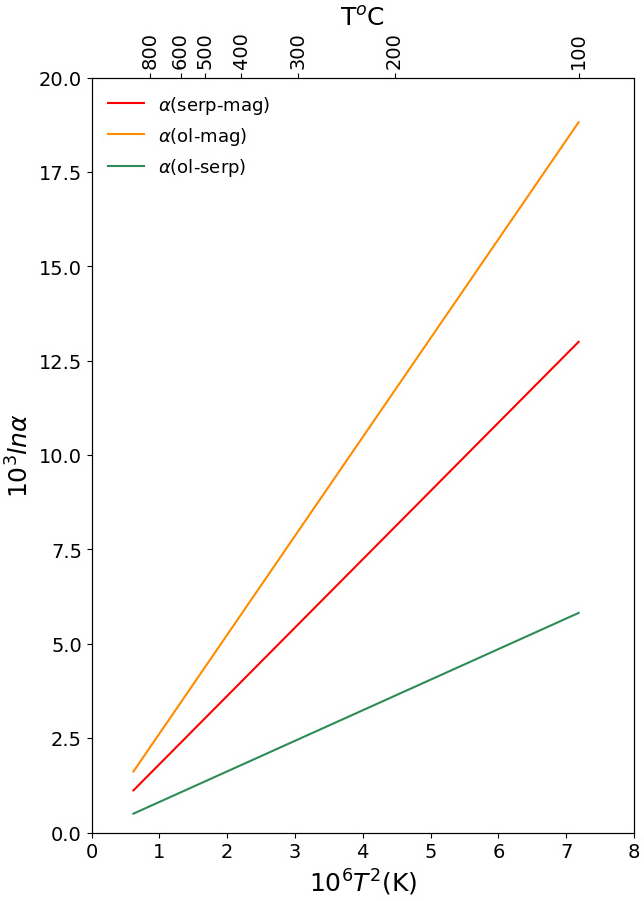

Figure 3.8: The ol-mag, serp-mag and ol-serp oxygen isotope geothermometers. Temperature can be converted into $1000 ln\alpha$, where Where $\alpha = {}^{18}O/{}^{16}O_{mineral1}/{}^{18}O/{}^{16}O_{mineral2}$. Note that the ol-serp geothermometer is shallower than the others, leading to greater uncertainty at higher temperatures.

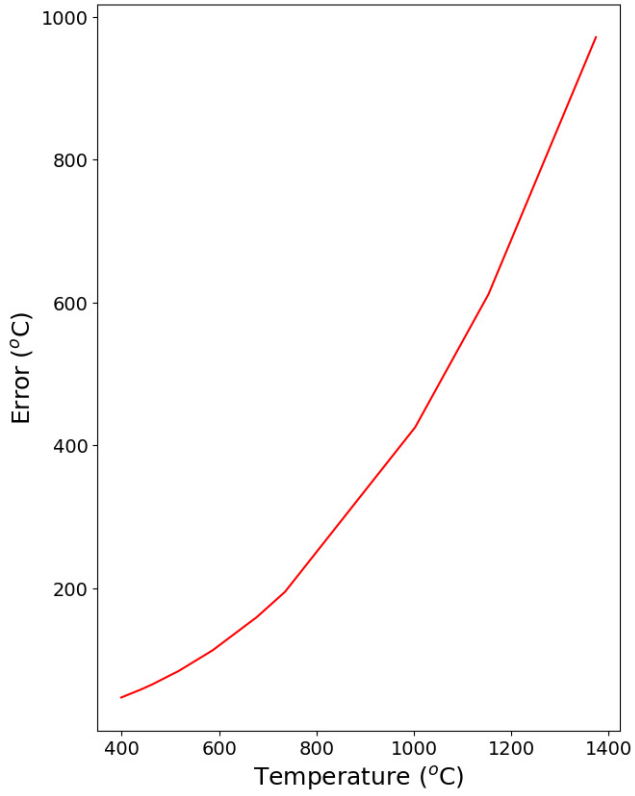

Figure 3.9: As the temperature recorded by the serpentine-olivine thermometer increases, so does the error. This is because the ‰ difference in $\delta^{18}O$ between the measured olivine and serpentine crystals decreases as the temperature increases.

3.8 Conclusion

We present a large data set of *in-situ* δ^{11}B and B concentrations in phases in partially dehydrated serpentinites. From this data we learn that secondary olivine can host in the region of 2 to 30 ppm B that is noticably heavy in isotopic signature. When compared to the average serpentine value in the same sample, we isolate different relationships that would otherwise be obscured by whole-rock data. Zermatt has the largest fractionation between the olivines and the serpentines, but their olivines are the only ones in the whole suite that contain equilibrium concentrations of B. Therefore, we suggest that the $\sim$+10‰ fractionation actually represents equilibrium fractionation between olivine and serpentine in a closed system. All of the other samples show fractionation that is smaller than $\sim$+10‰, but the olivines also contain much more B than the serpentine. We suggest that these olivines must have been exposed to a ^{10}B-rich fluid during their growth. This fluid is modelled to have an exclusively positive δ^{11}B, which could be expelled from either dehydrating meta-basalts or meta-sediments. These conclusions tie in well with the proximity of different lithologies. Zermatt is the only location where the serpentinite is isolated in the centre of a 2km wide ultramafic body, hence its apparent closed system signature. Whereas the other localities (Voltri, Almirez, Valle d'Aosta and Monviso) are much closer to different lithologies and have likely been exposed to their expelled fluids during subduction. In addition, this data set provides evidence for a reservoir of ^{11}B-rich secondary olivines that can be further subducted into the mantle.

One final notable item is the discovery of negative δ^{11}B in ocean floor serpentinites. This discovery throws our current understanding of the B composition of the subducting slab into uncertainty. It is likely that the B composition of the oceanic lithosphere is very heterogeneous, which could explain the wide spread in arc lava compositions. But it also makes modelling the B cycle very difficult because there is a wide range of possible starting compositions.

We will now move on to dehydrated serpentinites in a different geological setting: a contact aureole, to see if the same patterns can been seen there, or if there is something completely different.

Chapter 4

Contact Aureole Serpentinites

Valmalenco

"There is nothing like looking, if you want to find something. You certainly usually find something, if you look, but it is not always quite the something you were after."

J.R.R. Tolkien, The Hobbit

4.1 Foreword

Initially we embarked on this project to use the serpentinites of Valmalenco (dehydrated serpentinites in a contact aureole) as a 'natural laboratory' away from the complicated subduction zone environment. Our aim was to study the behaviour of B and its isotopes in a 'closed system' and compare this behaviour to what we found in the subduction zone serpentinites. However, we quickly discovered that complicated fluid interactions are universal to serpentinite dehydration whether they occur in a subduction zone or a contact metamorphism aureole. This chapter gives an interesting comparison to subduction zone serpentinites, along with adding to the complicated history of the dehydration associated with the Bergell intrusion in Valmalenco.

4.2 Introduction

The serpentinites of Valmalenco hold a particularly special acclamation in the study of deserpentinization, as it was here, in the Malenco unit that the first prograde serpentinite dehydration reactions were identified (Trommsdorff and Evans, 1972). Deserpentinization has recently become implicated in the delivery of volatiles to the mantle wedge (as discussed in chapter 1). But there have been only few works to date that study this enigmatic reaction, especially in terms of the volatile composition of deserpentinization fluids. The contact aureole serpentinites of Valmalenco represent a unique opportunity to study deserpentinization away from subduction zone inputs and contamination, as many subducted ophiolite terrains are heavily contaminated with external fluids (as discussed in section 3.5). B isotopes are increasingly used to track fluids in serpentinite systems due to their large B concentrations and positive δ^{11}B. Here we present *in-situ* B and δ^{11}B from a suite of partially dehydrated serpentinites from a contact aureole in Valmalenco, Italy. B isotopes in secondary olivine reveal different fluid processes occurring in different parts of the aureole and suggest that contact aureoles are subject to the same complex fluid processes as subduction zones.

4.2.1 Geological background

The samples in this study were collected from two serpentinite bodies, Preda Rossa (PR) and Alpe Zocca (AZO), in the Malenco Unit, Valmalenco, Southern Alps (see Fig.4.2). The serpentinites and meta-peridotites of Valmalenco have a long history of metamorphism and deformation which is well summarised in detail by Trommsdorff et al. (2005) and their T-time metamorphic history is shown in Fig.4.1. The Malenco unit is thought to represent a section of Permian continental crust-mantle transition, with the lower crustal metapelites welded to the underlying upper ultramafic mantle by a Permian gabbro. This whole unit underwent granulite facies metamorphism while at depth. During rifting, the Malenco unit was exhumed and metasomatized, and the sub-continental peridotitic mantle was serpentinized. The Malenco serpentinite is Mesozoic in age and forms a large ultramafic nappe of $\sim$170 km^2 (Trommsdorff and Evans, 1972) to 200 km^2 in area and 2 km thick (Peretti et al., 1992). The Malenco

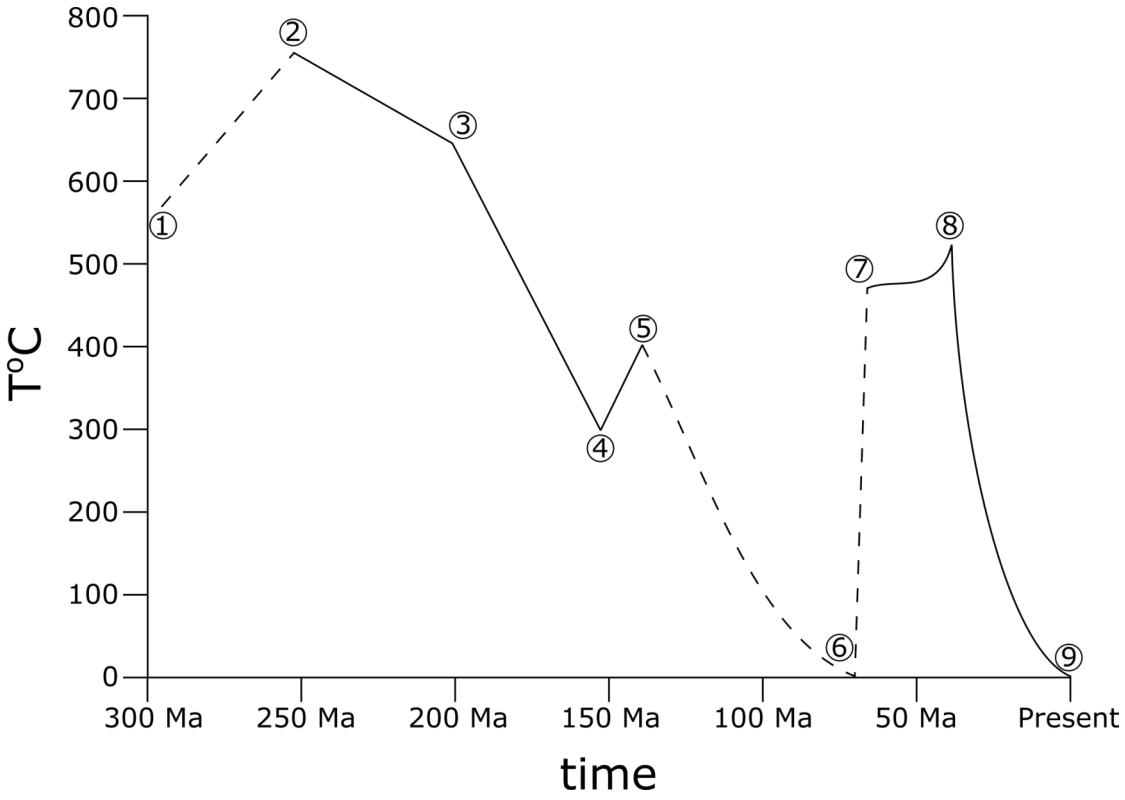

Figure 4.1: Temperature-time plot of the history of the malenco serpentinites, adapted from Trommsdorff et al. (2005). (1) The Malenco ultramafic unit starts as the malenco peridotite upper mantle underneath the Permian crust. Temperature is estimated using the standard geotherm under continental crust. (2) Intrusion of the Permian gabbros and granulite facie metamorphism occured over the next 50My, possibly peaking at the end of the Permian, with temperatues falling due to the intrusions cooling. (3) Retrograde hydration and exhumation of the Malenco granulite occured over the late Triassic/Jurassic and resulted in (4) low temperature serpentinization. (5) Intrusion of the Forno basalts and their rodingisation and accompanying slight temperature increase. (6) Possible exhumation to surface to allow deposition of ophicarbonates on Malenco Unit serpentinites. (7) Late Cretaceous Alpine metamorphism to greenschist facies conditions. (8) Intrusion of the Bergell intrusives and accompanying temperature rise results in deserpentinization of the Malenco unit serpentinites. (9) Exhumation to present day exposure.

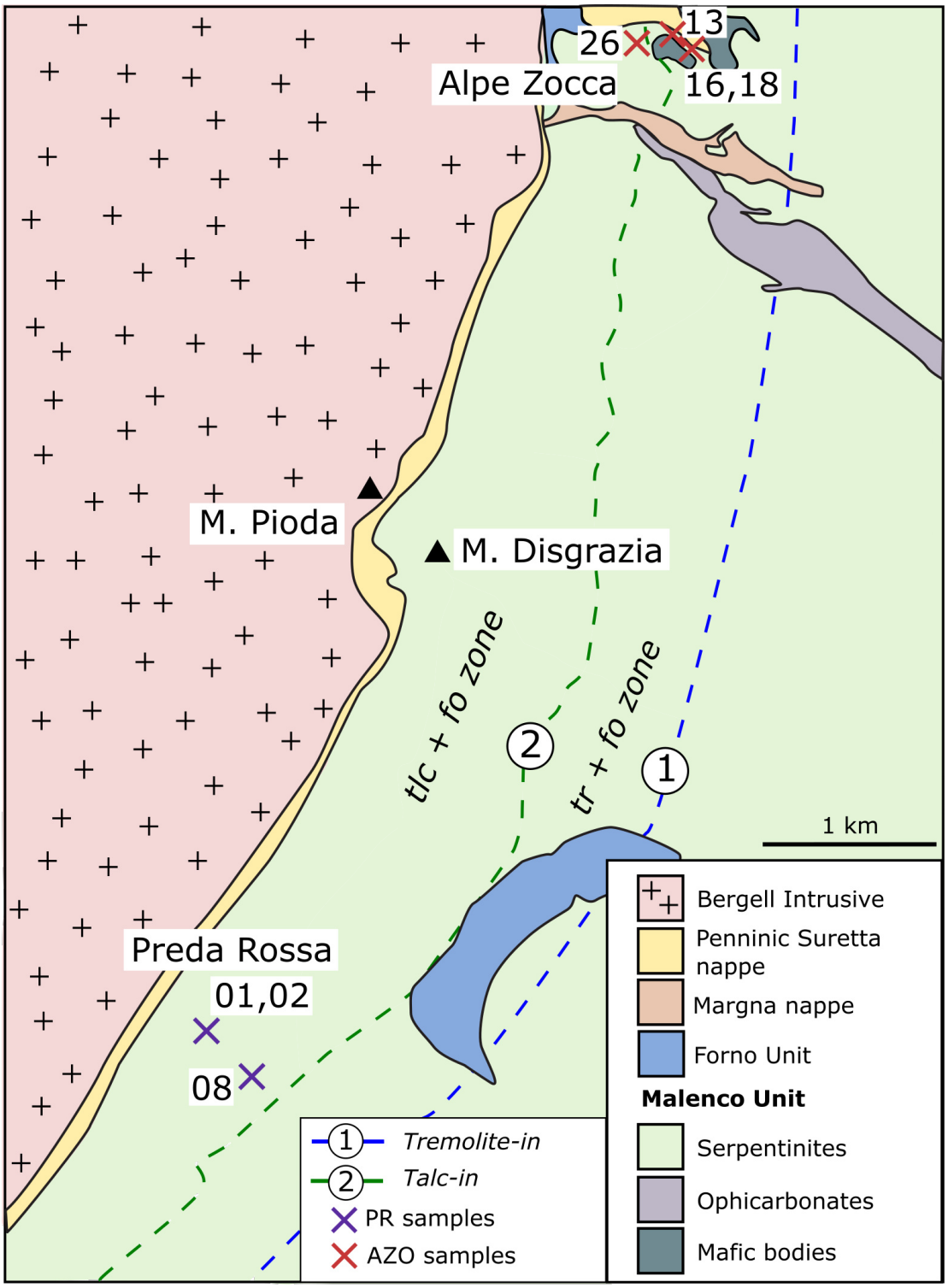

Figure 4.2: Map of the geology of the Malenco area with sample locations. Map adapted from Trommsdorff and Connolly (1996) and appendix S1 of Lafay et al. (2019).

unit is intruded by dykes from the Forno unit which underwent rodingisation during exhumation. Oxygen isotope data confirmed that both rodingisation and serpentinization processes occurred due to infiltrating seawater (Jochum et al., 2010; Burkhard and O'Neil, 1988). There is no distinct boundary between the Forno and Malenco units, with the latter likely the oceanward continuation of the former. After exhumation, the Malenco unit experienced lower greenschist facies metamorphism as a result of Alpine orogenic deformation. Two Alpine orogenic cycles are present in Valmalenco; E-W thrusting and later extension. The regional metamorphism and deformation produced a schistose rock with a greenschist facies mineral assemblage: antigorite + olivine + diopside + chlorite + magnetite; with minor titano-clinohumite and brucite (Trommsdorff and Evans, 1972). At 32Ma and 30Ma the Malenco unit was intruded by the Bergell intrusives; a suite of calc-alkaline igneous rocks of two main compositions: medium-grained hornblende tonalite and a granodiorite. Bergell magma Sr and O-isotopes are elevated above mantle array and its $\mathcal{E}$Nd bulk values are mixed between mantle and crust (Gregory et al., 2009). These data indicate that the source is an enriched lithospheric mantle source, with enrichment caused by metasomatism due to fluids derived from the dehydrating subducted slab. The shared mantle and crustal Nd values indicate that the magma assimilated crustal material as it ascended to the surface, and underwent fractional crystalisation.

Contact metamorphism from these intrusives triggered deserpentinization of the Malenco unit, which is reflected in the oxygen and hydrogen isotopes: Malenco serpentinites to the east show oceanic δ^{18}O and δD signatures, whereas serpentinites closer to the intrusion show lower δD and higher δ^{18}O, interpreted as contamination by the contact metamorphism (Burkhard and O'Neil, 1988). The contact aureole contains phases consistent with the CaO-MgO-SiO_2-CO_2-H_2O system (Trommsdorff and Connolly, 1990) and the X_{CO_2} phase diagram at 3.5kbar fluid pressure can be found in Fig.4.3. Clearly, X_{CO_2} is variable throughout the aureole owing to the variation in phase assemblages seen. In particular, the two locatlities described in this chapter show different phase assemblages. AZO samples are typically atg-serpentinites containing olivine, chlorite, serpentine (lzd overprint and antigorite), talc, some tremolite

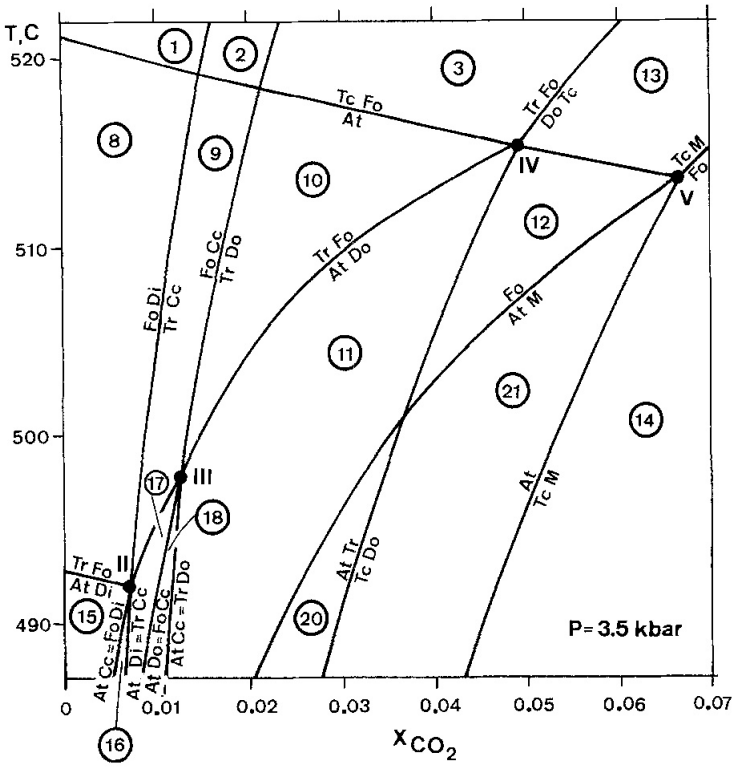

Figure 4.3: X_{CO_2} phase diagram for the Bergell aureole at 3.5kbar fluid pressure, directly from (Trommsdorff and Connolly, 1990).

and rare dolomite. PR samples are typically chl-dunites/lherzolites containing predominantly olivine with minor chlorite, tremolite, some talc and rare serpentine. Modal abundances of phases in each sample can be found in Table. 4.2. At temperatures of roughly 500°C, X_{CO_2} in the PR samples is likely to be <0.1 (in section 8 of Fig.4.3) and for the AZO samples between 0.01 and 0.03 (in section 11 of Fig.4.3) owing to the presence of Dolomite but lack of Magnesite or Calcite.

It is important, given the evidence for fluid movement through the aureole, to place the Malenco serpentinites in lithological context. The Malenco ultramafic unit borders the southeastern edge of the Bergell tonalite intrusives (as seen in Fig.4.2). The contact zone between these units is marked with thin (<10 m thick) lenses of Penninic Suretta nappe (Trommsdorff and Connolly, 1996) which comprises both basement rocks, predominantly biotite schist and gneiss, metapelite and amphibolite, and a sedimentary cover which comprises metaconglomerate and fine grained quartzite overlain by pure and impure calcite and dolomite marbles (Trommsdorff et al., 2005).The Margna nappe is part of the austroalpine unit and comprises gabbros and lower crustal granulites (Trommsdorff et al., 2005). The Forno Unit comprises a mid-ocean ridge basalt type lithology with preserved pillow lavas. As shown on Fig.4.2, the AZO samples were taken from close proximity to the Suretta nappe basement and sedimentary rocks, mafic bodies and ophicarbonates within the Malenco unit, Forno unit MORB and the Margna nappe gneisses. Conversely, the PR samples are relatively isolated within the Malenco unit ultramafic rocks.

On the boundary between the Bergell intrusive and the Malenco Unit sits the Suretta nappe (deformed Mesozoic carbonates and gneissic basement rocks) which is parallel to the Preda Rossa shear zone. This shear zone is syn-magmatic (Berger and Gieré, 1995; Berger et al., 1996) and was active during the contact metamorphism of the surrounding serpentinites. The Preda Rossa shear zone extends from Valle di Preda Rossa along the contact between the Suretta nappe and the Bergell intrusive and beyond, terminating in Valle Sissone. Fig 4.4 shows a cross section from the SW to the NE of the bergell intrusion (just missing Valmalenco) from Rosenberg

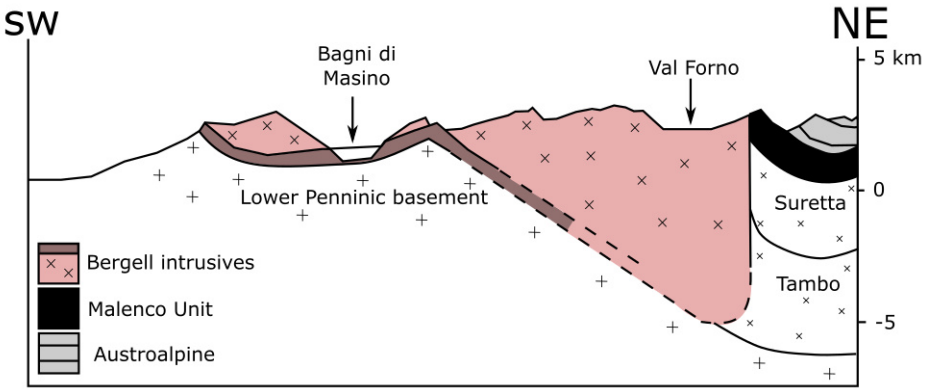

Figure 4.4: Cross section showing the relationship between the basement nappes (suretta and tambo), the malenco unit and the bergell intrusive rocks, adapted from Rosenberg et al. (1995).

et al. (1995). The eastern border of the pluton shows a discordant contact between the intrusives and the basement which is overprinted by a foliation that is parallel to the intrusive margin. The country rock surrounding the pluton dip gently east until they abruptly steepen when in close proximity to the pluton and form an asymmetric synform (as seen in Fig. 4.4). The axial trace is parallel to the intrusive contact (Rosenberg et al., 1995).

The vast majority of the Malenco serpentinite was originally harzburgite, except the rocks with greater proportions of tremolite and less talc, which are most likely of lherzolite origin (Trommsdorff and Evans, 1972). This lithology defines the composition of the metamorphosed aureole. The Bergell contact aureole comprises 4 zones in order of increasing metamorphic grade (as presented in Trommsdorff and Evans, 1972): a. atg-ol-diopside, b. atg-ol-trem, c. tlc-ol-trem and d. anthophyllite-ol-trem (sometimes enst). Two generations of olivine have been identified in the Malenco serpentinite (Peretti et al., 1992) and it is the metamorphic (2nd gen) olivine that form the subject of this study.

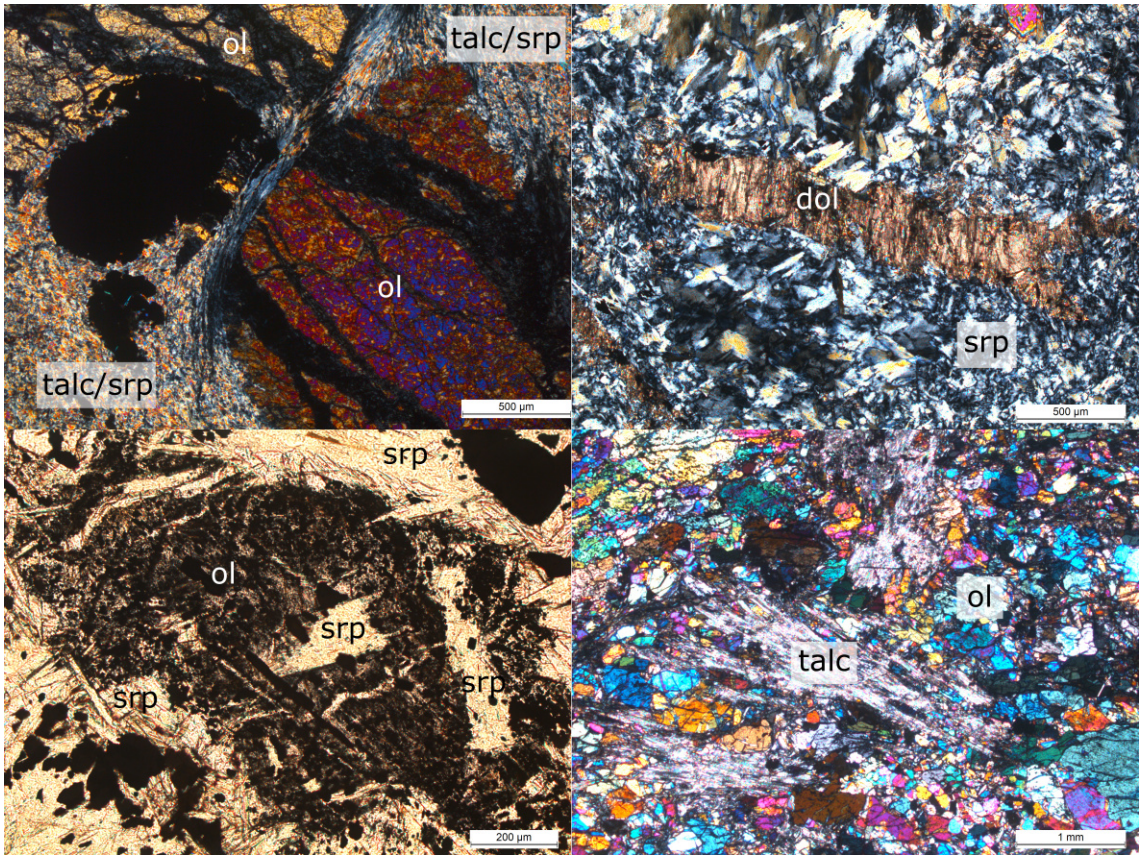

Figure 4.5: Example textures from the Valmalenco serpentinites. (Top right) AZO-13 talc/antigorite mix around large metamorphic olivines which are cut by black lizardite veins of a later overprint. (Top left) AZO-16 large antigorite crystals surround a large (1mm long) dolomite crystal. (Bottom right) AZO-16 secondary olivine included with flakes of antigorite. (Bottom left) PR02 Olivine and talc inter-grown texture.

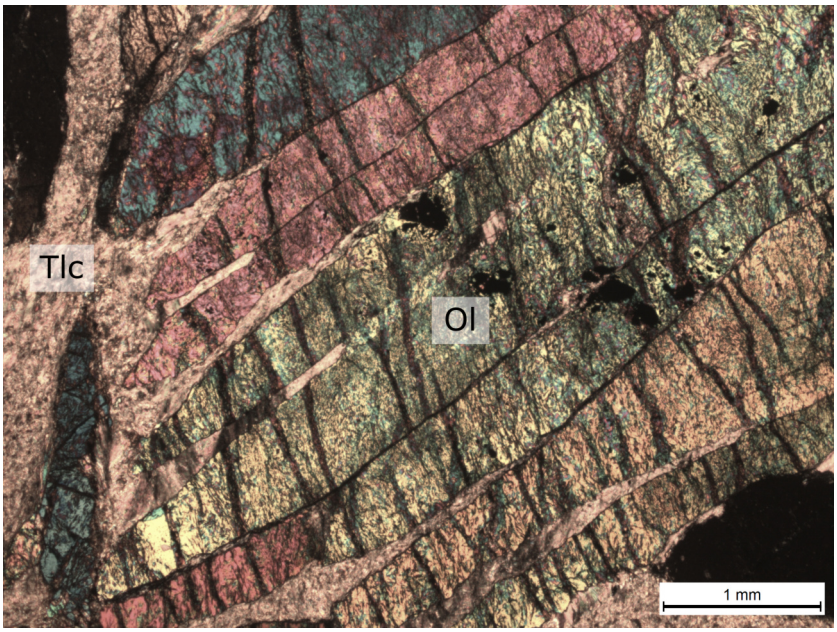

Figure 4.6: Jack Straw texture in sample AZO-26. Elongate ol with slight lizardite overprint veining, often several mm long and in preferred orientation.

4.2.2 Sample descriptions

Samples were obtained from Romain Lafay (as in Lafay et al., 2019) and come from two locations in Valmalenco, Italy (see Fig.4.2) Alpe Zocca (AZO, in vicinity of 46.3°N, 9.8°E) and Preda Rossa (PR, in vicinity of 46.2°N, 9.7°E). AZO samples are typically atg-serpentinites containing olivine, chlorite, serpentine (lzd overprint and antigorite), talc and some tremolite. PR samples are typically chl-dunites/lherzolites containing predominantly olivine with minor chlorite, tremolite, some talc and rare serpentine. Modal abundances of phases in each sample can be found in Table. 4.1.

AZO-13-S

Serpentinite with bastite and mesh texture (lizardite), some antigorite and magnetite. This sample boarders onto talc/olivine assemblage seen in AZO-13.

Sample	Location	Phase ID	Proportion
AZO-13	46.29514°N 9.76903°E	Olivine	30%
		Serpentine	15%
		Chlorite	10%
		Talc	25%
		Vein Lizardite	20%
AZO-13-S	46.29514°N 9.76903°E	Serpentine	100%
AZO-16	46.29483°N 9.76906°E	Olivine	10%
		Serpentine	75%
		Amphibole	15%
AZO-18	46.29483°N 9.76906°E	Olivine	48%
		Serpentine	15%
		Amphibole	2%
		Talc	15%
		Vein Lizardite	20%
AZO-26	46.29459°N 9.76595°E	Olivine	40%
		Amphibole	1%
		Talc	59%
AZO-26-S	46.29459°N 9.76595°E	Serpentine	100%
PR01	46.24559°N 9.73253°E	Olivine	90%
		Chlorite	10%
PR02	46.24559°N 9.73253°E	Olivine	85%
		Serpentine	1%
		Chlorite	9%
		Talc	5%
PR08	46.24322°N 9.73571°E	Olivine	40%
		Chlorite	40%
		Amphibole	20%

Table 4.1: Phase compositions of all Valmalenco serpentinites.

AZO-13

Large 2-3mm secondary olivines are cut by 50-100μm lizardite veins and smaller <1mm olivines are preserved in mesh cores. The smaller olivines are likely relic, given their texture. The olivines are surrounded by an intergrown talc/antigorite texture. Talc and antigorite intergrowths are on μm scale with individual crystals <50μm. Talc crystals are more abundant and often larger. Talc/antigorite patches appear to cut lizardite in some places (as in Fig.4.5) but in other cases the lizardite cuts the talc. This partial lack of lizardite cutting talc is because olivine hydrates to lizardite but talc does not, thus when the later lizardite overprint occured, lizardite only formed in the olivines.

AZO-16

Atg makes up the bulk of this rock with clusters of olivine and amphibole. Atg blades are up to 0.5mm but many are <0.1mm, the larger atg crystals typically cluster together within the matrix of smaller atg crystals. Olivine varies from 0.5 to 1mm but often edges are not well defined and they look like interstitial growth. There are rare, small ($\sim$ 1 mm) amphibole crystals also present (as seen in Fig.4.5).

AZO-18

Predominantly elongated Jack-straw-textured-olivine on mm scale which are similar to those pictured in see Fig.4.6 (which are seen and described in other prograde serpentinite bodies associated with regional metamorphism, e.g. Bakke and Korneliussen, 1986). Cut by veins of serpentine with a preferred orientation. In between olivine are patches of talc, atg associated with olivine crystals: i.e. on the rims or included. Accessory amphibole present in matrix also.

AZO-26-S

Highly chloritzed serpentinite suffering from high retrograde alteration. This sample was analysed with the others but has been left out of the discussion owing to the heavy retrograde alteration.

AZO-26

Large Jack-straw-textured-olivine phenocrysts (mm scale) in a matrix of inter-grown talc and antigorite, see Fig.4.6 for an image of the Jack Straw-textured olivines.

PR01

Sample is predominantly olivine of which there are two groups split by size: larger are 1-2mm and smaller are 50-200μm. Rare serpentine/chlorite crystals occur in patches around olivines and there is a late stage srp/chl veining overprint. Small olivines form in clusters around the edges of larger olivines and form diffuse vein structures. Large olivines are heavily fractured and have inclusions, whereas small olivines are less fractured and typically contain no inclusions.

PR02

Sample contains large (1mm by 3-4mm) talc crystals, but they are not dominant. Most of the sample is made of olivine. Olivine in this sample is mostly small (50-300μm) and forms diffuse vein structures around large talc crystals. Rare serpentine and chlorite crystals are present on edges or included within small olivines. Smaller talc crystals are present in rare clusters.

PR08

Strikingly different to other PR samples, with the main matrix composed of very fine (<50um) olivine, tremolite and chlorite. Larger ($\sim$0.5mm) opaque minerals and olivines are cut by serpentine veins and larger tremolite are also present. Tremolite crystals have a weak preferred orientation (as seen in Fig.4.5).

Summary

Overall, AZO (Alpe Zocca) serpentinites are abundant in serpentine, contain talc, and minor amphibole and chlorite, whereas PR (Preda Rossa) serpentinites are typically lacking, or contain very fine, serpentine and talc and contain chlorite and more instances of tremolite. Most samples contain two groups of olivine: large (>1mm) and

small (<1mm) and all samples preserve olivine in close association with (common or rare) antigorite either adjacent to or as inclusions. Some serpentine is too small to measure on the SIMS (<20μm) and therefore much of the PR serpentine is not reflected in the geochemical results.

4.2.3 Contact aureoles

Contact metamorphism occurs around hot igneous intrusions where heat from the intrusion diffuses through the surrounding, cooler, country rock. The country rock that has undergone metamorphism forms the metamorphic aureole. The peak metamorphic facies is defined by the minerals present that formed at the highest temperature, usually the closest to the intrusion. The size and shape of the aureole depends on the size and shape of the intrusion and the difference in temperature between the two rocks. Magmatic fluids may also penetrate the country rock, causing hydrothermal metamorphism and advecting heat. This effect has been modelled by Cui et al. (2001), who describe 3 distinctive fluid flow regimes. Firstly, an early down-temperature flow of released magmatic fluids. Secondly, during peak metamorphism, small, flat convection cells develop near the intrusive body. Finally, there is a late down-temperature fluid flow in the upper aureole, and an up-temperature fluid flow from the middle to lower aureole. Permeability of the country rock is also an important factor, where greater permeability promotes fluid flow and heat advection. When the permeability is high enough ($> 10^{-16} m^2$) the heat advection by fluids is significant.

A thermal model for the Bergell aureole was developed by Trommsdorff and Connolly (1996), see Fig.4.7. They report a peak temperature of $\sim$560 to 580°C next to the intrusion which decreases quickly to 500 to 520°C at 1000 m (the samples in this study are all within the first 1km of the contact aureole) then more slowly to 380 to 435°C by 4000m away. This model is based on an initial country rock temperature of 350°C, due to the geothermal gradient (which is roughly 25–30 °C/km) at 10-12km depth. The model is a simple conduction model (Fig.4.7) and the computed maximum temperatures show great agreement with the inferred metamorphic isograds (Trommsdorff and Connolly, 1996). They conclude that since such agreement was met with a simple convection model, heat advection through fluid focusing or free fluid convection

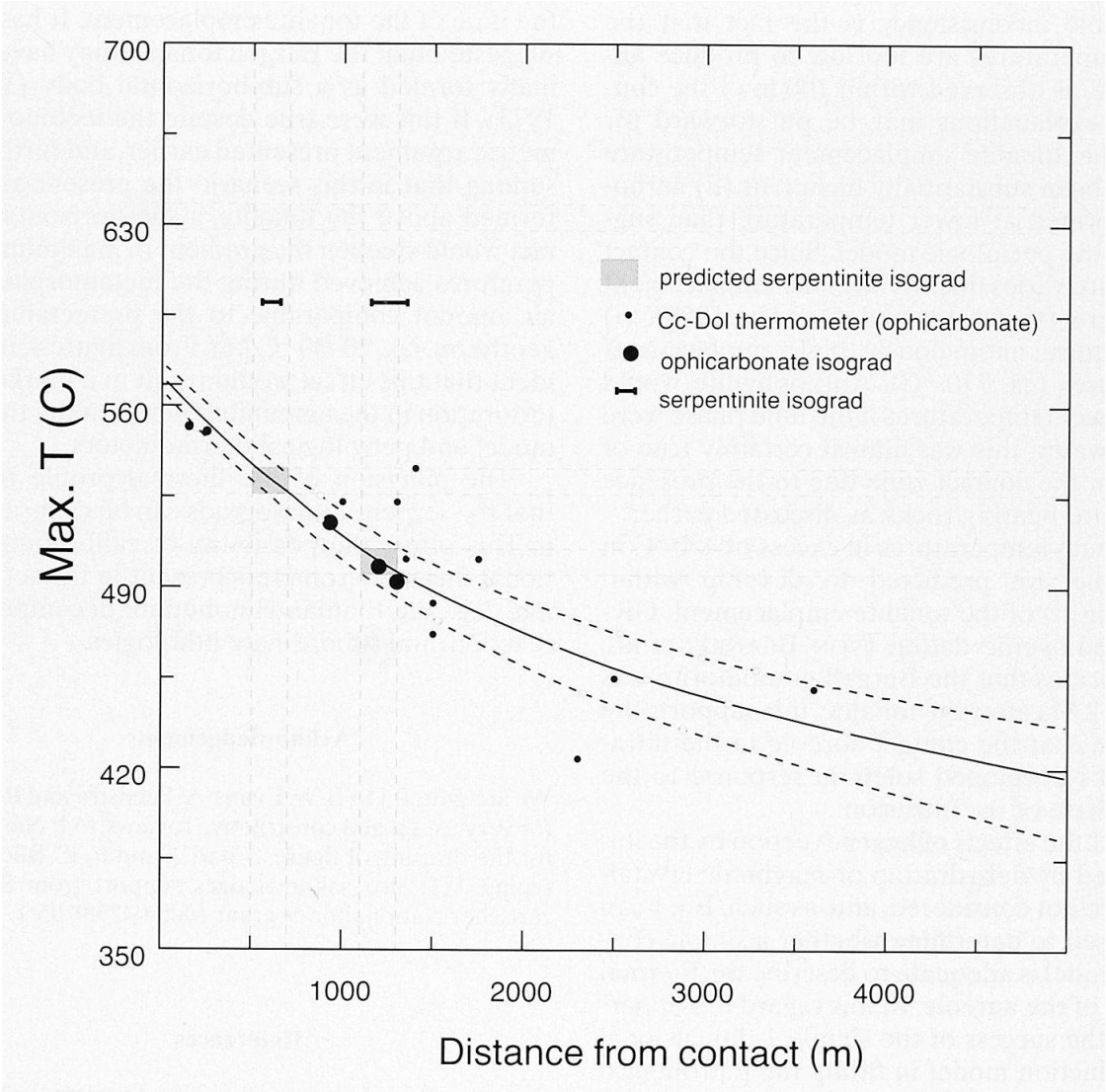

Figure 4.7: T-Distance for Bergell aureole taken directly from Trommsdorff and Connolly (1996), which depicts the computed distribution of maximum temperatures in the Bergell aureole, where the initial country rock temperature is 350°C and dashed lines indicates profiles where initial T=330°C to 370°C.

are not important in this aureole.

4.3 Results

4.3.1 Major elements

Olivine

The PR and AZO metamorphic olivines have broadly similar major element compositions. All samples have similar NiO contents (0.15 to 0.5 wt%) but can be separated by MnO and Mg# (as seen in Fig.B.3). AZO-13,-18 and PR08 share the same range of MnO and Mg# values (0.19 to 0.25 wt% MnO and Mg# 90 to 92), whilst PR01 and PR02 have 0.05 to 0.1 wt% less MnO (0.15 to 0.17) than the AZO samples and PR08. In addition PR01 has Mg# at 92-93, whereas PR02 sits lower at around 91-92. AZO-26, although having a similar MnO range to AZO-13,-18 and PR08, has much lower Mg# (86 to 88). FeO also seperates the olivines with PR08 having the lowest ($\sim$7.5 wt%), AZO-26 the highest ($\sim$12 wt%) with an average of the whole set of $\sim$8 wt%.

Antigorite

PR and AZO antigorite major element composition is very similar, though due to a lack of serpentine in the PR samples, there is only antigorite data from PR02. PR02 antigorite has very similar composition (especially Mg# and Al_2O_3) to AZO-13-S, and -16 (all within Mg# 94 to 96 and Al_2O_3 1 to 3 wt%, see Fig.B.5). AZO-13 and -18 antigorite have Al_2O_3 values at around 2-4 wt% and again similar Mg# values (94-96). Serpentine from AZO-26-S is a chemical out-lier from the other serpentine with lower Mg# of 86 to 89 and much higher Al_2O_3 of 15 to 17 wt% (due to retrograde alteration) and it is likely that this serpentine has been chloritized. Antigorite across the sample set typically has low MnO (<0.1 wt%) and low NiO (<0.2 wt%).

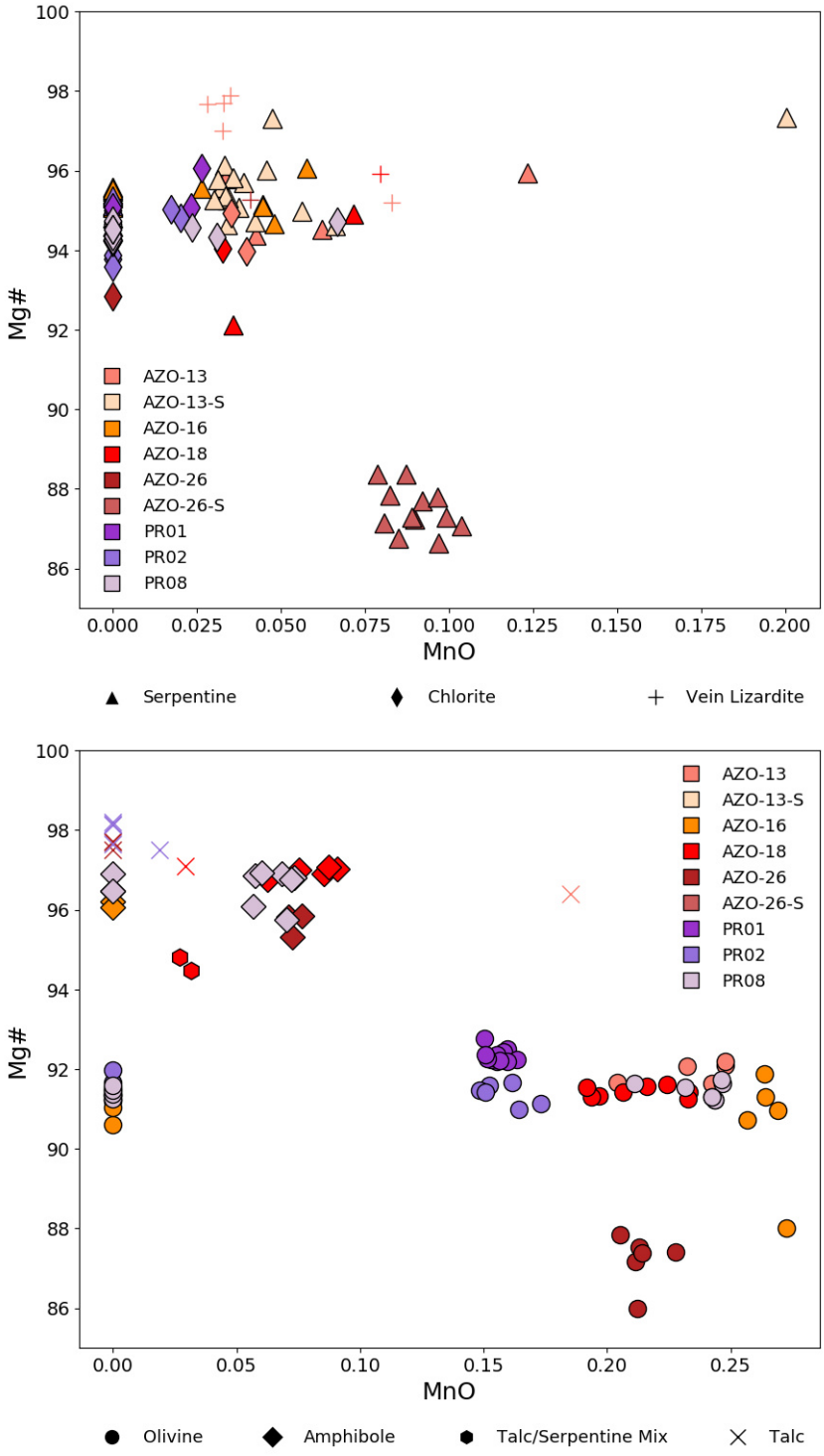

Figure 4.8: (Above) Mg# vs MnO for serpentinite phases serpentine, chlorite and vein lizardite. There is a positive correlation in the antigorite serpentine. (Below) Mg# vs MnO for phases formed during the formation of the Bergell aureole, including: talc, olivine, amphibole and the talc/serpentine mixture.

Chlorite

The PR chlorites from PR01,-02 and -08 are compositionally very similar with Al_2O_3 8 to 16 wt%, Mg# 94 to 96, NiO 0.14 to 0.24 wt % and MnO 0 to 0.04 wt%. AZO-13 chlorite has 6 to 10 wt% Al_2O_3 and Mg# 94 to 95, and AZO-18 chlorite has 10 wt% Al_2O_3 and Mg# 94.

Other

Tremolite across the sample set have broadly similar major element compositions. Mg# range from 95 to 98, NiO and MnO are low (<0.2 wt%) and Al_2O_3 is also low (<0.6 wt%). The different samples are separated slightly from each other in Fig.B.2, With PR samples having generally higher Mg# >96.5 whereas AZO are generally <96.5. Talc Mg# ranges from 96 to 98.5, with the higher numbers belonging to the PR talc ($\sim$98) and the lower to the AZO talc (96 to 98). Talc has low MnO, Al_2O_3 and Nio (<0.2-0.3 wt%).

4.3.2 Fluid mobile elements and Boron isotopes

Olivine

AZO samples contain olivine with high B (1.8-21 μg g^{-1}), with spinifex-like olivine B concentrations at the higher end (>11 μg g^{-1}). PR01,-02, AZO-13 and -26 olivines have the highest B (10 to 21 μg g^{-1}) and AZO-16,-18 and PR08 olivines have lower B (0 to 5 μg g^{-1}). The small olivines in PR01 show the same concentration of B as the larger olivines, however, the small olivines in PR02 have much less B (0.4-0.7 μg g^{-1}) B than the larger olivines. Olivine is the only phase to contain significant (>0.1 μg g^{-1}) Li with a range of 0.8 to 15.0 μg g^{-1}. AZO-16 olivines shows the highest concentrations of Li 1-15 μg g^{-1}, whereas the rest of the samples have similar Li <6 μg g^{-1}. Olivines do not contain signigicant F (<50 μg g^{-1}) or Cl (<25 μg g^{-1}) compared to other phases.

δ^{11}B reveals a major divide between the two main groups: AZO olivines have light δ^{11}B (-12.1 to +1.9 ‰) and PR olivines show a heavier signature (+1.3 to +24.7 ‰).

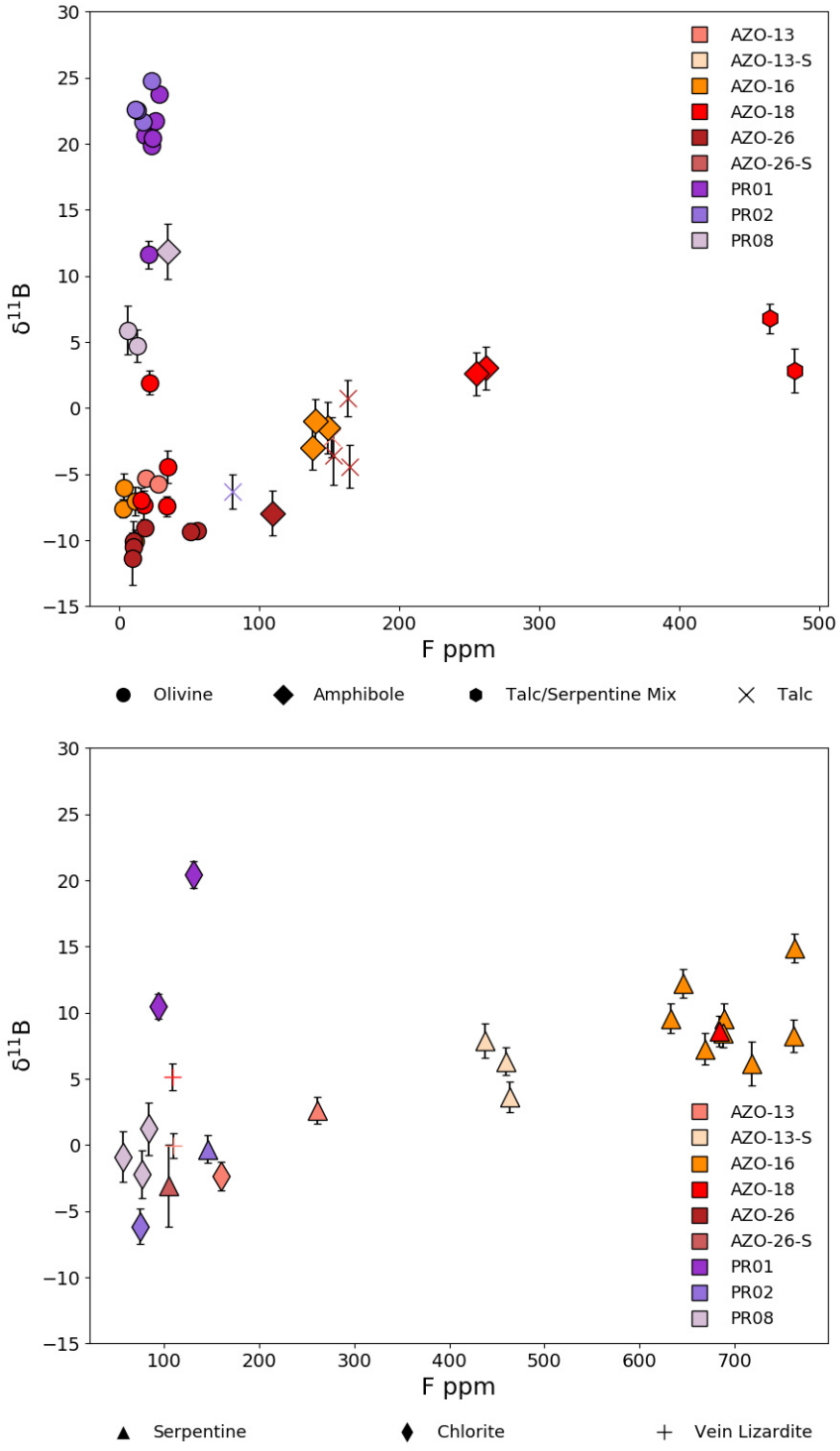

Figure 4.9: (Above) δ^{11}B vs F for phases formed during the formation of the Bergell aureole, including: talc, olivine, amphibole and the talc/serpentine mixture. (Below) δ^{11}B vs F for serpentinite phases serpentine, chlorite and vein lizardite. There is a positive correlation in the antigorite serpentine.

Antigorite

AZO samples often contain an antigorite/talc mixture formed of intergrown atg and talc crystals on the 10's μm scale. Since the two phases cannot be distinguished on the SIMS visual output, it was often difficult to measure the phases separately. Clean antigorite measurements were identified by correct water and aluminium totals. Antigorite that was measured contains 2.4-16.6 μg g^{-1} B and 0.1 - 11 μg g^{-1} Li, except for that in AZO-26-S which has low B 0.3-0.5 μg g^{-1} and low Li 0.4-0.5 μg g^{-1}. PR samples contain very little, and relatively small serpentine crystals. Therefore only one was successfully measured on SIMS and shows 13.3 μg g^{-1} B and 0.4 μg g^{-1} Li. Antigorite serpentine in AZO-13,-13-S, -16,-18,-26 and PR02 has high F (105 to 855 μg g^{-1}) and low Cl (5 to 190 μg g^{-1}), especially those from the former 4 AZO samples, see Fig.B.8. When F is compared to δ^{11}B there is a positive correlation in the antigorite serpentine that separates each sample. AZO-16 and -18 have the highest δ^{11}B and F and both analytes decrease in value to AZO-13-S to AZO-13 then to PR02 and AZO-26-S, which have the lowest δ^{11}B and F see Fig.B.4.

Only one serpentine was large enough for a SIMS spot (>20μm) in the PR samples. It has a much lower δ^{11}B than the olivine at -0.3 ‰. The AZO samples, however, contain abundant serpentine and show δ^{11}B much higher than the AZO olivine -0.1 to +14.9 ‰.

Chlorite

Chlorite contains low Cl and F. PR samples contain more chlorite than serpentine which has lower B 0.7-3.9 μg g^{-1} and low <0.7 μg g^{-1} Li.
δ^{11}B in PR chlorite varies considerably from -6.2 to +20.4 ‰.

Phase		AZO-13	AZO-13-S	AZO-16	AZO-18	AZO-26	AZO-26-S	PR01	PR02	PR08
Olivine	**B μg g^{-1}**	13.8		3.7	4.7	5.6		16.2	10.5	2.5
	***1*σ**	*2.8*		*1.0*	*0.5*	*2.0*		*1.1*	*3.2*	*1.4*
	δ^{11}B	-4.7‰		-8.2‰	-4.9‰	-9.7‰		19.7‰	22.9‰	7.9‰
	***1*σ**	*0.7‰*		*0.8‰*	*1.2‰*	*0.5‰*		*1.7‰*	*0.7‰*	*2.8‰*
	Abundance	30%		10%	48%	40%		90%	85%	40%
Serpentine	**B μg g^{-1}**	13.9	4.2	3.6	4.9		0.4		14.2	
	***1*σ**	*2.7*	*0.5*	*0.5*			*0.1*			
	δ^{11}B	2.6‰	6.4‰	9.3‰	8.6‰		-0.3‰		-0.3‰	
	***1*σ**		*1.0‰*	*0.8‰*			*1.4‰*			
	Abundance	15%	100%	75%	15%		100%		1%	
Chlorite	**B μg g^{-1}**	24.9						4.3	2.7	1.4
	***1*σ**	*5.7*						*0.7*	*1.9*	*0.2*
	δ^{11}B	-2.3‰						15.4‰	-6.2‰	-0.6‰
	***1*σ**							*5.0‰*		*1.0‰*
	Abundance	10%						10%	10%	40%
Amphibole	**B μg g^{-1}**			1.4	2.3	1.6				0.8
	***1*σ**			*0.0*	*0.1*	*0.2*				
	δ^{11}B			-1.8‰	2.8‰	-9.3‰				10.6‰
	***1*σ**			*0.6‰*	*0.2‰*	*1.3‰*				*0.7‰*

Phase		**AZO-13**	**AZO-13-S**	**AZO-16**	**AZO-18**	**AZO-26**	**AZO-26-S**	**PR01**	**PR02**	**PR08**
	Abundance			15%	2%	1%				20%
Talc	**B μg g^{-1}**	4.1			7.3	2.3			1.2	
	***1*σ**	*1.9*				*1.2*			*0.3*	
	δ^{11}B	-2.2‰			1.0‰	-2.4‰			-6.3‰	
	***1*σ**					*1.6‰*				
	Abundance	25%			15%	59%			5%	
Vein Lzd	**B μg g^{-1}**	131.2			11.5					
	***1*σ**	*50.3*								
	δ^{11}B	-0.1‰			5.3‰					
	***1*σ**				*0.2‰*					
	Abundance	20%			20%					
Calculated Bulk B μg g^{-1}		35.9	4.2	3.3	6.4	3.6	0.4	15	19.3	1.7
***1*σ**		*50.9*	*0.5*	*1.1*	*0.5*	*2.7*	*0.1*	*1.3*	*3.8*	*1.4*
Calculated Bulk δ^{11}B		-1.8‰	6.4‰	5.9‰	0.2‰	-5.4‰	-0.3‰	19.2‰	18.5‰	5‰
***1*σ**		*0.7‰*	*1.0‰*	*1.3‰*	*1.2‰*	*2.7‰*	*1.4‰*	*5.3‰*	*0.7‰*	*3.0‰*

Table 4.2: Average B and δ^{11}B compositions of each phase in each sample with estimated modal abudance. Where 1σ values are missing, only one measurement was available. NB: AZO-18 talc composition was calculated using serpentine and mix data assuming the mix comprises 50:50 talc serpentine.

Other

Talc and tremolite across the whole suite typically contain little to no B and Li, <2.4 μg g^{-1} and <0.4 μg g^{-1}, respectively for tremolite and <4.7 μg g^{-1} B and <1.8 μg g^{-1} Li for talc. Talc contains moderate F (50 to 170 μg g^{-1}) and little Cl (2 to 150 μg g^{-1}) compared to the other phases. Amphibole is also similar (34 to 260 μg g^{-1} F and 2 to 16 μg g^{-1} Cl). Talc typically shows light δ^{11}B (-6.3 ‰ to +0.7 ‰) and there is no difference between the AZO and PR samples. Whereas amphibole varies considerably between the two sample locations with AZO being much lighter (-10.6 to +3.0 ‰) and PR much heavier(+9.3 to +11.8 ‰). Vein lizardite is present and measurable in samples AZO-13 and -18, but they have quite different B compositions. In sample AZO-13 the veins have δ^{11}B of -0.1‰ and B of 274 μg g^{-1}, whereas AZO-18 has δ^{11}B of $\sim$+5.3‰ and B of 11.5 μg g^{-1}. Vein lizardite in both samples has high Cl (360 to 1075 μg g^{-1}) but low F (90 to 110 μg g^{-1}) compared to other phases (see Fig.B.19).

4.4 Summary Data

Table 4.3: The average FME compositions of each phase in every sample.

Sample	Phase	H_2O wt%	Li	F	Cl
AZO-13	CHL	11.3	10.2	124.6	181.0
AZO-13	MAG				
AZO-13	MIX	9.3	11.6	260.1	89.7
AZO-13	OL	0.0	3.1	22.7	9.0
AZO-13	SRP	13.8	5.6	248.9	129.8
AZO-13	TLC	5.9	16.1	159.3	45.9
AZO-13	VEIN LZ	14.0	0.4	98.2	570.9
AZO-13-S	MAG				
AZO-13-S	SRP	14.2	0.5	437.5	22.0
AZO-16	AMPH	2.2	0.1	142.1	5.1
AZO-16	OL	0.0	8.3	6.6	9.9

Sample	Phase	H_2O wt%	Li	F	Cl
AZO-16	SRP	12.7	0.0	709.5	11.8
AZO-18	AMPH	2.4	0.1	258.2	9.0
AZO-18	CHL				
AZO-18	MIX	10.1	0.2	499.1	19.7
AZO-18	OL	0.0	2.6	24.3	5.5
AZO-18	SRP	12.3	0.4	683.9	37.4
AZO-18	TLC				
AZO-18	VEIN LZ	15.1	0.0	108.6	633.9
AZO-26	AMPH	2.5	0.3	114.8	11.1
AZO-26	CHL				
AZO-26	CR-SPINEL				
AZO-26	MIX	10.2	0.1	167.4	94.4
AZO-26	OL	0.0	2.2	25.6	9.5
AZO-26	TLC	5.8	0.1	160.0	78.3
AZO-26	VEIN LZ				
AZO-26-S	SRP	15.0	0.4	115.4	19.0
PR01	CHL	13.5	0.4	112.8	34.6
PR01	NI-SPINEL				
PR01	OL	0.1	1.0	22.8	10.8
PR02	CHL	12.3	0.3	84.5	75.7
PR02	OL	0.0	2.0	11.9	8.7
PR02	SRP	11.9	0.4	146.4	138.1
PR02	TLC	5.7	1.3	80.2	7.8
PR08	AMPH	2.3	0.0	34.1	7.2
PR08	CHL	13.1	0.1	72.7	24.3
PR08	OL	0.1	2.3	10.7	3.8

Table 4.4: The average Major compositions of each phase in every sample.

Sample	Phase	MgO	SiO_2	FeO	Na_2O	Al_2O_3	P_2O_5	CaO	Cr_2O_3	MnO	NiO	K_2O	TiO	Mg#
AZO-13	CHL	35.1	35.5	3.7	0.0	7.9	0.0	0.0	0.4	0.0	0.2	0.0	0.0	94.5
AZO-13	MAG	1.1	0.0	85.9	0.0	0.0	0.0	0.0	6.4	0.2	0.6	0.0	0.2	2.2
AZO-13	OL	51.0	41.2	8.0	0.0	0.0	0.0	0.0	0.1	0.2	0.3	0.0	0.0	91.9
AZO-13	SRP	36.6	41.9	3.3	0.0	3.4	0.0	0.0	0.3	0.1	0.1	0.0	0.0	95.2
AZO-13	TLC	33.5	55.0	2.2	0.0	0.3	0.0	0.0	0.0	0.2	0.2	0.0	0.0	96.4
AZO-13	VEIN LZ	40.0	41.0	2.1	0.0	0.2	0.0	0.0	0.0	0.0	0.2	0.0	0.0	97.1
AZO-13-S	MAG	1.4	0.0	83.6	0.0	0.0	0.0	0.0	8.1	0.4	0.5	0.0	0.4	2.8
AZO-13-S	SRP	38.7	42.2	3.2	0.0	1.8	0.0	0.0	0.2	0.0	0.1	0.0	0.0	95.5
AZO-16	AMPH	23.9	58.9	1.7	0.0	0.1	0.0	13.3	0.0	0.0	0.1	0.0	0.0	96.2
AZO-16	OL	50.2	40.8	9.0	0.0	0.0	0.0	0.0	0.1	0.1	0.2	0.0	0.0	90.8
AZO-16	SRP	38.3	42.7	3.4	0.0	1.6	0.0	0.0	0.1	0.0	0.1	0.0	0.0	95.3
AZO-18	AMPH	24.1	58.2	1.4	0.1	0.1	0.0	13.3	0.0	0.1	0.1	0.0	0.0	96.9
AZO-18	CHL	34.0	34.8	3.8	0.0	10.0	0.0	0.0	1.6	0.0	0.1	0.0	0.0	94.0
AZO-18	MIX	35.2	42.1	3.6	0.0	4.9	0.0	0.0	0.8	0.0	0.1	0.0	0.0	94.6
AZO-18	OL	50.0	40.6	8.3	0.0	0.1	0.0	0.1	0.0	0.2	0.2	0.0	0.0	91.4
AZO-18	SRP	38.5	37.2	4.9	0.0	2.1	0.0	0.0	0.6	0.1	0.1	0.0	0.0	93.5
AZO-18	TLC	31.1	59.9	1.7	0.0	1.3	0.0	0.0	0.2	0.0	0.1	0.0	0.0	97.1

Sample	Phase	MgO	SiO_2	FeO	Na_2O	Al_2O_3	P_2O_5	CaO	Cr_2O_3	MnO	NiO	K_2O	TiO	Mg#
AZO-18	VEIN LZ	42.2	37.5	3.2	0.0	0.1	0.0	0.0	0.0	0.1	0.2	0.0	0.0	95.9
AZO-26	AMPH	23.9	58.0	1.9	0.1	0.3	0.0	13.2	0.0	0.1	0.1	0.0	0.0	95.7
AZO-26	CHL	33.6	32.1	4.6	0.0	11.8	0.0	0.0	0.0	0.0	0.2	0.0	0.0	92.8
AZO-26	CR-SPINEL	2.9	0.2	61.6	0.0	0.4	0.0	0.0	27.1	0.5	0.4	0.0	0.0	7.8
AZO-26	OL	47.3	40.0	12.3	0.0	0.0	0.0	0.0	0.1	0.2	0.3	0.0	0.0	87.2
AZO-26	TLC	30.6	61.8	1.4	0.0	0.2	0.0	0.0	0.0	0.0	0.2	0.0	0.0	97.6
AZO-26	VEIN LZ	40.5	39.9	3.6	0.0	0.2	0.0	0.0	0.0	0.0	0.3	0.0	0.0	95.3
AZO-26-S	SRP	30.0	30.9	7.7	0.0	16.1	0.0	0.0	0.1	0.1	0.2	0.0	0.0	87.5
PR01	CHL	34.5	34.3	3.1	0.0	11.3	0.0	0.0	1.1	0.0	0.2	0.0	0.0	95.2
PR01	NI-SPINEL	0.0	0.0	40.8	0.0	0.0	0.0	0.0	0.0	0.0	40.6	0.0	0.0	
PR01	OL	51.1	41.1	7.5	0.0	0.0	0.0	0.0	0.0	0.2	0.3	0.0	0.0	92.3
PR02	CHL	34.0	35.0	3.7	0.0	11.9	0.0	0.0	0.1	0.0	0.2	0.0	0.0	94.3
PR02	OL	50.6	41.3	8.4	0.0	0.0	0.0	0.0	0.0	0.1	0.3	0.0	0.0	91.5
PR02	SRP	39.3	43.7	3.8	0.0	1.3	0.0	0.0	0.0	0.0	0.1	0.0	0.0	94.9
PR02	TLC	31.2	63.8	1.2	0.0	0.1	0.0	0.0	0.0	0.0	0.1	0.0	0.0	97.9
PR08	AMPH	23.7	57.7	1.5	0.1	0.3	0.0	13.5	0.0	0.1	0.1	0.0	0.1	96.6
PR08	CHL	34.2	33.3	3.6	0.0	13.2	0.0	0.0	0.0	0.0	0.2	0.0	0.0	94.5
PR08	OL	50.0	40.9	8.3	0.0	0.0	0.0	0.0	0.0	0.1	0.3	0.0	0.0	91.5

4.5 Discussion

4.5.1 Jack-straw-textured-olivine

Lafay et al. (2019) suggest that the Jack-straw-textured-olivine in the Malenco rocks grew at the lowest reaction affinities (partial derivative of Gibb's free energy with respect to extent of reaction i.e. the degree to which a chemical reaction occurs) where nucleation is sparse. These are areas of lower heating rate, further from the intrusion. However, it is interesting that within the population of AZO serpentinites, two have well developed Jack-straw-textured-olivine (18 and 26) whereas the other two do not (16 and 13). This does not seem to correlate with the distance from the intrusion: as AZO-13 is closer to the intrusion than AZO-18. Additionally, there is no difference in B isotope behaviour between those samples with Jack-straw texture and those without. It is clear in this situation that whatever is controlling the B isotopic composition of the AZO olivines, is not affected by mineral growth kinetics.

4.5.2 F in AZO samples.

Fig.4.9 shows a correlation between F and δ^{11}B in the AZO samples. PR phases all have low F, whereas AZO serpentine, talc, amphibole and chlorite have F >100 μg g^{-1}. Those phases with higher F also have heavier δ^{11}B. This trend is not seen in the secondary olivine, but more dominantly in the primary serpentinite minerals. Therefore this correlation is likely to reflect a trend in the serpentinite protolith as B was added to the rock. This indicates that the Valmalenco serpentinite protolith was widely heterogeneous, given that these variable samples can occur naturally within a few 10's of ms of each other.

4.5.3 The differences between PR and AZO olivines

The two different sample locations, Preda Rossa (PR) and Alpe Zocca (AZO), form two isotopically distinct groups of metamorphic olivines (see Fig.4.10). PR olivines have positive δ^{11}B (+1.3 to +24.7). AZO olivines have mostly negative δ^{11}B (-11.9 to +1.9). These differences could be caused by difference in protolith composition. We

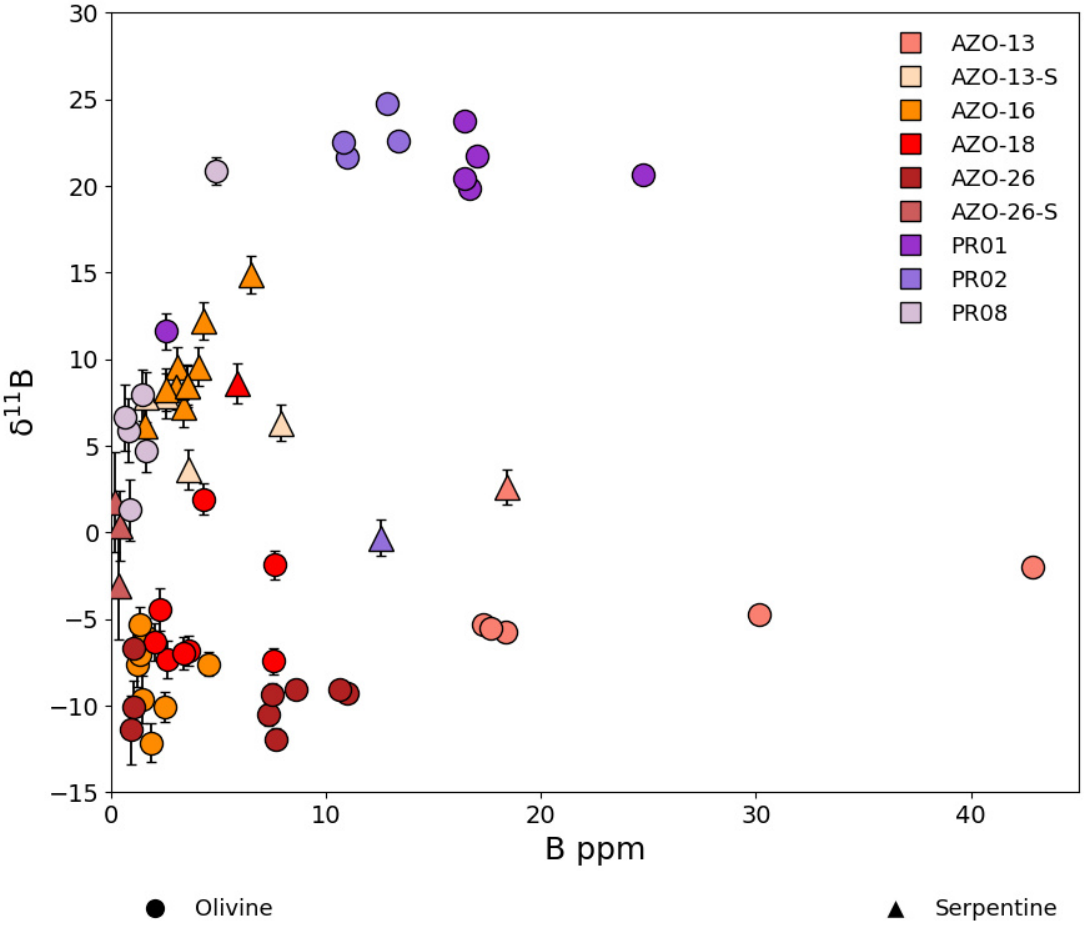

Figure 4.10: δ^{11}B vs B for olivine and serpentine phases in all samples. PR olivines and AZO olivines have strikingly different δ^{11}B, and PR olivines are slightly more enriched in B.

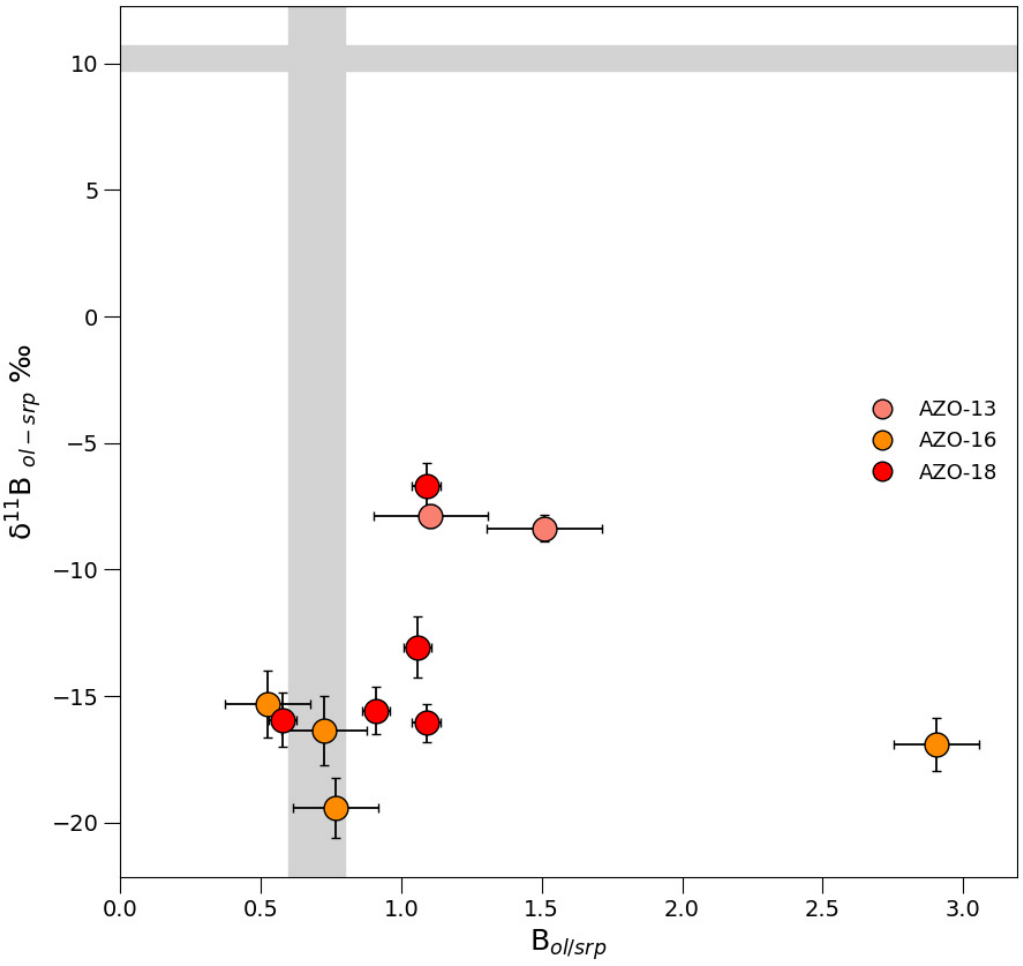

Figure 4.11: Diagram comparing metamorphic olivine compositions with the average composition of co-existing serpentine, where $[B]_{ol/srp}$ and $\Delta^{11}B_{ol-srp} = \delta^{11}B$ are defined in caption of Fig.3.4. Grey bars indicate equilibrium fractionation.

were able to analyse one PR serpentine (from samples PR02) which is identical in major element chemistry to AZO serpentines (see Figs. B.6 to B.7). The PR serpentine has a greater B than most AZO serpentines (9.3 μg g^{-1} vs $\sim$ 5 μg g^{-1}) and lower δ^{11}B (-0.3‰ vs $\sim$ +5‰). If this single serpentine from Preda Rossa is representative of the protolith it would suggest that PR olivines have a more positive δ^{11}B than the serpentine, showing the opposite behaviour to the AZO olivines. However, it is rather tenuous to base the composition of the protolith on one serpentine analysis, therefore this analysis provides only an indication of the protolith composition and it would not be valid to use this measurement in any $\Delta^{11}B_{ol-srp}$ calculation. Serpentine makes up only 1% of the PR02 sample and its δ^{11}B value may have deviated from its original value if deserpentinisation was slow and the serpentine had time to requilibrate with the olivine/fluid.

To explore whether differences in protolith alone can account for the differences between the two groups of olivines, we would need to see the same relative relationship between the olivine and serpentine. AZO olivines are 6.7 to 21.5 ‰ (average 12 ‰) lower than the AZO serpentine, see Fig.4.11. This means that the original PR protolith would need to have δ^{11}B of 26 to 47‰. Such high δ^{11}B do exist in nature but are extremely rare in serpentinites, especially since nothing in this sample suite measures as high, particularly the one successful PR02 serpentine measurement. Therefore it is most likely that the PR olivines show a different relationship to their protolith than the AZO olivines. This indicates that different processes have occured in the Alpe Zocca and Preda Rossa localities that have led to these isotopically distinct olivines.

4.5.4 The differences between Preda Rossa and Alpe Zocca localities

The two localities record different peak metamorphic temperatures (see Fig.4.12). The temperature of crystallisation has been calculated using mineralogy, and the thermal gradient calculated in Trommsdorff and Connolly (1996). In order of closest to the Bergell intrusive-country rock contact: PR01 and -02 are at $\sim$420m, AZO-26 is at $\sim$560m, PR08 is at $\sim$745m, and AZO-13, -16 and -18 are at $\sim$840m. Contact meta-

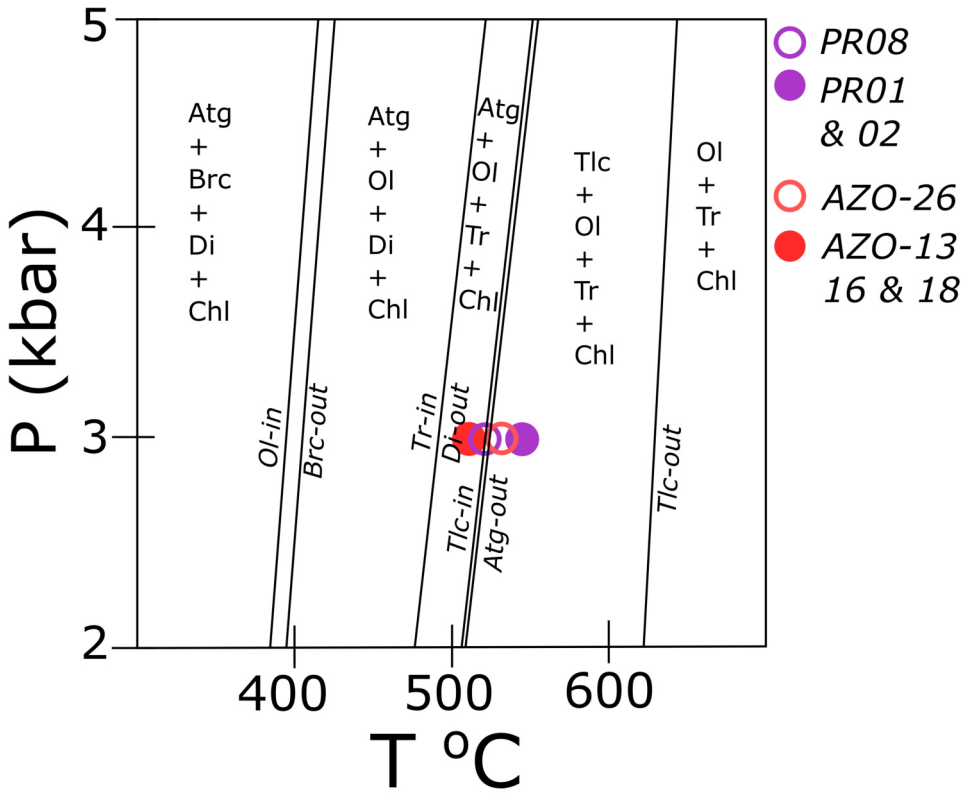

Figure 4.12: PT diagram with serpentine dehydration phase boundaries and relative conditions of the Preda Rossa (PR) and Alpe Zocca (AZO) samples. Crystallisation pressure for the contact aureole has been calculated at 3 +/- 1 kbar (Taken from Trommsdorff and Connolly, 1996)

morphic temperatures are ∼545°C, ∼536°C, ∼525°C and ∼519°C respectively. Temperature has a significant effect on the fractionation of B isotopes (see section 5.4.1 for in depth explanation) and at these temperatures the range of equilibrium $\Delta^{11}B_{ol-srp}$ is likely around +9.7‰ to +10.7‰ (based on B isotope fractionation between trigonal and tetrhedral phases in experimental study by Williams et al., 2001 and the fractionation seen in natural samples in Chapter 3 of this thesis). We can reliably calculate $\Delta^{11}B_{ol-srp}$ for the AZO samples due to the abundance of both secondary olivine and serpentine, which averages around -15‰. However, it cannot be reliably calculated for PR samples, since there is only one clean serpentine measurement. All we can conclude is that the AZO olivines are not in equilibrium with the serpentine. This is contrary to our prediction that deserpentinization in the Bergell aureole occurred in a closed system 'laboratory' and can be used to study the process without the external fluid influence present in subduction zones.
The two groups of samples also differ in terms of % dehydration (roughly equivalent to % olivine): The rocks from Preda Rossa likely sit very close to 100% dehydration, whereas the AZO rocks are much closer to 5 to 10% dehydration. This difference is down to the temperature experienced by the different localities. However, as shown by the dehydration models in Fig.4.13, higher % dehydration only leads to lower $\delta^{11}B$, therefore the difference in $\delta^{11}B$ between PR and AZO samples is not down to % dehydration. Clearly there has either been some outside influence that has altered B isotope composition of the AZO olivines.

The AZO olivines could be preserving disequilibrium due to fractional dehydration i.e. as fluid is produced it is removed from the system. AZO samples are partially deserpentinized, evidenced by the presence of both secondary olivine and serpentine. Fractional vs equilibrium dehydration has been modelled in Fig.4.13. During fractional dehydration fluid is removed after every 1% dehydration, whereas during equilibrium dehydration the fluid remains in the system and equilibrates with the olivine and serpentine. Fig.4.13 shows that under each different set of dehydration conditions (pH changes, equilibrium vs fractional dehydration), olivine still retains a higher $\delta^{11}B$ than the serpentine. Therefore, since AZO olivines have a lower $\delta^{11}B$ than the serpentine

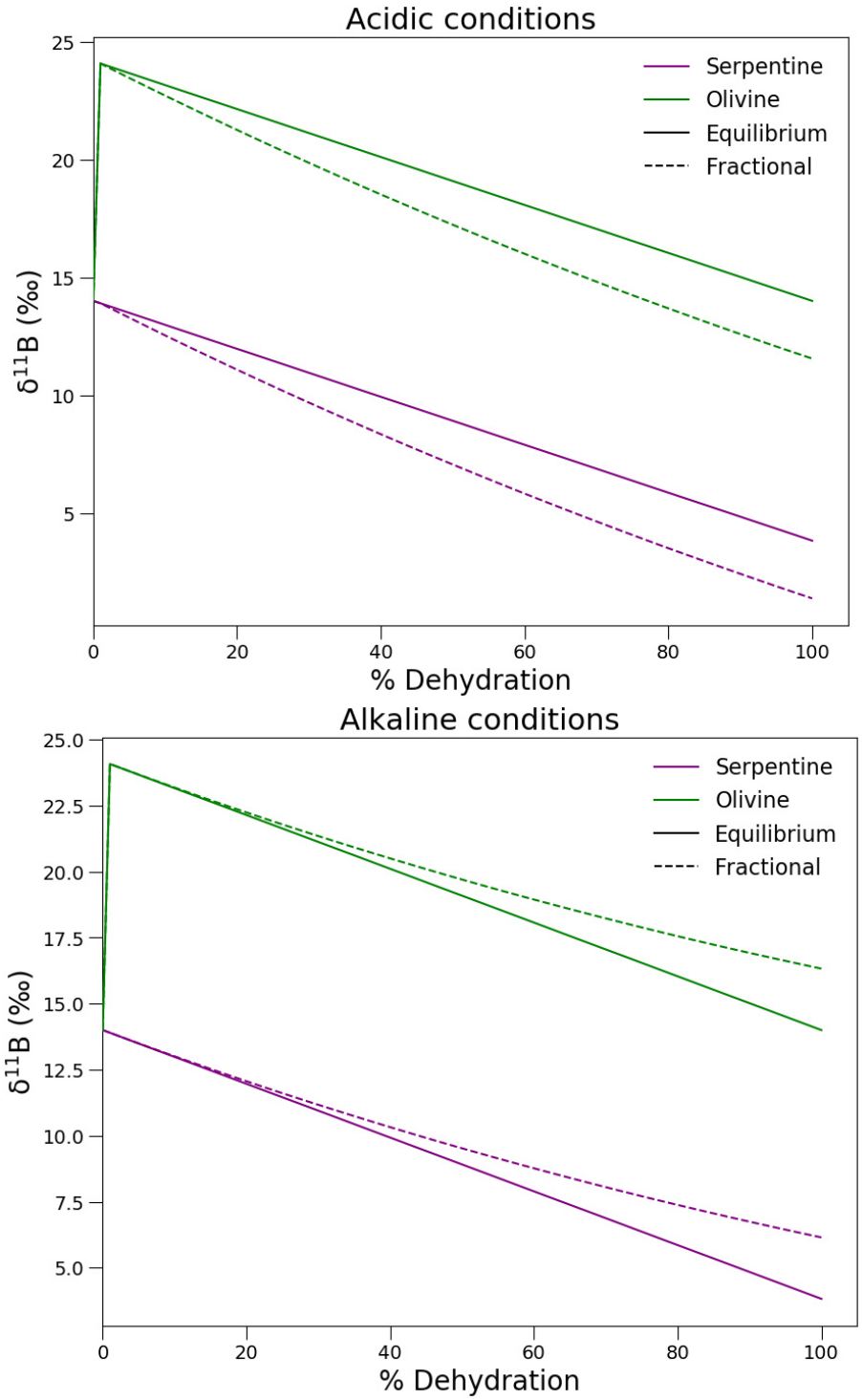

Figure 4.13: Two dehydration models for acidic and alkaline conditions at 600°C. This model assumes fractionation between iii and iv coordination based on Williams et al. (2001) of 10.2‰ and $^{ol/srp}D_B$ of 0.72, based on $^{fl/res}D_B$ of 4 from Tenthorey and Herman (2004). In acidic conditions the serpentine and fluid B isotope fractionation is +10.2‰ and during alkaline conditions, the fractionation is +0‰ NB:Fluid compositions are not plotted in this figure, $\Delta^{11}B_{ol-srp}$ has been kept fixed.

(as seen in Fig.4.11), they must not have dehydrated in a closed or 'exit-only' system. There must be an external negative δ^{11}B influence and that dehydration alone cannot account for the negative δ^{11}B.

Fluid flow in the Bergell contact aureole was originally described as 'forced' and 'not well mixed' by Trommsdorff and Connolly (1996) based on the agreement between the field phase relations and a computed simple convection model for heat dispersal. Lafay et al. (2019) add, based on the presence of micro-scale talc veinlets, that fluid production is likely rapid and that the veinlets possibly represent fossilized evidence for cracking resulting from high pore pressures during dehydration. All of this indicates some level of fluid movement through the aureole. It is clear from the B isotope data that the AZO samples have interacted with a fluid of vastly different δ^{11}B. In addition, the AZO samples are from a sliver of serpentinite wedged between gneisses, mafic bodies and Mesozoic carbonates (see Fig.4.2). Sample AZO-16 contains dolomite (see Fig.4.5) indicating some interaction with carbonate-rich fluids. It is likely that the comment of 'not well mixed' stems from a belief that fluid flow was not widespread throughout the aureole. However, since the AZO samples are so proximal to other lithologies, fluid would not need to travel far to interact with many different rock types in this location. Rapid fluid production without causing heat advection or any channelising of fluids requires rapid draining of fluids for balance; an open system. This system would allow many passes of fluid with more negative δ^{11}B than the AZO serpentinites, like that suggested by McCaig et al., 2018, therefore providing a method for the addition of high concentrations of ^{10}B and the reduction of the δ^{11}B of the growing secondary olivines.

The composition of possible infiltrating fluids can be modelled using the B composition of secondary olivine compared to serpentine. Using the same external fluid model as described in section 2.4, the composition of the external fluid has been modelled for the Valmalenco samples (Fig.4.14). Trommsdorff and Connolly (1996) suggest that there isn't likely to be any more fluid volume than 25$\%$ as this is the predicted volume change associated with the serpentinite metamorphism. We can calculate the volume of fluid produced during the deserpentinization of the malenco unit serpentinites us-

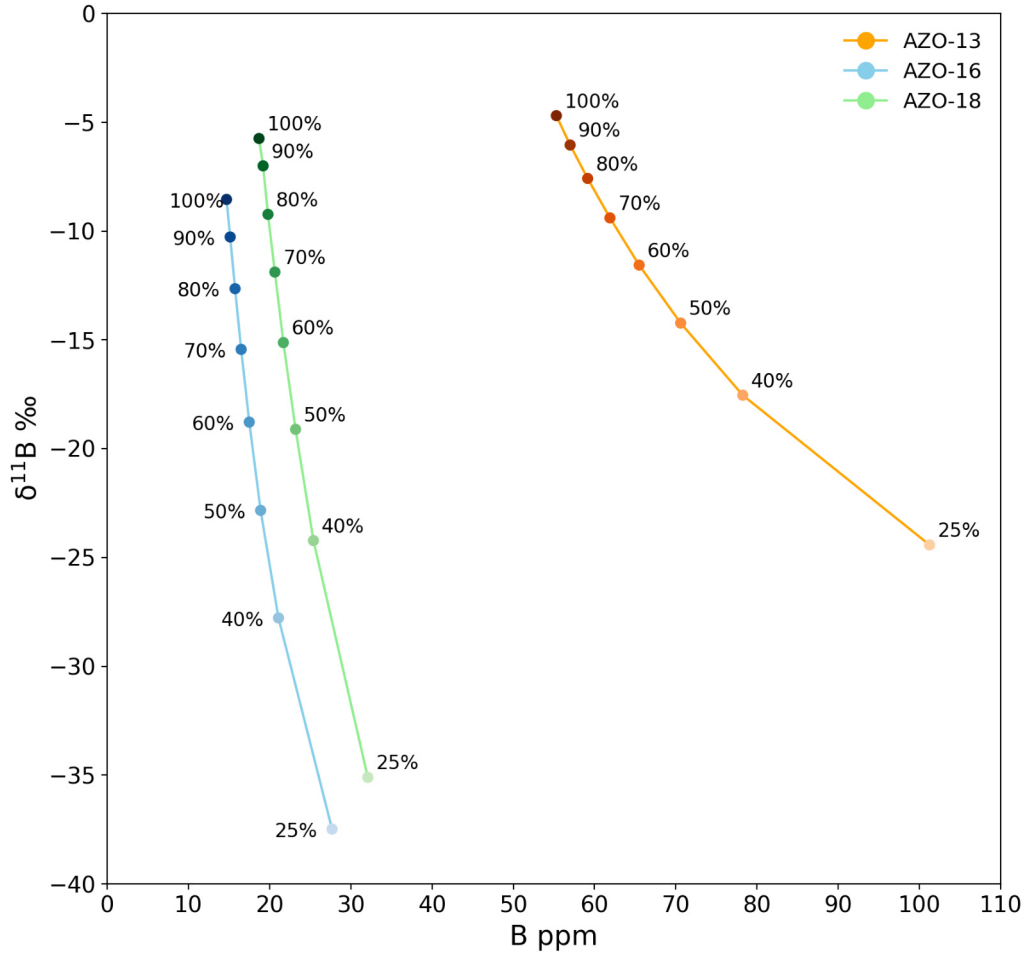

Figure 4.14: Results for the composition of potential external infiltrating fluids at the time of secondary olivine growth for each sample. Sample AZO-26 was not included because it lacks serpentine. Each marker represents the average composition of the external fluid at that fraction. Percentage labels are fraction of external fluid. Size of the markers represents 1σ error. Modelled under acidic conditions (fluid has preference for ^{11}B).

ing the following three assumptions: that the density of water in these conditions is 1 kg/cm^3, the density of the dehydrating serpeninite body is close to 2.7 kg/cm^3 (given that the AZO samples are predominantly serpentine) and the maximum weight % fluid produced by the dehydration is 13 wt%. Since the AZO serpentinites are still mostly serpentine, the total weight% fluid released during deserpentinization is likely much less than the maximum. AZO-13 and -18 comprise approximately 15% serpentine, whereas AZO-16 comprises 75%. If we assume that the rock was fully serpentinized (a reasonable assumption based on the lack of relic ultramafic minerals), this can roughly equate to the % fluid released during their dehyration: 11 wt% for the former and 3.25 wt% for the latter. This translates to fluid/rock ratios of 0.33 and 0.09 respectively.

For AZO-16, it is reasonable to imagine that this fraction of fluid (0.09) could be released at once, paired with another 64% (25 vol% total fluid volume - 9 vol% produced by serpentine dehydration, leaves 16 vol% space for external fluid which is 64% of total fluid volume) of external fluid and not exceed the 25 vol%. However, according to Fig.4.14, 64% would require the external fluid to have a composition of $\sim$ ^{11}B -17 ‰ which is extremely light for fluids which typically prefer heavy B. Although Tourmaline is known to have low δ^{11}B and can be as low as -20.1 to -26.8‰ in tourmaline from pegmatites (Slack et al., 1989) and -23 to -29.9‰ in tourmalines from a pegmatitic granite in Swaziland (Chaussidon and Albarède, 1991), considering that the rocks surrounding the Alpe Zocca region include metapelites, ophicarbonates, metagabbros and gneisses, it is unlikely that the fluid would be so light.

For AZO-13 and -18, clearly not all 33 vol% fluid can be released at once without exceeding the 25 vol% limit proposed by Trommsdorff and Connolly (1996). Therefore, in both situations, it is more reasonable to assume that the fluid is released in small batches and removed. This method allows both fluid to be released but not exceed the volume limit, and for more than 64% external fluid to be added, allowing a more realistic δ^{11}B of the source ($\sim$ ^{11}B -10 ‰ or heavier). This indicates fluid movement through the serpentinite body during dehydration and that the percentage of external fluid added likely far exceeds the amount produced by dehydration.

Meta-sediments are known to show negative δ^{11}B (De Hoog and Savov, 2018 and references therein) and have previously been implicated in reducing the δ^{11}B of serpentinites (e.g. Cannaò et al., 2016). Therefore, we suggest that the largely negative signature of the AZO samples is due to interaction with negative fluids from the dehydrating meta-sediment/gneiss units surrounding it.

We do not know if the PR olivines show evidence for external fluid infiltration because we cannot compare them to their parental serpentine. However, it is most likely that they haven't been inundated with ^{10}B-rich fluids like the AZO samples, given their highly positive δ^{11}B. This makes sense considering that they are isolated from other lithologies within a large ultramafic body (see Fig.4.2). They may still have been infiltrated by fluids from the surrounding serpentinite, but that would be difficult to identify since they are likely to have very similar δ^{11}B.

4.6 Conclusion

B isotopes are particularly sensitive to fluid movements in contact aureole settings. The AZO samples are situated very close to other lithologies (meta-sediments/gneisses) and they record negative δ^{11}B. The PR samples are isolated within a large mafic body and record positive δ^{11}B. We suggest that these differences are caused by AZO olivines equilibrating with ^{10}B-rich fluids from the surrounding lithologies, whereas the PR olivines remained isolated from such fluids. In summary, the aureole does not represent a closed system 'laboratory' for which to study the behaviour of B isotopes in equilibrium, but evidences fluid movement and inter-connectivity between different lithologies during contact metamorphism.

Chapter 5

Olivine growth experiments

"All that is gold does not glitter, Not all those who wander are lost"

J.R.R. Tolkien, The Lord of the Rings

5.1 Introduction

Using boron isotopes in subduction zone geochemistry is a relatively new application, with review papers on the subject only being published over the last few years (e.g. De Hoog and Savov, 2018; Marschall et al., 2017). One problem with using B isotopes to understand subduction zone processes is the lack of data on the equilibrium fractionation of the isotopes in ultramafic rocks. In fact, Marschall (2018) states that there is a noticeable lack of fluid-mineral B isotope fractionation data for serpentinites. There have been studies on B partitioning (Spandler et al., 2014; Tenthorey and Herman, 2004), Li isotope partitioning in serpentinites (Wunder et al., 2009) and B isotope fractionation between minerals and fluid (Williams and Hervig, 2004), but never on all three together.

Not knowing how B partitions between ultramafic minerals and fluid limits our ability to model the deep B cycle. With these data we can more accurately predict the B and δ^{11}B composition of serpentinite dehydration fluids and the contribution of these fluids to the B cycle.

5.1.1 Previous work

Williams et al. (2001) performed silicate-fluid B isotope fractionation experiments, specifically looking at smectite and fluid B isotope partitioning. These experiments were performed in a hydrothermal reaction vessel. The experiments were run at 300-350°C and 100 MPa for 120 days (in order to reach equilibrium), and there was a ratio of 1:1 water to mineral. Boric acid was added to the fluid and the initial pH was 6.8. Samples were quenched under vaccum and the fluid contents were collected in a U-tube cold trap. However, B isotopes fractionate during this process, so instead they measured the solid clays for their B and δ^{11}B composition. Williams et al. (2001) found that the fractionation was -16‰ at 300°C and -13 ‰ at 350°C, which they tied to experiments from Hervig et al. (2002) looking at B isotope fractionation between silicate melts and fluids. Their combined work resulted in the equation:

$$\Delta_{mineral-water} = -10.12 * 1000/T(K) + 2.44 \tag{5.1}$$

Williams et al. (2001) conclude that this data may be a close proxy for the fractionation expected for other tetrahedral mineral sites. However, as previously discussed in Chapter 3, B is thought to substitute into olivine in trigonal coordination (as a complex with OH, Ingrin et al., 2014), and possesses substantially lighter δ^{11}B than serpentine, which incorporates B in tetrahedral sites. Therefore, it is possible that $\Delta^{11}B_{ol-fl}$ is quite different to $\Delta^{11}B_{mineral-fl}$ calculated in Williams et al. (2001).

Tenthorey and Herman (2004) conducted experiments looking at B concentration in dehydrated serpentinites, specifically targeting fluid/residue partitioning behaviour. They conducted piston-cylinder experiments in which the fluid was captured in diamond traps. In these experiments the dehydration fluids are allowed to equilibrate with the residue. The experiments were conducted at 3 GPa and 750°C and lasted for 7 days. They found $^{fl/res}D_B$ (fluid/residue distribution coefficient) of 3-5 indicating that B is less incompatible in serpentinite residue than other fluid-mobile elements.

Serpentine dehydration reactions were run by Wunder et al. (2009) and aimed to measure the Li isotope ratio in lizardite (lzd) and antigorite (atg) breakdown fluids. The experiments were performed between 200-400°C and at 0.2-0.4 GPa for the lzd-fluid

and 500°C and 4GPa for the atg-fluid experiments and they lasted between 14-31 days. For the atg-fluid experiment they used 90 wt% starting material and 10 wt% fluid. After the experiment they separated solid from the fluid phases by filtration, after piercing the capsule in 80°C doubly distilled water. Both phases were measured for their Li isotopes. Li concentrations in the solids were highly variable even between experiments that had the same starting composition. But the Li isotopes were more consistent, showing similar Δ^7 Li$_{solid^{\sim}fluid}$ across all 5 experiments, ranging from -4.8 to +0.9‰, and a positive correlation with temperature.

Spandler et al. (2014) successfully measured serpentinite dehydration fluids by trapping them in San Carlos olivines. Experiments were run in a piston-cylinder apparatus with serpentinite starting mix and fractured San Carlos olivine chips in a 6.7mm capsule. The conditions were 3.5 to 4 GPa and between 700 and 900°C. In order for the fractures in the olivine to fully heal and capture the dehydration fluids, experiments were run between 11 and 28 days. These experiments yielded serpentinite dehydration fluids in the fully healed cracks of the San Carlos olivine. They measured the B concentration in the fluid and the fluid-hosting olivine (15.8 and 1.2 μg g^{-1} respectively), which gives a $^{fl/ol}D_B$ value of 13.1. B diffuses from the fluid into the olivine host during the 11 to 28 day-long experiments. Unfortunately, olivine and orthopyroxene in the depleted residue was not measured due to analytical restrictions. Furthermore, they did not investigate δ^{11}B of the fluids or the olivines. However, this value does vary from the $^{fl/ol}D_B$ of 3 to 5 found in Tenthorey and Herman (2004). The reason for this might be that the measured residue in Tenthorey and Herman (2004) also contains pyroxene, which could account for some of the retention of B. Though Tenthorey and Herman (2004) argue that olivine is the dominant B sink given $^{ol/opx}D_B$ of 1.3-3. Another reason is that the olivine measured in Spandler et al. (2014) is not metamorphic (i.e. formed by serpentine breakdown, or even grown in the presence of B-rich fluid) which may have an effect on boron incorporation, as the method for incorporating B into primary olivine is by diffusion only. Therefore the value of 13.1 is not highly reliable, as it is difficult to prove equilibrium.

This chapter discusses two different experimental methods that were employed, the first to study B isotope fractionation during simulated serpentine dehydration and the second to quantify $\Delta^{11}B_{ol-fl}$. The first method was unsuccessful due to B contamination issues and small grain size of the product. The second method has yielded interesting B concentration and $\delta^{11}B$ data which is discussed, along with its caveats, and advise on how it may be used to give insight to subduction zone processes.

5.2 Methods

5.2.1 Analytical

Major elements were gathered by EMPA using the same methods described in section 2.1 and FME were measured using the cameca 4f-ims SIMS at Edinburgh using the same methods described in section 2.2. The B isotopes were measured using the Cameca IMS 7f-Geo at the University of Edinburgh EMMAC facility. The 7f has a shorter acquisition time than the 1270 and the hyperion ion source provides a more stable beam. Mostly, the methods are similar to what is described in section 2.3. However, since these olivines are pure forsterite, we needed additional standards. Table.2.2 displays the standards used on the 7f.

Two additional olivine standards were measured as part of this project, Koh, which is an Fe-rich olivine from Pakistan contains $\sim$56 μg g^{-1} B and $\delta^{11}B$ of -4.7‰ (as measured in Pisa and Bristol) and Fo, which is pure forsterite, contains $\sim$360 μg g^{-1} B and $\delta^{11}B$ of -13.6‰ (as measured in Pisa and Bristol). Koh has an instrument mass fractionation (IMF) of around +2‰ whereas Fo has an IMF of -5‰.

5.2.2 End-loaded piston cylinder set up

Sample Cell

The sample is placed inside a 5 mm long metal capsule. The type of metal and its diameter depends on the type of experiment and the temperature. Fluid was put into

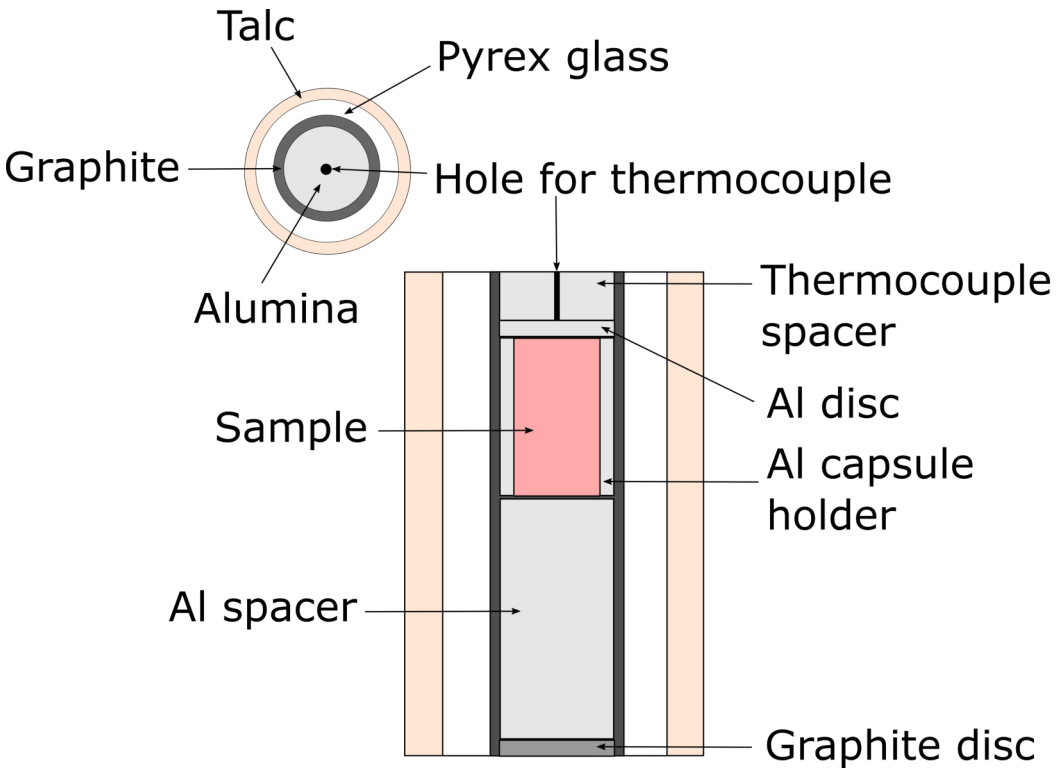

Figure 5.1: Structure of the experimental cell.

the bottom of the capsule and the mixture poured on top of it to avoid loss of fluid on welding. The capsule is placed inside an alumina sleeve and then inserted into a cell along with alumina spacers and discs (see Fig. 5.1). One problem with using this cell is the possible contamination of B from the Pyrex glass. This has been noted in piston cylinder experiments previously, but adding the alumina sleeve and disc appear to isolate the capsule from the Pyrex (Brooker, 1998). The cell is then loaded into the piston cylinder, an end load of 150 tons is applied and then the sample is taken to 1/3 required pressure before starting to increase temperature. Temperature is added at a rate of about 100-200°C per minute. Temperature is measured using a type R thermocouple (Pt and Pt13%Rh), which is accurate to about 10°C. After the 48 hours, the capsules were rapidly quenched to below 100°C in <10 seconds by turning off the power. Pressure was added during quenching to offset the pressure drop associated with cooling, resulting in an isobaric quench.

5.2.3 Haplogranite capture method

The aim was to dehydrate natural serpentinite, grow secondary olivine and capture the fluid in haplogranite melt. When quenched the haplogranite glass can be measured by SIMS to determine the δ^{11}B of the fluids. The δ^{11}B of the olivine can be either measured (grain size permitting) or calculated based on the starting serpentinite composition.

Experimental design

This method required a double capsule set up: an inner 2 mm diameter gold capsule which was filled with a 2x2x2 mm cube of serpentinite. The serpentinite was collected from Zermatt and has $\sim$ 40 μg g^{-1} B. The outer capsule was 3 mm diameter capsule made of 50:50 silver:palladium. Conditions were set at 2 GPa and 750°C to simulate serpentinite dehydration conditions and were run for 24 hours for complete dehydration (1 experiment was completed successfully to evidence this).

Contamination issues

A blank experiment was run to check for B contamination from the borosilicate glass in the cell. The blank recorded $\sim$10 μg g^{-1} of contamination from the cell over the course of the experiment. Since this is 25% of the total B in the experiment (sourced from the 40 μg g^{-1} in the starting serpentinite), it would have a considerable effect on the δ^{11}B of the fluids. Fundamentally it would be incredibly difficult to obtain a 'true' δ^{11}B for the fluids with so much contamination. Therefore, this methodology had to be abandoned.

5.2.4 Olivine growth method

The aim of this experiment was to grow olivine in the presence of a B-rich fluid at different temperatures and pH to determine $\Delta^{11}B_{ol-fl}$ and its dependence on these different conditions.

Molecule	Weight	Percentage
SiO_2	0.2374g	33.1%
MgO	0.4749g	66.1%
$B(OH)_3$	0.0056g	0.8%

Table 5.1: Starting mix composition for olivine growth experiments. This mix was made from combining the three constituents in an agate mortar and mixed together with the pestle. These tools were cleaned thoroughly before and after use to limit the amount of B contamination.

Experimental design

A single platinum capsule (4mm diameter) was filled with powdered SiO_2, fluid and starting mix (see table 5.1) and welded at both ends. The fluid was added with a B-free micro litre pipette to the bottom of the capsule, to avoid evaporation on welding. The type of fluid changed depending on the required pH, for the acidic experiments just distilled water was added and for the alkaline experiments a 0.3M NaOH solution was added. Table 5.2 contains the composition and experimental conditions of all 8 successful experiments. Each experiment was run for between 1.95 to 2.5 hours at 1600°C first to homogenise the mixture and then lowered to the run temperature and left between 46.6 to 48.3 hours (resulting in total experiment lengths of 48.7 to 50.8 hours). Full run documentation can be found in appendix A.3.4. We did not make porosity estimations, but it was clear that each experiment was porous from the inflated shape of the capsule after the experiment (see Fig.5.2), loose grains and micron-scale holes. This indicates that fluid was present and able to equilibrate with the olivines during the experiment (as in Tenthorey and Herman, 2004). Fluid/rock ratios (where rock = starting mix + excess SiO_2) varied between 0.25 and 0.3.

	Exp #4	Exp #5	Exp #6	Exp #7	Exp #8	Exp #9	Exp #10	Exp #11
Temperature °C	1000	1000	1100	900	900	1000	1100	900
Capsule weight (g)	0.3204	0.4009	0.4424	0.4848	0.4873	0.4133	0.4666	0.424
Capsule +SiO_2(g)	0.3245	0.4048	0.4477	0.4898	0.4922	0.4177	0.471	0.4281
Total SiO_2 (g)	0.0041	0.0039	0.0053	0.005	0.0049	0.0044	0.0044	0.0041
Distilled H_2O (μl)	14	14	14	14	4	0	0	0
0.3M NaOH (μl)	0	0	0	0	10	14	14	14
Capsule + Fluid (g)	0.3362	0.4174	0.46	0.5035	0.5048	0.4305	0.4831	0.4429
Starting mix (g)	0.0447	0.0429	0.0419	0.0411	0.0461	0.0439	0.0444	0.0441
Total weight (g)	0.3809	0.4603	0.5019	0.5446	0.5509	0.4744	0.5275	0.487
pH*	4.7	4.7	4.7	4.8	9.0	9.3	9.2	9.4

Table 5.2: List of capsule compositions for each experiment. Pressure for each experiment was consistent at 5300 psi. *Calculated at room pressure and temperature.

5.3 Results

5.3.1 Sample description

11 experiments were run between 900 and 1100°C and at 2GPa. Every experiment contains olivine and most contain pyroxene in the product. There were 3 unsuccessful experiments before experiment 4. Experiments 1 to 3 contained a starting mix with several wt% B, and 10 wt% fluid. Experiment 1 was 1000°C, 2GPa and 48 hours, but it lost water during the experiment, the capsule came out flat and deformed (for an example see Fig. 5.3) and the olivine was extremely fine grained. Experiment 2 and 3 were run at the same conditions, and again came out deformed. However, the crystal size was large and there was some porosity indicating that a small amount of fluid was retained. Experiment 2 contained no excess Si added to the bottom of the capsule. This meant that it was Si undersaturated, evidenced by the formation of periclase (MgO), forsterite and enstatite. However, Exp 3 did have excess Si added to capsule so no periclase was formed, only an enstatite/olivine intergrowth. Experiments 4 to 11 had a different starting mix to the previous 3 which contains roughly 5000-6000 μg g^{-1} B, and 22 wt% fluid and this fluid/rock ratio was deemed more realistic than the previous experiments. Since experiments 4 to 11 all grew large crystals and retained enough fluid to inflate the capsules they were deemed successful enough to analyse the B composition. Both starting mixes, even with the excess Si added to the capsule were slightly Si-under-saturated and the presence of pyroxene is due to small heterogeneities within the capsule.

5.3.2 Major Elements

The major element data (collected by EMPA) confirm that the olivines grown in experiments 4-11 are pure forsterite with Mg# 100. These experiments all also contain small amount of pyroxene ($\sim$5%), except experiments 10 and 7 (but much of the sample inside these capsules was lost during polishing, potentially including pyroxene). Major element analysis confirms that these pyroxenes are pure enstatite. However, the pyroxenes in experiments 4 and 11 have 8 to 10 wt% Al_2O_3 which is unrealistically high

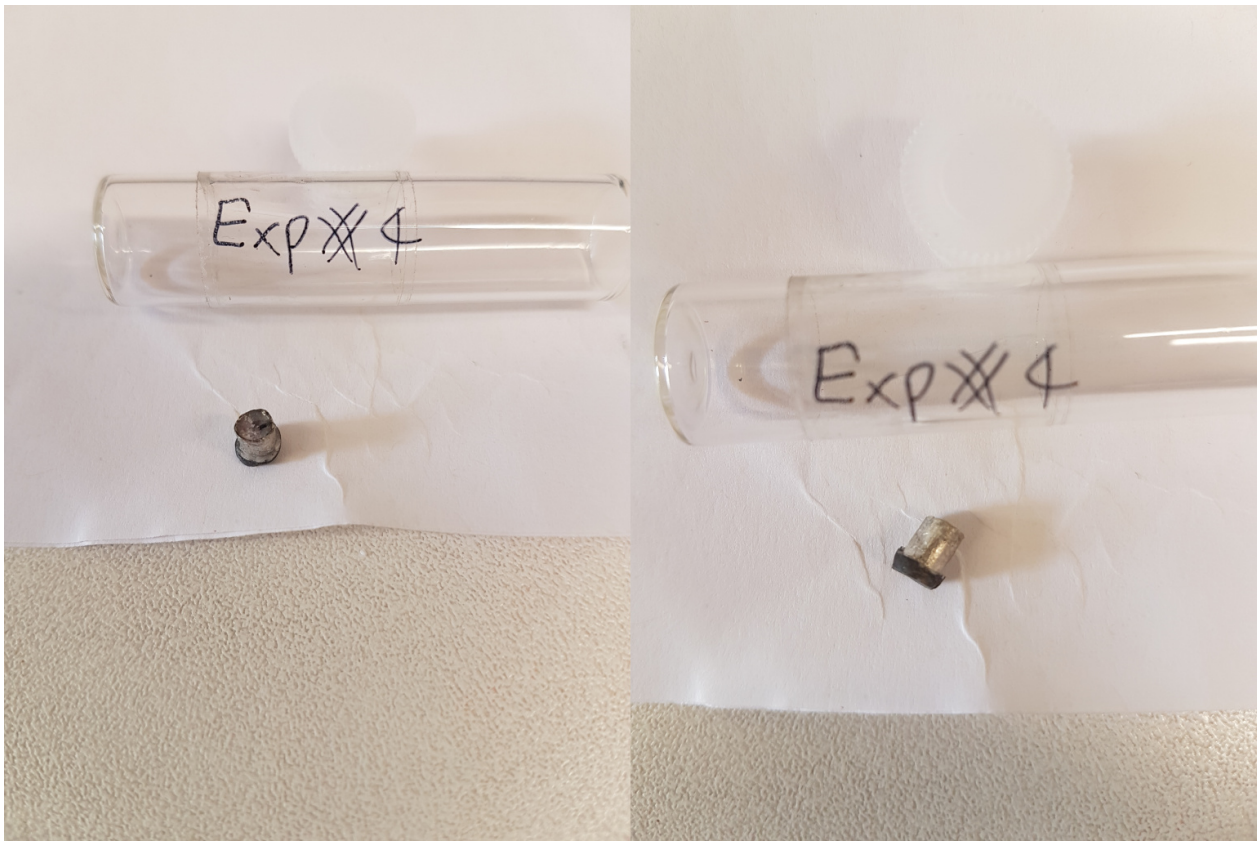

Figure 5.2: Photograph of a capsule after an experiment on its side and from above. Capsule is bright silver, the duller, darker material is the remnant of the Al-sleeve. Capsule is inflated, a typical sign of being filled with fluid.

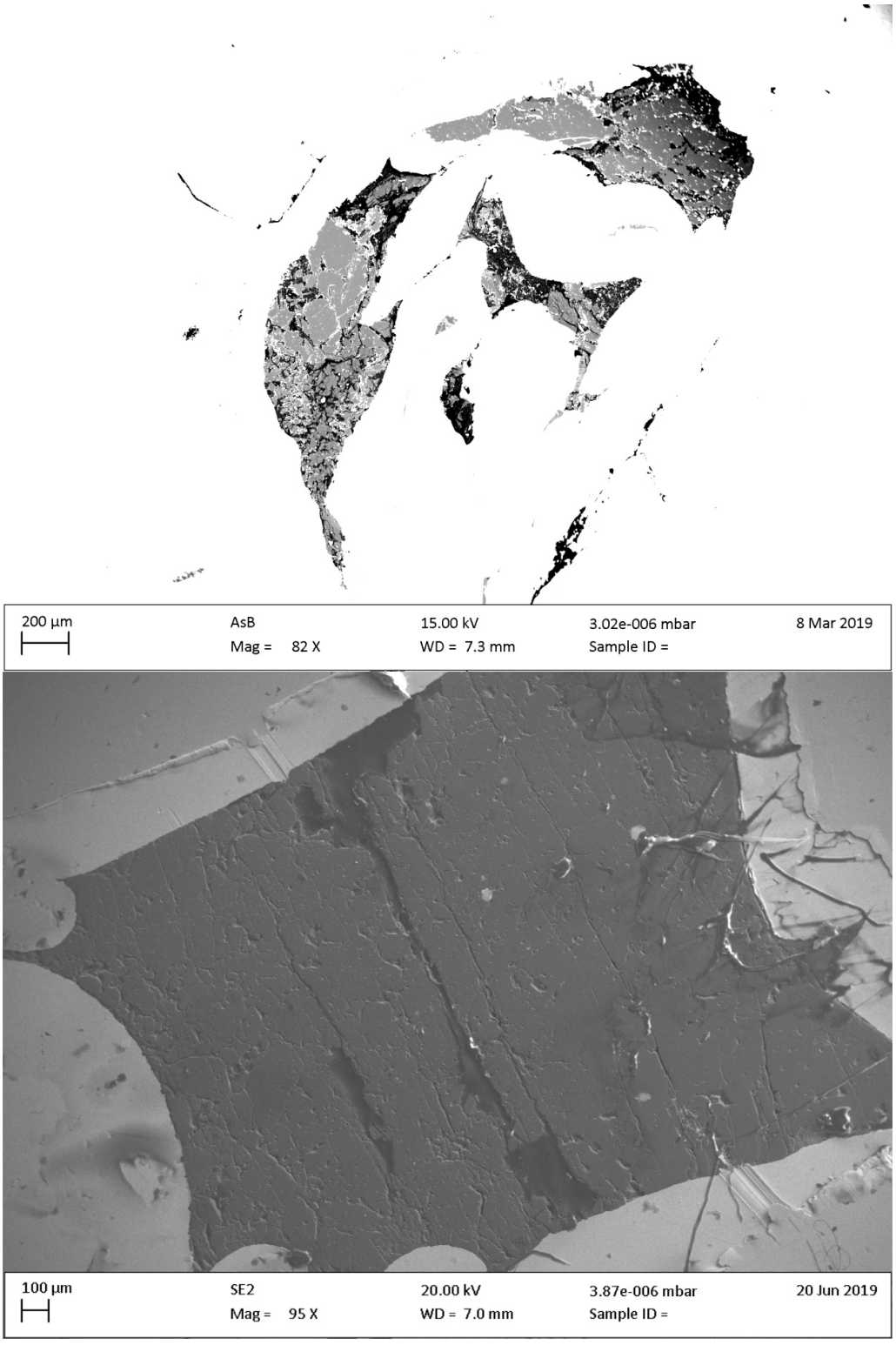

Figure 5.3: An example of the difference in shape between a fluid-filled capsule and a non-fluid-filled capsule. (Above) Exp 2, Si undersatured, capsule is deformed and flat. (Below) Exp 9, Si saturated, capsule is fully inflated and rectangular.

for it to come from contamination of the starting mix. If it is contamination with pure Al_2O_3 powder in the lab, there would be no B contamination, and since the olivines do not contain Al, $\Delta^{11}B_{ol-fl}$ would not be affected. However, in experiments 4 and 11 the high Al is also paired with high B (600 to 900 μg g^{-1}) compared the the B concentration in other experiments (<250 μg g^{-1}). This correlation suggests that the Al is sourced from the alumina capsule holder during the experiment and the B likely from the pyrex glass. Therefore, I made the decision to eliminate them from the discussion. Experiment 8 was also eliminated on account of a large chunk of Si powder still present in the corner of the experiment. It is likely that in this case the experiment did not mix well, which explains the high variability in B concentration throughout the capsule.

SiO_2 contents in the olivines range from 41-44 wt% and MgO ranges from 56-59 wt%. All other elements are at trace levels (<0.2 wt%), the biggest contaminant being CaO. SiO_2 in the pyroxenes range between 52-61 wt%, if you include the high Al pyroxenes from 4 and 11 and 58-60 wt% if you exclude them. MgO in the pyroxenes range between 35-39 wt%, if you include the high Al pyroxenes from 4 and 11 and 38-39 wt% if you exclude them. These numbers are different to the initial starting mix composition because excess Si was added to the capsule.

5.3.3 B concentration

B concentrations (collected on both the 4f and 7f) in the 5 successful experiments are variable and range from 42 to 481μg g^{-1} (with variations on the scale of 50 to 200 μg g^{-1}). Experiment 5 records 69-280 μg g^{-1} in the olivine and 96-143 μg g^{-1} in the pyroxene, experiment 6 records 42-268 μg g^{-1} in the olivine and 232-251 μg g^{-1} in the pyroxene, experiment 7 records 74-131 μg g^{-1} in the olivine, experiment 9 records 320-481 μg g^{-1} in the olivine and 117-214 μg g^{-1} in the pyroxene and finally experiment 10 records 21-197 μg g^{-1} in the olivine. B concentrations in the three excluded experiments (4, 11 and 8) are incredibly variable (ranges of 200 to 500 μg g^{-1} and up to 6900 μg g^{-1} in exp 8) and much higher concentrations than the rest of the experiments. Experiment 4 records 70-605 μg g^{-1} in the olivine and 426-642 μg

g^{-1} in the pyroxene, experiment 8 records 240-640 μg g^{-1} in the olivine and 875-7700 μg g^{-1} in the pyroxene and experiment 11 records 30-544 μg g^{-1} in the olivine and 395-782 μg g^{-1} in the pyroxene. Full data is available in Appendix A.3.2.

5.3.4 B isotopes

δ^{11}B (collected on the 7f) in the 5 successful experiment ranges between -10.1 to +6.9‰. Experiment 5 records δ^{11}B of -8.2 to -1.0‰ in the olivine and δ^{11}B of -2.8 to +2.9‰ in the pyroxene, experiment 6 records δ^{11}B of -10.1 to +0.9‰ in the olivine and δ^{11}B of +6.2 to +6.6‰ in the pyroxene, experiment 7 records δ^{11}B of -4.5 to -1.9‰ in the olivine, experiment 9 records δ^{11}B of -8.0 to -1.3‰ in the olivine and δ^{11}B of +6.9‰ in the pyroxene and finally experiment 10 records -8.4 to +0.2‰ in the olivine. B isotope compositions in the three excluded experiments (4, 11 and 8) are much lighter than the other experiments and δ^{11}B ranges between -19.5 to +0.6‰. Experiment 4 records δ^{11}B of -12.6 to -10.1‰ in the olivine and δ^{11}B of -7.4 to -7.2‰ in the pyroxene, experiment 8 records δ^{11}B of -8.9 to +-2.2‰ in the olivine and δ^{11}B of -3.6‰ in the pyroxene and experiment 11 records δ^{11}B of -13.6 to +0.6‰ in the olivine and δ^{11}B of -19.5 to -6.5‰ in the pyroxene. Full data is available in Appendix A.3.2.

Experiment	$^{Fl/Ol}D_B$	$\triangle^{11}B_{ol-fl}$		B ppm	*B error*	$^{11}B/^{10}B$	*$^{11}B/^{10}B$ error*	^{11}B	*^{11}B error*	^{10}B	*^{10}B error*	$\delta^{11}B$	*$\delta^{11}B$ error*
Exp 5	**23.9**	**-2.7 ‰**	Olivine	223.0	*±22.9*	4.0342	*±0.0069*	178.7	*±23.3*	44.3	*±4.5*	-2.3 ‰	*±1.7 ‰*
	±2.5	**±1.7 ‰**	$Fluid_{start}$	6158.0	*0**	4.0437	*0**	4937.1	*0**	1220.9	*0**	+0.0 ‰	*0**
			$Fluid_{end}$	5338.0	*±81.2*	4.0451	*±0.0011*	4279.9	*±65.1*	1058.1	*±16.1*	+0.4 ‰	*±0.3 ‰*
Exp 6	**26.1**	**-2.4 ‰**	Olivine	206.3	*±22.8*	4.0351	*±0.0079*	165.3	*±23.2*	41	*±4.5*	-2.1 ‰	*±2.0 ‰*
	±2.9	**±2.0 ‰**	$Fluid_{start}$	6161.2	*0**	4.0437	*0**	4939.6	*0**	1221.6	*0**	+0.0 ‰	*0**
			$Fluid_{end}$	5375.2	*±87.6*	4.0449	*±0.0012*	4309.7	*±70.2*	1065.5	*±17.4*	+0.3 ‰	*±0.3 ‰*
Exp 7	**52.4**	**-3.6 ‰**	Olivine	97.3	*±6.8*	4.03	*±0.0026*	78	*±6.9*	19.3	*±1.4*	-3.4 ‰	*±0.6 ‰*
	±3.7	**±0.6 ‰**	$Fluid_{start}$	5426	*0**	4.0437	*0**	4350.2	*0**	1075.8	*0**	+0.0 ‰	*0**
			$Fluid_{end}$	5101.2	*±22.2*	4.0445	*±0.0002*	4090	*±17.8*	1011.2	*±4.4*	+0.2 ‰	*±0.04 ‰*
Exp 9	**12.9**	**-4.9 ‰**	Olivine	373.1	*±22.7*	4.0284	*±0.0039*	298.9	*±23.1*	74.2	*±4.5*	-3.8 ‰	*±1.0 ‰*
	±0.5	**±1.0 ‰**	$Fluid_{start}$	6203.1	*0**	4.0437	*0**	4973.2	*0**	1229.9	*0**	+0.0 ‰	*0**
			$Fluid_{end}$	4808.6	*±47.6*	4.0481	*±0.0011*	3856	*±38.1*	952.6	*±9.5*	+1.1 ‰	*±0.3 ‰*
Exp 10	**91.2**	**-4.5 ‰**	Olivine	69.7	*±11.3*	4.0262	*±0.0038*	55.9	*±11.5*	13.9	*±2.2*	-4.3 ‰	*±1.0 ‰*
	±14.7	**±1.0 ‰**	$Fluid_{start}$	6636.7	*0**	4.0437	*0**	5320.9	*0**	1315.9	*0**	+0.0 ‰	*0**
			$Fluid_{end}$	6358.9	*±44.1*	4.0444	*±0.0002*	5098.3	*±35.4*	1260.6	*±8.8*	+0.2 ‰	*±0.05 ‰*

Table 5.3: B concentration and δ^{11}B data for experiments. Fluid start values were calculated using weight of fluid and $B(OH)_3$ added to capsule. Fluid end values are mass balanced. *There is no displayable error on the fluid start values because there is 0.0005 error on the weighing scales and no error on the δ^{11}B of the NIST951 standard used for $B(OH)_3$. NB: we are assuming a closed system, which is reasonable given the evidence for fluid presence at the experiment end (i.e. inflated capsule and pore space).

5.4 B diffusion

B is generally expected to diffuse slowly, but this has never been tested. B diffusion through olivine could cause significant problems for these experiments as it may lead to isotope fractionation. B diffusion would be quicker at higher temperatures, but Fig.5.4 shows that there is no correlation between B and temperature. Therefore, I do not expect B diffusion to be of much concern for these experiments.

5.5 Discussion

$^{fl/ol}D_B$ and $\Delta^{11}B_{ol-fl}$ have been calculated using the following equations for the above data and can be found in table 5.3.

$$^{fl/ol}D_B = \frac{B_{average\ fluid}}{B_{average\ olivine}} \tag{5.2}$$

$$\Delta^{11}B_{ol-fl} = \delta^{11}B_{average\ olivine} - \delta^{11}B_{average\ fluid} \tag{5.3}$$

B concentration is highly variable in most of the successful experiments (5,6,7,9 and 10), but this is also seen in experiments by Wunder et al. (2009), who found highly variable Li concentrations. As a result of the variable B concentrations, $^{fl/ol}D_B$ is also variable (see Table.5.3), but neither $^{fl/ol}D_B$ nor B concentration correlates with temperature, length of experiment, pH, fluid/rock ratio or any major element (most importantly Al_2O_3). A lack of correlation with Al_2O_3 means that it is unlikely that B was sourced from outside the capsule during the experiment, since a capsule leak would incorporate both Al from the capsule sleeve and B from the borosilicate glass at the same time. Therefore it is safe to assume that B was sourced directly from the fluid as the olivine grew. This also means that the experiment must have remained sealed meaning that B loss from the capsule is negligible. It is possible that there is B zoning in the olivines, which would result from not reaching equilibrium with the fluids, which may explain the highly variable values seen, especially since only a few SIMS data points could be collected on each sample. This also raises the problem of disequilibrium: if the olivine and fluid did not equilibrate, the absolute $^{fl/ol}D_B$ produced in these

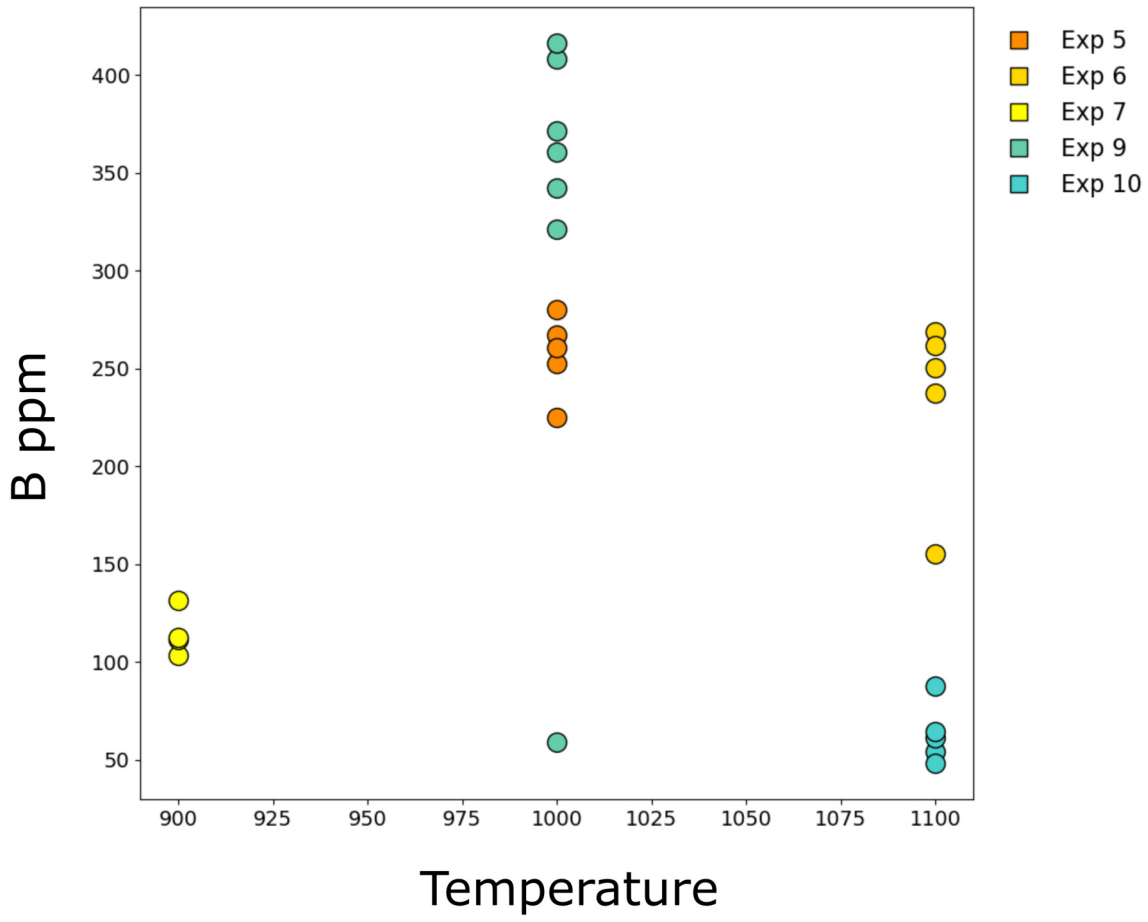

Figure 5.4: B concentration vs temperature of only olivines in each successful experiment. There is no correlation with B content.

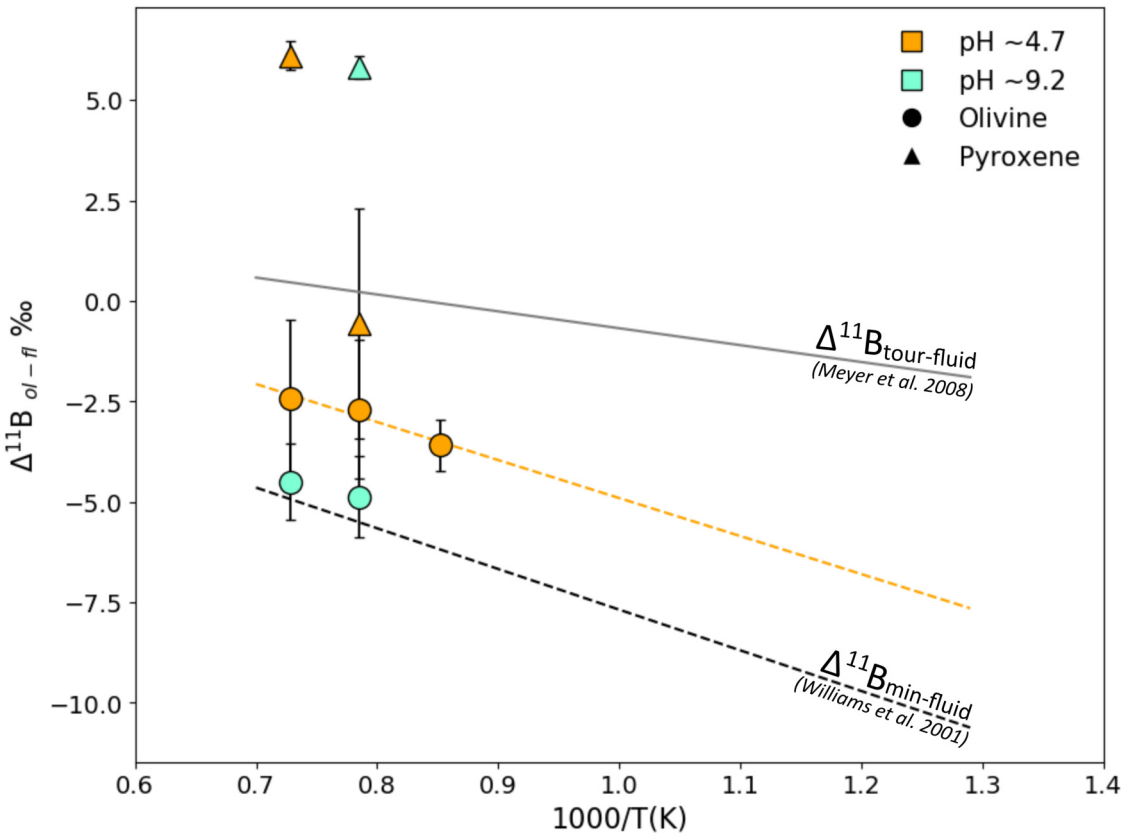

Figure 5.5: $\Delta^{11}B_{ol-fl}$ vs 1000/Temperature (Kelvin) for all five successful experiments. There is a positive correlation between $\Delta^{11}B_{ol-fl}$ and temperature which for the acidic experiments has been extended to lower temperatures (orange dashed line). This extrapolation is compared to other published $\Delta^{11}B$ studies: $\Delta^{11}B_{min-fl}$ where mineral=illite Williams et al. (2001) and $\Delta^{11}B_{tour-fl}$ from Meyer et al. (2008). Illite incorporates tetrahedral B and tourmaline incorporates trigonal B.

experiments don't necessarily represent equilibrium values.

Despite this, $\Delta^{11}B_{ol-fl}$ may be more reliable than ${}^{fl/ol}D_B$, because 1 σ on the average $\delta^{11}B$ of olivine is smaller than 1 σ on the average B concentrations (see Table.5.3). Additionally, there is a positive correlation between $\Delta^{11}B_{ol-fl}$ and temperature in the acidic experiments, see Fig.5.5. Is this correlation what we would expect to see based on basic chemical principles? The next few sub sections explore these data in the context of the relationship between $\Delta^{11}B_{ol-fl}$ and temperature, pH and coordination.

5.5.1 The effect of pH and temperature on B isotope fractionation

The reaction of boric acid with water is shown below:

$$B(OH)_3 + 2H_2O \rightleftharpoons [B(OH)_4]^- + H_3O^+ \tag{5.4}$$

The relative abundances of $B(OH)_3$ and $B(OH)_4^-$ dissolved in fluid can be nicely explained by Fig.5.6 taken from Boschi et al. (2008) looking at the species of B dissolved in seawater at different pH. As the figure shows, the switch between dominantly $B(OH)_3$ and dominantly $B(OH)_4^-$ is not instantaneous and occurs over a few pH units. At lower pH where $B(OH)_3$ is the dominant B species dissolved in water, ^{11}B will be preferentially incorporated, and the opposite at higher pH (>8.5 at room PT).

The isotopic exchange constant (K) a.k.a. equilibrium constant, decreases with temperature (Liu and Tossell, 2005), so that at 1100°C K is close to 1. This means that there should be very little fractionation between boric acid, borate and silicates at 1100°C. In light of this, we would expect the higher temperature experiments to show a $\Delta^{11}B_{ol-fl}$ closer to 0 and the lower temperature experiments to show $\Delta^{11}B_{ol-fl}$ further from 0. This relationship is seen in these experiments (see Fig.5.5).

K also decreases with increasing pH, meaning that the K value of B between silicates (with tetrahedrally coordinated B) and seawater is lower in $B(OH)_4^-$ dominated

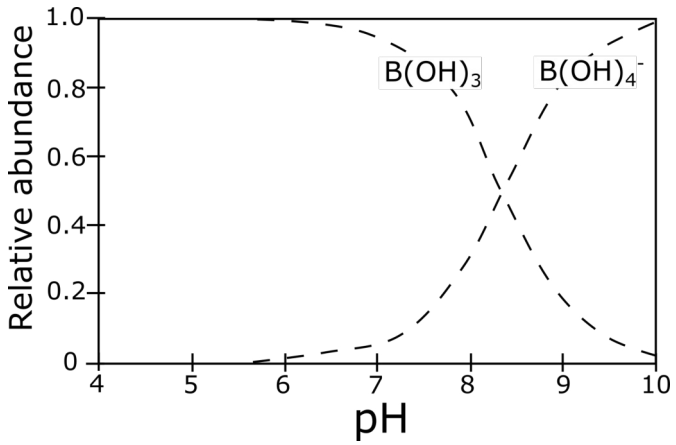

Figure 5.6: Distribution of boric acid and borate in seawater, taken directly from Boschi et al. (2008).

fluid than in $B(OH)_3$ dominated fluids (Liu and Tossell, 2005). This means that at a lower pH the fractionation of boron isotopes between silicates (with IV coordinated B) and fluid should be greater (i.e. further from 0). However, the behaviour of these experiments with pH does not match with the predicted B isotope partitioning behaviour between fluid and tetrahedrally coordinated B in silicates. The experiments were run at 2 different pH calculated at room temperature to be $\sim$4.7 and $\sim$9.2. It is worth noting, that in these pH conditions *at room temperature* we would expect the fluids in the lower pH experiment to be $B(OH)_3$ dominated and fluids in the higher pH experiment to be $B(OH)_4^-$ dominated. However, there is evidence for temperature to effect the position of equilibrium (the $B(OH)_3$ /$B(OH)_4^-$ switch over) (Boschi et al., 2008). But there is no data for the position of equilibrium at such high temperatures and pressures. It is likely that fluids at 4.2 pH will still be $B(OH)_3$ dominated, but 9.2 pH is close enough to equilibrium to throw the nature of the B species into uncertainty. However, regardless of the position of equilibrium, the experiments in this study are still contrary to the expected smaller fractionation with increasing pH. Instead, the higher pH experiment records a greater fractionation between fluid and olivine then the lower pH, (see Fig.5.5). The theory assumes that B is tetrahedrally coordinated in olivine. However, Ingrin et al. (2014) found that B (when coupled with OH) can be trigonally coordinated in olivine. Therefore, perhaps it is useful to discuss the partitioning behaviour between fluid and silicates that incorporate B trigonally.

It is not valid to assume that BO_4 bonding in aqueous solution ($B(OH)_4^-$) is the same as its bonding in tetrahedrally coordinated silicates and that therefore there is no isotopic fractionation between them (Liu and Tossell, 2005). This is because each molecule has a different 'reduced isotope partition function ratio' (RPFR) which is a value that essentially represents how attractive a molecule is to an isotope. Liu and Tossell (2005) discovered that tetrahedral B in silicates has a much lower RPFR to tetrahedral B in borate meaning that B in silicates will be isotopically lighter. Despite being focused on tetrahedral B, this theory can help explain B isotope fractionation between minerals and fluids. For example, Meyer et al. (2008) found fractionation between acidic fluids and tourmaline, both of which preferably incorporate ^{11}B, and that tourmaline is isotopically lighter than the fluids (see Fig.5.5).

However, this theory still does not explain why the fractionation between olivine and acidic fluids does not follow suit with either tetrahedrally coordinated silicates or trigonally coordinated silicates and acidic fluid (see Fig.5.5), instead it plots somewhere in-between. This could be explained by B incorporation into olivine in both trigonal and tetrahedral form, though this would need testing by FTIR. In the lower pH experiments the fluid has a high preference for ^{11}B. In the higher pH experiments, we are uncertain on the dominant B species. If it is $B(OH)_3$ dominated and the B is tetrahedrally coordinated in the olivine $\Delta^{11}B_{ol-fl}$ would be negative. This $\Delta^{11}B_{ol-fl}$ would shift closer to 0 if the B in olivine was trigonally coordinated. If the fluid is $B(OH)_4^-$ dominated and the B in olivine is tetrahedrally coordinated $\Delta^{11}B_{ol-fl}$ would be close to 0 and negative. If the B in olivine is trigonally coordinated $\Delta^{11}B_{ol-fl}$ could be close to 0 but positive.

We can rule out trigonal coordination in $B(OH)_4^-$ dominated fluids, since the $\Delta^{11}B_{ol-fl}$ in 9.2 pH experiments is negative. But there is not real way to rule out any of the other 3 options as we do not know exactly what 'closer to 0' would translate to. We also cannot tell whether the room PT pH of 9.2 would lead to borate or boric acid species dominance in the fluid during the experiment, though it is perhaps more likely to be borate dominated. However, the 9.2 pH experiments plot very close to the $\Delta^{11}B_{min-fl}$ calculated by Williams et al. (2001) that measured the fractionation between acidic

fluids and tetrahedrally coordinated B in silicates. This could be a coincidence or it could indicate that B is tetrahedrally coordinated in these olivines. Interestingly, this explanation implies that fluid pH controls how B is coordinated in olivine, trigonal incorporation in acidic fluids and tetrahedral incorporation in more alkaline fluids. At lower pH the activity of H^+ ions is increased with the dissociation of water:

$$H_2O \rightleftharpoons OH^- + H^+ \tag{5.5}$$

If olivine incorporates B in trigonal form only when associated with H (Ingrin et al., 2014), then the increased H^+ activity in lower pH could increase the trigonal incorporation of B in olivine. This is a testable hypothesis and to do so would require measuring H in these olivines to see if there is a correlation between H and B concentration and if H incorporation changed with pH.

5.5.2 Implications for use in geosciences

At 2 GPa, the breakdown of antigorite occurs between $\sim$500 and 700°C. According to the extrapolation on Fig.5.5 the $\Delta^{11}B_{ol-fl}$ at these temperatures will be -7.5 to -5 ‰ in acidic conditions. The acidic fractionation has a similar gradient (1000/t(K) vs $\Delta^{11}B_{ol-fl}$) to the experiments in Williams et al. (2001), (-9.45 vs -10.12 respectively). However, the fractionation line in Fig.5.5 is roughly 2-3 ‰ higher than the line in Williams et al. (2001). This suggests that olivine has a greater preference for ^{11}B than other silicates (or at least the ones involved in previous $\Delta^{11}B_{min-fl}$ calculations). But olivine also shows a preference for ^{10}B compared to acidic fluid. One possible explanation is that olivine incorporates B in both tetrahedral and trigonal coordination, the former like a normal silicate and the latter as described in Ingrin et al. (2014).
Based on the data in Table.5.3, the B concentration of the fluids eventually driven off dehydrating serpentinites could be 4-22% lower than the B concentration of the fluids initially produced by serpentine breakdown, just by the retention of B in secondary olivine and pyroxene.

5.5.3 Contribution of serpentinites to subduction zone fluids

Serpentinites may contribute greatly to subduction zone slab fluids and several authors have already tried to quantify this using B isotopes, such as Scambelluri and Tonarini (2012). The authors here use serpentinite veins as a proxy for the composition of serpentinite fluids and get a rough contribution of around 40% serpentinite fluids to the overall slab fluid. In this section, using the data from this chapter and chapter 3, I estimate the composition of serpentinite dehydration fluids and their subsequent contribution to slab fluids.

Since B has low diffusivity in haplogranitic melts, little to no B isotope fractionation occurs at melt crystallisation temperatures, (Marschall et al., 2017). Any B isotope fractionation, therefore, must occur during hydration/dehydration reactions. pH drastically changes the way B isotopes fractionates (Leeman and Sisson, 2002; Klochko et al., 2006; Kakihana et al., 1977), as explained in section 1.2.1 of the thesis. It is currently assumed that heavy ^{11}B preferentially fractionates into the fluid phase during subduction (i.e. Cannaó et al., 2015), indicating a low-medium pH (<10) where the dominant B species in the fluid is $B(OH)_3$ (Boric acid) with III coordination of B, which is preferred by the heavier ^{11}B. Work by Galvez et al. (2016) may support this as they modelled that the pH of fluids in equilibrium with mantle rocks are close to acid-base neutrality. However, Scambelluri and Tonarini (2012) find that Erro-Tobbio serpentinites show little loss of ^{11}B, potentially explained by high pH, which is consequently also found in serpentinization fluids analysed by Mottl et al. (2003). In this case $B(OH)_4^-$ is the dominant species in crustal fluids with IV coordination of B preferred by the lighter ^{10}B, making the fluids richer in ^{10}B. So, there are two pH scenarios, either the fluids are more acidic and richer in ^{11}B, or they are more basic and richer in ^{10}B. Only a $\Delta^{11}B_{ol-fl}$ for acidic conditions has been calculated in this chapter, because we don't have a good estimate for $\Delta^{11}B_{ol-fl}$ in alkaline conditions at 600-700°C as it would only be based on 2 points. Therefore, I will only model dehydration in acidic conditions.

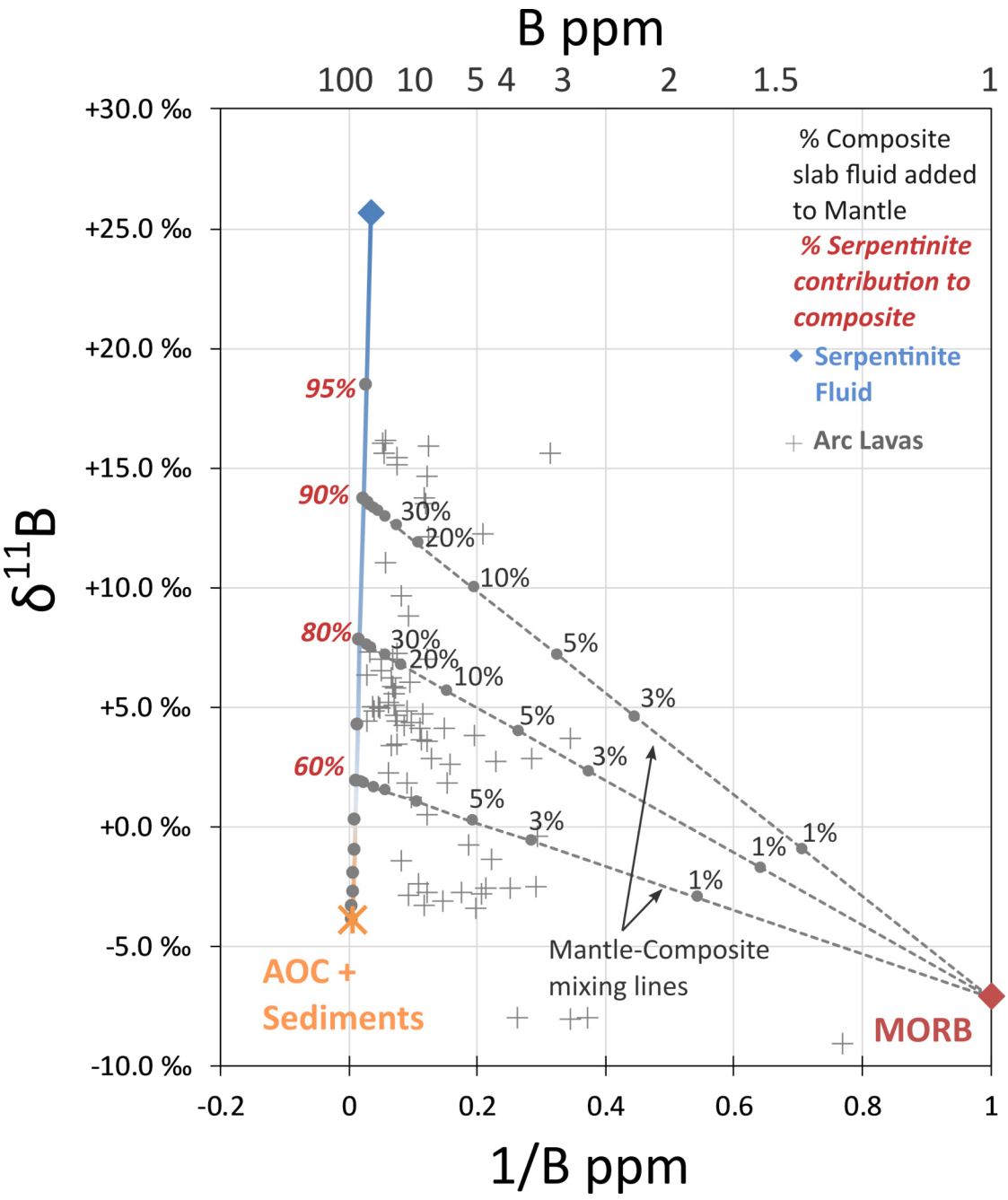

Figure 5.7: Estimated fluid composition in acidic conditions mixed with AOC+Seds and Mantle to produce arc lavas. Model uses $\Delta^{11}B_{ol-fl}$ of -6‰ for around 600°C break down of antigorite to olivine.

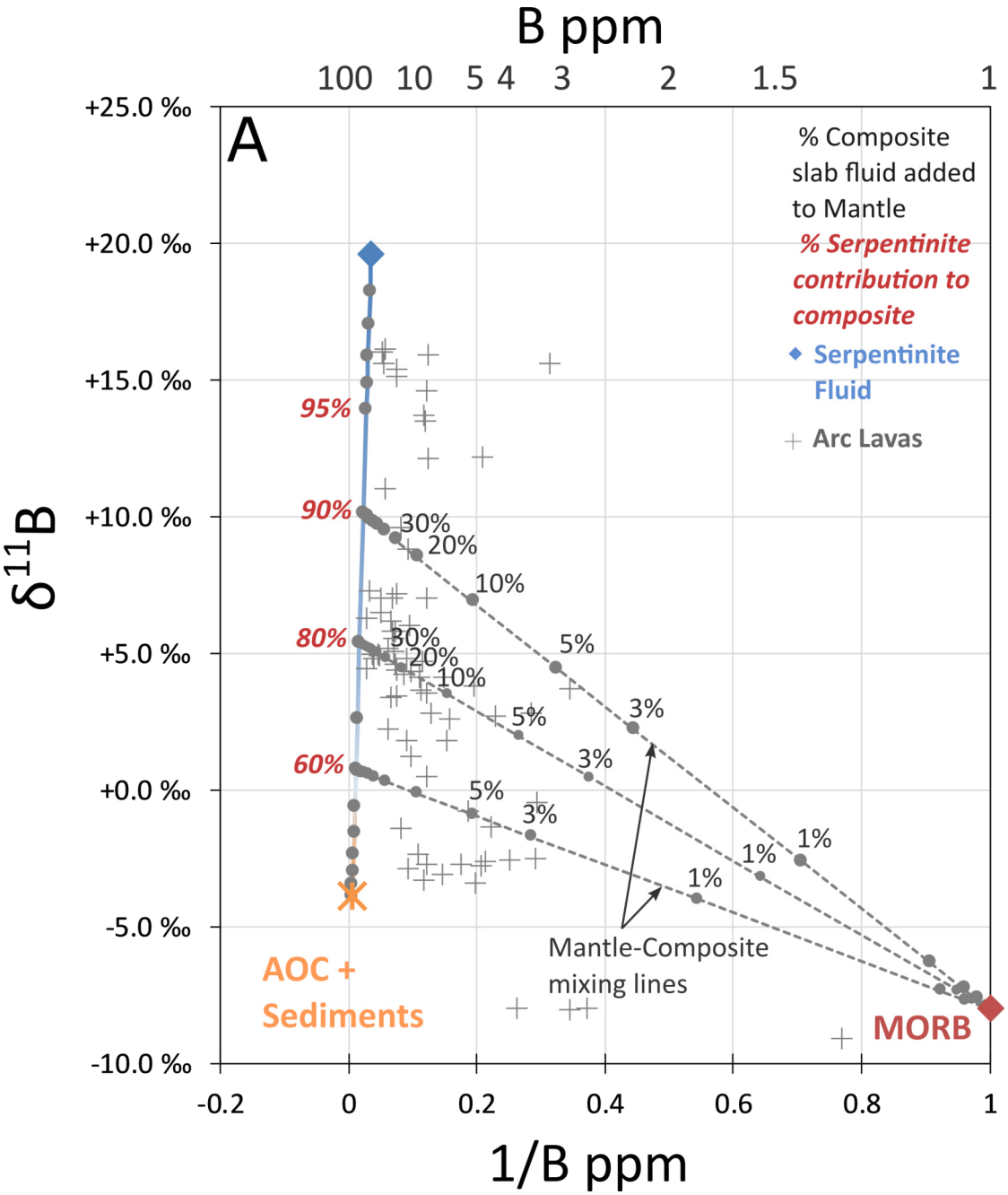

Figure 5.8: Estimated fluid composition in acidic conditions mixed with AOC+Seds and Mantle to produce arc lavas. Model uses $\Delta^{11}B_{ol-fl}$ of -9.8‰ for around 600°C break down of antigorite to olivine. This is the value from Williams et al. (2001) and serves as a comparison to Fig.5.7.

I have taken the $\Delta^{11}B_{ol-fl}$ of -6‰ which represents dehydration at around 600°C. I have applied this to the suite of Zermatt secondary olivines (from chapter 3), because these are the most likely natural secondary olivines to be in isotopic equilibrium. I have then averaged the fluid data and used the average (blue diamond) on the 3-way mixing diagram in Fig.5.7. The average estimate fluid value is then mixed with AOC + meta-sediments (slab fluid, taken from Leeman et al., 2017; Tonarini et al., 2011). Different compositions of this mixed fluid were then mixed with depleted mantle in order to recreate the δ^{11}B values of arc lavas (Scambelluri and Tonarini, 2012). For comparison, Fig.5.8 shows the predicted mixing model using $\Delta^{11}B_{ol-fl}$ of -9.8‰ as predicted by Williams et al. (2001). It simply shifts the composition of the fluid down by 3.8 ‰ leading to a greater % contribution from serpentinites in slab fluids.

This model shows that the variation in arc lava δ^{11}B could be down to varying serpentinite inputs. Some arc lavas seem to have very high serpentinite inputs, whereas some lava compositions can be formed by just mixing AOC+Seds with MORB. The majority of arc lavas can be created by a composite slab mixture of 60 to 80% serpentinite (from Fig.5.7). This suggests that serpentinites dominate the B budget for many subducted slab fluids and have the second greatest influence over the δ^{11}B of arc magmas (second to depleted mantle compositions). This potentially applies to the water budget too, since almost all hydrous, high PT phases incorporate B in some way. In addition, this model supports hypotheses that claim antigorite and/or chlorite are the main fluid-producing phases at sub-arc depths (e.g. Vils et al., 2009; Spandler et al., 2014). This model excludes phengite, even though it is present in sediments and AOC, since it is stable at much higher PT conditions than serpentine, (1000°C at 8-10 GPa) and can reach 260-360km in depth which is too deep to influence the chemistry of arc lavas (Domanik and Holloway, 1996). However, the several limitations (see section 5.5) need to be taken into account when considering the validity of this model. Before more experiments of this like are completed these numbers must be treated as estimates.

5.5.4 Pyroxene

On average pyroxene takes up less B, with $^{ol/px}D_B$ of 1.9, 0.9 and 2.2 in exp 5,6 and 9 respectively. The pyroxene in these experiments measured on average heavier δ^{11}B than the olivine. $\Delta^{11}B_{px-fl}$ are -0.6‰ ±4.9‰, +6.1‰ ±4.1‰ and +5.8‰ ±2.5‰ in exp 5,6 and 9 respectively. Pyroxene makes up less than 5% of each capsule, but appears to have a much stronger preference for ^{11}B than the olivine. This fits with evidence presented in Hålenius et al. (2010), suggesting that clinopyroxene incorporates B in trigonal coordination. $\Delta^{11}B_{px-fl}$ does not correlate with temperature, as it should, which is likely down to poor sample size: each experiment with pyroxene yielded only 1 or 2 crystals that were large enough to measure on the SIMS. This data suggests that metamorphic pyroxene may also be a substantial source of B for the deeper mantle, and potentially a source of ^{11}B as well.

5.5.5 Temperature effect with the addition of NaOH

It is worth noting that in experiments 9 and 10, NaOH was added to increase the pH, it's disassociation reaction is shown by the reaction below:

$$NaOH \rightleftharpoons Na^+ + OH^- \tag{5.6}$$

This reaction is exothermic and will be suppressed by higher temperatures. This will reduce the production of OH^- ions thus decreasing pH. Decreasing the pH favours the LHS of Eq.5.4, which opposes the effect of increased temperature. Therefore the effect of temperature on B isotope fractionation should be less pronounced (a lower gradient of 1000/t(K) vs $\Delta^{11}B_{ol-fl}$) in the experiments with added NaOH. It is impossible to say whether or not this relationship is seen in Fig.5.5. This is because there are only two experiments with added NaOH (blue points) and it would be inaccurate to extrapolate a line of best fit, meaning that the gradients cannot be compared.

5.6 Limitations

There are several caveats that must be discussed when trying to interpret this data and apply it to natural subduction zone systems. Firstly, the compositions of the experiments are not natural. The olivines and pyroxenes that are formed in these experiments are pure forsterite and enstatite (Mg#100), the kind of which is not often found in nature. Secondary olivines in chapter 3 and 4 usually have Mg# 80-95. Therefore it is worth noting that $\Delta^{11}B_{ol-fl}$ in this chapter is calculated on pure forsterite and it may not necessarily represent $\Delta^{11}B_{ol-fl}$ of natural secondary olivines. In addition, the olivines are not secondary i.e. do not form from antigorite breakdown, instead they form from SiO, MgO and $B(OH)_3$ powder, meaning that the concentration of other fluid-mobile-elements is negligible, which may also effect B incorporation in natural olivine.

Secondly, there is an unrealistically high amount of B added to the experiments. Although this was necessary to overcome potential contamination issues, it is unlikely that any natural fluid in subduction zones would have B concentrations of over 5000 ppm.

5.7 Conclusion

This data suggests that B coordination in olivine is different to other silicates (as in Williams et al., 2001; Hervig et al., 2002; Meyer et al., 2008) and fluid. This can be explained by B being both trigonally and tetrahedrally coordinated in olivine. This preference changes with pH: in a more acidic pH there is a higher preference for ^{11}B (trigonal) and in a more alkaline pH there is a higher preference for ^{10}B (tetrahedral). This work may also have some broader implications for the B cycle. B mixing diagrams in Fig.5.7 predict that a fluid with 60 to 80% (acidic fluid pH) deserpentinitization fluid is needed to mix with the mantle to explain the B composition the majority of arc lava magmas. This suggests that serpentinites dominate the B budget for the downgoing slab.

However, before these claims can be substantiated, further evidence must be gath-

ered. In order to gain a full understanding of how $^{fl/ol}D_B$ and $\Delta^{11}B_{ol-fl}$ change in different conditions, the experiments would need to be run longer to ensure equilibrium, run at a much higher pH to ensure alkaline (fluid favouring ^{10}B) conditions and repeats of all experiments at all temperatures and pH to check for reproducibility. In addition, adding FeO and small amounts of other fluid-mobile-elements commonly found in natural secondary olivines and reducing the amount of B in the fluid will help to bring the experiment closer to simulating the natural system.

Chapter 6

Conclusions and Further Work Recommendations

"The Road goes ever on and on
Out from the door where it began.
Now far ahead the Road has gone.
Let others follow, if they can!
Let them a journey new begin.
But I at last with weary feet
Will turn towards the lighted inn,
My evening-rest and sleep to meet."

J.R.R. Tolkien, The Lord of the Rings

6.1 Conclusions

Here follows an enumerated list of all the conclusions that can be made from the data presented in this thesis.

6.1.1 Chapter 3: Subduction Zone Serpentinites

1. Secondary olivine can host in the region of 2 to 30 ppm B that is noticably heavy in isotopic signature
2. Zermatt serpentinites collected in the vicinity of Trokener Steg show little to no evidence for exposure to external fluids
3. Voltri, Valle d'Aosta, Almirez and Monviso serpentinites preserve evidence for exposure to ^{10}B-rich fluids during dehydration
4. External fluids in Voltri, Almirez and Monviso are exclusively positive and could be sourced from dehydrating meta-basalts or meta-sediments
5. External fluid infiltration is more likely near the subduction interface where different lithologies are intercalated and faults provide pathways for fluids
6. ^{11}B-rich secondary olivines are recycled deeper into the mantle
7. The B composition of the oceanic lithosphere is likely to be heterogeneous

6.1.2 Chapter 4: Contact Aureole Serpentinites

1. Contact aureole serpentinites show the same relationship between B isotopic signature and geological setting to subduction zone serpentinites

   - The AZO samples are situated very close to other lithologies and they record negative δ^{11}B

   - The PR samples are isolated within a large mafic body and record positive δ^{11}B

2. This evidences fluid movement between different lithologies during contact metamorphism
3. Fluid mobility appears to be universally present during serpentinite dehydration, regardless to whether the serpentinite is at depth or near the surface

4. The main factor controlling the B isotopic composition of secondary olivines is the presence and composition of any external infiltrating fluid. The presence of external fluid is controlled by how close the nearest different lithology is

5. The Valmalenco aureole is not a closed system laboratory and should not be used to describe equilibrium processes

6.1.3 Chapter 5: Experiments

1. B coordination in olivine may be different to B coordination other silicates

2. B coordination in olivine may change with the pH of the fluid

    - In lower pH there is a higher preference for ^{11}B (trigonal)

    - In higher pH there is a higher preference for ^{10}B (tetrahedral)

3. If this partitioning behaviour is true, 3-way mixing models suggest that serpentinites dominate the B budget in the slab

6.1.4 Final words

The main conclusion from all three chapters in this thesis is that olivine and their B record are both a treasure trove of information and a great deal more complicated than previously realised. By studying the B record in secondary olivine we have learnt that the subduction interface is a bustling metropolis of fluids moving from one lithology to another and that this movement is likely enabled by metamorphic permeability. External fluids moving through serpentinites often have lower δ^{11}B and consequently reduce the δ^{11}B of secondary olivine. Serpentinites that are geologically isolated do not encounter externally derived fluids and retain their higher δ^{11}B (relative to serpentine). This pattern is also observed in contact aureoles and is therefore likely a universal phenomena that should be carefully considered when studying serpentinites. Secondary olivines may also be a source of positive δ^{11}B for the lower mantle and more work is required to study where this signal goes beyond sub-arc depths. We have also learned that there is very likely to be isotopic fractionation between olivine

and fluid, even if B is coordinated in the same way in both. Though, these experiments do not encompass the full picture and should be continued in order to assess partitioning behaviour over the whole pH range.

6.2 Recommendations for Further Work

A list of suggested further work needed to expand on this data and its implications.

1. *B isotope study of meta-sediments and metabastites in Valmalenco, Monviso, Erro-Tobbio and Almirez*. Currently the estimate for the composition of the external fluids in both the subduction and contact aureole settings is based upon a model. Therefore, a very interesting project would be to collect B isotopic data for the lithologies surrounding these serpentinites and compare that to the estimated model compositions. For example, whole-rock B isotopic measurements of the mafic bodies and mesozoic carbonates and gneisses surrounding the AZO samples in Valmalenco would reveal if these rocks have δ^{11}B light enough to contaminate the AZO olivines.

2. *In-situ B isotope study of meta-sediments and metabastites in general.In-situ* B isotopic data is not available for sediments and altered oceanic crust. If this data was collected it could shed light on the homogeneity of these lithologies and what the composition of the main dehydrating phases would be. The best project would look at partially dehydrated rocks that preserve both hydrous minerals and their break down products to check for isotopic heterogeneities.

3. *Tracking heavy δ^{11}B in olivine deeper into the mantle*. Implications that olivines enable the deep subduction of ^{11}B should be compared to B isotopic data from OIB or other plume-related magma to see if this signal is recycled. If it is not, we must answer the question 'why?' and figure out what happens to the B post sub-arc depths.

4. *Further olivine growth experiments*. The experiments require a great deal of additional further work:

- Reruns at 1100, 1000 and 900 to check reproducibility.

- Runs at lower temperatures and higher pHs to extend the trends. Temperatures down to 600/700 would be ideal if growth times and sizes are not significantly reduced. A starting pH of 11 would ensure borate dominanace in fluids.

- Changing the starting mix to have lower B (around 1000 ppm would be ideal) and higher FeO content to simulate more natural conditions, though redox would also need to be considered.

Appendix A

Equations used in handling data

A.1 Calculating [B]$_{ol-srp}$ and $\triangle^{11}$B$_{ol-srp}$

[B]$_{ol-srp}$ and Δ^{11}B$_{ol-srp}$ are calculated for each olivine by comparing its composition to the average serpentine composition in that same sample. Thus, each data point on Fig.3 in the main text represents an olivine grain measured by SIMS that has been normalised to the average serpentine composition in that same sample (also measured by SIMS).

$$[B]_{ol-srp} = \frac{B_{ol}}{av\ B_{srp}} \tag{A.1}$$

$$\Delta^{11}B_{ol-srp} = \delta^{11}B_{ol} - av\ \delta^{11}B_{srp} \tag{A.2}$$

Where:

$$av\ B_{srp} = \frac{B^1_{srp} + B^2_{srp} + B^3_{srp} \ldots}{count} \tag{A.3}$$

$$av\ \delta^{11}B_{srp} = \frac{\delta^{11}B^1_{srp} + \delta^{11}B^2_{srp} + \delta^{11}B^3_{srp} \ldots}{count} \tag{A.4}$$

Count = the number of serpentine analyses collected in the same sample as the olivine. I.e. For sample Vis5b there are 4 serpentine analyses and 5 olivine analyses. However, only 3 of the olivine analyses were measured for their B concentration

on the 4f, therefore only 3 $\Delta^{11}B_{ol-srp}$ vs $[B]_{ol-srp}$ can be calculated and plotted on Fig.3 (main text). The count of serpentine analyses in this case is 4 for $[B]_{ol-srp}$ and 3 for $\Delta^{11}B_{ol-srp}$.

A.2 Calculating 'best guess' equilibrium $D_B^{ol/srp}$

$D_B^{ol/srp}$ is calculated using the following equation:

$$D_B^{ol/srp} = \frac{B_{ol}}{B_{srp}} \tag{A.5}$$

Where:

$$B_{ol} = \frac{B_{srp}}{D^{fl/ol} \times Fr_{fl} \times Fr_{ol}} \tag{A.6}$$

$D^{fl/ol}$ = 3 to 5

Fr_{fl}= 0.13

Fr_{ol}= 0.87

Fr is the fraction of either olivine or fluid produced by the breakdown of serpentine. We model this based on serpentine containing 13 wt% fluid. $D^{fl/ol}$ is based on the values from Tenthorey and Herman (2004).

Appendix B

Data

B.1 Data for Chapter 3: Alps and Betic Cordillera

Here is presented the data used in Chapter 3 of the thesis. Each data point has a number that can be used to locate the position of the pit in the corrsponding sample. These images can be found in Appendix B.

B.1.1 Major elements data tables

Table B.1: Major element data for all phases in the main samples described in Chapter 1. Data for Voltri sample VT-8 are averages and sourced from De Hoog et al. (2014).

Sample	Phase	FeO	MgO	SiO_2	Na_2O	Al_2O_3	P_2O_5	CaO	MnO	NiO	Cr_2O_3	K_2O	TiO_2	Total
DC47	OL	8	51.3	41.8	0	0	0	0	0.4	0.3	0	0	0	101.8
DC47	OL	7.8	51.1	41.6	0	0	0	0	0.4	0.4	0	0	0	101.2
DC47	OL	8.5	51.9	41.4	0	0	0	0	0.4	0.3	0	0	0	102.5
DC47	OL	8.1	51.2	40.9	0	0	0	0	0.4	0.3	0	0	0	100.9
DC47	SRP	2.8	39.3	43.4	0	2.1	0	0	0	0.1	0.3	0	0	88.1
DC47	BAS	2.7	39.9	43.7	0	1.7	0	0	0	0.1	0.2	0	0	88.3
DC47	BAS	2.5	39.4	43.2	0	2	0	0	0	0.1	0.3	0	0	87.5
DC47	SRP	2.6	39.6	44.2	0	1.2	0	0	0.1	0.1	0.3	0	0	88.1
ZS17-8	CLH	3	53.6	37.4	0	0	0	0	0.4	0.2	0	0	3.8	98.4
ZS17-8	CLH	3.9	53.2	37.4	0	0	0	0	0.3	0.2	0	0	3.3	98.4
ZS17-8	CLH	4.5	52.3	37.2	0	0	0	0	0.3	0.2	0	0	3.7	98.3
ZS17-8	CLH	4.3	52.9	37.8	0	0	0	0	0.3	0.2	0	0	3.4	98.8
ZS17-8	OL	3.6	55.1	41.4	0	0	0	0	0.3	0.2	0	0	0	100.6
ZS17-8	CLH	3.6	52.7	37.2	0	0	0	0	0.3	0.2	0	0	4.1	98.1
ZS17-8	PX	0.7	18.4	55.2	0	0	0	25.5	0.1	0	0	0	0	99.9

Sample	Phase	FeO	MgO	SiO_2	Na_2O	Al_2O_3	P_2O_5	CaO	MnO	NiO	Cr_2O_3	K_2O	TiO	Total
ZS17-8	SRP	2.2	40.2	42.5	0	2.1	0	0	0	0.1	0.4	0	0	87.5
ZS17-8	SRP	2	40.6	42.7	0	2.1	0	0	0.1	0.1	0.2	0	0	87.7
ZS17-8	SRP	1.9	40.5	43.1	0	2	0	0	0	0.1	0.2	0	0	87.8
ZS17-8	SRP	2	41	44.1	0	1.8	0	0	0	0.1	0.1	0	0	89.1
ZS17-8	SRP	2.2	40.4	43.1	0	2	0	0	0	0.1	0.4	0	0	88.2
ZS17-8	BAS	2.1	39.8	42.9	0	2.3	0	0	0	0.1	0.5	0	0	87.6
ZS17-8	BAS	2	40.2	42.7	0	2.1	0	0	0	0.1	0.8	0	0	87.8
ZS17-9	CHL	3.3	35.8	34	0	11.7	0	0	0	0.1	0	0	0	84.9
ZS17-9	OL	4.4	54.5	41.2	0	0	0	0	0.2	0.2	0	0	0	100.5
ZS17-9	OL	4.2	53.9	41.6	0	0	0	0	0.2	0.2	0	0	0	100.2
ZS17-9	OL	4.3	54.5	41	0	0	0	0	0.2	0.3	0	0	0	100.3
ZS17-9	OL	4.5	53.9	42.1	0	0	0	0	0.3	0.3	0	0	0	101.1
ZS17-9	OL	4.4	54.8	41.5	0	0	0	0	0.2	0.2	0	0	0	101.1
ZS17-9	OL	4.4	54.2	41.8	0	0	0	0	0.2	0.2	0	0	0	100.9
ZS17-9	SRP	2.3	39.6	42.8	0	1.9	0	0	0	0.1	0.4	0	0	87.1
ZS17-9	SRP	1.9	39.6	42.4	0	1.8	0	0	0	0.1	0.6	0	0	86.5
ZS17-9	SRP	2.3	39.9	42.7	0	1.6	0	0	0	0.1	0.4	0	0	87.1
ZS17-9	SRP	2.1	39.8	42.8	0	1.9	0	0	0	0.1	0.2	0	0	86.9
ZS17-9	SRP	2.3	39.3	43	0	2.2	0	0	0	0.1	0.5	0	0	87.3

Sample	Phase	FeO	MgO	SiO_2	Na_2O	Al_2O_3	P_2O_5	CaO	MnO	NiO	Cr_2O_3	K_2O	TiO	Total
ZS1	SRP	2	39.9	43.1	0	1.6	0	0	0	0.1	0.4	0	0	87.1
ZS1	SRP	2.1	39.3	42.1	0	1.8	0	0	0.1	0.1	0.6	0	0	86
ZS1	SRP	1.8	40	43.2	0	1.7	0	0	0	0.1	0.4	0	0	87.1
ZS1	SRP	0	0	0	0	0	0	0	0	0	0	0	0	0
ZS1	SRP	2.1	40	43.5	0	1.9	0	0	0	0.1	0.3	0	0	87.3
ZS1	SRP	1.8	40	43.5	0	1.7	0	0	0	0.1	0.2	0	0	87.9
ZS1	OL	6.1	53	40.4	0	0	0	0	0.2	0.3	0	0	0	100
ZS1	OL	5.9	52.5	41.4	0	0	0	0	0.3	0.3	0	0	0	100.4
ZS1	OL	6	52.7	41.7	0	0	0	0	0.3	0.2	0	0	0	101
ZS1	OL	6.2	52.3	41.6	0	0	0	0	0.2	0.3	0	0	0	100.6
ZS1	OL	5.9	52.9	41.5	0	0	0	0	0.3	0.3	0	0	0	101
ZS1	OL	5.7	53.3	42.1	0	0	0	0	0.3	0.2	0	0	0	101.6
DC84	OL	8.7	50.6	40.1	0	0	0	0	0.2	0	0	0	0	99.6
DC84	OL	12.9	46.6	39.5	0	0	0	0	0.3	0	0	0	0	99.6
DC84	SRP	3	38.1	41.7	0	2.3	0	0	0	0.1	0.9	0	0	86
DC84	SRP	3	38.9	42.8	0.2	1.3	0	0.1	0	0	0.4	0	0	86.7
DC84	SRP	3.1	38.5	42.3	0.1	1.7	0	0.1	0	0	0.5	0	0	86.4
DC84	SRP	3	38.5	42.4	0	2	0	0	0	0.2	0.8	0	0	87
DC84	SRP	3	39	42.4	0	1.5	0	0	0	0	0.5	0	0	86.6

Sample	Phase	FeO	MgO	SiO_2	Na_2O	Al_2O_3	P_2O_5	CaO	MnO	NiO	Cr_2O_3	K_2O	TiO	Total
Vis5b	SRP	0	0	0	0	0	0	0	0	0	0	0	0	0
Vis5b	SRP	3.1	39	43.3	0	1.7	0	0	0	0.2	0.3	0	0	87.6
Vis5b	SRP	2.9	38.8	42.8	0	2.2	0	0	0	0.2	0.7	0	0	87.6
Vis5b	SRP	2.8	39.1	43	0	1.7	0	0	0	0.1	0.4	0	0	87.2
Vis5b	OL	0	0	0	0	0	0	0	0	0	0	0	0	0
Vis5b	OL	10.8	48.2	39.7	0	0	0	0	0.4	0.5	0	0	0	99.5
Vis5b	OL	10.8	48	39.9	0	0	0	0	0.5	0.2	0	0	0	99.4
AL98-4	ATG	3.4	37.6	42	0	2.3	0	0	0	0.1	0.3	0	0	85.8
AL98-4	ATG	2.9	38.7	40.9	0	2.5	0	0	0	0.1	0.6	0	0	85.7
AL98-4	ATG	3.5	37.3	41.8	0	2.2	0	0	0.1	0.1	0.4	0	0	85.5
AL98-4	ATG	3.4	37.3	41.9	0	2.2	0	0	0	0.1	0.5	0	0	85.5
AL98-4	ATG	3.5	37.6	41.7	0	2.2	0	0	0	0.1	0.4	0	0	85.5
AL98-4	ATG	3.4	37.3	42.2	0	2.1	0	0	0	0.2	0.5	0	0	85.7
AL98-4	ATG	3.2	37.5	42.1	0	2.1	0	0	0	0.1	0.3	0	0	85.4
AL98-4	ATG	3.6	37.2	41.9	0	2	0	0	0	0.1	0.4	0	0	85.3
AL98-4	ATG	3.4	37.6	41.9	0	2.1	0	0	0	0.1	0.6	0	0	85.7
AL98-4	ATG	3.6	37.3	41.6	0	2.3	0	0	0.1	0.1	0.6	0	0	85.5
AL98-4	TLC	1.2	30.8	62.6	0.1	0.3	0	0	0	0.1	0	0	0	95.1
AL98-4	OL	7.7	51.1	40.8	0	0	0	0	0.3	0.3	0	0	0	100.2

Sample	Phase	FeO	MgO	SiO_2	Na_2O	Al_2O_3	P_2O_5	CaO	MnO	NiO	Cr_2O_3	K_2O	TiO	Total
AL98-4	OL	7.7	50.7	40.8	0	0	0	0	0.3	0.3	0	0	0	99.9
AL98-4	OL	7.6	50.1	41	0	0	0	0	0.3	0.3	0	0	0	99.3
AL98-4	OL	7.6	49.7	41.2	0	0	0	0	0.3	0.3	0	0	0	99.2
AL98-4	OL	7.9	49.1	40.6	0	0	0	0	0.3	0.3	0	0	0	98.2
AL98-4	OL	8.1	50.4	40.8	0	0	0	0	0.3	0.3	0	0	0	99.9
AL98-4	OL	8	50.6	40.8	0	0	0	0	0.3	0.3	0	0	0	100
AL98-4	OL	8.1	50.5	40.8	0	0	0	0	0.3	0.3	0	0	0	99.9
AL98-4	OL	7.6	51.1	40.8	0	0	0	0	0.3	0.3	0	0	0	99.9
AL98-4	OL	7.7	50.8	40.9	0	0	0	0	0.3	0.3	0	0	0	100
VT8	CHN	12.71	42.64	32.69	n.a.	0.01		0.01	0.44	0.14	0.12		7.76	99.52
VT8	CHU	13.02	44.13	36.53	n.a.	0		0	0.44	0.2	0.08		4.72	100.62
VT8	CPX1	2.72	15.26	51.26	0.31	5.46		22.91	0.05	0.02	1.12		0.4	99.51
VT8	CPX2	1.91	17.57	54.46	0	0.05		25.58	0.1	0	0.02		0.01	99.7
VT8	CHU	12.17	44.78	34.92	n.a.	0		0.01	0.39	0.14	0.04		5.39	100.11
VT8	MAG	30.63	0.43	0.17	n.a.	0.05		0	0.09	0.24	3.48		0.41	99.31
VT8	OL1	12.6	46.82	40.03	0	0		0.007	0.347	0.315	0		0	100.19
VT8	OL2	12.13	46.71	39.26	0	0		0.005	0.294	0.296	0.045		0.861	100.47
VT8	ATG	3.66	37	41.54	0	2.56		0.02	0.05	0.07	0.11		0.01	97.54

Table B.2: Major element data for samples not described in detail in this thesis.

Sample	Phase	FeO	MgO	SiO_2	Na_2O	Al_2O_3	P_2O_5	CaO	MnO	NiO	Cr_2O_3	K_2O	TiO_2	Total
BCh9(10)	SRP	3.9	38.8	44.2	0.0	0.4	0.0	0.0	0.1	0.1	0.0			87.6
BCh9(10)	SRP	3.9	40.6	43.1	0.0	0.1	0.0	0.0	0.1	0.2	0.0			88.1
BCh9(10)	SRP	3.8	38.6	44.4	0.0	0.4	0.0	0.1	0.1	0.1	0.0			87.5
BCh9(10)	SRP	3.8	38.5	44.6	0.0	0.4	0.0	0.0	0.1	0.1	0.0			87.6
BCh9(10)	SRP	4.6	39.7	41.6	0.1	0.2	0.0	0.1	0.1	0.2	0.0			86.5
BCh9(11)	SRP	3.3	39.7	42.2	0.0	0.1	0.0	0.1	0.1	0.2	0.0			85.6
BCh9(11)	SRP	3.5	39.1	43.3	0.0	0.2	0.0	0.1	0.1	0.3	0.0			86.5
BCh9(11)	SRP	4.9	37.5	43.3	0.0	0.6	0.0	0.1	0.1	0.1	0.0			86.8
BCh9(9)	AMPH	2.2	24.8	57.5	0.3	1.5		12.6	0.1	0.0	0.2	0.0	0.2	99.4
BCh9(9)	AMPH	2.4	27.3	54.9	0.0	0.8		10.3	0.1	0.1	0.9	0.0	0.0	96.8
BCh9(9)	SRP	4.7	34.5	42.3	0.1	3.9	0.0	2.3	0.1	0.1	1.2			89.2
BCh9(9)	SRP	5.0	33.3	41.9	0.1	4.0	0.0	2.8	0.1	0.1	1.2			88.5
BCh9(9)	SRP	4.7	34.2	41.4	0.1	3.7	0.0	1.9	0.1	0.1	1.1			87.4
BCh9(9)	SRP	8.7	38.7	40.7	0.0	0.1	0.0	0.1	0.1	0.2	0.0			88.5
BCh9(9)	SRP	6.1	36.8	40.7	0.0	1.8	0.0	0.1	0.1	0.1	0.7			86.3
BCh9(9)	SRP	3.8	36.9	46.5	0.0	0.9	0.0	0.1	0.1	0.2	0.0			88.6
BLOCK B	GLASS	12.0	3.5	54.3	0.4	13.3	0.3	7.2	0.2	0.0	0.0		2.4	93.6

Sample	Phase	FeO	MgO	SiO_2	Na_2O	Al_2O_3	P_2O_5	CaO	MnO	NiO	Cr_2O_3	K_2O	TiO_2	Total
DC27a	MAG	90.2	0.3	0.0		0.0		0.0	0.3	0.4	1.8		0.1	93.0
DC27a	PX	2.9	16.0	51.4	1.1	6.6		20.8	0.1	0.0	0.8	0.0	0.4	100.0
DC27a	PX	0.6	18.6	55.3	0.0	0.0		26.1	0.1	0.0	0.0	0.0	0.0	100.8
DC27a	SRP	3.4	38.2	41.1	0.0	2.8	0.0	0.0	0.1	0.1	0.2			85.9
DC27a	SRP	3.4	38.3	42.2	0.0	3.2	0.0	0.0	0.1	0.1	0.3			87.6
DC27a	SRP	3.6	38.7	41.3	0.0	2.8	0.0	0.0	0.1	0.1	0.3			86.9
DC-8	SRP	5.8	37.1	41.8	0.0	1.8	0.0	0.0	0.1	0.2	0.2			87.0
DC-8	SRP	6.2	37.4	42.6	0.0	1.3	0.0	0.0	0.1	0.1	0.1			87.9
DC-8	SRP	5.9	36.6	43.1	0.0	1.6	0.0	0.0	0.1	0.2	0.4			88.0
LZ27a1	CHL	3.8	34.1	34.4	0.0	12.6	0.0	0.0	0.0	0.2	0.7			85.9
LZ27a1	CHL	4.1	34.6	34.7	0.0	13.2		0.0	0.0	0.3	0.7	0.0	0.0	87.7
LZ27a1	CHL	3.9	34.5	34.4	0.0	13.3		0.0	0.0	0.3			0.0	86.4
LZ27a1	CHL	4.1	34.7	34.6	0.0	12.0		0.0	0.0	0.2			0.0	85.7
LZ27a1	PX	3.2	17.1	54.4	0.0	0.1		25.8	0.1	0.0	0.0	0.0	0.0	100.7
LZ27a1	PX	3.7	17.1	54.9	0.2	0.2		25.0	0.3	0.0	0.1	0.0	0.1	101.5
LZ27a1	SRP	4.1	37.6	42.6	0.0	2.2	0.0	0.0	0.0	0.2	0.0			86.7
LZ27a1	SRP	4.1	38.4	43.6	0.0	1.6	0.0	0.0	0.0	0.2	0.1			88.0
LZ27a1	SRP	3.8	38.2	43.2	0.0	1.7	0.0	0.0	0.0	0.2	0.1			87.1
LZ34b	CHL	3.1	34.9	37.4	0.3	10.0		0.1	0.0	0.2			0.0	86.1

Sample	Phase	FeO	MgO	SiO_2	Na_2O	Al_2O_3	P_2O_5	CaO	MnO	NiO	Cr_2O_3	K_2O	TiO_2	Total
LZ34b	CHL	3.2	36.4	37.9	0.0	9.8		0.0	0.0	0.2			0.0	87.7
LZ34b	MAG	91.6	0.3	0.1		0.0		0.0	0.0	0.4	0.2		0.1	92.8
LZ34b	OL	10.4	48.6	41.2	0.0	0.0	0.0	0.0	0.3	0.4	0.0		0.0	100.9
LZ34b	OL	10.7	48.3	40.4	0.0	0.1	0.0	0.0	0.3	0.4	0.0		0.0	100.2
LZ34b	OL	11.2	48.6	40.4	0.0	0.0	0.0	0.0	0.3	0.4	0.0		0.2	101.1
LZ34b	SRP	3.2	38.9	43.0	0.0	1.5	0.0	0.0	0.0	0.2	0.0			86.8
LZ34b	SRP	3.6	38.9	42.8	0.0	1.8	0.0	0.0	0.0	0.2	0.0			87.5
LZ34b	SRP	3.5	38.0	42.0	0.0	3.5	0.0	0.0	0.0	0.2	0.1			87.2
LZ34c	OL	10.8	49.0	40.5	0.0	0.0	0.1	0.0	0.3	0.3	0.0		0.0	101.0
LZ34c	OL	10.7	49.1	40.2	0.0	0.0	0.0	0.0	0.3	0.3	0.0		0.0	100.6
LZ34c	OL	10.9	48.6	40.6	0.0	0.0	0.1	0.0	0.3	0.3	0.0		0.0	100.9
LZ34c	OL	11.1	48.7	40.1	0.0	0.0	0.0	0.0	0.3	0.3	0.0		0.0	100.6
LZ34c	OL	11.1	49.1	40.5	0.0	0.0	0.0	0.0	0.3	0.3	0.0		0.0	101.3
LZ34c	SRP	3.3	37.8	43.2	0.1	2.1	0.0	0.0	0.0	0.2	0.0			86.9
LZ34c	SRP	3.0	38.1	43.5	0.1	1.9	0.0	0.0	0.0	0.2	0.0			86.8
LZ34c	SRP	3.5	38.0	43.2	0.0	2.2	0.0	0.0	0.1	0.2	0.0			87.3
LZ34c	SRP	3.3	38.3	42.8	0.0	1.9	0.0	0.0	0.0	0.2	0.0			86.6
LZ34c	SRP	3.3	38.4	43.7	0.0	1.9	0.0	0.0	0.0	0.2	0.0			87.5
LZC01(1)	OL	9.5	49.2	40.8	0.0	0.0	0.0	0.0	0.1	0.4	0.0		0.0	100.1

Sample	Phase	FeO	MgO	SiO_2	Na_2O	Al_2O_3	P_2O_5	CaO	MnO	NiO	Cr_2O_3	K_2O	TiO_2	Total
LZC01(1)	OL	10.1	49.5	40.4	0.0	0.1	0.0	0.3	0.1	0.4	0.0		0.0	100.8
LZC01(1)	SRP	7.4	36.7	37.8	0.2	0.0	0.0	0.1	0.1	0.3	0.0			82.6
LZC01(1)	SRP	2.8	40.0	42.0	0.0	0.0	0.0	0.0	0.0	0.2	0.0			85.1
LZC01(1)	SRP	4.6	40.0	39.4	0.0	0.0	0.0	0.0	0.1	0.3	0.0			84.5
LZC02(1)	OL	11.7	48.4	41.4	0.0	0.0	0.0	0.0	0.2	0.4	0.0		0.0	102.1
LZC02(1)	OL	10.4	48.7	40.3	0.0	0.0	0.0	0.0	0.1	0.4	0.0		0.0	99.9
LZC02(1)	OL	10.1	50.0	40.4	0.0	0.0	0.0	0.0	0.1	0.4	0.0		0.0	101.0
LZC02(1)	PX	6.3	33.0	55.7	0.0	2.8		1.8	0.1	0.1	0.8	0.0	0.2	100.8
LZC02(1)	PX	6.5	33.5	55.5	0.0	2.5		1.3	0.1	0.1	0.7	0.0	0.2	100.4
LZC02(1)	SRP	3.2	38.3	42.8	0.0	2.1	0.0	0.0	0.0	0.1	0.5			87.1
LZC02(1)	SRP	4.6	38.1	41.8	0.0	1.8	0.0	0.0	0.0	0.1	0.6			87.0
LZC02(14)	PX	6.7	34.3	56.2	0.0	2.2		1.0	0.1	0.1	0.6	0.0	0.2	101.3
LZC02(14)	SRP	5.5	37.9	42.5	0.0	1.1		0.0	0.1	0.1	0.5	0.0	0.0	87.7
LZC02(14)	SRP	4.5	37.6	36.0	0.1	2.1	0.0	0.1	0.2	0.0	0.8			81.4
LZC02(14)	SRP	4.5	37.8	37.1	0.1	1.8	0.0	0.1	0.2	0.0	0.7			82.4
LZC02(14)	SRP	2.1	40.8	42.5	0.0	0.2	0.0	0.0	0.1	0.0	0.0			85.8
LZC02(15)	OL	9.7	50.1	40.1	0.0	0.0	0.0	0.0	0.1	0.4	0.0		0.0	100.4
LZC02(15)	OL	10.0	49.8	39.9	0.0	0.0	0.0	0.0	0.1	0.4	0.0		0.0	100.4
LZC02(15)	PX	6.5	34.1	55.6	0.0	2.5		0.5	0.2	0.1	0.6	0.0	0.2	100.4

Sample	Phase	FeO	MgO	SiO_2	Na_2O	Al_2O_3	P_2O_5	CaO	MnO	NiO	Cr_2O_3	K_2O	TiO_2	Total
LZC02(15)	PX	6.6	33.8	55.8	0.0	2.8		0.9	0.1	0.1	0.8	0.0	0.2	101.1
LZC02(15)	SRP	4.3	39.2	44.2	0.0	0.5	0.0	0.0	0.0	0.2	0.1			88.5
LZC02(15)	SRP	11.6	30.1	39.5	0.2	0.9	0.0	0.1	0.7	0.2	0.0			83.4
LZC02(15)	SRP	9.5	34.2	39.5	0.1	0.7	0.0	0.1	0.3	0.5	0.0			84.8
LZC02(15)	SRP	10.1	33.2	39.3	0.1	1.7	0.0	0.1	0.5	0.0	0.0			85.1
MM15(3)	SRP	3.0	40.2	41.7	0.0	1.3	0.0	0.0	0.0	0.1	0.0			86.3
MM15(3)	SRP	3.4	38.6	41.0	0.1	1.9	0.0	0.0	0.0	0.6	0.0			85.7
MM15(3)	SRP	3.0	39.0	41.2	0.0	1.8	0.0	0.0	0.1	0.4	0.0			85.6
MM15(3)	SRP	3.2	39.5	41.5	0.0	1.9	0.0	0.0	0.1	0.5	0.0			86.8
MM15(4)	srp	2.9	36.9	41.2	0.0	2.1	0.0	2.3	0.1	0.0	1.1			86.7
MM15(4)	srp	3.0	36.0	41.2	0.1	2.3	0.0	2.7	0.1	0.1	1.0			86.5
MM15(4)	SRP	3.5	38.5	40.1	0.0	1.6	0.0	0.1	0.1	0.0	1.0			84.9
MM15(4)	SRP	3.2	39.5	42.3	0.0	1.7	0.0	0.0	0.1	0.0	0.1			87.0
ODP(6)	SRP	2.7	36.4	38.2	0.1	2.7	0.0	0.0	0.1	0.3	1.2			81.9
ODP(6)	SRP	2.6	36.1	37.3	0.2	2.5	0.0	0.1	0.1	0.3	1.2			80.3
ODP(6)	SRP	2.0	39.4	39.4	0.0	1.7	0.0	0.0	0.1	0.1	2.0			84.7
ODP(6)	SRP	1.6	38.8	41.0	0.2	0.9	0.0	0.0	0.0	0.2	0.0			82.8
ODP(7)	SRP	1.3	39.2	40.9	0.1	1.0	0.0	0.0	0.1	0.1	0.0			82.8
ODP(7)	SRP	1.4	39.5	40.7	0.1	1.0	0.0	0.0	0.1	0.1	0.0			83.0

Sample	Phase	FeO	MgO	SiO_2	Na_2O	Al_2O_3	P_2O_5	CaO	MnO	NiO	Cr_2O_3	K_2O	TiO_2	Total
ODP(7)	SRP	1.5	39.2	40.5	0.1	0.9	0.0	0.0	0.1	0.1	0.0			82.3
Vis1	SRP	2.7	39.4	42.6	0.0	1.5		0.0	0.1	0.0	0.7	0.0	0.0	87.1
Vis1	SRP	3.1	38.9	42.9	0.0	1.5	0.0	0.0	0.1	0.0	0.4			86.9
Vis1	SRP	3.0	38.7	41.4	0.0	2.9	0.0	0.0	0.1	0.0	0.4			86.5
Vis1	SRP	2.9	39.0	41.1	0.0	2.8	0.0	0.0	0.1	0.0	0.4			86.3
Vis1	SRP	2.7	38.8	41.4	0.0	2.8	0.0	0.0	0.1	0.0	0.4			86.2
ZS17-1	OL	2.7	55.3	42.9	0.0	0.0	0.0	0.0	0.3	0.2	0.0		0.0	101.4
ZS17-1	OL	2.3	55.4	42.2	0.0	0.0	0.0	0.0	0.3	0.3	0.0		0.0	100.5
ZS17-1	OL	3.0	55.2	41.9	0.0	0.0	0.0	0.0	0.3	0.2	0.0		0.0	100.6
ZS17-1	SRP	1.7	40.3	43.7	0.0	1.5	0.0	0.0	0.0	0.1	0.0			87.4
ZS17-1	SRP	1.7	40.3	43.3	0.0	1.3	0.0	0.0	0.0	0.1	0.2			86.9
ZS17-1	SRP	1.6	40.4	43.6	0.0	1.4	0.0	0.0	0.0	0.1	0.1			87.1
ZS17-1	SRP	2.2	40.6	42.6	0.0	1.9		0.0	0.1	0.1	0.2	0.0	0.0	87.7
ZS17-1	SRP	1.6	40.3	42.7	0.0	1.2	0.0	0.0	0.0	0.1	0.1			86.1
ZS17-1	SRP	1.5	40.4	44.4	0.0	1.2	0.0	0.0	0.0	0.1	0.2			87.8
ZS17-1	SRP	1.9	40.4	43.2	0.0	1.4	0.0	0.0	0.0	0.1	0.1			87.2
ZS17-2	OL	2.0	56.4	42.8	0.0	0.0	0.0	0.0	0.4	0.2	0.0		0.5	102.2
ZS17-2	OL	1.6	57.0	42.4	0.0	0.5	0.0	0.0	0.3	0.2	0.1		0.0	101.9
ZS17-2	OL	1.9	56.2	42.9	0.0	0.0	0.0	0.0	0.4	0.2	0.0		0.0	101.6

Sample	Phase	FeO	MgO	SiO_2	Na_2O	Al_2O_3	P_2O_5	CaO	MnO	NiO	Cr_2O_3	K_2O	TiO_2	Total
ZS17-2	OL	2.1	56.1	42.3	0.0	0.0	0.0	0.0	0.4	0.2	0.0		0.1	101.2
ZS17-2	OL	2.2	55.9	42.9	0.0	0.0	0.0	0.0	0.4	0.3	0.0		0.0	101.8
ZS17-2	SRP	1.4	40.0	44.0	0.0	1.2	0.0	0.0	0.0	0.1	0.2			87.0
ZS17-2	SRP	1.7	40.5	43.7	0.0	1.3	0.0	0.0	0.0	0.1	0.1			87.5
ZS17-2	SRP	1.5	40.6	44.0	0.0	1.2	0.0	0.0	0.0	0.1	0.1			87.6
ZS17-2	SRP	1.3	40.5	44.3	0.0	1.2	0.0	0.0	0.0	0.1	0.1			87.6
ZS17-2	SRP	1.8	40.4	44.0	0.0	1.3	0.0	0.0	0.0	0.1	0.1			87.8
ZS17-2	SRP	1.4	40.5	43.8	0.0	1.1	0.0	0.0	0.0	0.1	0.1			86.9
ZS17-4	OL	2.4	56.1	42.0	0.0	0.0	0.0	0.0	0.3	0.1	0.0		0.0	100.9
ZS17-4	OL	2.7	55.9	41.6	0.0	0.0	0.0	0.0	0.3	0.2	0.0		0.0	100.8
ZS17-4	SRP	1.6	39.9	43.1	0.0	1.5	0.0	0.0	0.0	0.1	0.1			86.3
ZS17-4	SRP	1.7	40.5	43.4	0.0	1.2	0.0	0.0	0.0	0.1	0.1			87.0
ZS17-6	Chu	3.1	52.8	38.3	0.0	0.0	0.0	0.0	0.4	0.1	0.0			94.8
ZS17-6	Chu	2.5	51.7	38.7	0.0	3.4	0.0	0.0	0.3	0.1	0.1			96.7
ZS17-6	MAG	89.1	2.8	0.1		0.0		0.0	0.5	0.4	0.3		0.0	93.4
ZS17-6	OL	2.7	55.7	41.7	0.0	0.0	0.0	0.0	0.3	0.2	0.0			100.6
ZS17-6	OL	3.1	55.2	41.9	0.0	0.0	0.0	0.0	0.4	0.2	0.0			100.8
ZS17-6	OL	4.0	54.5	41.7	0.0	0.0	0.0	0.0	0.3	0.2	0.0			100.8
ZS17-6	OL	2.8	55.2	42.6	0.0	0.0	0.0	0.0	0.3	0.2	0.0			101.1

Sample	Phase	FeO	MgO	SiO_2	Na_2O	Al_2O_3	P_2O_5	CaO	MnO	NiO	Cr_2O_3	K_2O	TiO_2	Total
ZS17-6	PX	0.5	18.8	56.3	0.0	0.0		26.4	0.1	0.0	0.0	0.0	0.0	102.1
ZS17-6	PX	0.6	18.5	55.6	0.0	0.0		26.3	0.1	0.0	0.0	0.0	0.0	101.2
ZS17-6	SRP	2.2	40.0	43.1	0.0	2.2	0.0	0.0	0.0	0.1	0.5			88.1
ZS17-6	SRP	2.3	40.4	43.7	0.0	2.2	0.0	0.0	0.0	0.0	0.3			89.0
ZS17-6	SRP	2.2	40.2	43.0	0.0	2.0	0.0	0.0	0.0	0.1	0.1			87.6
ZS17-6	SRP	2.2	40.3	43.5	0.0	2.1	0.0	0.0	0.0	0.0	0.2			88.5
ZS17-6	SRP	2.1	40.2	43.7	0.0	1.8	0.0	0.0	0.0	0.0	0.1			88.0

B.1.2 Trace elements and Boron isotopes data tables

Table B.3: B isotope and FME compositions of all main samples described in Chapter 1

Sample	Phase	1270 spot	δ^{11}B	δ^{11}*B error*	4f Spot	B	H_2O wt%	Li	F	Cl
ZS17-9	CHL	88	+16.0 ‰	±*1.3* ‰	23	1.6	13.1	0.1	17.3	32.7
ZS17-9	OL	84	+26.0 ‰	±*1.0* ‰	20	1.8	0	1.2	7.6	0.8
ZS17-9	OL	86	+25.9 ‰	±*0.9* ‰	22	2.3	0	0.6	9.6	2.4
ZS17-9	OL	89	+26.6 ‰	±*1.0* ‰	24	1.9	0	1.5	8.3	0.7
ZS17-9	OL	91	+27.5 ‰	±*0.9* ‰	27	3.2	0.1	0.4	7.7	6.9
ZS17-9	OL	92	+26.6 ‰	±*0.8* ‰	28	1.7	0	0.8	8.9	3.8
ZS17-9	OL	93	+25.3 ‰	±*1.1* ‰	30	1.9	0	1.2	5.1	2.2
ZS17-9	SRP	83	+18.3 ‰	±*1.4* ‰	19	2.7	13.9	0	19.3	5.9
ZS17-9	SRP	85	+18.6 ‰	±*1.2* ‰	31	3.3	14.2	0	10.8	9.3
ZS17-9	SRP	87	+19.2 ‰	±*1.2* ‰	21	1.7	13.5	0	16	3.8
ZS17-9	SRP	90	+21.8 ‰	±*1.3* ‰	25	1.6	14.7	0	27.1	2.5
ZS17-9	SRP	94	+19.2 ‰	±*1.2* ‰	29	5.6	13.6	0	16.9	8.4
ZS17-8	CLH	67	+16.5 ‰	±*1.1* ‰	49	6.5	1.7	0.5	126.5	7.8
ZS17-8	CLH	76	+17.0 ‰	±*0.7* ‰	39	4.8	1.7	0.4	104.4	7.8
ZS17-8	CLH	74	+20.1 ‰	±*0.8* ‰	38	5.3	1.7	0.3	115.2	5.5
ZS17-8	CLH	77	+17.6 ‰	±*0.7* ‰						

Sample	Phase	1270 spot	δ^{11}B	δ^{11}*B error*	4f Spot	B	H_2O wt%	Li	F	Cl
ZS17-8	CLH	62	+22.5 ‰	±*0.7* ‰						
ZS17-8	OL	66	+25.5 ‰	±*0.9* ‰	47	4.9	0	1.7	11	4.2
ZS17-8	OL				6	5.4	0	3.1	46.1	6.2
ZS17-8	PX	70	+15.5 ‰	±*1.3* ‰	42	1.7	0	0.2	3.7	5.9
ZS17-8	PX HALO	71		±*1.0* ‰	41	23.9	14.6	0	12.3	10.1
ZS17-8	PX HALO	73		±*0.9* ‰	40	29	14.6	0	16.5	13.2
ZS17-8	SRP	63	+5.8 ‰	±*1.1* ‰	35	5.3	13.6	0	26.4	7.8
ZS17-8	SRP	65	+9.7 ‰	±*1.1* ‰	46	3.6	14.3	0	13.2	7.6
ZS17-8	SRP	68	+11.4 ‰	±*1.1* ‰						
ZS17-8	SRP	72	+7.4 ‰	±*1.1* ‰	43	10.1	13.9	0	18	5.8
ZS17-8	SRP	75	+17.6 ‰	±*1.2* ‰	37	3.2	14.4	0	19	10.8
ZS1	OL	ol11	+21.1 ‰	±*1.0* ‰	35	8.5	0	0.5	7.7	8.8
ZS1	OL	ol12	+19.9 ‰	±*1.2* ‰	40	8.7	0	1	5.9	5.7
ZS1	OL	ol15	+18.5 ‰	±*1.0* ‰						
ZS1	OL	ol2	+13.8 ‰	±*0.9* ‰	33	15.1	0	1	7.1	10.5
ZS1	OL	ol3	+18.1 ‰	±*1.0* ‰						
ZS1	OL	ol4	+18.3 ‰	±*1.2* ‰						
ZS1	OL	ol7	+17.8 ‰	±*1.1* ‰	27	7.9	0	0.4	6.1	1.8
ZS1	OL	ol8	+17.9 ‰	±*1.1* ‰	34	5.9	0	0.6	8.8	1.8

Sample	Phase	1270 spot	δ^{11}B	δ^{11}*B error*	4f Spot	B	H_2O wt%	Li	F	Cl
ZS1	OL	1	+13.5 ‰	±*0.9* ‰		8.3		0.5		
ZS1	OL	2	+13.4 ‰	±*0.9* ‰		6.7		0.5		
ZS1	OL	3	+16.7 ‰	±*0.9* ‰		8		0.8		
ZS1	OL	6	+12.8 ‰	±*0.9* ‰		5.5		0.6		
ZS1	OL	5	+13.8 ‰	±*1.1* ‰		5.3		0.7		
ZS1	OL	10	+10.2 ‰	±*0.7* ‰		7.8		1.2		
ZS1	OL					7.6		1.3		
ZS1	OL					8.4		0.9		
ZS1	SRP	atg1	-0.6 ‰	±*1.0* ‰	37	27.7	12.7	0	403.2	65.6
ZS1	SRP	atg1	+1.4 ‰	±*1.0* ‰	36	16.9	12.7	0	145.5	25.6
ZS1	SRP	atg1	+9.1 ‰	±*1.0* ‰	39	21	14.1	0	119.4	78.9
ZS1	SRP	atg1	+10.7 ‰	±*1.0* ‰	38	50.5	14.5	0	598	84.4
ZS1	SRP	atg5	+10.6 ‰	±*1.0* ‰	26	13.8	13.1	0	104.6	85.7
ZS1	SRP	atg6	+12.7 ‰	±*1.1* ‰	29	22.4	14	0	126	90
ZS1	SRP	atg9	+13.7 ‰	±*1.1* ‰	25	12.8	13.4	0	124.7	39.2
ZS1	SRP	4	+5.7 ‰	±*0.8* ‰						
ZS1	SRP	7	-4.7 ‰	±*1.5* ‰						
ZS1	SRP	8	+6.4 ‰	±*0.8* ‰						
ZS1	SRP	9	+3.0 ‰	±*0.7* ‰						

Sample	Phase	1270 spot	δ^{11}B	δ^{11}*B error*	4f Spot	B	H_2O wt%	Li	F	Cl
ZS1	SRP	12	+1.3 ‰	±*0.8* ‰						
ZS1	SRP	13	+5.3 ‰	±*0.7* ‰						
ZS1	SRP					22.2		0	2.3	
ZS1	SRP					7.1		0	1.5	
ZS1	SRP					5.7		0	1.9	
ZS1	SRP					14.2		0	1.5	
DC47	BAS	38	+21.0 ‰	±*1.0* ‰	107	10.5	12.5	0	21.5	39.2
DC47	BAS	39	+20.2 ‰	±*1.0* ‰	108	10.2	12.9	0	19.5	32.2
DC47	OL	36	+18.0 ‰	±*0.3* ‰	105	18.6	0	0.1	11.4	11.5
DC47	OL	40	+18.6 ‰	±*0.3* ‰	109	28.6	0	0.5	12	12.8
DC47	OL	42	+17.1 ‰	±*0.3* ‰	111	15.4	0	0.2	12.1	9.9
DC47	OL	41	+18.1 ‰	±*0.2* ‰	112	16.8	0	0.3	11	8.6
DC47	SRP	37	+20.1 ‰	±*1.0* ‰	106	7.4	13.3	0	23.7	19.7
DC47	SRP	43	+19.0 ‰	±*0.9* ‰	110	16.7	12.8	0	20.7	36.6
VT8-3	OL	ol2	+19.6 ‰	±*1.0* ‰		14.4	0	48.2	17.2	48.1
VT8-3	OL	ol3	+20.7 ‰	±*1.0* ‰		18.6	0	3.7	19.3	23
VT8-3	OL	ol4	+20.4 ‰	±*1.0* ‰		13.2	0	13.6	8.3	24.5
VT8-3	OL	ol1	+19.1 ‰	±*1.0* ‰		17.4	0.1	3.6	12.9	270.8
VT8-3	SRP	atg1	+18.2 ‰	±*1.2* ‰		13.6	14.1	0.1	590.8	41.8

Sample	Phase	1270 spot	δ^{11}B	δ^{11}*B error*	4f Spot	B	H_2O wt%	Li	F	Cl
VT8-3	SRP	atg2	+17.2 ‰	±*1.1* ‰		10.5	14.2	0.1	195.6	49.4
Vis5b	OL	ol02a	+12.3 ‰	±*0.9* ‰						
Vis5b	OL	ol02	+10.7 ‰	±*1.0* ‰	115	8	0	0.1	4.1	2.4
Vis5b	OL	ol04	+9.5 ‰	±*0.9* ‰						
Vis5b	OL	ol01	+12.5 ‰	±*0.9* ‰	118	12.6	0	0.3	6.8	11
Vis5b	OL	ol06	+12.9 ‰	±*0.9* ‰	116	11.2	0.1	0.1	8.8	6.5
Vis5b	SRP	atg01	+20.0 ‰	±*1.3* ‰	73	1.8	14.2	0	14	18.1
Vis5b	SRP	atg02	+20.8 ‰	±*1.2* ‰	74	2.9	13.7	0	28.9	25.3
Vis5b	SRP	atg04	+19.6 ‰	±*1.5* ‰	13	1.6	13.1	0	19.1	35.3
Vis5b	SRP				75	11.1	11.2	0.1	90.6	76.1
DC84	OL	47	+13.0 ‰	±*0.3* ‰	11	7.2	0	0	10.2	5.7
DC84	OL	53	+12.5 ‰	±*0.3* ‰	13	21.7	0	0.1	27.4	13.2
DC84	PX	57	+10.1 ‰	±*1.8* ‰	15	0.5	0.1	1.3	10.2	12.7
DC84	SRP	52	+19.1 ‰	±*1.0* ‰	12	3.6	12.2	0	17.1	16.5
DC84	SRP	50	+20.0 ‰	±*1.0* ‰	9	7.1	12.9	0	18	31
DC84	SRP	49	+20.2 ‰	±*1.0* ‰	7	5	12.6	0	12.2	13.9
DC84	SRP	55	+19.9 ‰	±*1.2* ‰	16	2.7	12.7	0	16.6	18
DC84	SRP	56	+21.3 ‰	±*1.0* ‰	18	7.4	13	0	12	13
AL98-4	OL	10	+26.9 ‰	±*1.0* ‰		5.5		3.9	44	12.8

Sample	Phase	1270 spot	δ^{11}B	δ^{11}*B error*	4f Spot	B	H_2O wt%	Li	F	Cl
AL98-4	OL	11	+19.1 ‰	±*1.1* ‰		5.9		4.4	27.3	22.6
AL98-4	OL	15	+20.9 ‰	±*1.2* ‰		5.3		3.3	25	13.2
AL98-4	OL	16	+25.6 ‰	±*1.1* ‰		9.5		2.7	23.8	11.6
AL98-4	SRP	12	+24.4 ‰	±*1.2* ‰		4.2		0.2	69.5	65.3
AL98-4	SRP	17	+22.6 ‰	±*1.1* ‰		7		0.2	163.2	178.1

Table B.4: B isotope and FME composition of extra samples that are not discussed in detail as part of this project. Rb, Sr, Ba and Cs data is available for some samples in the digital version of this table. LZDV= Lizardite vein, late stage overprint.

Sample	**Phase**	**1271 spot**	δ^{11}**B**	δ^{11}***B er***	**4f spot**	**B 1270**	**B 4f**	**Li**	**F**	**Cl**	**H_2O wt%**
DC27A	PX	27	+0.6 ‰	±*0.7* ‰	85	2.6	45.9	1.1	5.7	0.0	0.5
DC27A	SRP	26	+14.6 ‰	±*0.9* ‰	84	15.2	15.4	0.0	44.6	16.4	12.6
DC27A	SRP	28	+14.4 ‰	±*0.9* ‰	88	26.6	25.7	0.0	46.2	13.5	12.7
DC27A	SRP	29	+12.4 ‰	±*0.9* ‰	87	12.9	30.2	0.0	44.4	8.4	12.7
DC-8	SRP	118	+3.1 ‰	±*1.2* ‰		2.5					
DC-8	SRP	117	+3.3 ‰	±*1.0* ‰		3.5					
DC-8	SRP	119	+6.1 ‰	±*1.2* ‰		2.7					
ZS17-1	OL	8	+8.5 ‰	±*0.1* ‰	70	85.6	106.6	0.6	120.1	30.8	0.0
ZS17-1	OL	4	+7.6 ‰	±*0.2* ‰	72	62.7	116.3	0.9	96.1	47.9	0.0
ZS17-1	SRP	9	+6.7 ‰	±*0.9* ‰	71	17.5	26.4	0.0	317.5	13.5	14.0
ZS17-1	SRP	7	+6.9 ‰	±*0.9* ‰							
ZS17-1	SRP	6	+7.9 ‰	±*0.9* ‰	68	26.5	51.1	0.0	319.7	46.2	13.7
ZS17-1	SRP	5	+7.0 ‰	±*0.9* ‰	76	18.4	115.2	0.0	320.2	52.6	14.0
ZS17-2	OL	33	+7.8 ‰	±*0.2* ‰	93	56.1	95.5	0.7	76.5	34.2	0.5
ZS17-2	OL	34	+8.1 ‰	±*0.2* ‰	94	59.6	106.4	0.8	86.8	44.0	0.4
ZS17-2	OL	30	+3.5 ‰	±*0.2* ‰	90	52.9	96.5	5.3	124.5	28.1	0.0

Sample	Phase	1270 spot	δ^{11}B	δ^{11}*B err*	4f spot	B 1270	B 4f	Li	F	Cl	H_2O wt%
ZS17-2	SRP	35	+8.8 ‰	±*0.9* ‰	95	41.3	51.3	0.0	310.8	46.4	13.6
ZS17-2	SRP	31	+7.4 ‰	±*0.9* ‰	91	20.5	46.2	0.0	321.8	14.4	14.9
ZS17-2	SRP	32	+7.4 ‰	±*0.9* ‰	92	22.7	41.8	0.0	292.0	11.1	13.7
ZS17-2	SRP	123	+7.4 ‰	±*0.9* ‰							
ZS17-3	SRP	44	+2.9 ‰	±*1.0* ‰	116	6.6	3.8	0.0	48.0	13.2	13.2
ZS17-3	SRP	45	+2.9 ‰	±*1.0* ‰	117	6.0	7.8	0.0	43.7	25.9	13.4
ZS17-3	SRP	46	+1.7 ‰	±*1.0* ‰	118	6.2	4.6	0.0	42.8	35.7	12.7
ZS17-4	OL	1	+21.8 ‰	±*0.5* ‰	119	6.6	10.5	1.4	18.5	15.2	0.1
ZS17-4	SRP	3	+5.6 ‰	±*1.1* ‰	121	3.6	4.0	0.0	59.9	17.6	13.8
ZS17-4	SRP	2	+12.3 ‰	±*1.2* ‰	122	2.8	2.8	0.0	39.0	4.2	14.2
ZS17-5	SRP	58	+15.3 ‰	±*1.2* ‰	103	3.5	2.9	0.0	40.9	8.3	13.4
ZS17-5	SRP	59	+1.9 ‰	±*1.1* ‰	104	10.9	8.2	0.0	50.4	28.3	12.9
ZS17-5	SRP	60	+5.6 ‰	±*1.3* ‰	101	2.7	3.5	0.0	47.6	4.1	13.5
ZS17-6	CLH	105	+27.3 ‰	±*1.0* ‰	62	4.5	11.9	0.3	657.5	9.8	1.8
ZS17-6	OL	103	+16.2 ‰	±*0.5* ‰	58	7.3	11.5	1.4	18.7	18.4	0.3
ZS17-6	SRP	107	+1.1 ‰	±*1.1* ‰	59	5.0	6.3	0.0	50.1	8.9	13.2
ZS17-6	SRP	101	-2.3 ‰	±*1.1* ‰		3.0					
ZS17-6	SRP	104	+4.5 ‰	±*1.0* ‰	57	4.5	4.4	0.0	39.9	6.1	14.0
ZS17-7	SRP	81	+6.1 ‰	±*1.0* ‰	52	8.3	16.9	0.0	20.5	11.3	13.6

Sample	Phase	1270 spot	δ^{11}B	δ^{11}*B err*	4f spot	B 1270	B 4f	Li	F	Cl	H_2O wt%
ZS17-7	SRP	82	+7.2 ‰	±*0.9* ‰	53	14.9	40.2	0.0	17.1	24.3	14.4
Bch9-10	ATG	atg02	+21.6 ‰	±*0.4* ‰	atg02		22.8	0.4	82.3	97.4	12.3
BCh9-10	ATG	atg04	+21.5 ‰	±*0.4* ‰	atg01		15.3	0.4	102.1	94.3	12.3
BCh9-10	MESH MIX	atg03	+18.9 ‰	±*0.3* ‰	atg03		103.9	0.2	107.6	196.0	13.1
BCh9-10	MESH MIX	atg05	+28.6 ‰	±*0.3* ‰			35.2				12.0
BCh9-10	MESH MIX	atg06	+22.1 ‰	±*0.4* ‰			21.3				12.3
BCh9-10	MESH MIX	atg07	+25.1 ‰	±*0.4* ‰			26.7		30.1	111.6	12.3
BCh9-11	MESH	mesh01	+21.2 ‰	±*0.3* ‰			31.5		30.0	131.5	
BCh9-11	MESH	mesh02	+27.7 ‰	±*0.3* ‰			34.0				12.1
BCh9-11	MESH	mesh03	+25.2 ‰	±*0.3* ‰			44.5		25.8	70.7	12.1
BCh9-11	MESH	mesh05	+26.1 ‰	±*0.3* ‰			28.0				
BCh9-11	MESH	mesh06	+29.4 ‰	±*0.3* ‰			42.6				
BCh9-9	BAS	bas01	+22.3 ‰	±*0.3* ‰	bas01		33.2	7.6	105.8	98.1	12.2
BCh9-9	BAS	bas02	+18.9 ‰	±*0.3* ‰	bas02		41.7	9.1	140.9	170.4	12.3
BCh9-9	BAS	mesh02	+21.5 ‰	±*0.3* ‰	mesh02		55.9	1.0	174.4	174.9	11.9
BCh9-9	BAS	bas03	+19.0 ‰	±*0.3* ‰			38.1				12.0
BCh9-9	BAS	bas04	+18.7 ‰	±*0.4* ‰	bas01		33.2	7.6	105.8	98.1	11.9
BCh9-9	BAS	bas05	+19.3 ‰	±*0.3* ‰			29.1				
BCh9-9	MESH	mesh03	+27.5 ‰	±*0.4* ‰	mesh01		38.1	0.2	94.1	163.5	13.6

Sample	Phase	1270 spot	δ^{11}B	δ^{11}*B err*	4f spot	B 1270	B 4f	Li	F	Cl	H_2O wt%
BCh9-9	TRM	px02	+4.5 ‰	±*1.3* ‰	px02		1.2	0.0	12.4	308.4	2.2
BCh9-9	TRM	px03	+18.6 ‰	±*0.2* ‰	px01		1.1	0.0	11.4	169.9	2.2
LZ27a1	ATG	atg01	+8.0 ‰		atg01		5.4	0.4	234.5	103.8	12.3
LZ27a1	ATG	atg04	+2.3 ‰	±*1.0* ‰	atg04		5.0	0.4	193.4	184.5	12.1
LZ27a1	ATG	atg05	+3.3 ‰	±*1.9* ‰	atg05		1.9	0.2	107.6	374.3	12.2
LZ27a1	ATG				atg02		2.1	0.1	125.0	259.2	6.9
LZ27a1	ATG				atg03		1.1	0.1	92.2	290.4	11.8
LZ27a1	CHL	chl06	-6.9 ‰	±*1.6* ‰	chl01		1.1	0.1	88.2	105.9	14.2
LZ27a1	CHL	chl04	+6.2 ‰		chl04		1.6	0.1	155.1	79.6	12.0
LZ27a1	CHL				chl02		1.2	0.1	104.4	111.9	12.2
LZ27a1	CHL				chl03		1.8	0.2	125.1	82.3	12.9
LZ27a1	CHL				chl05		1.4	0.1	80.1	203.0	11.8
LZ27a1	CHL				px01		1.1	0.7	35.5	35.6	12.1
LZ27a1	CLH	px02	+3.9 ‰	±*1.8* ‰	px02		1.9	0.5	41.8	65.5	11.9
LZ27a1	MET PX	xx01	+8.1 ‰	±*0.0* ‰	xx01		3.5	11.0	79.8	116.2	0.0
LZ27a1	PX				px02		1.9	0.5	41.8	65.5	0.0
LZ34b	ATG	atg01	+11.0 ‰	±*0.8* ‰	atg01		1.7	0.1	86.9	335.0	11.7
LZ34b	ATG	atg07	+15.1 ‰	±*1.5* ‰	atg06		0.8	0.0	110.6	300.1	12.2
LZ34b	ATG				atg02		0.8	0.0	55.5	407.8	11.1

Sample	Phase	1270 spot	δ^{11}B	δ^{11}*B err*	4f spot	B 1270	B 4f	Li	F	Cl	H_2O wt%
LZ34b	ATG				atg03		1.4	0.0	95.7	227.7	11.9
LZ34b	ATG				atg04		0.3	0.0	71.4	415.4	12.2
LZ34b	ATG				atg05		1.1	0.1	90.8	285.1	12.1
LZ34b	CHL	chl01	+15.4 ‰	±*0.7* ‰	chl01		8.9	0.1	295.9	124.9	12.0
LZ34b	CHL	chl03	+8.0 ‰	±*0.6* ‰	chl03		7.7	0.1	238.8	166.2	13.0
LZ34b	CHL				chl02		9.1	0.1	311.7	141.6	14.4
LZ34b	OL	ol05	+14.3 ‰	±*0.3* ‰	ol05		0.1	13.6	10.6	7.3	0.1
LZ34b	OL	ol01	+1.9 ‰	±*0.6* ‰	ol01		0.0	12.7	10.5	15.2	0.0
LZ34b	OL				ol02		0.1	12.4	17.3	17.5	0.1
LZ34b	OL				ol03		0.2	12.1	21.5	12.7	0.1
LZ34b	OL				ol04		0.1	13.2	11.3	4.6	0.0
LZ34c	ATG	atg04	+10.5 ‰	±*0.7* ‰	atg04		8.8	1.2	94.7	121.7	12.2
LZ34c	ATG	atg05	+4.4 ‰	±*0.7* ‰	atg05		6.5	0.8	118.4	127.7	12.2
LZ34c	ATG	atg06	+10.2 ‰	±*0.7* ‰			6.3				12.2
LZ34c	ATG	atg03a	+9.8 ‰	±*0.6* ‰	atg03		8.5	1.1	171.0	86.8	12.2
LZ34c	ATG	atg02	+11.4 ‰	±*0.8* ‰	atg02		8.1	1.0	125.8	94.1	12.3
LZ34c	ATG				atg01		8.2	1.0	152.5	271.8	12.5
LZ34c	OL	ol01	+0.7 ‰	±*0.7* ‰	ol01		0.4	11.5	10.2	20.4	0.0
LZ34c	OL	ol04	+6.7 ‰	±*0.3* ‰							0.0

Sample	Phase	1270 spot	δ^{11}B	δ^{11}*B err*	4f spot	B 1270	B 4f	Li	F	Cl	H_2O wt%
LZ34c	OL				ol02		0.1	16.0	7.8	13.9	0.0
LZ34c	OL				ol03		0.2	20.6	11.0	21.7	0.0
LZC02-1	ATGV	atg04	+12.7 ‰	±*0.9* ‰	atg03		0.7	0.0	55.5	170.7	12.1
LZC02-1	ATGV	atg01	+10.2 ‰	±*1.0* ‰	atg01		3.1	0.3	65.0	240.0	12.2
LZC02-1	ATGV				atg02		3.0	0.3	84.4	195.0	13.5
LZC02-1	LZDV	xx02	+20.5 ‰	±*0.4* ‰	xx02		23.5				
LZC02-1	LZDV	xx01	+19.9 ‰	±*0.3* ‰	xx01		37.7				
LZC02-1	OL	ol04	+29.6 ‰	±*1.0* ‰	ol02		0.0	1.7	17.8	5.6	0.0
LZC02-1	OL	ol02	-21.1 ‰				0.0				
LZC02-1	OL	ol01	+7.2 ‰				0.2				0.0
LZC02-1	OL	ol05	+20.2 ‰	±*1.8* ‰	ol01		0.1	1.3	19.4	12.8	0.0
LZC02-1	OL	ol06	+73.7 ‰				0.0				
LZC02-1	OL	ol07	+4.7 ‰				0.0				0.0
LZC02-1	OL	ol08	+22.1 ‰				0.1				0.0
LZC02-1	OL				ol03		0.0	1.4	16.5	2.3	0.0
LZC02-1	PX	px01	-6.4 ‰	±*1.6* ‰	px01		0.0	0.3	8.8	29.0	0.0
LZC02-1	PX	px02	-8.2 ‰	±*1.5* ‰	px02		0.2	0.2	5.8	25.0	0.2
LZC02-1	PX				px03		0.0	0.2	10.4	17.2	0.0
LZC02-14	BAS	atg02	+21.4 ‰	±*0.3* ‰	atg02		62.6	0.5	224.3	6889.7	14.2

Sample	Phase	1270 spot	δ^{11}B	δ^{11}*B err*	4f spot	B 1270	B 4f	Li	F	Cl	H_2O wt%
LZC02-14	BAS	atg01	+21.5 ‰	±*0.2* ‰	atg01		64.0	0.6	231.0	5387.2	15.4
LZC02-14	BAS	atg07	+21.0 ‰	±*0.3* ‰	atg03		77.7	0.7	242.9	6366.5	14.9
LZC02-14	BAS				atg04		5.7	0.1	122.1	225.0	14.2
LZC02-14	MESH	atg06	+18.5 ‰	±*0.5* ‰	atg06		22.2	0.1	216.1	599.2	15.7
LZC02-14	MESH	atg08	+20.9 ‰	±*0.5* ‰			20.4				
LZC02-14	MESH	atg09	+18.7 ‰	±*0.4* ‰	atg05		17.3	0.1	141.0	341.1	12.1
LZC02-14	PX	px02	+1.0 ‰	±*0.5* ‰	px02		0.2	0.2	9.0	2.1	12.1
LZC02-14	PX	px01	+5.0 ‰	±*0.3* ‰	px01		0.0	0.2	6.8	4.5	0.0
LZC02-15	ATGV	xx01	+18.9 ‰	±*1.1* ‰	xx01		4.7	0.1	83.0	248.5	12.3
LZC02-15	LZDV	atg03	+10.8 ‰	±*0.3* ‰	atg03		41.6	1.4	335.3	990.8	13.2
LZC02-15	LZDV	atg02	+27.8 ‰	±*0.3* ‰	atg02		30.2	0.8	186.5	767.8	13.9
LZC02-15	LZDV	atg04	+8.9 ‰	±*0.2* ‰			47.7				
LZC02-15	LZDV	atg05	+16.9 ‰	±*0.5* ‰			23.7				
LZC02-15	LZDV	atg06	+12.6 ‰	±*0.4* ‰			23.7				
LZC02-15	LZDV				atg01		29.2	0.5	125.7	965.4	13.7
LZC02-15	OL	ol02	+33.0 ‰	±*0.5* ‰	ol02		0.0	1.4	10.2	20.0	0.0
LZC02-15	OL	ol04	+21.0 ‰	±*1.3* ‰			0.8				0.0
LZC02-15	OL				ol01		2.9	1.8	24.5	14.5	0.4
LZC02-15	OL				ol03		0.4	1.4	13.9	2.3	0.0

Sample	Phase	1270 spot	δ^{11}B	δ^{11}*B err*	4f spot	B 1270	B 4f	Li	F	Cl	H_2O wt%
LZC02-15	OL				ol04		0.2	1.4	6.7	1.2	0.0
LZC02-15	PX	px03	-2.1 ‰				0.1				0.0
LZC02-15	PX	px01	-7.8 ‰		px01		0.0	0.1	6.7	2.9	0.0
LZC02-15	PX	px02	+61.7 ‰		px02		0.0	0.1	9.0	0.0	0.0
MM15-3	MESH MIX	mesh01	+13.3 ‰	±*0.4* ‰	mesh01		33.1	0.3	128.8	374.6	12.1
MM15-3	MESH MIX	atg01	+14.0 ‰	±*0.5* ‰	atg01		13.2				12.1
MM15-3	MESH MIX	mesh02	+13.6 ‰	±*0.3* ‰			22.6				
MM15-3	MESH MIX	atg02	+14.4 ‰	±*0.4* ‰	atg02		21.5				
MM15-3	MESH MIX	mesh03	+11.9 ‰	±*0.5* ‰			17.0				
MM15-3	MESH MIX	mesh04	+13.9 ‰	±*0.4* ‰			22.5				
MM15-3	MESH MIX	mesh05	+13.7 ‰	±*0.4* ‰			22.5				
MM15-4	BAS CR	bas01	+15.3 ‰	±*0.3* ‰	bas01		56.0	1.1	224.7	415.5	12.0
MM15-4	BAS CR	bas02	+16.0 ‰	±*0.3* ‰			30.4				
MM15-4	BAS CR	bas05	+15.7 ‰	±*0.3* ‰	bas05		50.7	0.9	148.7	424.0	
MM15-4	BAS RM	bas03	+15.8 ‰	±*0.3* ‰							
MM15-4	BAS RM	bas04	+15.8 ‰	±*0.3* ‰	bas04		52.8	0.7	147.8	546.3	12.0
MM15-4	BAS RM	bas07	+15.4 ‰	±*0.3* ‰							
MM15-4	BAS RM	bas06	+16.2 ‰	±*0.3* ‰	bas06		74.7	0.3	123.0	572.5	
MM15-4	MESH MIX	mesh03	+13.9 ‰	±*0.4* ‰	mesh03		30.6	0.2	119.7	198.7	12.2

Sample	Phase	1270 spot	δ^{11}B	δ^{11}*B err*	4f spot	B 1270	B 4f	Li	F	Cl	H_2O wt%
ODP6	BAS	mesh01a	+3.0 ‰	±*0.3* ‰	mesh02		50.9	0.4	806.6	1358.6	10.8
ODP6	BAS	mesh01b	+3.2 ‰	±*0.2* ‰	mesh01		53.2	0.3	894.0	1240.5	12.8
ODP6	BAS	bas01	+3.2 ‰	±*0.6* ‰	bas01		7.2	0.1	193.5	1353.3	13.5
ODP6	BAS	bas03	+4.8 ‰	±*0.5* ‰			12.6				
ODP6	BAS				bas02		13.5	0.1	261.0	1548.6	14.7
ODP7	MESH	atg03a	-1.1 ‰	±*0.4* ‰	atg03		16.8	0.1	198.2	394.6	13.6
ODP7	MESH	atg01	-1.6 ‰	±*0.4* ‰	atg01		16.7	0.1	195.2	442.7	13.5
ODP7	MESH	atg03b	-1.5 ‰	±*0.4* ‰			19.0				
ODP7	MESH				atg02		10.7	0.1	183.9	165.8	13.7
RO3	CHL	chl02	+10.8 ‰	±*0.9* ‰			3.8				
Vis1	ATG	atg02	+27.8 ‰	±*0.4* ‰	atg02		22.9	0.1	88.5	218.5	12.1
Vis1	ATG	atg03	+28.0 ‰	±*0.6* ‰	atg03		9.0	0.0	39.7	8.0	12.2
Vis1	ATG	px01	+22.7 ‰	±*0.7* ‰	px01		3.0	0.2	4.5	11.6	12.2
Vis1	ATG	atg04	+26.2 ‰	±*0.5* ‰	atg04		18.2				12.1
Vis1	ATG	atg01	+26.8 ‰	±*0.4* ‰	atg01		19.0	0.1	100.5	162.0	12.1
Vis1	MET PX	px03	+20.9 ‰	±*1.5* ‰	px02		3.3	0.3	5.0	15.3	0.2

B.1.3 Combined

These data were collected by all three analytical techniques (EMPA, 4f and 1270) on or very near to the same spot (see Appendix B for spot locations). This enables us to tie together and directly compare major, trace and isotopic data for an individual crystal.

Data table

This is the list of spot numbers from EMPA, 4f and 1270 that measure the same (or adjacent) crystals.

Table B.5: A list of all the linked ion probe and electron probe pits. Pits were linked by matching phase ID and proximity. Most often linked pits are situated on the same crystal, however, where crystal size is small linked pits may be on another crystal within 200μm of each other. Images of pit locations can be found in Appendix B.

Sample	Phase	1270 spot	4f spot	EMPA spot
DC47	OL	36	105	30
DC47	OL	40	109	34
DC47	OL	42	111	37
DC47	OL	41	112	38
DC47	ATG	37	106	31
DC47	BAS	38	107	32
DC47	BAS	39	108	33
DC47	ATG	43	110	40
DC84	OL	51	8	11
DC84	OL	48	6	2
DC84	OL	47	11	5
DC84	OL	53	13	6
DC84	OL	54	17	7
DC84	PX	57	15	
DC84	SRP	52	12	1

Sample	Phase	1270 spot	4f spot	EMPA spot
DC84	SRP	50	9	10
DC84	SRP	49	7	4
DC84	SRP	55	16	8
DC84	SRP	56	18	9
ZS17-8	CLH	61	36	10
ZS17-8	CLH	67	49	13
ZS17-8	CLH	76	39	26
ZS17-8	CLH	74	38	27
ZS17-8	CLH	77	38	29
ZS17-8	CLH	62	36	9
ZS17-8	OL	66	47	20
ZS17-8	PX	64	48	12
ZS17-8	PX	70	42	24
ZS17-8	SRP	63	35	11
ZS17-8	SRP	65	46	19
ZS17-8	srp	68		21
ZS17-8	srp	69		22
ZS17-8	SRP	72	43	25
ZS17-8	SRP	75	37	28
ZS17-8	SRP	71	41	23
ZS17-8	SRP	73	40	30
ZS17-9	CHL	88	23	17
ZS17-9	OL	84	20	13
ZS17-9	OL	86	22	16
ZS17-9	OL	89	24	18
ZS17-9	OL	91	27	23
ZS17-9	OL	92	28	24
ZS17-9	OL	93	30	25
ZS17-9	SRP	83	19	12

Sample	Phase	1270 spot	4f spot	EMPA spot
ZS17-9	SRP	85	31	14
ZS17-9	SRP	87	21	15
ZS17-9	SRP	90	25	20
ZS17-9	SRP	94	29	26
ZS1	OL	ol11	35	
ZS1	OL	ol12	40	
ZS1	OL	ol2	33	
ZS1	OL	ol7	27	
ZS1	OL	ol8	34	
ZS1	SRP	atg1	37	
ZS1	SRP	atg10	36	
ZS1	SRP	atg13	39	
ZS1	SRP	atg14	38	
ZS1	SRP	atg5	26	
ZS1	SRP	atg6	29	
ZS1	SRP	atg9	25	
Vis5b	srp	atg01	atg01	
Vis5b	srp	atg02	atg02	46
Vis5b	srp	atg04	atg04	45
Vis5b	srp		atg03	44
Vis5b	ol	ol02	115	42
Vis5b	ol	ol01	118	43
Vis5b	ol	ol04		47
Vis5b	ol	ol06	116	

B.2 Data for Chapter 4: Valmalenco

Here is presented the data used in Chapter 3 of the thesis. Each data point has a number that can be used to locate the position of the pit in the corrsponding sample.

These images can be found in Appendix B. This appendix also includes graphs that were created to help identify trends in the Valmalenco serpentinite data.

B.2.1 Major elements

Graphs

There are two types of graph presented here: Single graphs comparing alike phases from different samples. The purpose of these graphs is to display differences between samples. Multiple graphs comparing all phases from the same sample. The purpose of these graphs is to display differences between phases within a sample and across the sample set.

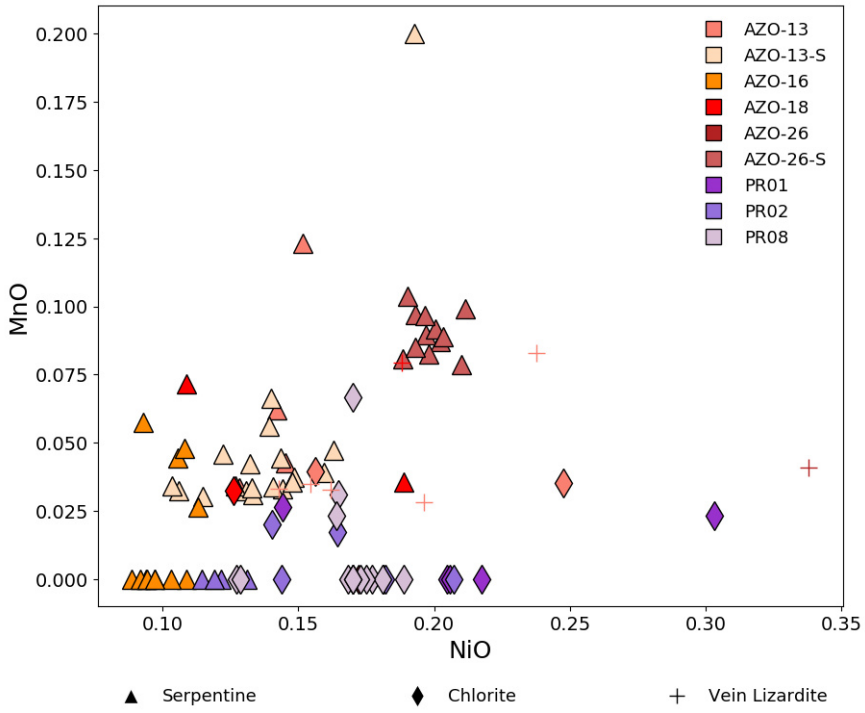

Figure B.1: NiO vs MnO for phases formed during the formation of the Bergell aureole, including: talc, olivine, amphibole and the talc/serpentine mixture. MnO is 0.05 wt% lower in PR01 and -02 olivines than in the rest of the olivines.

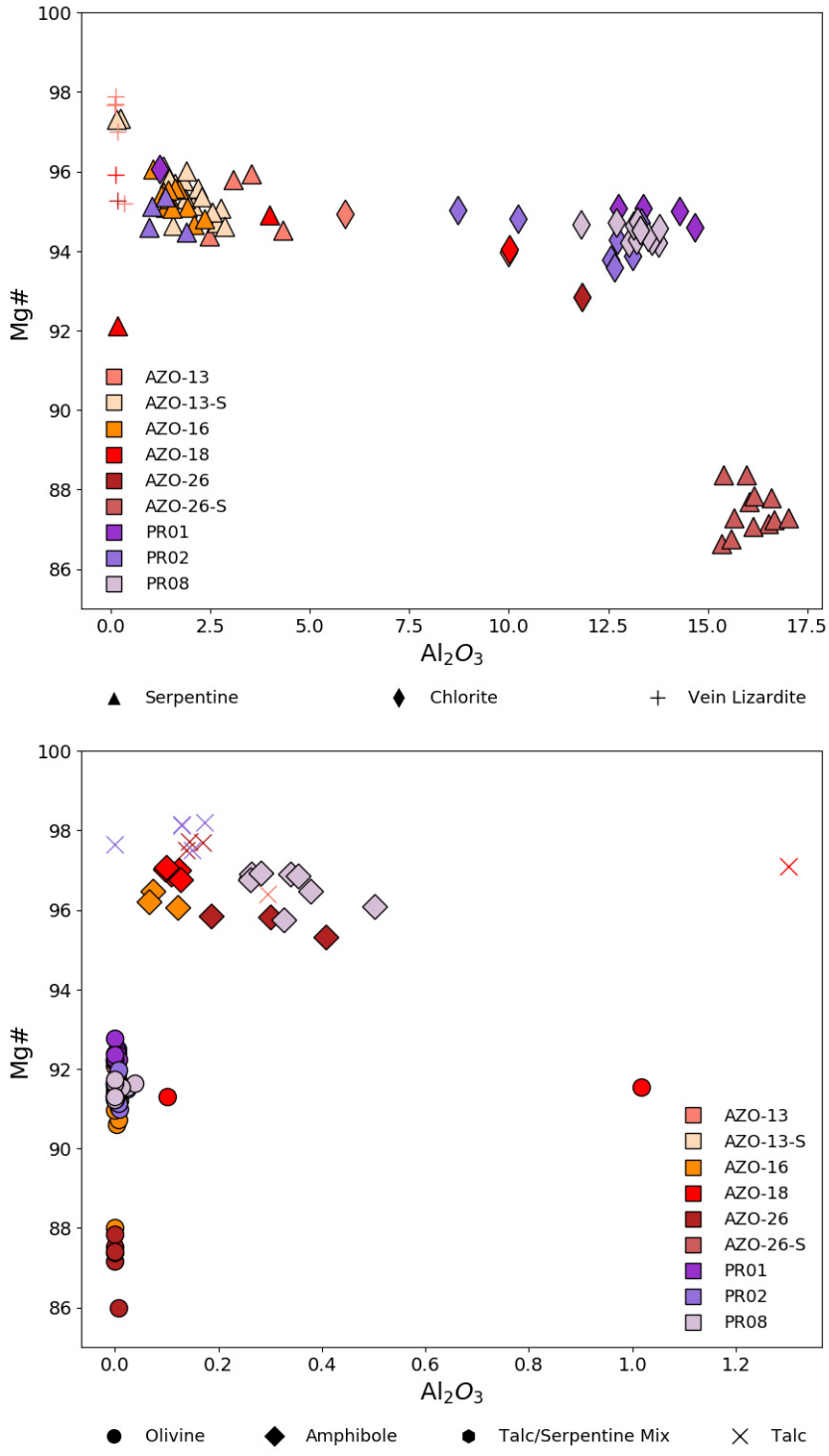

Figure B.2: (Above)Mg# vs Al_2O_3 δ^{11}B vs [F] for serpentinite phases serpentine, chlorite and vein lizardite. (Below) Mg# vs Al_2O_3 for phases formed during the formation of the Bergell aureole, including: talc, olivine and amphibole.

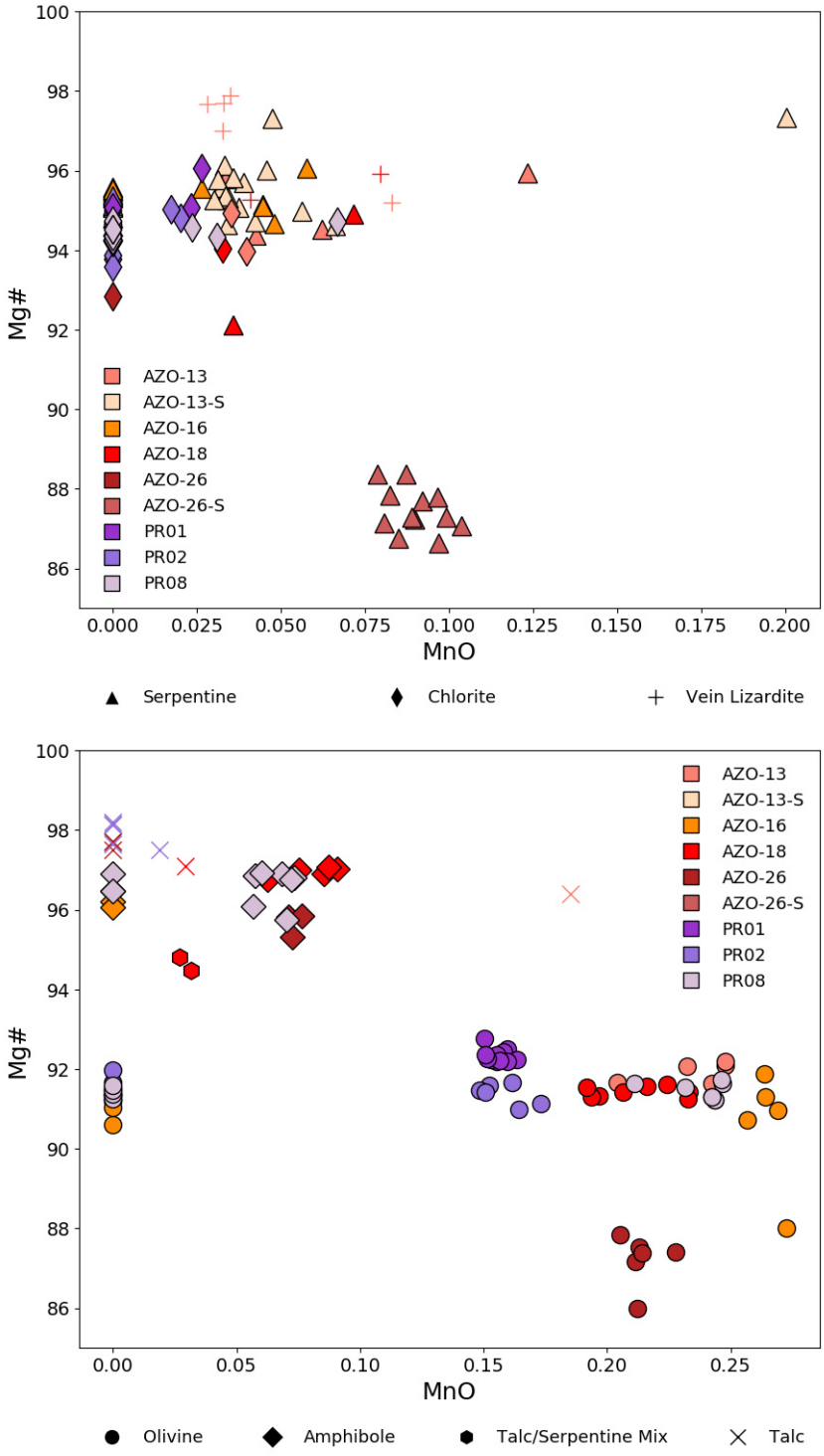

Figure B.3: (Above) Mg# vs MnO for serpentinite phases serpentine, chlorite and vein lizardite. There is a positive correlation in the antigorite serpentine. (Below) Mg# vs MnO for phases formed during the formation of the Bergell aureole, including: talc, olivine, amphibole and the talc/serpentine mixture.

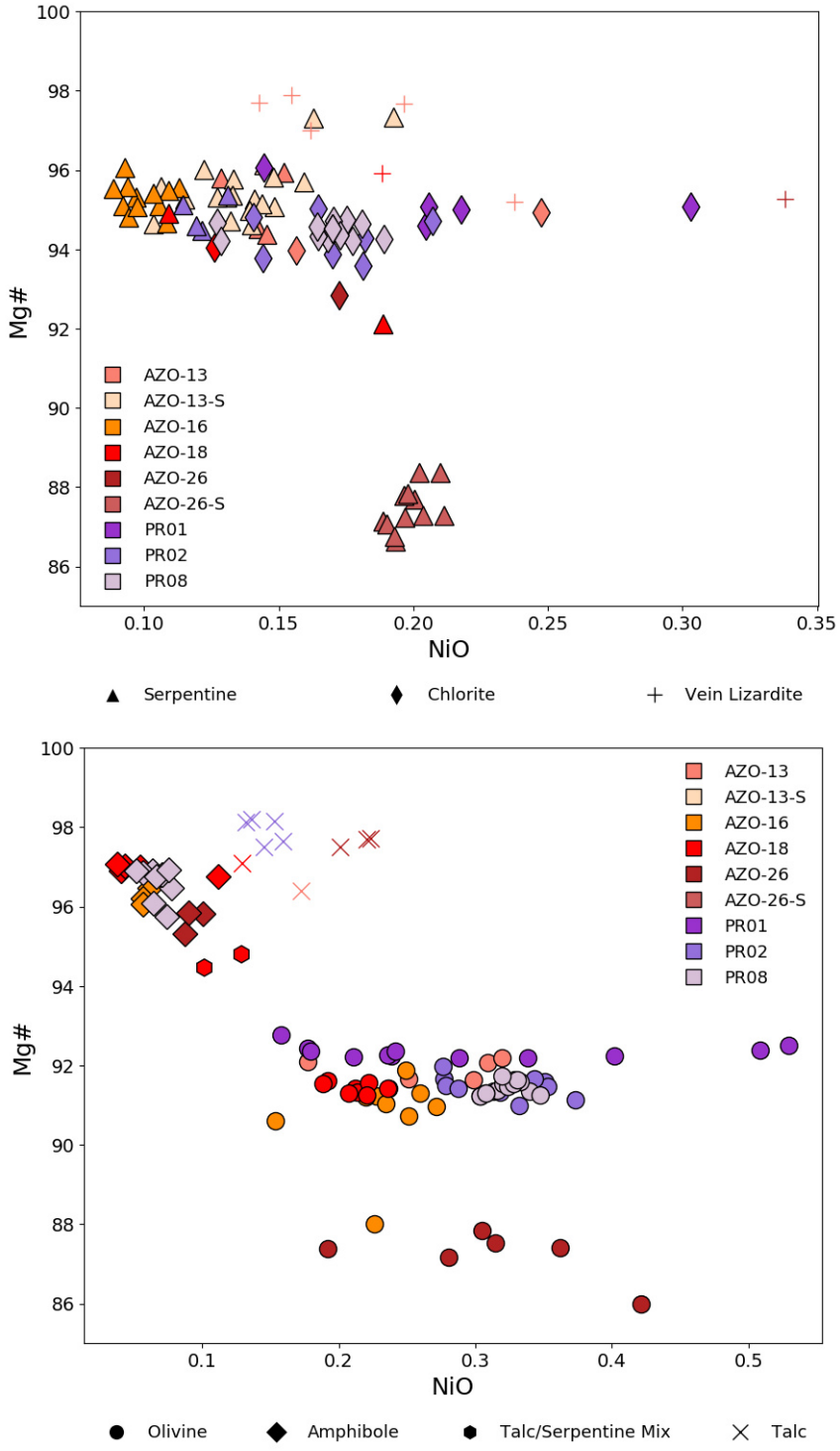

Figure B.4: (Above) Mg# vs NiO for serpentinite phases serpentine, chlorite and vein lizardite. There is a positive correlation in the antigorite serpentine. (Below) Mg# vs NiO for phases formed during the formation of the Bergell aureole, including: talc, olivine, amphibole and the talc/serpentine mixture.

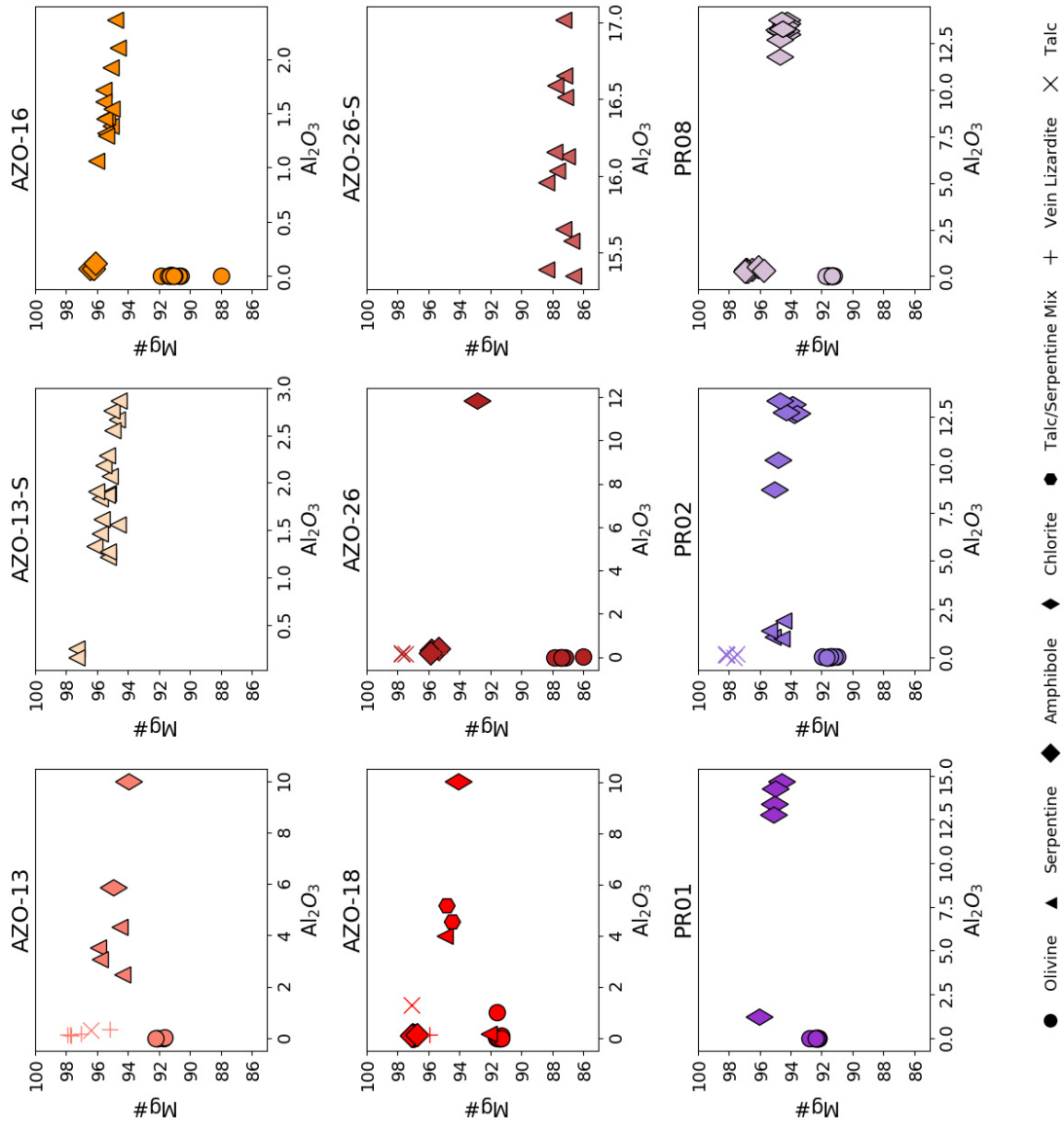

Figure B.5: Mg# vs Al_2O_3 for all phases in each sample.

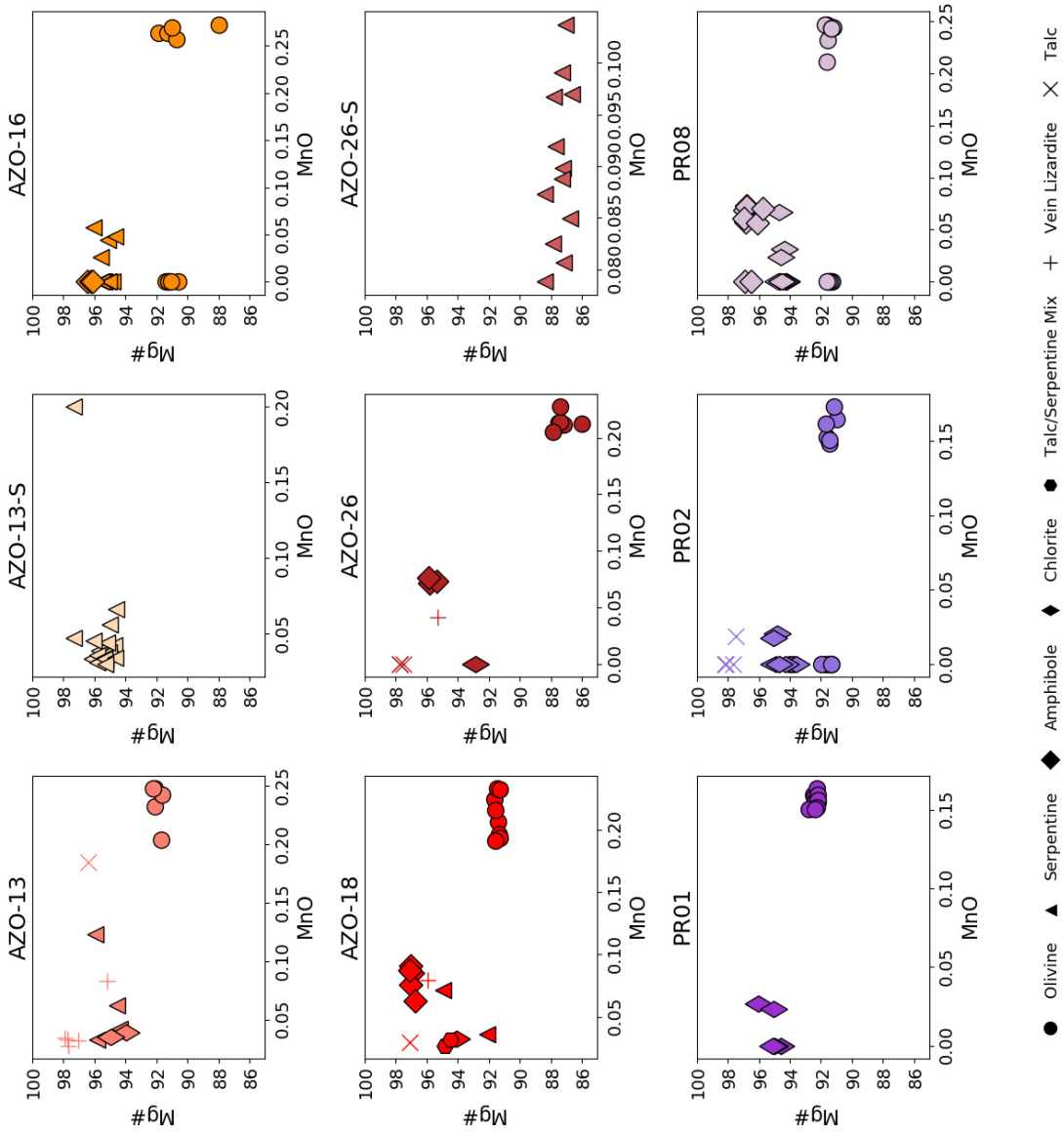

Figure B.6: Mg# vs MnO for all phases in each sample.

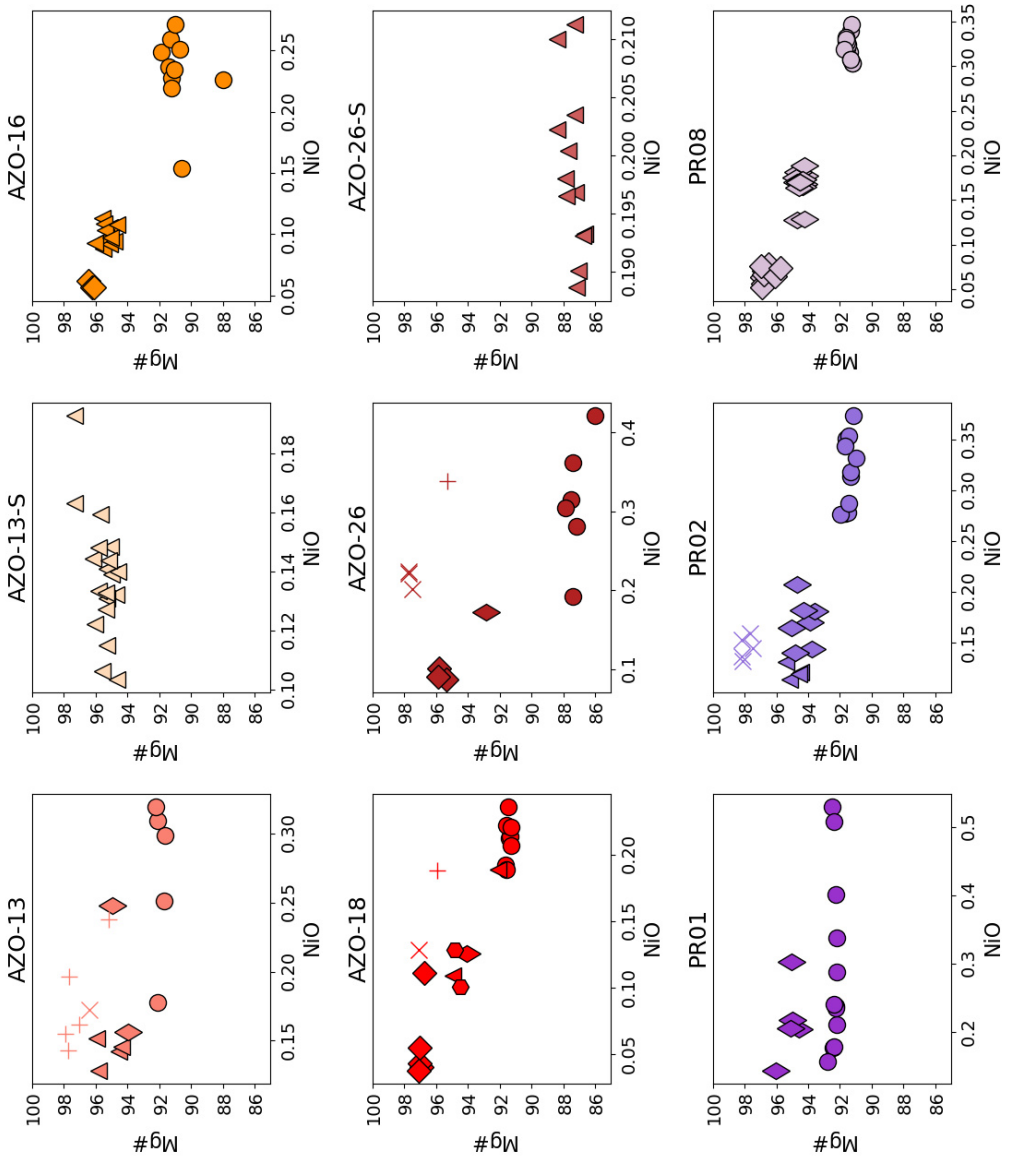

Figure B.7: Mg# vs NiO for all phases in each sample.

Major Element Data Table

Table B.6: Major data for all phases in Valmalenco samples. Elements that measured concentrations below the lower detection limit have been converted to 0.

Sample	Phase	N^O	MgO	SiO_2	FeO	Na_2O	Al_2O_3	CaO	Cr_2O_3	MnO	NiO	TiO_2	Total
AZO-13	***Chl***	11	35.68	35.54	3.40	0.01	5.88	0.02	0.73	0.04	0.25	0	81.56
AZO-13	***Chl***	15	34.59	35.54	3.95	0	10.00	0.02	0	0.04	0.16	0	84.31
AZO-13	***Mag***	4	1.09	0.03	85.91	0	0.03	0.01	6.40	0.21	0.64	0.23	94.63
AZO-13	***Ol***	19	51.17	40.99	7.71	0	0.01	0.01	0.04	0.25	0.32	0	100.50
AZO-13	***Ol***	10	50.97	41.13	7.81	0	0	0	0.16	0.23	0.31	0	100.62
AZO-13	***Ol***	5	51.22	41.26	8.33	0	0.01	0.01	0.44	0.24	0.30	0	101.80
AZO-13	***Ol***	1	50.45	41.36	8.17	0.01	0.01	0.01	0.04	0.20	0.25	0	100.50
AZO-13	***Ol***	12	50.99	41.28	7.79	0	0	0.01	0	0.25	0.18	0	100.51
AZO-13	***Srp***	6	34.03	46.40	2.56	0.01	3.53	0.01	0	0.12	0.15	0	86.81
AZO-13	***Srp***	9	37.65	40.52	3.99	0	2.47	0.01	0.51	0.04	0.15	0	85.34
AZO-13	***Srp***	18	36.66	39.16	3.78	0	4.34	0.02	0	0.06	0.14	0	84.16
AZO-13	***Srp***	8	37.98	41.41	2.96	0.01	3.07	0.01	0.84	0.03	0.13	0	86.45
AZO-13	***Tlc***	3	33.49	54.96	2.22	0.02	0.29	0.02	0	0.19	0.17	0	91.37
AZO-13	***Vein Lz***	17	37.79	39.06	3.40	0.01	0.34	0.04	0.03	0.08	0.24	0	80.99
AZO-13	***Vein Lz***	7	40.51	41.73	1.71	0.01	0.11	0.02	0	0.03	0.20	0	84.33

Sample	Phase	N^O	MgO	SiO_2	FeO	Na_2O	Al_2O_3	CaO	Cr_2O_3	MnO	NiO	TiO_2	Total
AZO-13	***Vein Lz***	20	40.26	41.60	2.21	0.02	0.17	0.03	0.02	0.03	0.16	0	84.52
AZO-13	***Vein Lz***	2	40.53	41.34	1.56	0.01	0.12	0.03	0	0.03	0.15	0	83.77
AZO-13	***Vein Lz***	13	40.89	41.44	1.72	0.01	0.12	0.02	0.03	0.03	0.14	0	84.40
AZO-13-S	***Mag***	36	1.36	0.01	83.60	0	0.04	0	8.15	0.41	0.52	0.38	94.66
AZO-13-S	***Srp***	22	39.74	42.55	1.94	0	0.25	0.04	0.02	0.20	0.19	0	84.95
AZO-13-S	***Srp***	26	41.20	40.89	2.03	0.01	0.16	0.02	0	0.05	0.16	0	84.52
AZO-13-S	***Srp***	28	38.93	43.24	3.12	0	1.61	0.01	0.10	0.04	0.16	0	87.21
AZO-13-S	***Srp***	23	37.96	41.44	3.50	0	2.76	0.01	0.57	0.04	0.15	0	86.42
AZO-13-S	***Srp***	25	39.06	42.61	3.03	0	1.47	0.01	0.19	0.04	0.15	0	86.55
AZO-13-S	***Srp***	37	39.06	43.09	2.79	0	1.33	0	0.07	0.03	0.14	0	86.53
AZO-13-S	***Srp***	27	38.26	41.81	3.48	0	2.07	0.01	0.37	0.04	0.14	0	86.18
AZO-13-S	***Srp***	32	38.78	42.74	3.44	0	1.22	0.01	0.19	0.03	0.14	0	86.55
AZO-13-S	***Srp***	24	37.71	40.84	3.82	0	2.87	0.01	0	0.07	0.14	0	85.46
AZO-13-S	***Srp***	21	38.07	41.91	3.58	0	2.56	0.01	0.40	0.06	0.14	0	86.72
AZO-13-S	***Srp***	30	38.79	42.46	3.04	0	1.83	0	0.19	0.03	0.13	0	86.49
AZO-13-S	***Srp***	34	38.58	42.04	3.34	0	2.29	0.01	0.40	0.03	0.13	0	86.83
AZO-13-S	***Srp***	31	37.93	41.17	3.77	0	2.67	0.01	0.39	0.04	0.13	0	86.13
AZO-13-S	***Srp***	38	38.39	42.86	3.37	0	1.88	0	0.19	0.03	0.13	0	86.87
AZO-13-S	***Srp***	33	38.00	41.88	3.32	0	1.87	0.01	0.34	0.03	0.13	0	85.59

Sample	Phase	N^O	MgO	SiO_2	FeO	Na_2O	Al_2O_3	CaO	Cr_2O_3	MnO	NiO	TiO_2	Total
AZO-13-S	***Srp***	35	38.57	42.24	2.85	0	1.91	0.01	0.29	0.05	0.12	0	86.04
AZO-13-S	***Srp***	40	38.68	42.99	3.42	0	1.27	0.01	0.16	0.03	0.11	0	86.68
AZO-13-S	***Srp***	29	38.62	41.81	3.19	0	2.19	0.01	0.32	0.03	0.11	0	86.27
AZO-13-S	***Srp***	39	38.32	42.93	3.87	0	1.56	0.01	0.03	0.03	0.10	0	86.87
AZO-16	***Amph***	43	23.76	58.73	1.55	0.04	0.07	13.02	0.03	0	0.06	0.01	97.28
AZO-16	***Amph***	38	23.94	59.20	1.74	0.04	0.12	13.42	0.02	0	0.06	0.01	98.59
AZO-16	***Amph***	37	24.12	58.87	1.69	0.04	0.07	13.41	0.03	0	0.06	0.01	98.32
AZO-16	***Ol***	19	49.87	40.56	8.83	0	0	0	0	0.27	0.27	0	99.82
AZO-16	***Ol***	20	50.12	40.78	8.51	0	0	0	0.21	0.26	0.26	0	100.17
AZO-16	***Ol***	14	50.29	40.91	9.17	0	0.01	0.01	0.07	0.26	0.25	0	100.97
AZO-16	***Ol***	12	50.41	40.90	7.93	0	0.00	0.01	0.02	0.26	0.25	0	99.79
AZO-16	***Ol***	40	50.63	41.59	8.47	0	0.01	0.00	0.05	0	0.24	0	100.99
AZO-16	***Ol***	16	49.38	39.19	12.00	0	0	0.01	0.08	0.27	0.23	0	101.16
AZO-16	***Ol***	41	50.31	41.82	8.82	0	0.01	0.00	0.01	0	0.23	0.00	101.20
AZO-16	***Ol***	34	50.17	40.49	8.59	0	0.00	0.02	0.07	0	0.23	0.00	99.59
AZO-16	***Ol***	45	49.99	40.59	8.59	0	0.01	0.01	0.09	0	0.22	0.00	99.50
AZO-16	***Ol***	49	50.53	41.04	9.34	0	0.00	0.00	0.03	0	0.15	0.01	101.10
AZO-16	***Srp***	15	38.39	42.29	3.17	0	1.71	0.01	0.34	0.03	0.11	0	86.06
AZO-16	***Srp***	39	38.03	42.56	3.21	0.00	1.32	0.01	0	0	0.11	0	86.00

Sample	Phase	N^O	MgO	SiO_2	FeO	Na_2O	Al_2O_3	CaO	Cr_2O_3	MnO	NiO	TiO_2	Total
AZO-16	***Srp***	17	37.74	40.16	3.79	0	2.10	0	0.82	0.05	0.11	0	84.77
AZO-16	***Srp***	13	38.19	41.98	3.51	0	1.38	0	0.47	0.04	0.11	0	85.69
AZO-16	***Srp***	42	38.90	43.85	3.33	0.00	1.29	0.00	0	0	0.10	0	87.48
AZO-16	***Srp***	48	38.62	43.09	3.57	0	1.54	0.05	0	0	0.10	0	86.97
AZO-16	***Srp***	47	37.74	43.42	3.30	0	1.47	0.01	0	0	0.10	0	86.98
AZO-16	***Srp***	44	37.71	43.13	3.68	0	2.36	0.01	0	0	0.09	0	86.98
AZO-16	***Srp***	36	39.11	42.90	3.23	0.00	1.61	0.02	0	0	0.09	0	86.95
AZO-16	***Srp***	18	38.03	43.48	2.78	0	1.06	0.01	0.03	0.06	0.09	0	85.55
AZO-16	***Srp***	46	38.41	41.47	3.53	0	1.92	0.01	0	0	0.09	0	85.43
AZO-16	***Srp***	35	39.12	44.28	3.25	0	1.45	0.02	0	0	0.09	0	88.21
AZO-18	***Amph***	3	23.90	58.10	1.29	0.06	0.10	13.52	0	0.09	0.04	0.01	97.10
AZO-18	***Amph***	5	24.31	58.15	1.33	0.06	0.10	13.29	0	0.09	0.04	0.01	97.39
AZO-18	***Amph***	1	24.36	58.44	1.35	0.06	0.12	13.39	0	0.08	0.05	0.01	97.87
AZO-18	***Amph***	9	24.03	58.27	1.44	0.07	0.13	13.05	0	0.06	0.11	0.01	97.18
AZO-18	***Amph***	6a	24.04	57.91	1.37	0.06	0.11	13.41	0	0.09	0.04	0.02	97.04
AZO-18	***Chl***	8a	34.04	34.82	3.85	0.01	10.02	0.01	1.59	0.03	0.13	0	84.50
AZO-18	***Mix***	1a	34.02	44.00	3.32	0.01	5.18	0.01	0.65	0.03	0.13	0	87.36
AZO-18	***Mix***	11	36.38	40.27	3.79	0	4.55	0.01	0.89	0.03	0.10	0	86.02
AZO-18	***Ol***	4	50.11	41.18	8.37	0	0.01	0.00	0	0.23	0.24	0	100.15

Sample	Phase	N^O	MgO	SiO_2	FeO	Na_2O	Al_2O_3	CaO	Cr_2O_3	MnO	NiO	TiO_2	Total
AZO-18	***Ol***	7a	49.98	40.72	8.20	0	0	0	0	0.22	0.22	0	99.36
AZO-18	***Ol***	9a	50.34	40.90	8.59	0	0	0.00	0	0.23	0.22	0	100.29
AZO-18	***Ol***	10	50.23	41.14	8.51	0	0	0.01	0	0.20	0.21	0	100.30
AZO-18	***Ol***	2a	50.09	41.03	8.38	0	0.00	0	0	0.21	0.21	0	99.94
AZO-18	***Ol***	6	48.55	38.36	8.25	0	0.10	1.06	0.06	0.19	0.21	0	96.79
AZO-18	***Ol***	3a	50.40	40.82	8.21	0	0.01	0	0	0.22	0.19	0	99.87
AZO-18	***Ol***	2	50.01	40.78	8.22	0	1.02	0.01	0.22	0.19	0.19	0	100.64
AZO-18	***Srp***	7	41.31	34.38	6.31	0	0.18	0.03	0	0.04	0.19	0	82.47
AZO-18	***Srp***	5a	35.62	40.09	3.40	0.01	3.99	0.01	1.18	0.07	0.11	0	84.49
AZO-18	***Tlc***	8	31.09	59.86	1.66	0.03	1.30	0.01	0.23	0.03	0.13	0	94.34
AZO-18	***Vein Lz***	4a	42.24	37.52	3.20	0.01	0.13	0.02	0	0.08	0.19	0	83.40
AZO-26	***Amph***	11	24.03	58.23	1.85	0.08	0.19	13.08	0	0.08	0.09	0.01	97.64
AZO-26	***Amph***	10	23.82	57.88	2.08	0.15	0.41	13.18	0	0.07	0.09	0.01	97.71
AZO-26	***Amph***	15	23.90	57.86	1.86	0.09	0.30	13.47	0	0.07	0.10	0.02	97.69
AZO-26	***Chl***	4	33.63	32.14	4.62	0.01	11.84	0.02	0	0	0.17	0.01	82.47
AZO-26	***Cr-Spi***	3	4.30	0.22	60.63	0	0.31	0.00	24.38	0.40	0.43	0	91.00
AZO-26	***Cr-Spi***	12	1.58	0.14	62.59	0	0.40	0.00	29.89	0.52	0.33	0	95.78
AZO-26	***Ol***	7	44.82	40.15	13.02	0	0.01	0.00	0.59	0.21	0.42	0	99.24
AZO-26	***Ol***	1	47.27	39.81	12.13	0	0	0.01	0.21	0.23	0.36	0	100.03

Sample	Phase	N^O	MgO	SiO_2	FeO	Na_2O	Al_2O_3	CaO	Cr_2O_3	MnO	NiO	TiO_2	Total
AZO-26	***Ol***	14	47.84	39.73	12.15	0	0	0.01	0	0.21	0.31	0	100.27
AZO-26	***Ol***	5	47.99	40.25	11.84	0	0	0.00	0	0.21	0.30	0	100.59
AZO-26	***Ol***	16	47.83	40.00	12.55	0	0	0	0	0.21	0.28	0	100.88
AZO-26	***Ol***	20	48.00	40.27	12.36	0	0	0.01	0	0.21	0.19	0	101.05
AZO-26	***Tlc***	13	30.74	61.87	1.27	0.05	0.14	0.01	0	0	0.22	0	94.31
AZO-26	***Tlc***	18	30.50	62.16	1.28	0.03	0.17	0.02	0	0	0.22	0	94.39
AZO-26	***Tlc***	6	30.56	62.22	1.39	0.03	0.14	0.01	0	0	0.20	0	94.56
AZO-26	***Tlc***	2	30.63	60.94	1.57	0.04	0.19	0.02	0	0.00	0.22	0	93.61
AZO-26	***Vein Lz***	19	40.46	39.95	3.58	0.01	0.18	0.02	0	0.04	0.34	0	84.58
AZO-26-S	***Srp***	7	30.72	31.80	7.21	0	15.39	0.02	0.12	0.08	0.21	0	85.56
AZO-26-S	***Srp***	11	30.33	31.14	7.87	0	15.65	0.02	0.40	0.09	0.20	0	85.70
AZO-26-S	***Srp***	10	30.54	31.11	7.17	0	15.96	0.02	0.14	0.09	0.20	0	85.22
AZO-26-S	***Srp***	4	30.16	31.72	7.55	0	16.03	0.01	0.13	0.09	0.20	0	85.90
AZO-26-S	***Srp***	9	30.34	31.04	7.49	0	16.16	0.01	0.11	0.08	0.20	0	85.43
AZO-26-S	***Srp***	2	29.84	30.33	7.78	0	16.65	0.01	0.13	0.09	0.20	0	85.04
AZO-26-S	***Srp***	3	28.74	29.62	7.90	0	15.35	0.02	0.09	0.10	0.19	0	82.02
AZO-26-S	***Srp***	12	29.63	30.77	8.05	0	15.57	0.01	0.42	0.08	0.19	0	84.74
AZO-26-S	***Srp***	8	29.83	30.73	7.90	0	16.13	0.01	0.07	0.10	0.19	0	84.96
AZO-26-S	***Srp***	1	29.79	30.07	7.84	0	16.51	0.02	0.16	0.08	0.19	0	84.66

Sample	Phase	N^O	MgO	SiO_2	FeO	Na_2O	Al_2O_3	CaO	Cr_2O_3	MnO	NiO	TiO_2	Total
AZO-26-S	***Srp***	5	30.09	31.29	7.46	0	16.59	0	0	0.10	0.20	0.01	85.75
AZO-26-S	***Srp***	6	30.10	31.26	7.82	0	17.02	0	0	0.10	0.21	0.02	86.53
PR01	***Chl***	22	33.60	31.82	3.11	0	13.38	0.02	2.71	0.02	0.30	0	84.97
PR01	***Chl***	26	34.16	32.88	3.15	0.02	12.75	0.02	2.52	0	0.21	0	85.73
PR01	***Chl***	27	38.72	43.10	2.83	0.01	1.23	0.01	0.18	0.03	0.14	0	86.24
PR01	***Chl***	23	33.00	32.23	3.09	0	14.28	0.03	0	0	0.22	0.02	82.88
PR01	***Chl***	11	33.10	31.53	3.37	0.01	14.67	0.01	0	0	0.20	0.03	82.95
PR01	***Ni-Spi***	20	0	0.02	40.83	0	0	0	0	0	40.63	0	82.47
PR01	***Ol***	21	51.55	41.17	7.45	0	0.01	0	0	0.16	0.53	0	100.88
PR01	***Ol***	24	51.11	41.08	7.51	0	0	0	0	0.16	0.51	0	100.37
PR01	***Ol***	10	50.96	41.22	7.64	0	0.01	0.00	0.02	0.16	0.40	0	100.43
PR01	***Ol***	12	50.90	41.17	7.68	0	0	0.01	0.02	0.16	0.34	0	100.27
PR01	***Ol***	29	51.23	41.31	7.72	0	0	0	0.02	0.16	0.29	0	100.73
PR01	***Ol***	17	51.21	40.90	7.54	0	0	0.01	0	0.15	0.24	0	100.06
PR01	***Ol***	18	51.09	41.22	7.65	0	0	0	0	0.15	0.24	0	100.36
PR01	***Ol***	15	50.65	41.65	7.57	0	0	0	0	0.15	0.24	0	100.27
PR01	***Ol***	13	51.04	41.17	7.69	0	0	0	0	0.16	0.21	0	100.28
PR01	***Ol***	16	51.36	41.02	7.57	0	0.01	0	0	0.16	0.18	0	100.29
PR01	***Ol***	19	50.93	40.97	7.43	0	0.01	0.01	0	0.16	0.18	0	99.68

Sample	Phase	N^O	MgO	SiO_2	FeO	Na_2O	Al_2O_3	CaO	Cr_2O_3	MnO	NiO	TiO_2	Total
PR01	***Ol***	14	51.45	40.90	7.14	0	0	0	0.02	0.15	0.16	0	99.82
PR02	***Amph***	63	31.46	64.84	1.03	0.04	0.17	0	0	0	0.14	0.01	97.69
PR02	***Amph***	58	31.02	62.88	1.34	0.03	0	0.01	0	0	0.16	0.02	95.53
PR02	***Amph***	50	31.06	63.49	1.42	0.03	0.15	0	0.02	0.02	0.15	0.01	96.39
PR02	***Amph***	59	31.26	64.33	1.06	0.04	0.13	0	0.03	0	0.13	0.02	97.04
PR02	***Chl***	65	33.70	33.08	3.35	0.02	13.32	0.02	0	0	0.21	0.01	83.73
PR02	***Chl***	55	35.01	36.02	3.42	0.02	10.23	0	0	0.02	0.14	0.01	84.87
PR02	***Chl***	53	33.67	33.02	4.11	0.01	12.65	0.01	0	0	0.18	0.02	83.68
PR02	***Chl***	3	33.92	33.73	3.94	0.01	13.11	0.01	0	0	0.17	0.02	84.90
PR02	***Chl***	11	33.74	33.06	3.99	0.00	12.56	0.01	0	0	0.14	0.02	83.52
PR02	***Chl***	61	34.08	42.31	3.17	0.02	8.71	0.01	0.95	0.02	0.16	0.02	89.45
PR02	***Chl***	56	33.65	33.73	3.64	0.01	12.72	0.01	0	0	0.18	0.02	83.99
PR02	***Ol***	1	49.95	40.86	8.44	0	0.01	0.00	0.01	0	0.32	0	99.60
PR02	***Ol***	52	51.31	41.87	8.39	0	0	0	0.00	0.15	0.35	0.00	102.08
PR02	***Ol***	13	49.91	41.05	7.77	0	0.01	0.00	0.01	0	0.28	0.00	99.03
PR02	***Ol***	54	51.09	41.98	8.50	0	0	0	0.01	0.15	0.35	0.00	102.07
PR02	***Ol***	8	49.98	41.23	8.45	0	0.00	0.00	0.01	0	0.31	0.00	99.98
PR02	***Ol***	12	50.09	40.98	8.29	0	0.02	0.00	0.02	0	0.28	0.00	99.68
PR02	***Ol***	57	50.63	41.08	8.78	0	0.01	0	0.01	0.17	0.37	0.00	101.06

Sample	Phase	N^O	MgO	SiO_2	FeO	Na_2O	Al_2O_3	CaO	Cr_2O_3	MnO	NiO	TiO_2	Total
PR02	***Ol***	6	50.37	41.19	8.18	0	0	0	0.01	0	0.28	0.00	100.02
PR02	***Ol***	64	51.19	41.72	8.29	0	0	0	0.01	0.16	0.34	0.00	101.73
PR02	***Ol***	60	50.70	40.88	8.46	0	0.01	0	0.02	0.15	0.29	0.00	100.53
PR02	***Ol***	51	51.08	41.35	9.00	0	0.01	0	0.01	0.16	0.33	0.00	101.95
PR02	***Srp***	16	39.62	43.62	3.43	0.01	1.37	0.00	0	0	0.13	0	88.18
PR02	***Srp***	5	38.53	43.63	4.02	0.00	1.91	0.00	0	0	0.12	0	88.23
PR02	***Srp***	15	40.01	43.88	4.08	0.00	0.98	0.00	0	0	0.12	0	89.07
PR02	***Srp***	4	39.09	43.81	3.56	0	1.03	0.00	0	0	0.11	0	87.62
PR02	***Tlc***	14	31.38	63.47	1.05	0.03	0.13	0.00	0.02	0	0.15	0.01	96.29
PR02	***Tlc***	7	31.88	59.59	0.00	0.03	0.26	0.01	0	0	0.16	0.01	91.95
PR02	***Tlc***	2	30.52	63.77	0.00	0.02	0.07	0.01	0	0	0.17	0.01	94.58
PR02	***Tlc***	9	30.63	63.45	0.00	0.02	0.07	0.01	0	0	0.17	0.01	94.36
PR02	***Tlc***	10	30.43	63.22	0.00	0.04	0.12	0.02	0	0	0.17	0.02	94.01
PR08	***Amph***	31	23.61	57.70	1.39	0.10	0.26	13.60	0	0.07	0.07	0.07	96.87
PR08	***Amph***	35	23.69	57.72	1.35	0.09	0.26	13.58	0	0.07	0.05	0.07	96.90
PR08	***Amph***	25	24.05	58.38	1.36	0.10	0.34	13.56	0.07	0	0.06	0.07	98.01
PR08	***Amph***	40	23.62	57.31	1.33	0.10	0.28	13.64	0	0.06	0.08	0.08	96.50
PR08	***Amph***	44	23.60	57.17	1.87	0.13	0.33	13.22	0	0.07	0.07	0.09	96.55
PR08	***Amph***	36	23.59	57.26	1.40	0.10	0.26	13.35	0	0.07	0.07	0.09	96.20

Sample	Phase	N^O	MgO	SiO_2	FeO	Na_2O	Al_2O_3	CaO	Cr_2O_3	MnO	NiO	TiO_2	Total
PR08	***Amph***	17	23.96	58.49	1.56	0.13	0.38	13.58	0.04	0	0.08	0.10	98.34
PR08	***Amph***	30	23.55	57.74	1.36	0.12	0.35	13.71	0	0.06	0.06	0.10	97.06
PR08	***Amph***	42	23.63	57.42	1.71	0.16	0.50	13.35	0	0.06	0.06	0.12	97.01
PR08	***Chl***	22	34.98	34.73	3.50	0.00	11.81	0.02	0	0	0.13	0.03	85.20
PR08	***Chl***	34	33.97	33.29	3.37	0.01	13.24	0.01	0	0	0.18	0.03	84.12
PR08	***Chl***	46	34.44	33.25	3.52	0	13.78	0	0	0.02	0.16	0.03	85.23
PR08	***Chl***	28	34.50	33.66	3.77	0.01	13.75	0.02	0	0	0.18	0.04	85.92
PR08	***Chl***	21	34.46	33.76	3.72	0.00	13.20	0.02	0	0	0.17	0.04	85.37
PR08	***Chl***	39	34.05	33.19	3.70	0	13.59	0.01	0	0	0.19	0.04	84.79
PR08	***Chl***	20	35.10	34.08	3.85	0.00	13.01	0.01	0	0	0.13	0.04	86.23
PR08	***Chl***	49	34.29	33.03	3.55	0	13.30	0.01	0	0	0.17	0.04	84.41
PR08	***Chl***	41	33.76	32.69	3.36	0.01	12.69	0.23	0	0.07	0.17	0.04	83.01
PR08	***Chl***	32	33.19	31.83	3.55	0	13.64	0.08	0	0.03	0.16	0.05	82.54
PR08	***Chl***	43	33.50	32.73	3.58	0	13.50	0.01	0	0	0.17	0.05	83.55
PR08	***Chl***	29	34.24	33.50	3.45	0.01	13.14	0.03	0	0	0.18	0.06	84.60
PR08	***Ol***	38	50.33	40.39	8.18	0	0	0.01	0	0.25	0.33	0	99.54
PR08	***Ol***	33	49.98	40.76	8.13	0	0.04	0.02	0	0.21	0.33	0	99.48
PR08	***Ol***	37	50.42	40.51	8.29	0	0.01	0	0	0.23	0.33	0	99.84
PR08	***Ol***	45	50.25	40.76	8.06	0	0	0.01	0	0.25	0.32	0	99.65

Sample	Phase	N^O	MgO	SiO_2	FeO	Na_2O	Al_2O_3	CaO	Cr_2O_3	MnO	NiO	TiO_2	Total
PR08	***Ol***	48	50.60	40.46	8.59	0	0	0.00	0	0.24	0.31	0	100.22
PR08	***Ol***	47	50.25	41.07	8.61	0	0	0.01	0	0.24	0.30	0	100.50
PR08	***Ol***	27	50.21	41.00	8.21	0	0	0.00	0.01	0	0.33	0.00	99.78
PR08	***Ol***	23	49.46	41.05	8.22	0	0.00	0.01	0.00	0	0.32	0.01	99.08
PR08	***Ol***	18	49.49	41.21	8.34	0	0	0.01	0.01	0	0.32	0.01	99.37
PR08	***Ol***	19	49.68	41.13	8.17	0	0.02	0.00	0.00	0	0.32	0.01	99.34
PR08	***Ol***	26	49.63	41.35	8.47	0	0.00	0.01	0.00	0	0.35	0.02	99.87
PR08	***Ol***	24	49.89	41.38	8.41	0	0.00	0.00	0.01	0	0.34	0.02	100.09

B.2.2 Trace elements and Boron isotopes

Graphs

There are two types of graph presented here: Single graphs comparing alike phases from different samples. The purpose of these graphs is to display differences between samples. Multiple graphs comparing all phases from the same sample. The purpose of these graphs is to display differences between phases within a sample and across the sample set.

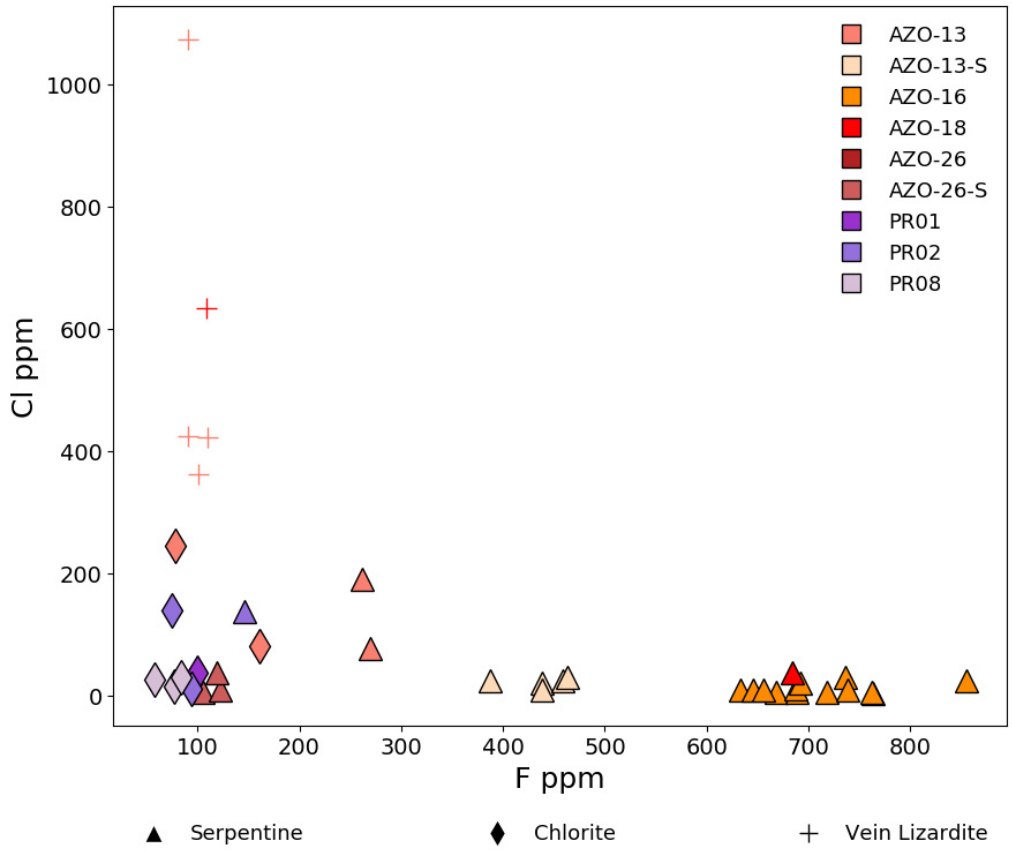

Figure B.8: F vs Cl for serpentinite phases serpentine, chlorite and vein lizardite. Vein lizardite has high F but low Cl, whereas the antigorite serpentine has high F and low Cl, especially those from the AZO samples. Chlorite contains low Cl and F.

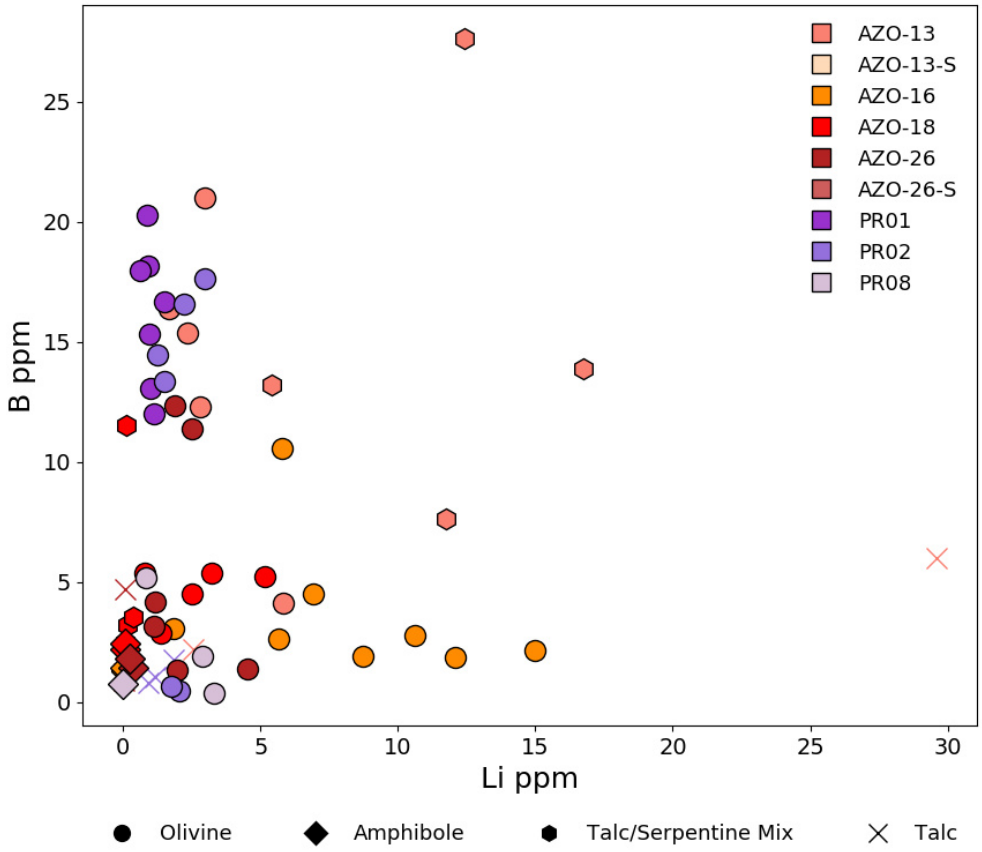

Figure B.9: Li vs B for phases formed during the formation of the Bergell aureole, including: talc, olivine, amphibole and the talc/serpentine mixture.

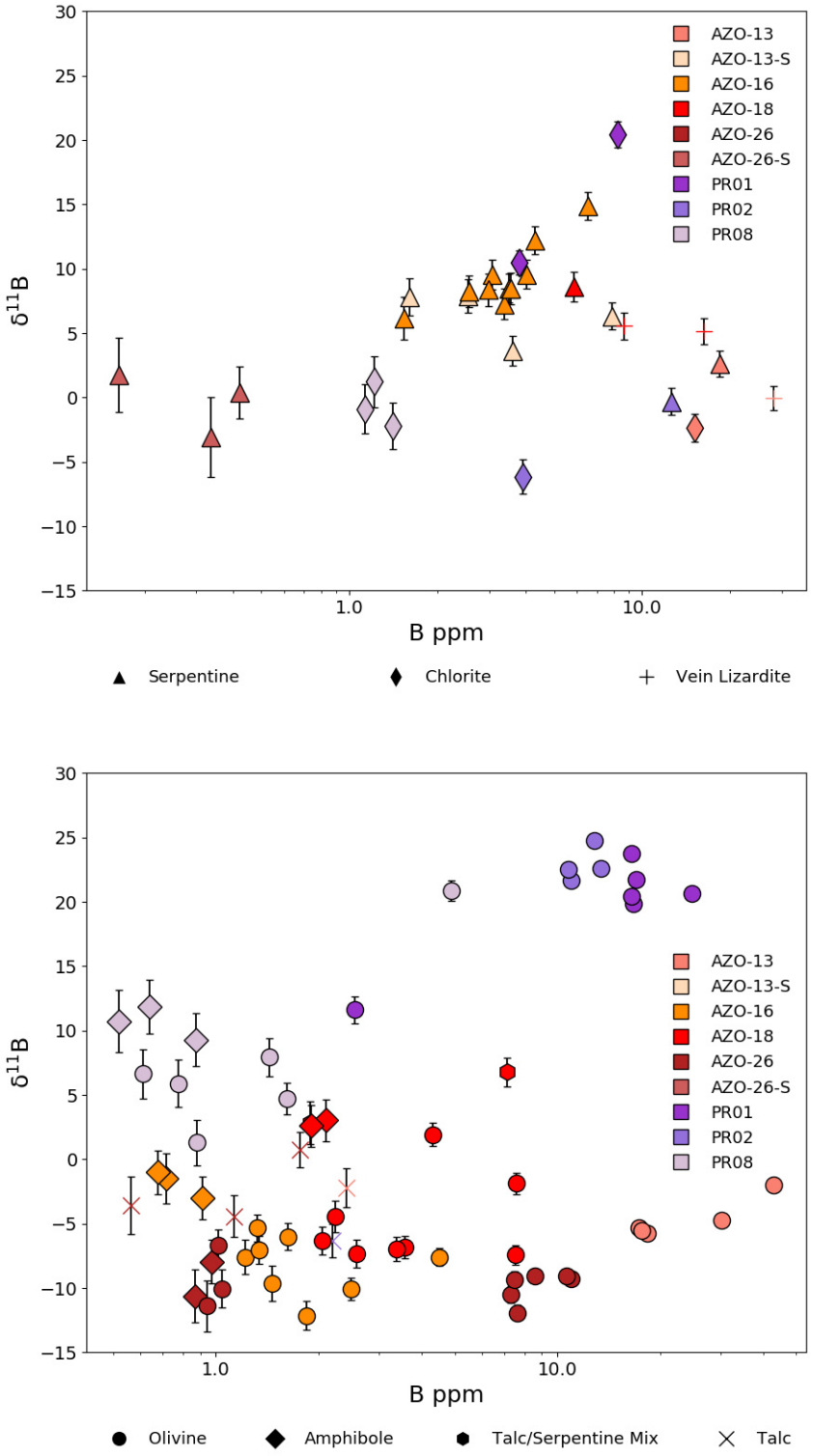

Figure B.10: (Above) δ^{11}B vs B for serpentinite phases serpentine and chlorite. (Below) δ^{11}B vs B for phases formed during the formation of the Bergell aureole, including: talc, olivine, amphibole and the talc/serpentine mixture.

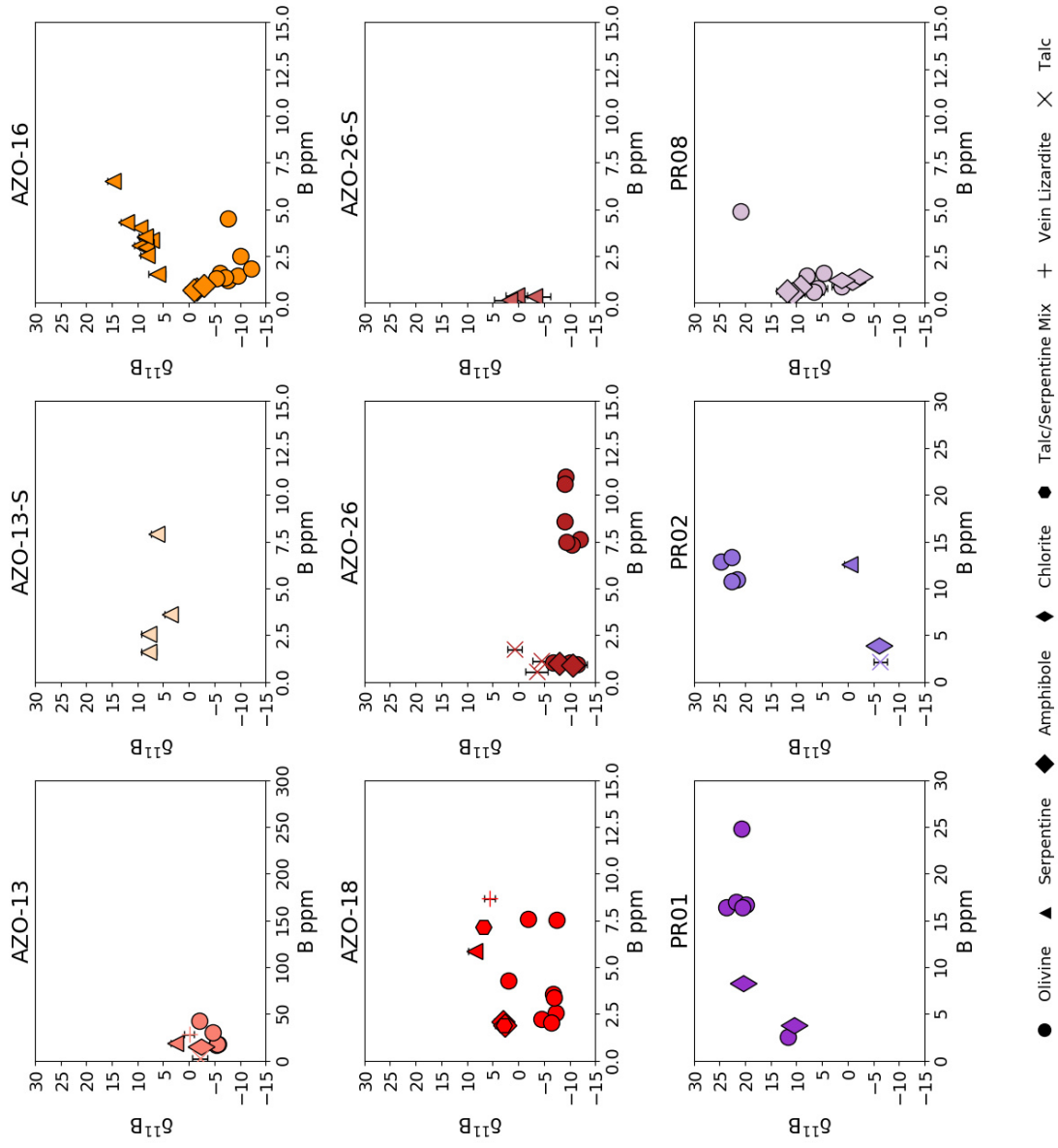

Figure B.11: δ^{11}B vs [B] for all phases in each sample. Srp has the highest δ^{11}B of all phases in the AZO samples. Whereas Ol has the highest δ^{11}B of all phases in the PR samples.

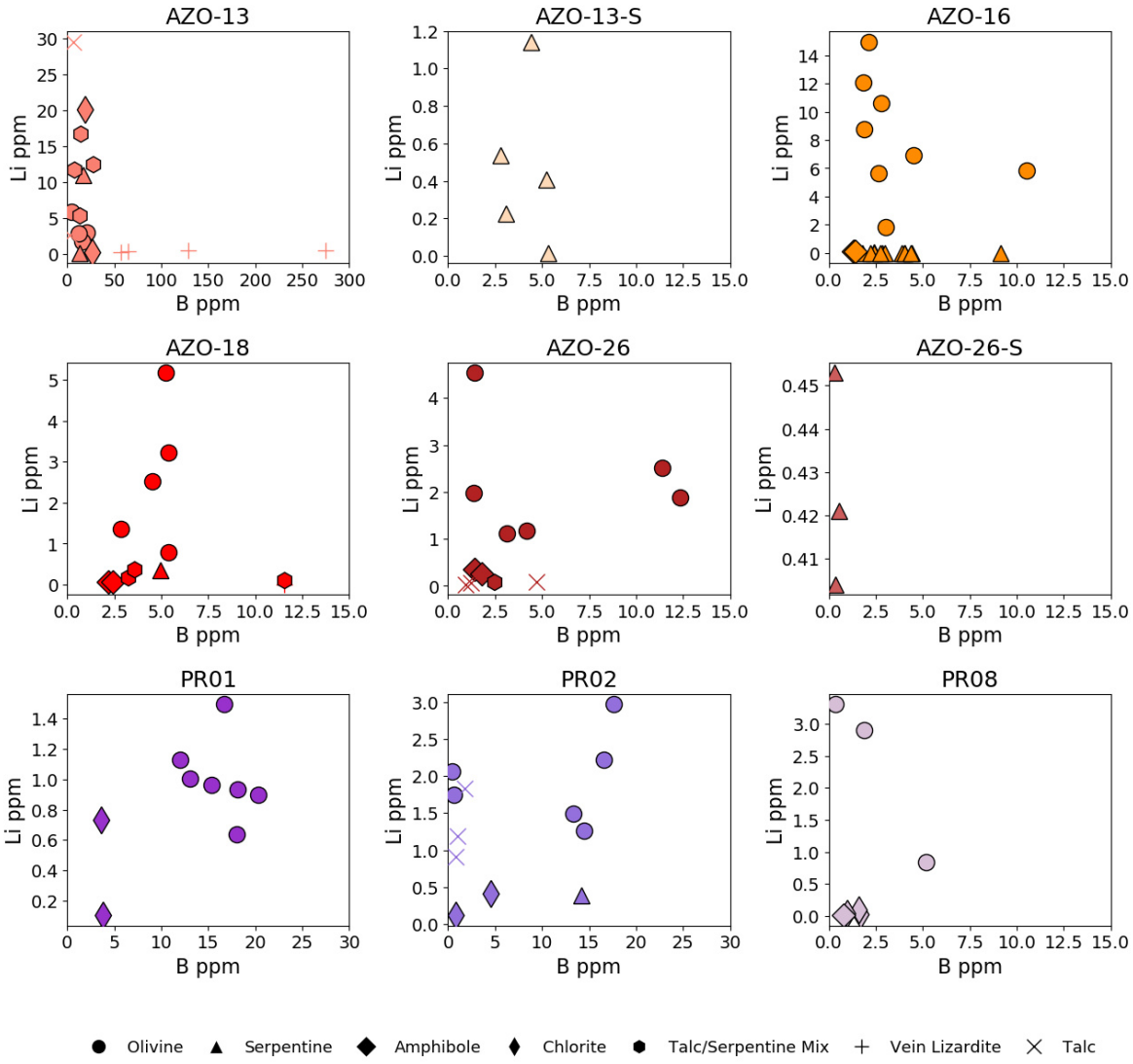

Figure B.12: B vs Li for all phases in each sample. There is no correlation between B and Li for any phase in any sample.

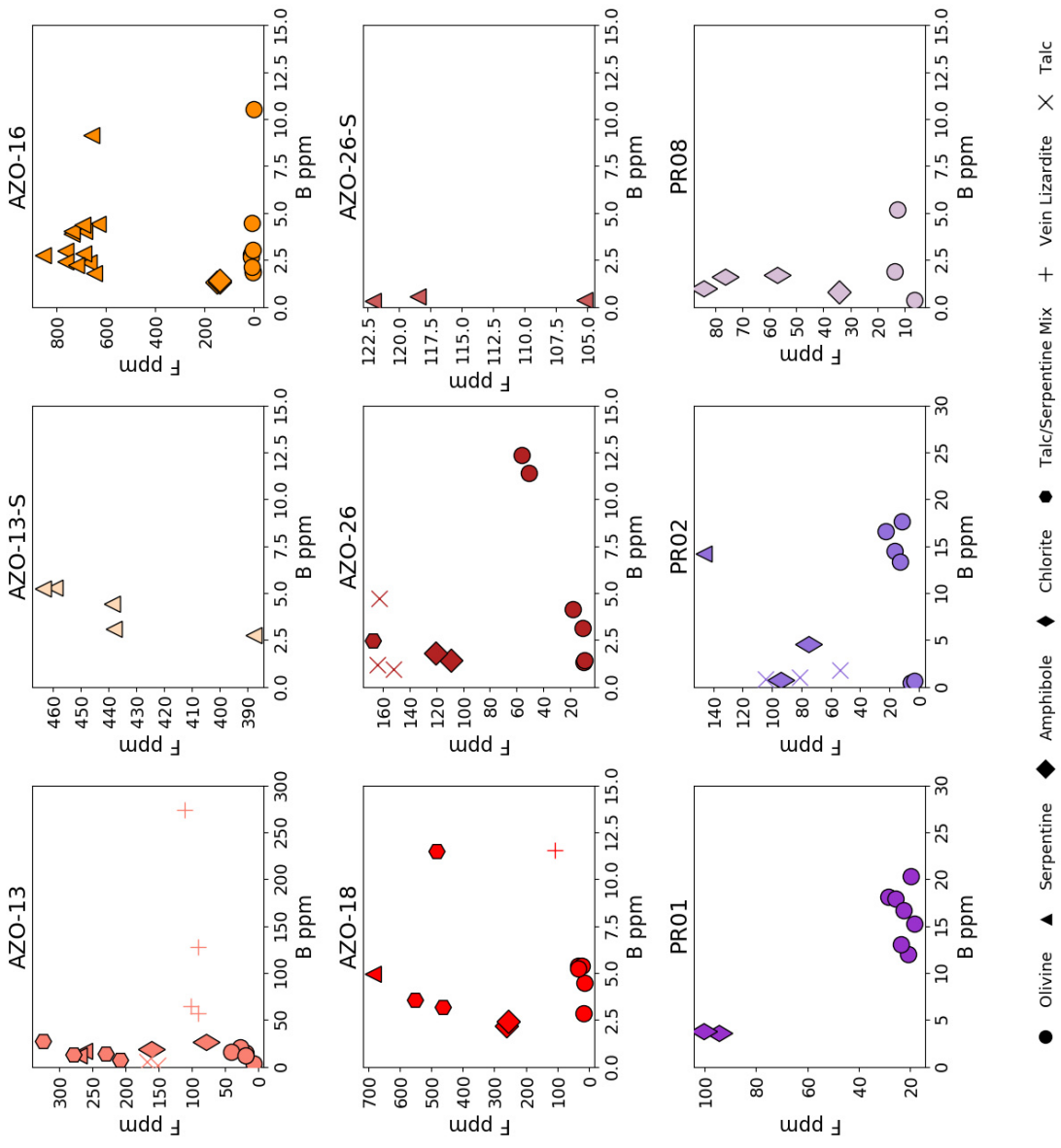

Figure B.13: B vs F for all phases in each sample.

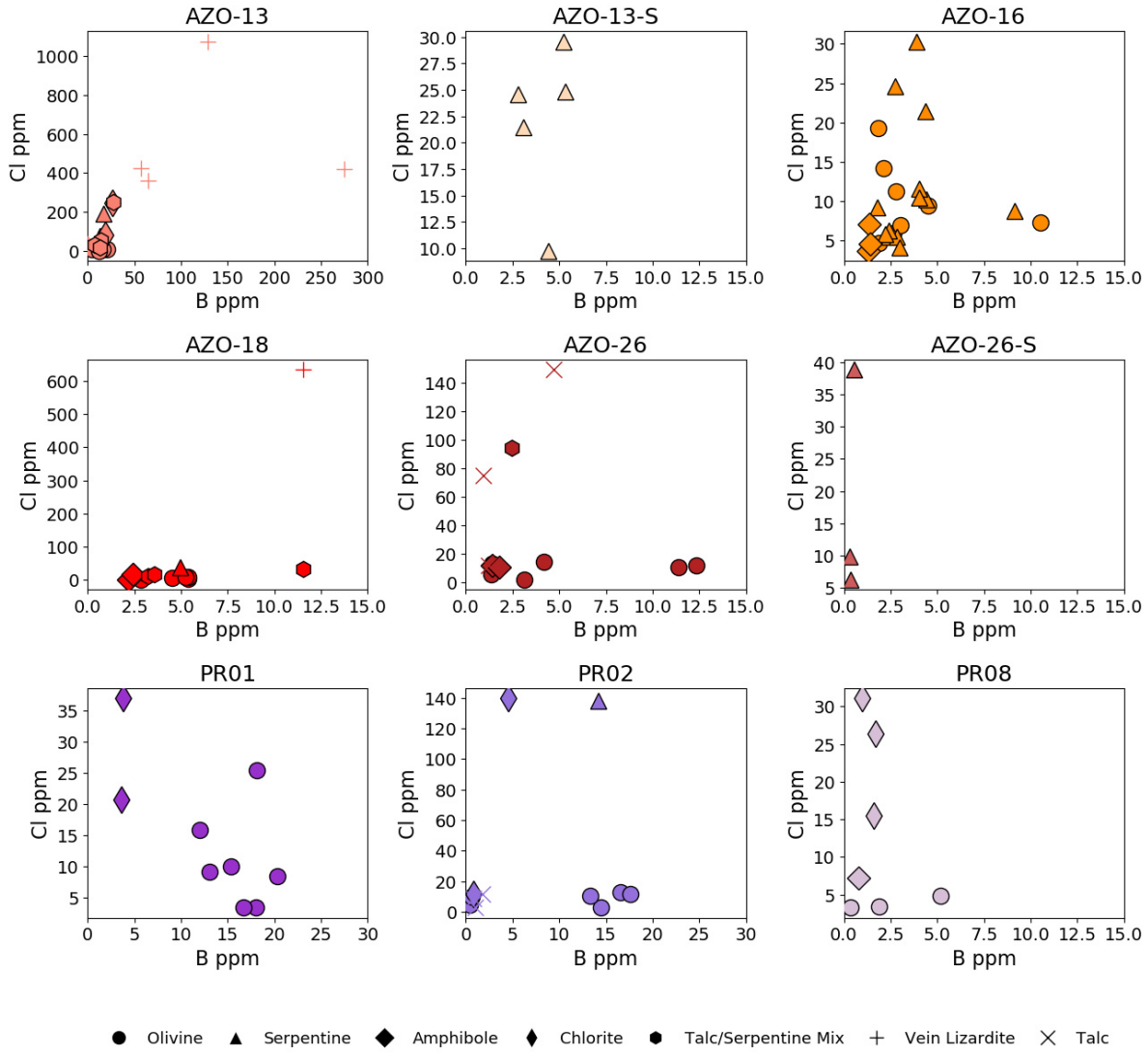

Figure B.14: B vs Cl for all phases in each sample

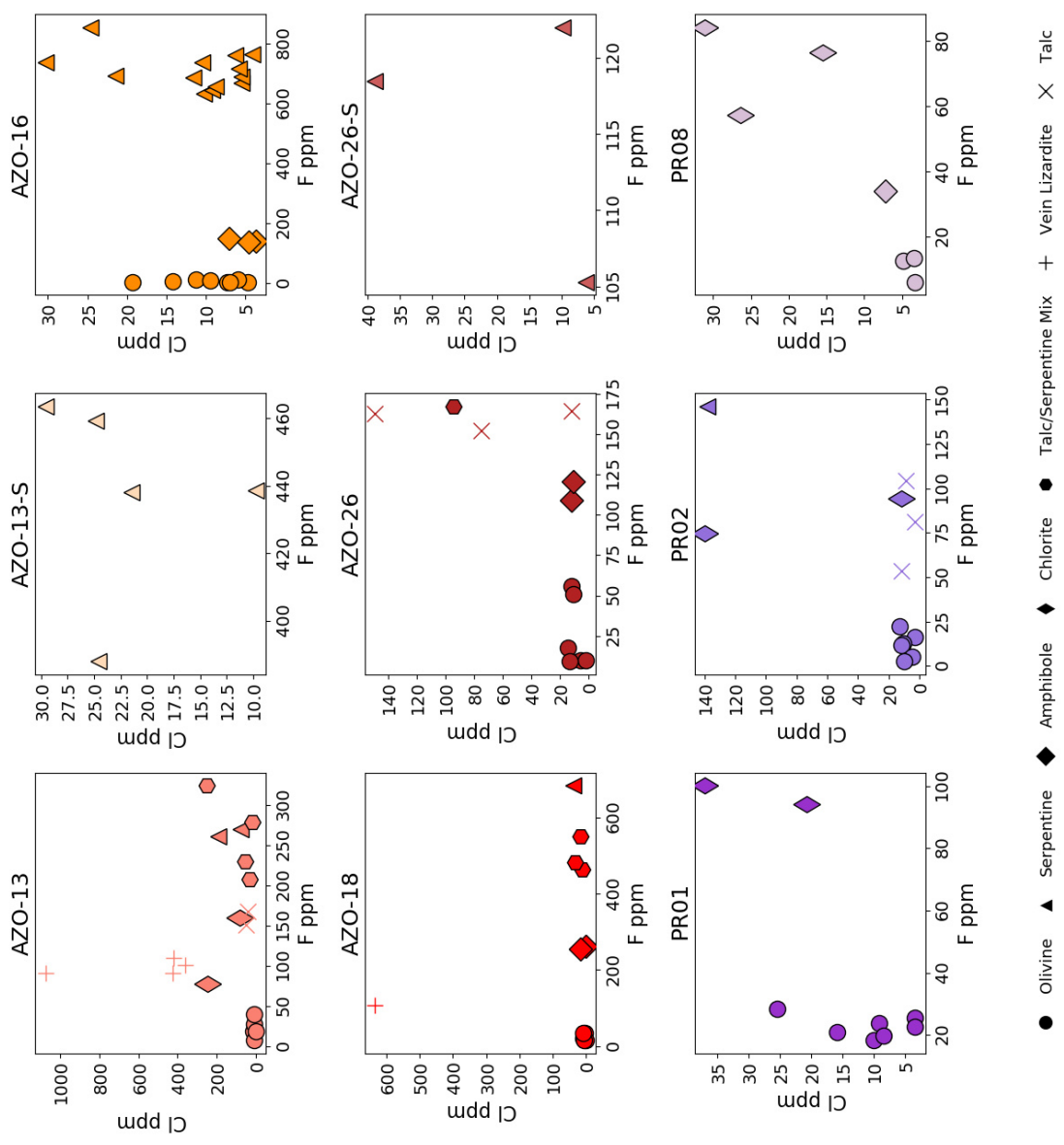

Figure B.15: Cl vs F for all phases in each sample

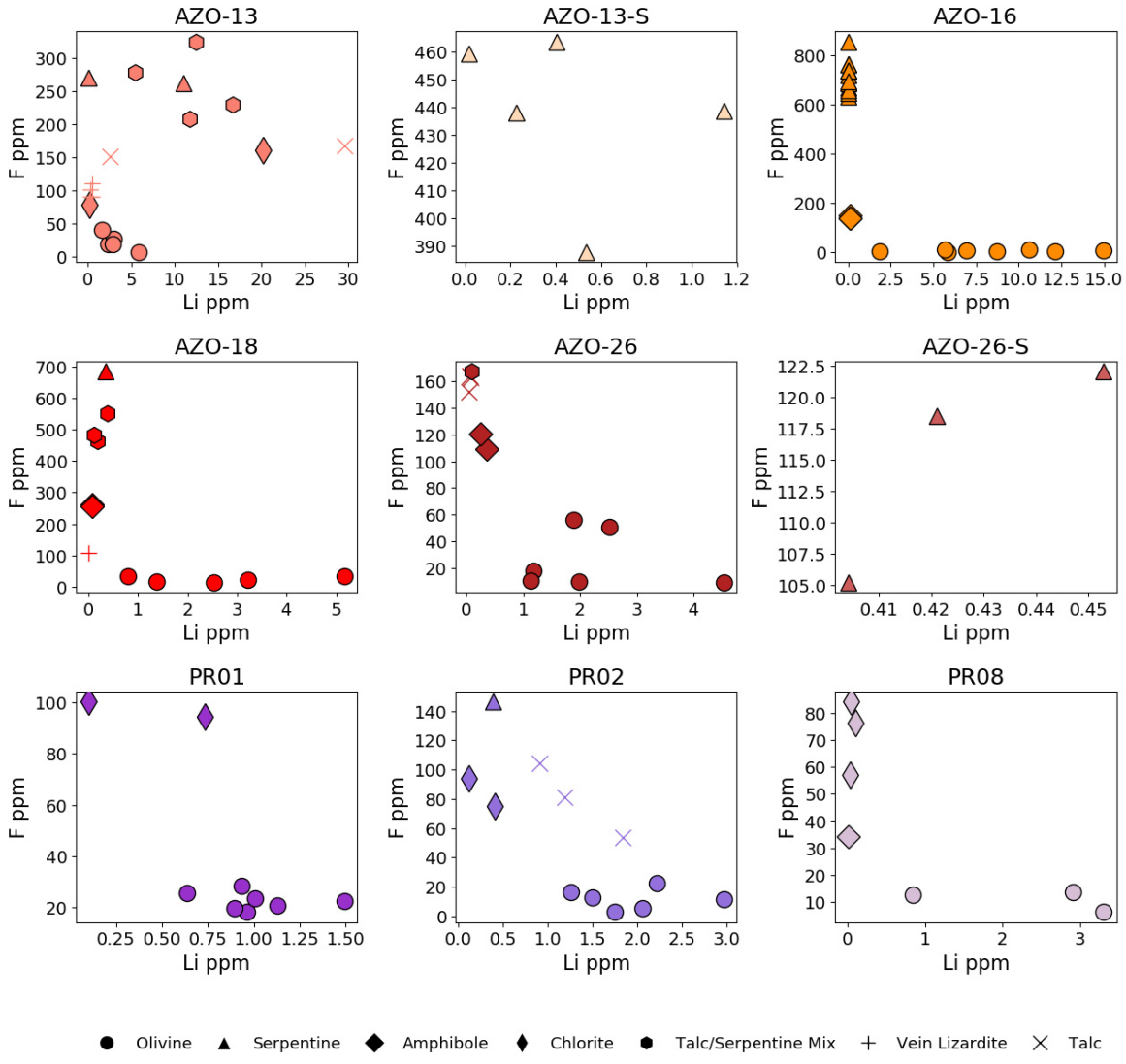

Figure B.16: Li vs F for all phases in each sample. In most samples phases that have significant concentrations of F (>10 ppm: Srp, Amph and Chl) also have negligible Li, whereas the opposite is true for Ol, which is the only phase to contain significant Li (>1 ppm). The exception is talc which in PR02 plots in between the two groups and in other samples it joins the majority of other phases. The high F phases are all hydrous, whereas Ol is the only anhydrous phase.

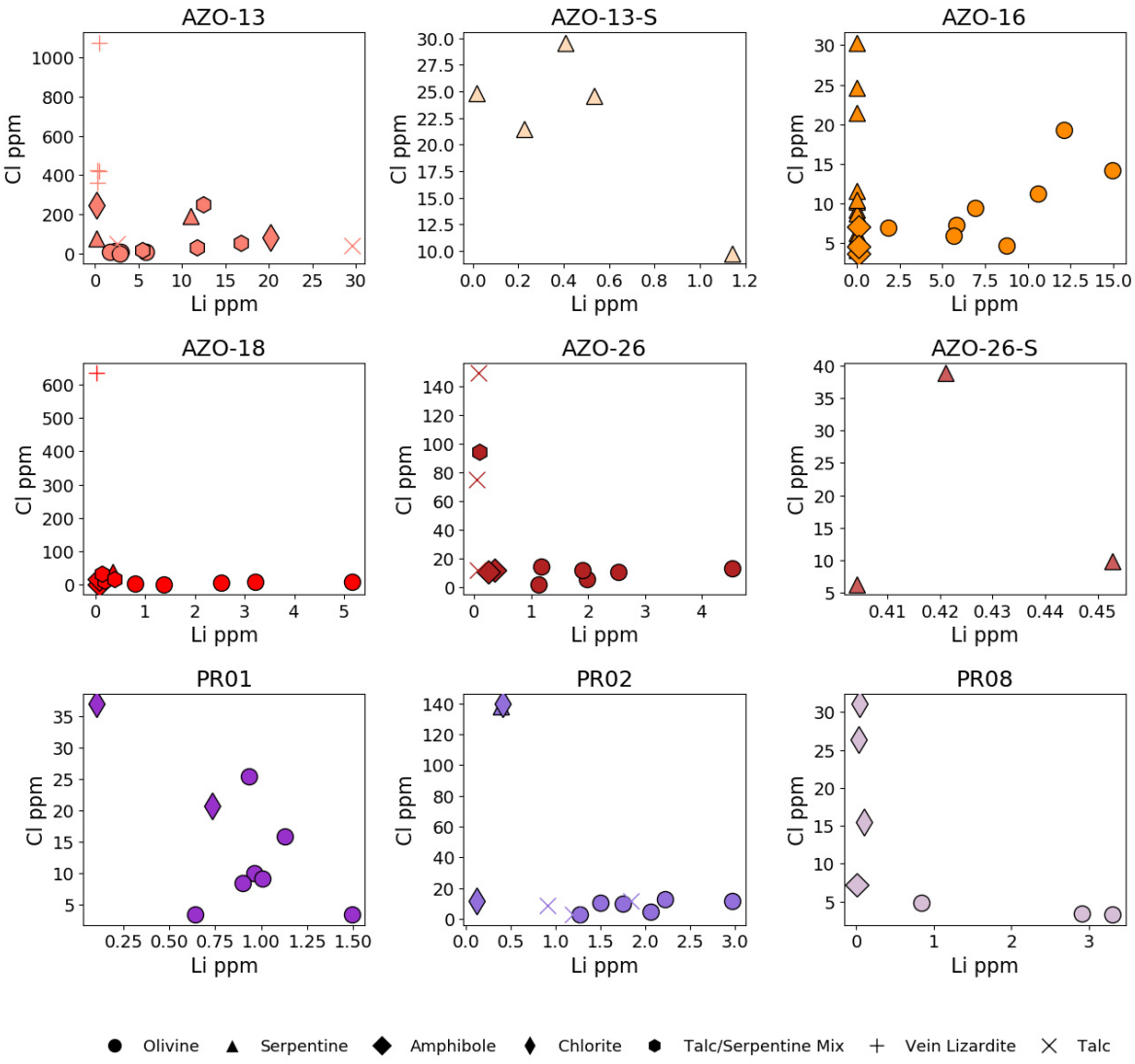

Figure B.17: Li vs Cl for all phases in each sample

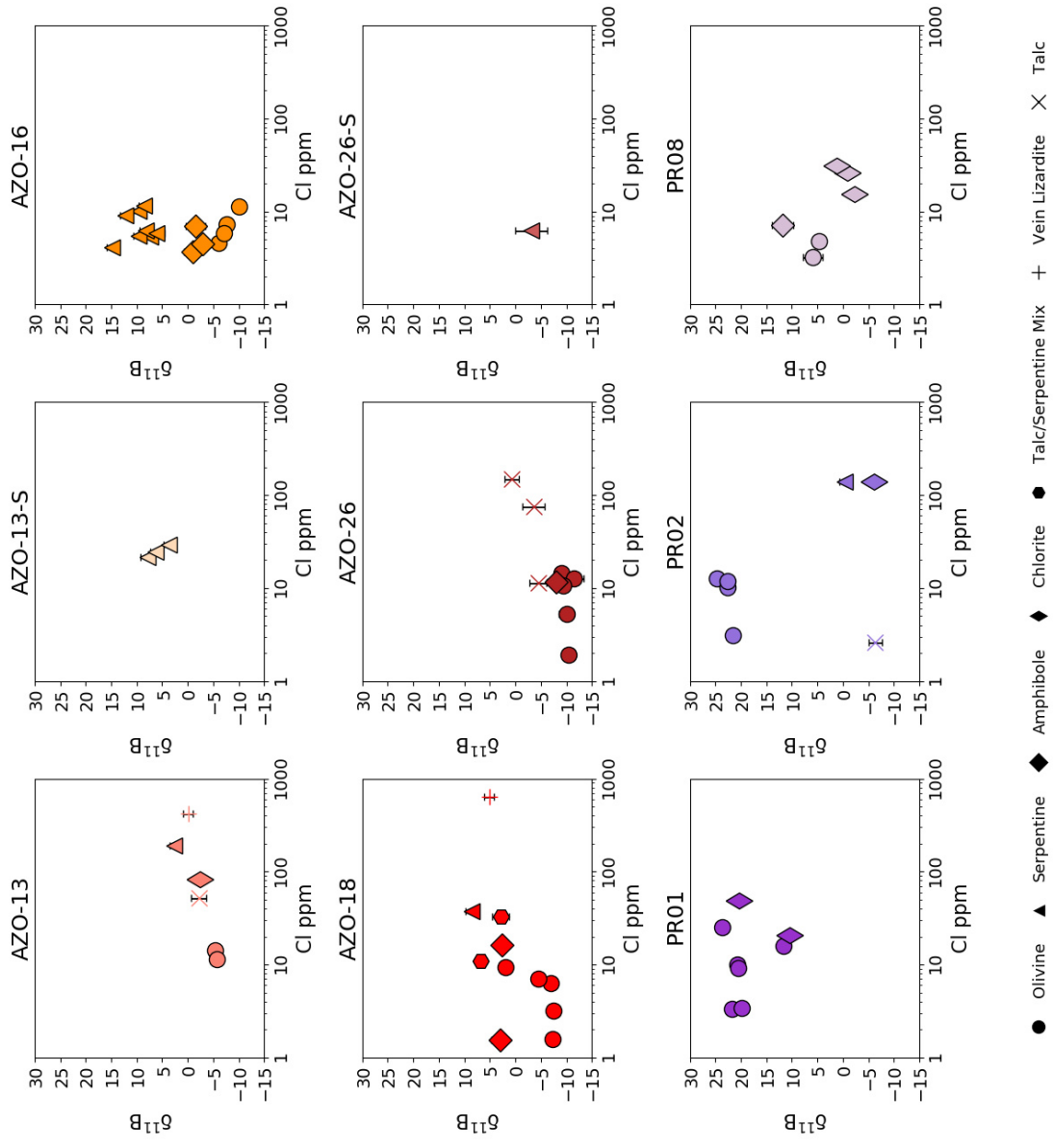

Figure B.18: δ^{11}B vs Cl for all phases in each sample.

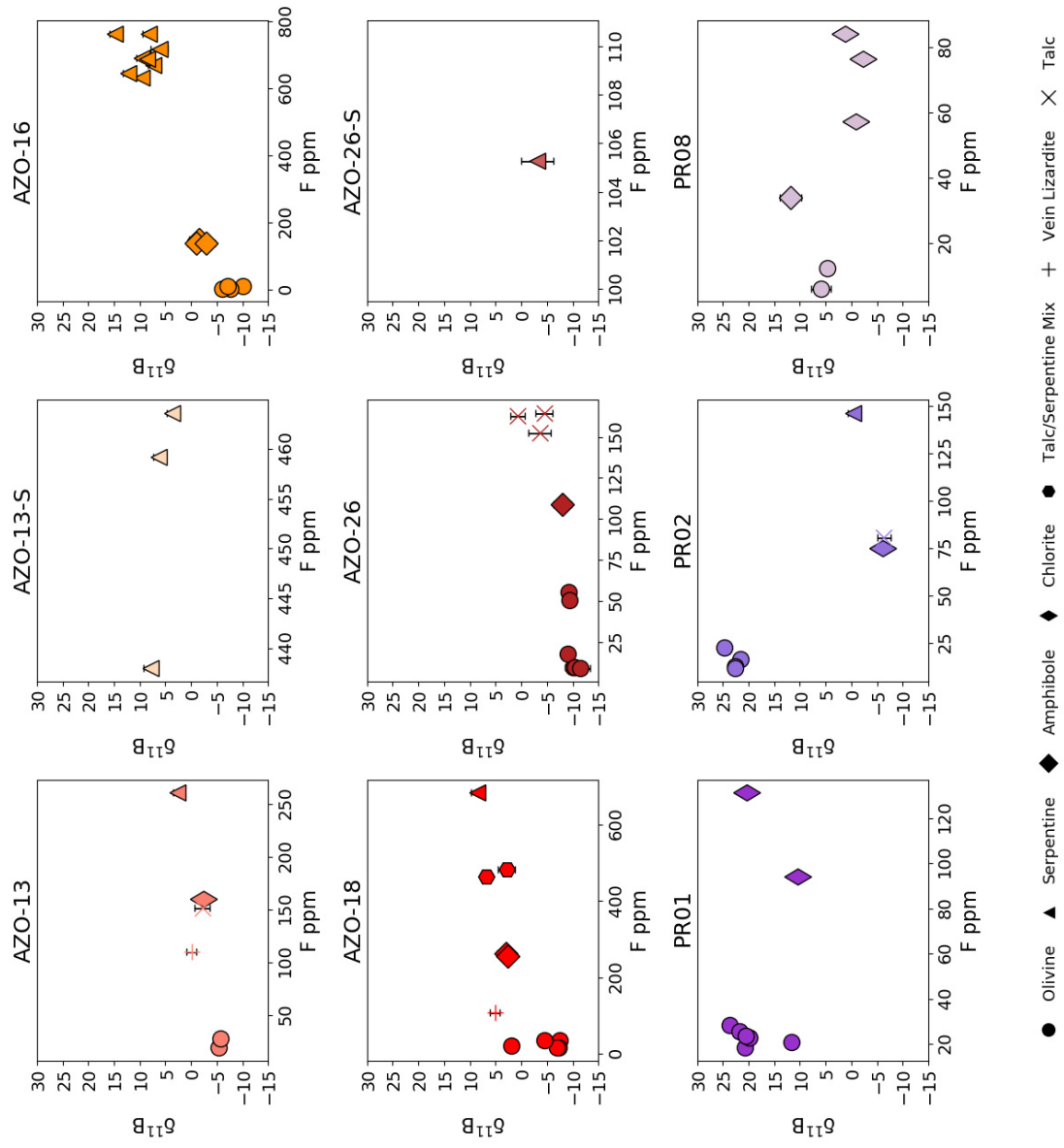

Figure B.19: δ^{11}B vs F for all phases in each sample. The correlation between δ^{11}B and F seen in sample AZO-16 and PR02 is an artefact of difference in δ^{11}B between Ol and Srp combined with the high concentration of F seen in Valmalenco Srps.

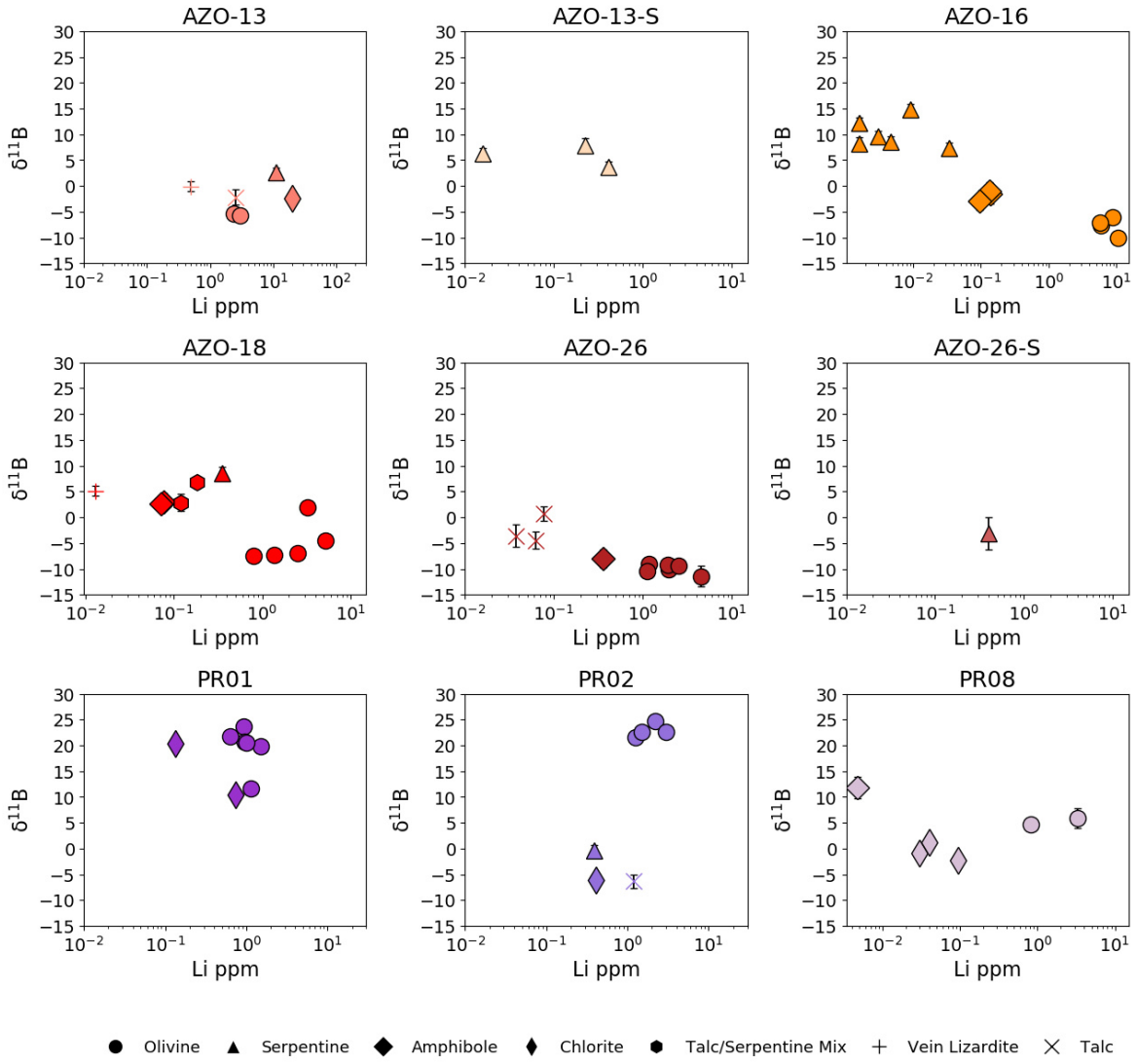

Figure B.20: δ^{11}B vs Li for all phases in each sample. There is no correlation between δ^{11}B and Li in any phase in any sample.

Data table

Table B.7: Valmalenco trace and boron isotope data collected on the SIMS 4f and SIMS 1270 respectively. Data N^{o}s can be located on the pit images in Appendix B.

Sample	Phase	1270 pit N^o	B (1270)	δ^{11}B	error	4f pit N^o	H_2O	Li	B	F	Cl
AZO-13	VEIN LZ	64	15.46	-0.1‰	0.5‰	8	14.38	0.5	274.37	110.37	422.37
AZO-13	OL	65	9.52	-5.3‰	0.5‰	29	0.05	2.36	15.36	18.99	14.28
AZO-13	OL	66	10.07	-5.8‰	0.5‰	27	0.01	2.96	20.98	27.67	11.35
AZO-13	CHL	67	8.3	-2.3‰	0.6‰	6	9.42	20.14	19.18	160.4	81.87
AZO-13	OL	68	9.72	-5.5‰	0.5‰						
AZO-13	OL	69	16.58	-4.7‰	0.4‰						
AZO-13	SRP	70	10.13	2.6‰	0.6‰	24	14.31	11.01	16.63	261.29	190.98
AZO-13	OL	71	23.59	-2.0‰	0.6‰						
AZO-13	TLC	72	1.33	-2.2‰	1.2‰	31	5.37	2.56	2.19	151.32	51.69
AZO-13	CHL					1	13.17	0.21	26.85	77.88	245.62
AZO-13	SRP					2	13.29	0.12	12.72	269.76	78.28
AZO-13	VEIN LZ					3	13.97	0.49	128.26	90.67	1074.92
AZO-13	VEIN LZ					4	14.61	0.23	57.19	90.8	424.36
AZO-13	VEIN LZ					5	12.95	0.27	64.85	100.98	361.95
AZO-13	OL					30	0	5.82	4.12	7.29	9.01

Sample	Phase	1270 pit N^o	B (1270)	δ^{11}B	error	4f pit N^o	H_2O	Li	B	F	Cl
AZO-13	MIX					32	10.61	12.42	27.64	324.43	250.62
AZO-13	OL					33	0.14	1.66	16.36	40.53	8.24
AZO-13	TLC					34	6.49	29.58	6	167.31	40.13
AZO-13	MIX					35	8.89	16.73	13.9	229.55	55.16
AZO-13	MIX					36	6.89	11.75	7.64	207.97	33.21
AZO-13	MIX					37	10.87	5.39	13.21	278.44	19.7
AZO-13	OL					38	0.03	2.81	12.31	19.21	1.99
AZO-13-S	SRP	1	2.18	7.9‰	1.0‰	13	14.4	0.23	3.1	437.97	21.46
AZO-13-S	SRP	2	6.75	6.3‰	0.6‰	9	12.7	0.02	5.3	459.22	24.83
AZO-13-S	SRP	3	3.09	3.6‰	0.8‰	10	16.11	0.41	5.23	463.6	29.59
AZO-13-S	SRP	4	1.38	7.8‰	1.2‰						
AZO-13-S	SRP					11	13.19	1.14	4.43	438.68	9.76
AZO-13-S	SRP					12	14.72	0.54	2.78	387.9	24.58
AZO-16	SRP	8	3.05	7.3‰	0.8‰	58	11.98	0.03	2.38	668.84	5.43
AZO-16	OL	9	2.24	-10.1‰	0.9‰	59	0.1	10.62	2.78	11.06	11.31
AZO-16	SRP	10	3.64	9.6‰	0.7‰	60	12.55	0	4.41	632.76	10.22
AZO-16	OL	11	4.06	-7.6‰	0.7‰	127	0	5.81	10.54	2.71	7.25
AZO-16	SRP	12	2.78	9.6‰	0.8‰	123	14.25	0	2.86	689.25	5.43
AZO-16	SRP	13	3.16	8.5‰	0.8‰	121	12.97	0	4.01	687.87	11.61

Sample	Phase	1270 pit N^o	B (1270)	δ^{11}B	error	4f pit N^o	H_2O	Li	B	F	Cl
AZO-16	OL	14	1.1	-7.6‰	1.3‰						
AZO-16	OL	15	1.46	-6.0‰	1.1‰	126	0	8.74	1.9	3.38	4.65
AZO-16	AMPH	16	0.65	-1.5‰	1.7‰	24	2.32	0.14	1.34	148.42	7.01
AZO-16	SRP	17	5.89	14.9‰	0.6‰	122	13.46	0.01	2.97	763.17	4.13
AZO-16	AMPH	18	0.61	-1.0‰	1.5‰	17	2.2	0.13	1.3	139.77	3.71
AZO-16	SRP	19	3.89	12.2‰	0.7‰	19	12.04	0	1.81	645.86	9.2
AZO-16	AMPH	20	0.83	-3.0‰	1.4‰	18	1.99	0.09	1.42	138.13	4.53
AZO-16	SRP	21	2.7	8.4‰	0.9‰						
AZO-16	OL	22	1.32	-9.6‰	1.4‰						
AZO-16	OL	23	1.66	-12.1‰	1.1‰						
AZO-16	SRP	24	2.32	8.2‰	0.9‰	21	12.29	0	2.41	761.92	6.23
AZO-16	OL	25	1.21	-7.1‰	1.1‰	22	0	5.68	2.63	11.06	5.92
AZO-16	OL	26	1.2	-5.3‰	1.0‰						
AZO-16	SRP	27	3.2	8.5‰	0.9‰						
AZO-16	SRP	28	1.38	6.1‰	1.4‰	23	12.28	0	2.2	717.71	5.81
AZO-16	SRP					53	12.4	0.01	2.76	855.25	24.63
AZO-16	OL					54	0	12.11	1.84	4.29	19.28
AZO-16	SRP					55	12.63	0	9.13	656	8.78
AZO-16	OL					56	0	14.98	2.14	7.05	14.16

Sample	Phase	1270 pit N^o	B (1270)	δ^{11}B	error	4f pit N^o	H_2O	Li	B	F	Cl
AZO-16	SRP					57	12.37	0	3.91	736.47	30.32
AZO-16	OL					61	0.13	6.92	4.49	9.8	9.44
AZO-16	SRP					62	13.43	0	4.04	738.64	10.41
AZO-16	SRP					124	12.96	0.01	4.38	692.45	21.42
AZO-16	OL					128	0.01	1.85	3.04	3.45	6.93
AZO-18	SRP	83	3.42	8.6‰	0.8‰	72	12.34	0.35	4.95	683.92	37.45
AZO-18	AMPH	84	1.23	3.0‰	1.3‰	75	2.31	0.08	2.18	261.65	1.55
AZO-18	OL	85	4.4	-7.4‰	0.7‰	73	0.17	0.79	5.39	33.91	3.16
AZO-18	VEIN LZ	86	9.51	5.2‰	0.6‰	70	15.14	0.01	11.52	108.56	633.94
AZO-18	OL	87	4.43	-1.9‰	0.8‰						
AZO-18	OL	88	2.09	-6.9‰	0.9‰						
AZO-18	OL	89	2.52	1.9‰	0.9‰	69	0.01	3.21	5.39	21.5	9.42
AZO-18	MIX	90	4.16	6.8‰	0.7‰	68	8.96	0.18	3.21	464.43	10.94
AZO-18	OL	91	1.51	-7.3‰	1.1‰	66	0.04	1.37	2.86	17.15	1.57
AZO-18	MIX	92	1.1	2.8‰	1.4‰	67	10.77	0.12	11.52	482.13	32.65
AZO-18	OL	93	1.97	-7.0‰	0.9‰	65	0.01	2.53	4.5	15.1	6.26
AZO-18	AMPH	94	1.11	2.6‰	1.4‰	64	2.41	0.07	2.42	254.66	16.39
AZO-18	OL	95	1.3	-4.5‰	1.2‰	76	0.01	5.17	5.24	34.08	7.07
AZO-18	VEIN LZ	96	5.06	5.5‰	0.6‰						

Sample	Phase	1270 pit N^o	B (1270)	δ^{11}B	error	4f pit N^o	H_2O	Li	B	F	Cl
AZO-18	OL	97	1.19	-6.3‰	1.1‰						
AZO-18	MIX					74	10.58	0.39	3.55	550.63	15.36
AZO-26	TLC	50	0.85	-4.4‰	1.6‰	16	5.93	0.06	1.2	164.59	11.39
AZO-26	OL	51	0.78	-10.1‰	1.5‰	42	0.01	1.98	1.34	9.9	5.3
AZO-26	OL	52	0.76	-6.7‰	1.3‰						
AZO-26	AMPH	53	0.73	-8.0‰	1.5‰	43	2.19	0.36	1.43	109.08	11.68
AZO-26	OL	54	8.25	-9.3‰	0.5‰	44	0.02	1.89	12.34	55.74	11.83
AZO-26	TLC	55	0.42	-3.6‰	2.2‰	17	5.83	0.04	0.92	152.51	74.72
AZO-26	OL	56	6.45	-9.1‰	0.6‰	45	0.03	1.17	4.16	17.93	14.4
AZO-26	OL	57	5.73	-11.9‰	0.6‰						
AZO-26	OL	58	5.5	-10.5‰	0.6‰	47	0.01	1.13	3.14	10.13	1.91
AZO-26	OL	59	0.71	-11.4‰	2.0‰	48	0.01	4.53	1.4	9.22	12.7
AZO-26	OL	60	7.96	-9.1‰	0.5‰						
AZO-26	OL	61	5.61	-9.3‰	0.6‰	41	0.17	2.52	11.38	50.79	10.64
AZO-26	TLC	62	1.32	0.7‰	1.4‰	15	5.72	0.08	4.7	162.8	148.92
AZO-26	AMPH	63	0.65	-10.6‰	1.9‰						
AZO-26	MIX					46	10.18	0.09	2.47	167.37	94.39
AZO-26	AMPH					49	2.77	0.25	1.82	120.49	10.58
AZO-26-S	SRP	5	0.55	-3.1‰	3.0‰	19	15.61	0.4	0.34	105.26	6.33

Sample	Phase	1270 pit N^o	B (1270)	δ^{11}B	error	4f pit N^o	H_2O	Li	B	F	Cl
AZO-26-S	SRP	6	0.69	0.4‰	1.8‰						
AZO-26-S	SRP	7	0.27	1.8‰	2.8‰						
AZO-26-S	SRP					18	15.47	0.45	0.3	122.03	9.84
AZO-26-S	SRP					22	14.06	0.42	0.54	118.46	38.79
PR01	OL	14	8.81	23.7‰	0.5‰	78	0.13	0.93	18.16	28.49	25.42
PR01	OL	15	0.45	3.7‰	2.2‰						
PR01	CHL	16	10.45	10.5‰	0.4‰	83	14.02	0.73	3.61	94.26	20.68
PR01	OL	17	13.28	20.6‰	0.4‰	84	0.2	0.96	15.31	18.23	10.04
PR01	CHL	18	13.12	20.4‰	0.4‰	82	12.94	0.1	3.83	100.21	36.97
PR01	OL	19	9.12	21.7‰	0.6‰	81	0.01	0.64	17.97	25.62	3.36
PR01	OL	20	9.49	19.8‰	0.5‰	85	0.08	1.49	16.67	22.62	3.38
PR01	OL	21	1.37	11.6‰	1.0‰	86	0.02	1.13	12.01	20.83	15.85
PR01	OL	22	8.81	20.5‰	0.5‰	87	0.01	1	13.07	23.74	9.08
PR01	OL					80	0.02	0.9	20.28	19.92	8.42
PR02	SRP	24	9.26	-0.3‰	0.6‰	96	11.89	0.38	14.19	146.35	138.07
PR02	OL	25	9.48	24.7‰	0.5‰	94	0.12	2.22	16.56	22.53	12.67
PR02	OL	26	8.1	21.7‰	0.5‰	97	0.06	1.26	14.45	16.55	3.13
PR02	TLC	27	1.62	-6.3‰	1.3‰	99	5.66	1.19	1.03	81.37	2.64
PR02	CHL	28	2.88	-6.2‰	1.0‰	98	12.01	0.41	4.55	74.86	139.74

Sample	Phase	1270 pit N^o	B (1270)	δ^{11}B	error	4f pit N^o	H_2O	Li	B	F	Cl
PR02	OL	29	7.95	22.6‰	0.6‰	100	0.07	1.5	13.35	12.78	10.27
PR02	OL	30	9.86	22.6‰	0.4‰	101	0.03	2.97	17.63	11.58	11.84
PR02	TLC					90	5.99	0.91	0.8	104.45	8.7
PR02	OL					91	0	2.06	0.44	5.25	4.6
PR02	CHL					92	12.53	0.12	0.77	94.24	11.59
PR02	OL					93	0	1.75	0.65	2.58	9.93
PR02	TLC					95	5.44	1.84	1.74	53.44	11.45
PR08	OL	38	0.53	5.9‰	1.9‰	106	0.01	3.31	0.37	6.08	3.26
PR08	OL	39	0.61	1.3‰	1.8‰						
PR08	OL	40	0.42	6.6‰	1.9‰						
PR08	CHL	41	0.78	-0.9‰	1.7‰	108	10.26	0.03	1.7	57.26	26.44
PR08	AMPH	42	0.6	9.3‰	1.9‰						
PR08	CHL	43	0.97	-2.2‰	1.6‰	105	13.83	0.09	1.62	76.54	15.46
PR08	OL	44	3.36	20.9‰	0.8‰	103	0.01	0.84	5.17	12.59	4.86
PR08	AMPH	45	0.36	10.7‰	2.2‰						
PR08	AMPH	46	0.44	11.8‰	1.9‰	102	2.32	0	0.77	34.1	7.21
PR08	OL	47	1.11	4.7‰	1.2‰						
PR08	OL	48	0.99	7.9‰	1.5‰						
PR08	CHL	49	0.84	1.2‰	1.7‰	104	15.22	0.04	0.97	84.3	31.08

Sample	Phase	1270 pit N^o	B (1270)	δ^{11}B	error	4f pit N^o	H_2O	Li	B	F	Cl
PR08	OL					109	0.23	2.91	1.9	13.45	3.46

B.2.3 Combined

Data for Chapter 4 was collected by all three analytical techniques (EMPA, 4f and 1270). Where data from different techniques is shown on the same graph (e.g. B vs Mg#), data was collected on or very near to the same spot (see Appendix B for spot locations). This enables us to tie together and directly compare major, trace and isotopic data for an individual crystal. Table B.8 is a compilation of the linked analytical pits used in the Valmalenco chapter. Followed a selection of graphs combining trace, isotope and major data.

Table B.8: A list of all the linked ion probe and electron probe pits. Pits were linked by matching phase ID and proximity. Most often linked pits are situated on the same crystal, however, where crystal size is small linked pits may be on another crystal within 200μm of each other. Images of pit locations can be found in Appendix B.

Sample	**Phase**	**Pit Number**		
		1270	4f	EMPA
AZO-13	VEIN LZ	64	8	13
AZO-13	OL	65	29	12
AZO-13	OL	66	27	
AZO-13	CHL	67	6	15
AZO-13	SRP	70	24	18
AZO-13	OL	71		10
AZO-13	TLC	72	31	
AZO-13	SRP		2	9
AZO-13	CHL		1	11
AZO-13	VEIN LZ		4	20
AZO-13-S	SRP	01	13	37
AZO-13-S	SRP	02	9	32
AZO-13-S	SRP	03	10	31
AZO-13-S	SRP	04		38
AZO-13-S	SRP		11	28

Sample	Phase	Pit Number		
		1270	4f	EMPA
AZO-13-S	SRP		12	23
AZO-16	SRP	08	58	13
AZO-16	OL	09	59	12
AZO-16	SRP	10	60	15
AZO-16	OL	11	127	49
AZO-16	SRP	12	123	47
AZO-16	SRP	13	121	39
AZO-16	OL	15	126	40
AZO-16	AMPH	16	24	43
AZO-16	SRP	17	122	42
AZO-16	AMPH	18	17	37
AZO-16	SRP	19	19	36
AZO-16	AMPH	20	18	38
AZO-16	OL	23		34
AZO-16	SRP	24	21	35
AZO-16	OL	25	22	45
AZO-16	SRP	28	23	46
AZO-16	OL		54	20
AZO-16	SRP		55	17
AZO-16	OL		56	16
AZO-16	SRP		57	18
AZO-16	OL		61	14
AZO-18	SRP	83	72	5a
AZO-18	AMPH	84	75	6a
AZO-18	OL	85	73	
AZO-18	VEIN LZ	86	70	4a
AZO-18	OL	88		3a
AZO-18	OL	89	69	2a

Sample	Phase	Pit Number		
		1270	4f	EMPA
AZO-18	MIX	90	68	1a
AZO-18	OL	91	66	10
AZO-18	MIX	92	67	11
AZO-18	OL	93	65	6
AZO-18	AMPH	94	64	5
AZO-18	OL	95	76	7a
AZO-26	TLC	50	16	18
AZO-26	OL	51	42	16
AZO-26	AMPH	53	43	15
AZO-26	OL	54	44	14
AZO-26	TLC	55	17	13
AZO-26	OL	56	45	20
AZO-26	OL	58	47	
AZO-26	OL	59	48	5
AZO-26	OL	60		1
AZO-26	OL	61	41	
AZO-26	TLC	62	15	2
AZO-26	AMPH		49	10
AZO-26-S	SRP	05	19	10
AZO-26-S	SRP		22	3
AZO-26-S	SRP		18	7
PR01	OL	14	78	21
PR01	OL	15		24
PR01	CHL	16	83	
PR01	OL	17	84	
PR01	CHL	18	82	27
PR01	OL	19	81	29
PR01	OL	20	85	19

Sample	Phase	Pit Number		
		1270	4f	EMPA
PR01	OL	21	86	18
PR01	OL	22	87	16
PR02	SRP	24	96	4
PR02	OL	25	94	6
PR02	OL	26	97	8
PR02	TLC	27	99	9
PR02	CHL	28	98	11
PR02	OL	29	100	12
PR02	OL	30	101	13
PR02	TLC		90	2
PR02	OL		91	1
PR02	CHL		92	3
PR02	TLC		95	7
PR08	OL	38	106	24
PR08	OL	40		26
PR08	CHL	41	108	28
PR08	AMPH	42		25
PR08	CHL	43	105	22
PR08	OL	44	103	18
PR08	AMPH	46	102	17
PR08	CHL	49	104	20

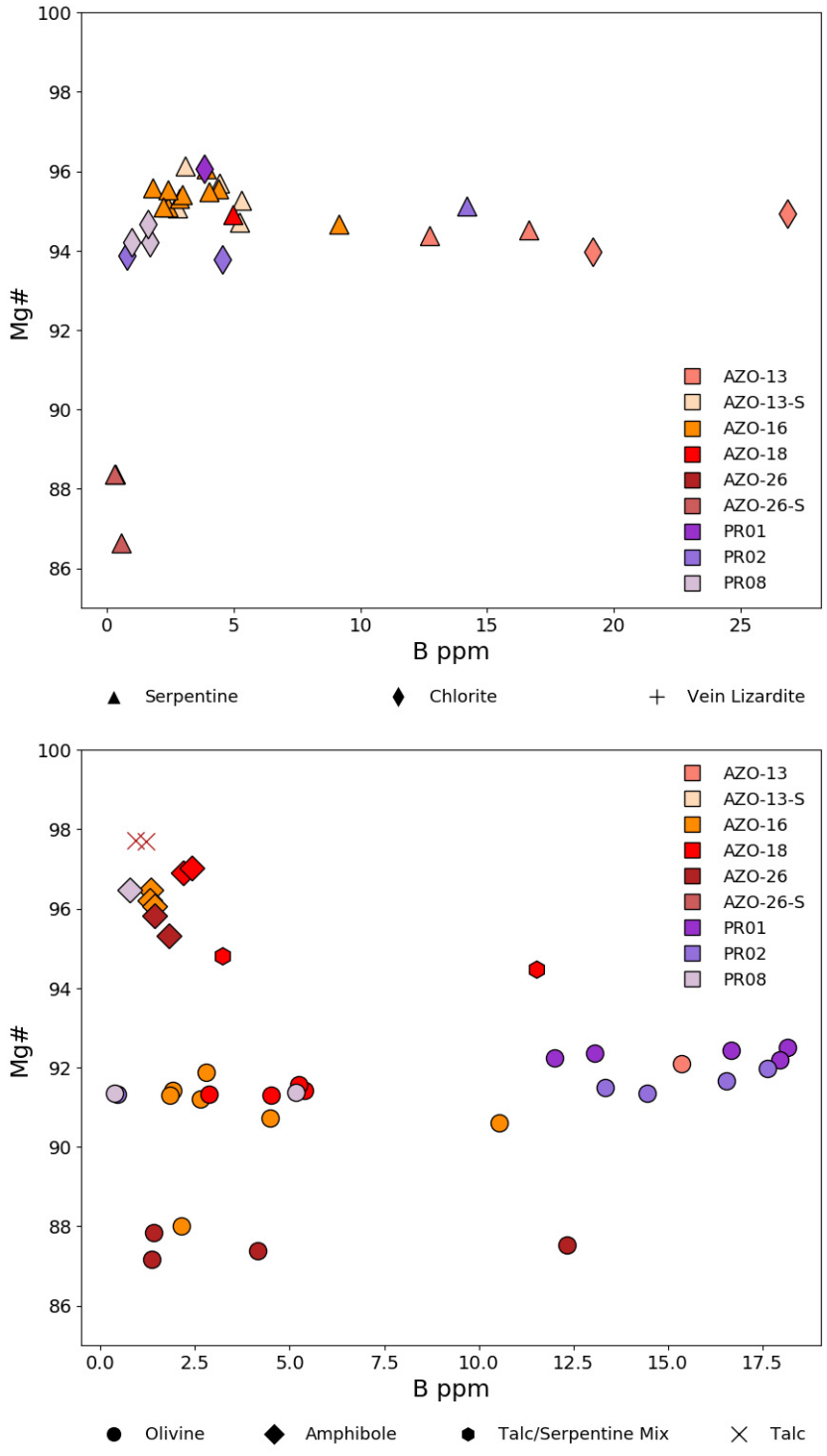

Figure B.21: (Above) Mg# vs B for serpentinite phases serpentine, chlorite and vein lizardite. (Below) Mg# vs B for phases formed during the formation of the Bergell aureole, including: talc, olivine, amphibole and the talc/serpentine mixture.

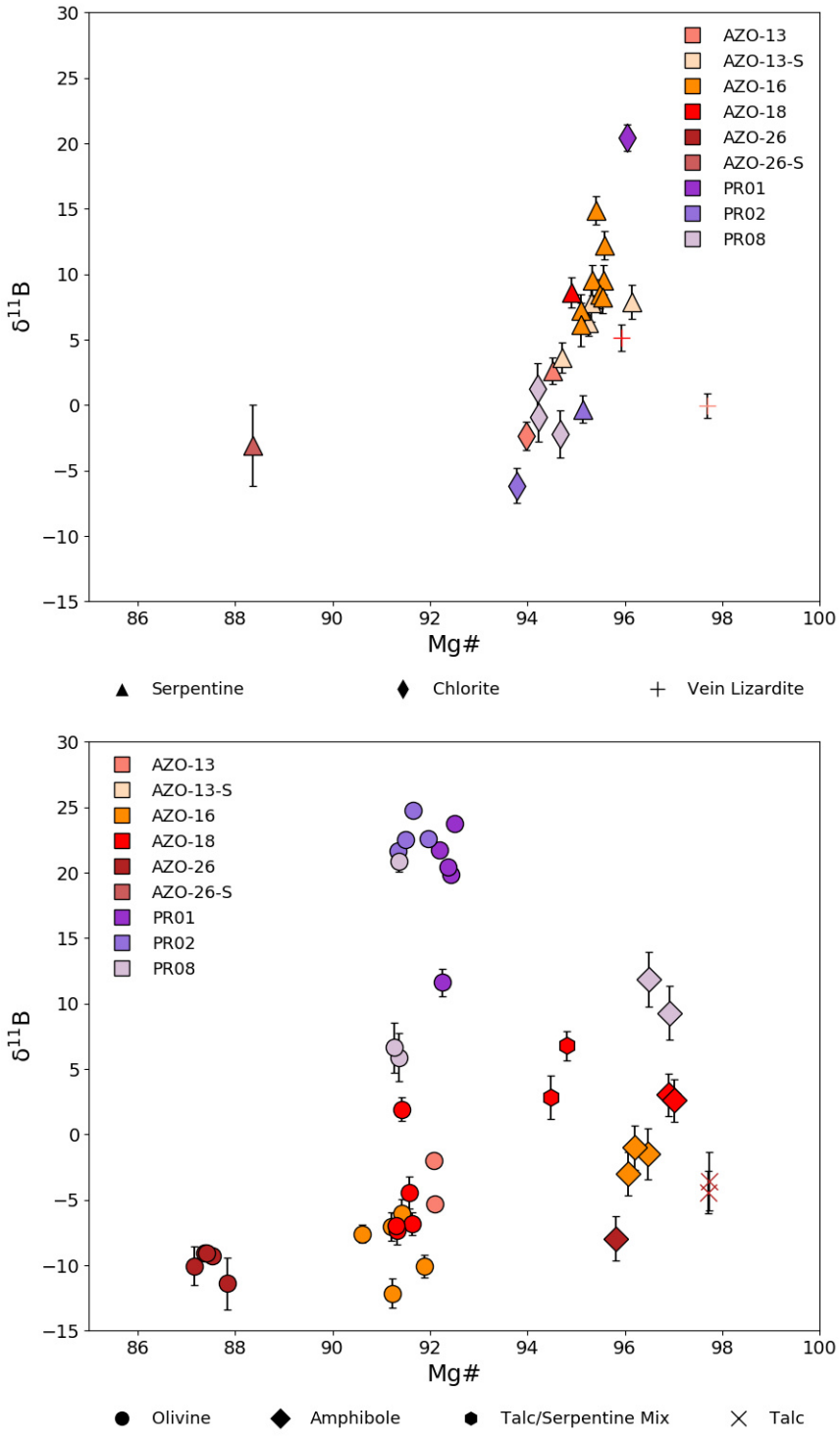

Figure B.22: (Above) Mg# vs δ^{11}B for serpentinite phases serpentine, chlorite and vein lizardite. (Below) Mg# vs δ^{11}B for phases formed during the formation of the Bergell aureole, including: talc, olivine, amphibole and the talc/serpentine mixture.

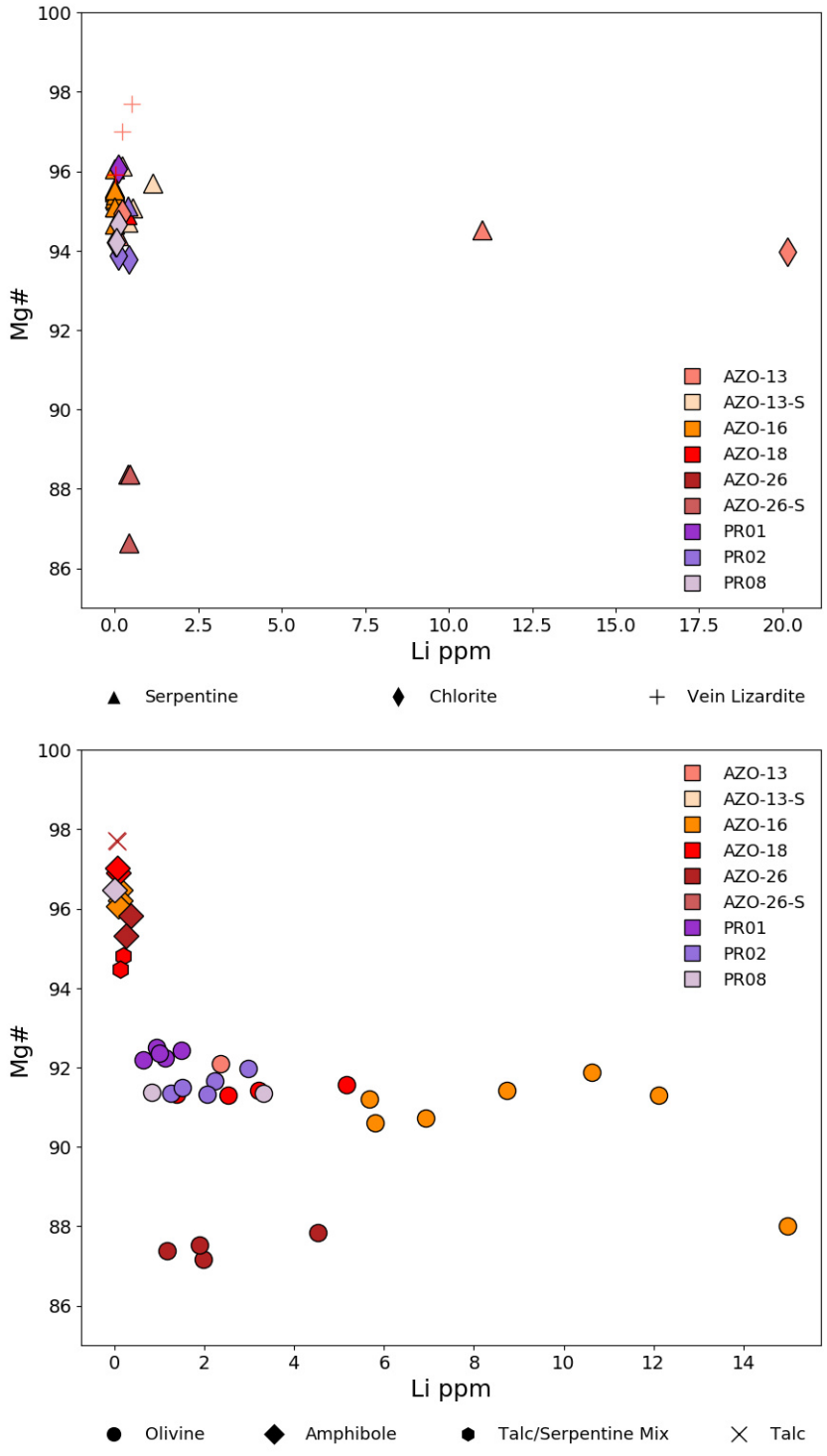

Figure B.23: (Above) Mg# vs Li for serpentinite phases serpentine, chlorite and vein lizardite. (Below) Mg# vs Li for phases formed during the formation of the Bergell aureole, including: talc, olivine, amphibole and the talc/serpentine mixture.

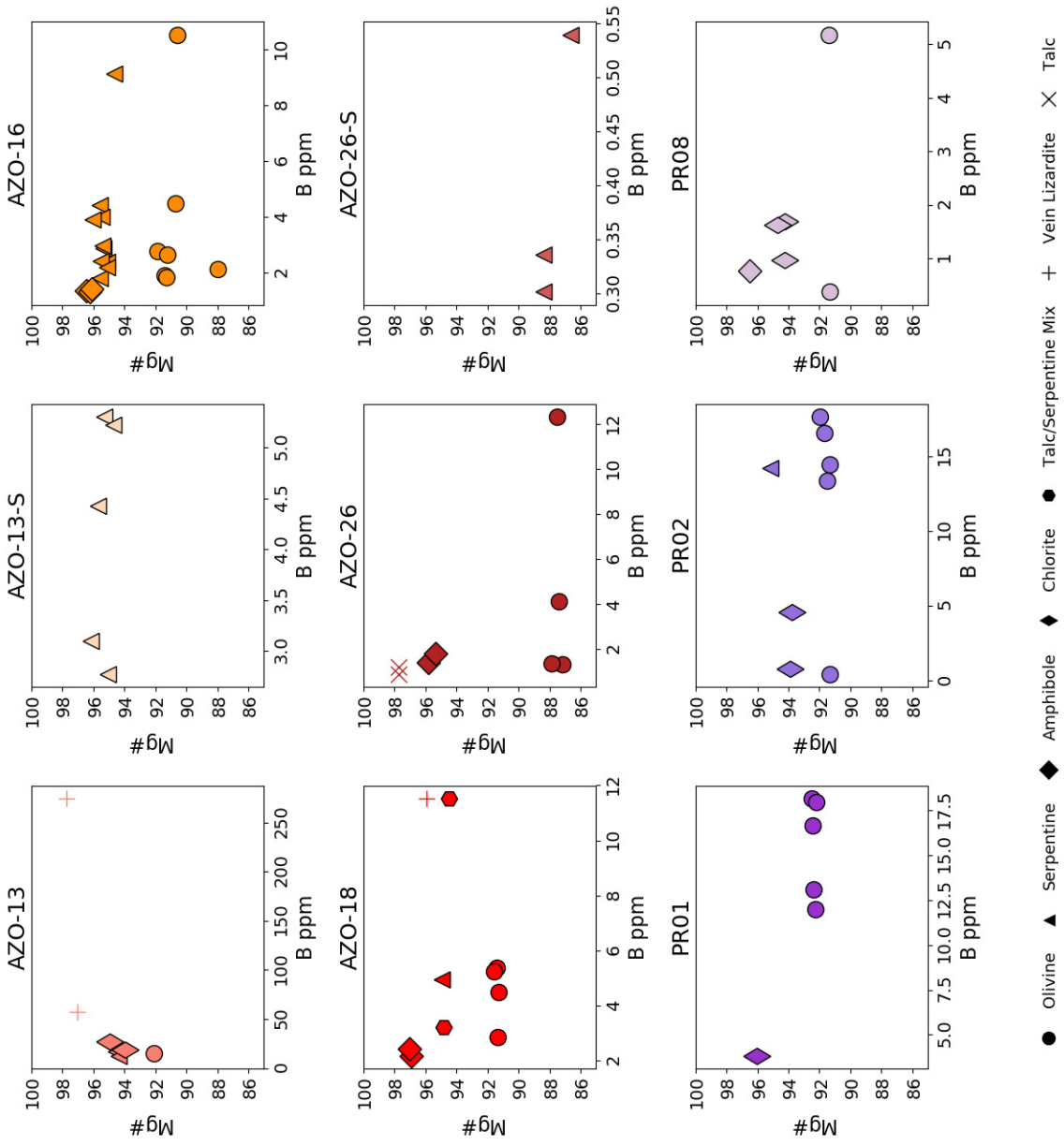

Figure B.24: Mg# vs B for all phases in each sample.

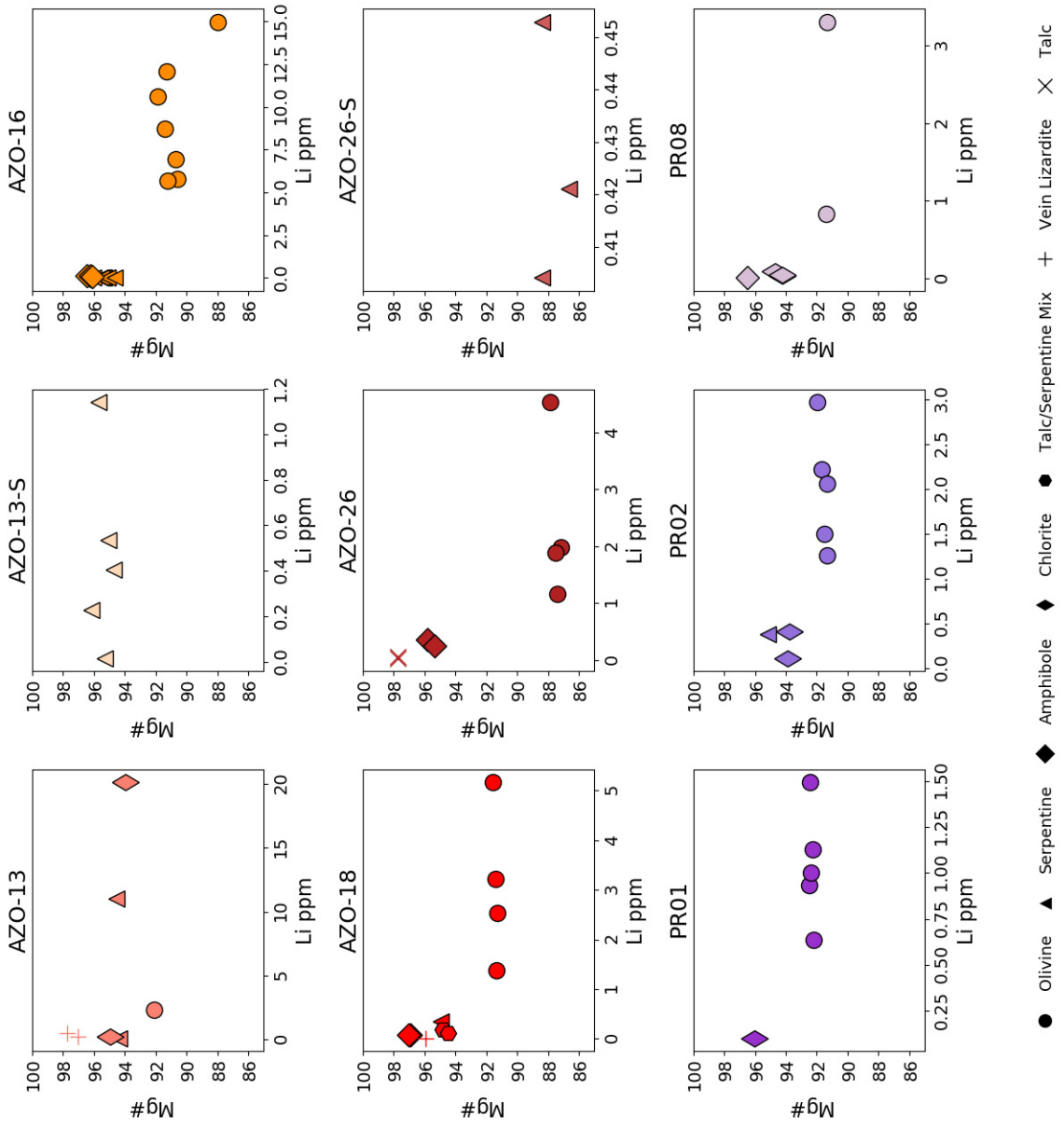

Figure B.25: Mg# vs Li for all phases in each sample.

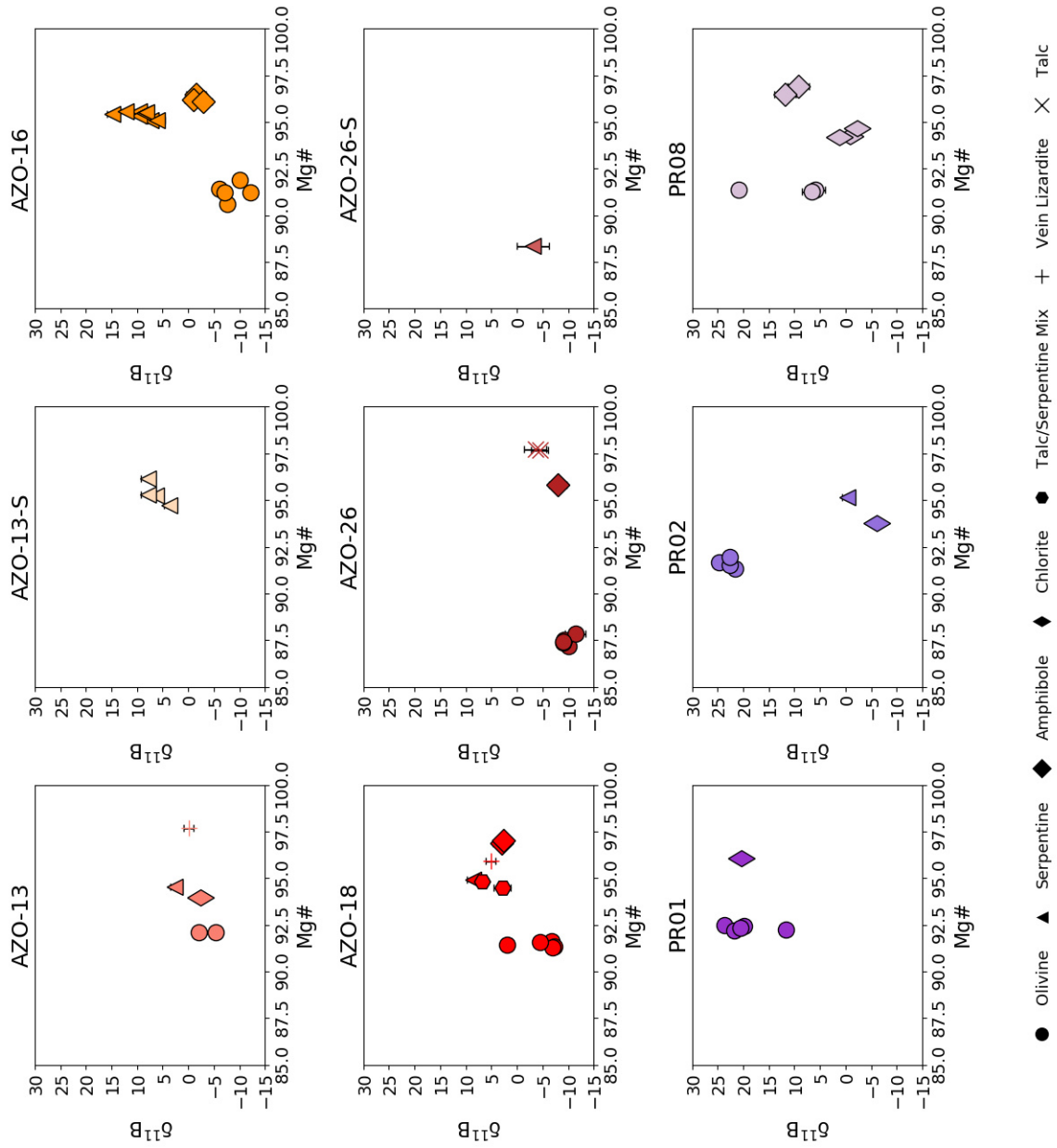

Figure B.26: δ^{11}B vs Mg# for all phases in each sample.

B.3 Data for Chapter 5: Experimental

B.3.1 Graphs

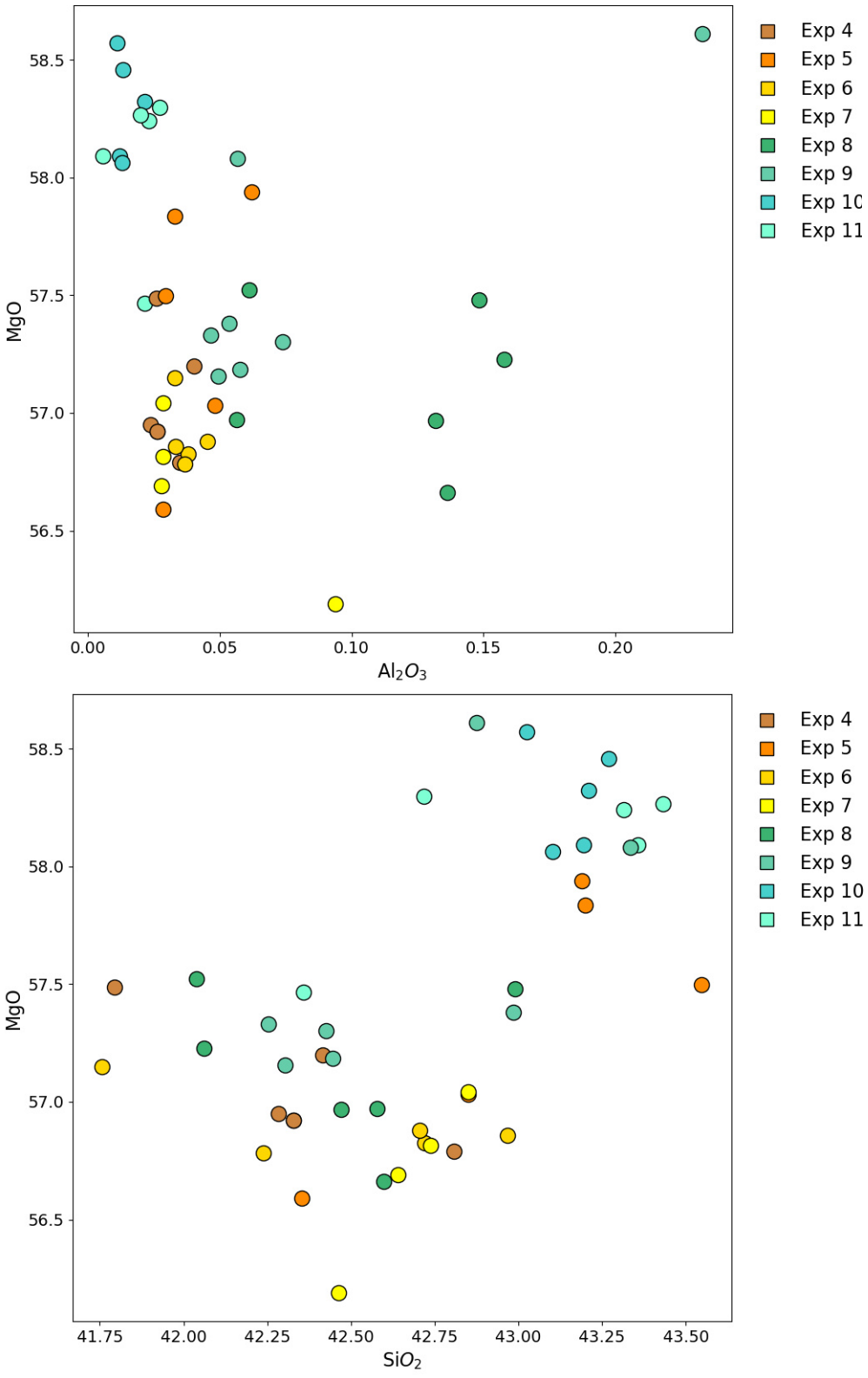

Figure B.27: (Above) Al_2O_3 vs MgO for olivine in all experiments. (Below) MgO vs SiO_2 for all olivines in experiments.

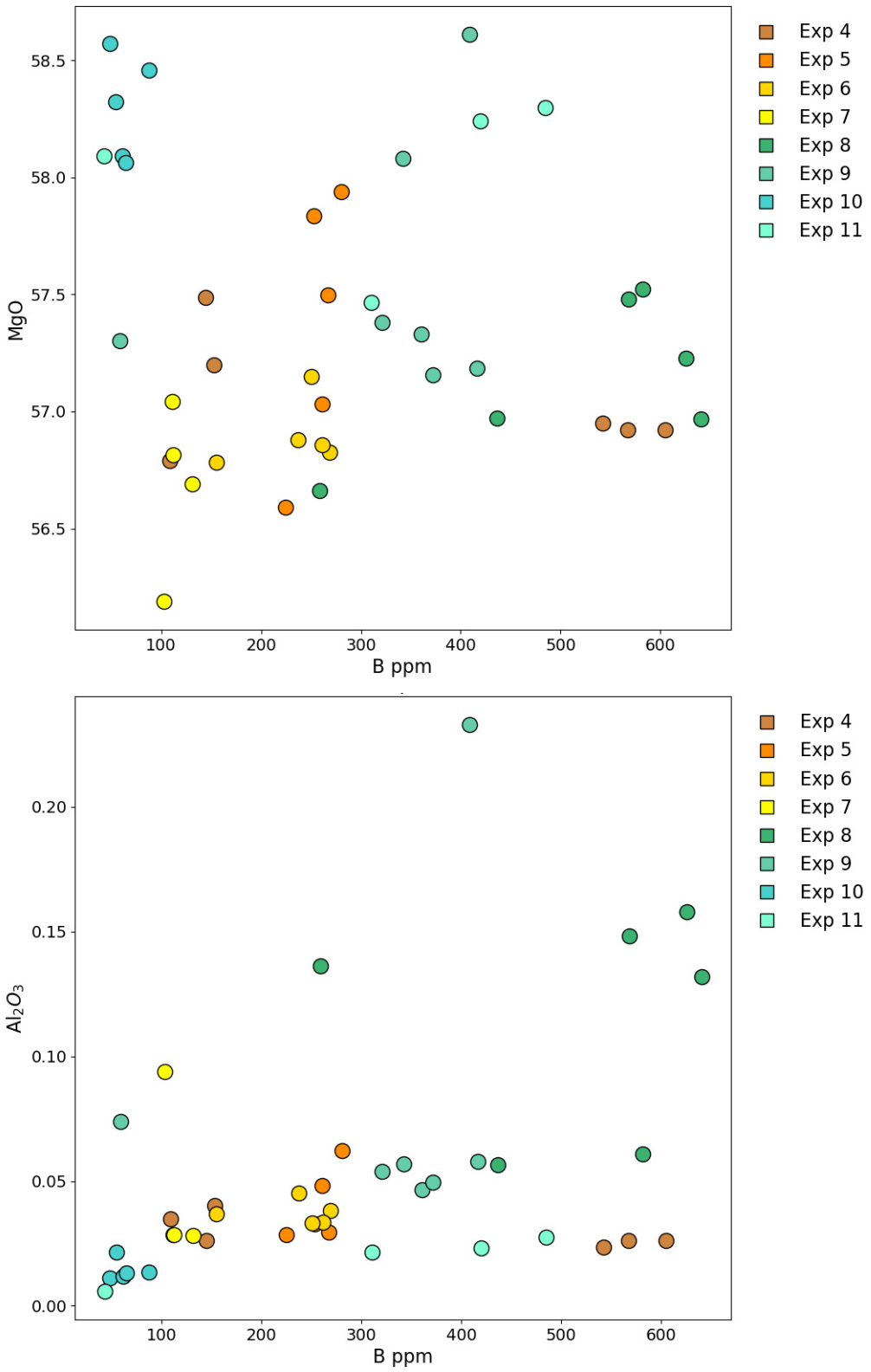

Figure B.28: (Above) B vs MgO for olivine in all experiments. There is no correlation. (Below) Al_2O_3 vs B ppm in all experiments, if each experiment is taken independently, there is no correlation between these elements.

B.3.2 Data

B and B isotope data

Table B.9: B and δ^{11}B values measured by 7f SIMS. With 4f B concentration for comparison

Experiment	Phase	7f pit n^o	δ^{11}B	δ^{11}*B error*	B (7f)	*B (7f) err*	4f pit n^o	B (4f)
Exp 10	ol	32	-1.4 ‰	±*1.4* ‰	52.8	±*0.3*	51	48.2
	ol	30	-0.5 ‰	±*1.4* ‰	46.2	±*0.2*	50	54.3
	ol	24	-2.4 ‰	±*1.3* ‰	64.2	±*0.3*	53	61.2
	ol	23	-2.4 ‰	±*1.4* ‰	59.8	±*0.3*	54	64.5
	ol	29	-1.8 ‰	±*1.3* ‰	56.4	±*0.3*	52	87.6
	ol	31	+0.2 ‰	±*1.8* ‰	20.9	±*0.1*		
	ol	26	-4.3 ‰	±*1.2* ‰	93.6	±*0.5*		
	ol	27	-8.4 ‰	±*1.4* ‰	196.9	±*1.0*		
Exp 11	ol	17	+0.6 ‰	±*1.5* ‰	30	±*0.1*	55	43.1
	ol	14	-13.6 ‰	±*1.1* ‰	259.7	±*1.3*	58	310.5
	ol	16	-12.8 ‰	±*1.1* ‰	438.9	±*2.1*	56	419.5
	ol	12	-12.6 ‰	±*1.1* ‰	543.6	±*2.6*	59	484.6
	ol	20	-2.0 ‰	±*1.6* ‰	29.8	±*0.1*		
	ol	18	-2.4 ‰	±*1.4* ‰	38.6	±*0.2*		

Experiment	Phase	7f pit n^o	δ^{11}B	δ^{11}*B error*	B (7f)	*B (7f) err*	4f pit n^o	B (4f)
	ol	19	-2.8 ‰	±*1.4* ‰	42.8	±*0.2*		
	ol	13	-7.8 ‰	±*1.3* ‰	73.3	±*0.4*	60	
	px	15	-19.7 ‰	±*1.1* ‰	782.1	±*3.8*	57	429.7
	px	22	-6.5 ‰	±*1.0* ‰	395.6	±*1.9*		
	px	21	-6.7 ‰	±*1.0* ‰	427.7	±*2.1*		
Exp 4	ol	39	-10.1 ‰	±*1.2* ‰	95.3	±*0.5*	12	108.6
	ol	35	-12.2 ‰	±*1.1* ‰	536.9	±*2.6*	13	144.4
	ol	33	-12.6 ‰	±*1.1* ‰	544.7	±*2.6*	10	152.9
	ol	36	-11.5 ‰	±*1.1* ‰	377	±*1.8*	14	542.1
	ol	34	-10.1 ‰	±*1.1* ‰	213.2	±*1.0*	15	567.3
	ol	41	-12.6 ‰	±*1.1* ‰	570.3	±*2.8*	11	605
	ol	40	-10.6 ‰	±*1.2* ‰	70.1	±*0.3*		
	px	38	-7.4 ‰	±*1.3* ‰	606.5	±*2.9*	17	426.2
	px	37	-7.2 ‰	±*1.0* ‰	641.4	±*3.1*	16	594.6
Exp 5	ol	46	-4.3 ‰	±*1.2* ‰	135.7	±*0.7*	6	224.8
	ol	44	-8.2 ‰	±*1.4* ‰	68.8	±*0.3*	4	252.7
	ol	45	-1.0 ‰	±*1.1* ‰	238.2	±*1.2*	9	260.8
	ol						8	267
	ol	42	-1.1 ‰	±*1.1* ‰	279.1	±*1.3*	3	280.2

Experiment	Phase	7f pit n^o	δ^{11}B	δ^{11}*B error*	B (7f)	*B (7f) err*	4f pit n^o	B (4f)
	px	47	+2.9 ‰	±*1.2* ‰	96.4	±*0.5*	7	115.9
	px	48	-2.8 ‰	±*1.5* ‰	116.4	±*0.6*	5	142.5
Exp 6	ol	10	+0.9 ‰	±*1.3* ‰	42.4	±*0.2*	22	155
	ol	7	-0.9 ‰	±*1.2* ‰	238.4	±*1.2*	20	237.4
	ol	8	-0.8 ‰	±*1.1* ‰	241.6	±*1.2*	21	250.2
	ol	6	-1.4 ‰	±*1.1* ‰	252.1	±*1.2*	19	261.5
	ol	5	-10.1 ‰	±*1.2* ‰	115.4	±*0.6*	18	268.6
	px	9	+6.2 ‰	±*1.1* ‰	232.4	±*1.1*		
	px	11	+6.6 ‰	±*1.1* ‰	251.1	±*1.2*		
Exp 7	ol	4	-4.5 ‰	±*1.3* ‰	89.1	±*0.4*	23	103.2
	ol	3	-1.9 ‰	±*1.3* ‰	74.6	±*0.4*	24	111.5
	ol	1	-2.6 ‰	±*1.3* ‰	78.5	±*0.4*	25	112.4
	ol	2	-4.3 ‰	±*1.3* ‰	77.6	±*0.4*	26	131.4
Exp 8	ol						44	259
	ol						49	430.6
	ol	53	-3.2 ‰	±*1.1* ‰	514.3	±*2.5*	48	436.3
	ol	50	-8.9 ‰	±*1.1* ‰	304	±*1.5*	42	567.8
	ol	52	-2.2 ‰	±*1.1* ‰	488.6	±*2.4*	47	581.9
	ol	49	-5.1 ‰	±*1.1* ‰	484.7	±*2.3*	43	625.7

Experiment	**Phase**	**7f pit n^o**	δ^{11}**B**	δ^{11}***B error***	**B (7f)**	***B (7f) err***	**4f pit n^o**	**B (4f)**
	ol						41	640.4
	px						45	7697
	px	51	-3.6 ‰	$\pm$*1.1* ‰	873	$\pm$*4.2*		
	px							
	px							
	si						46	2498.5
	si							
Exp 9	ol	57	-8.0 ‰	$\pm$*1.1* ‰	481.7	$\pm$*2.3*	40	321
	ol	58	-1.3 ‰	$\pm$*1.1* ‰	331.6	$\pm$*1.6*	39	342.5
	ol	56	-1.9 ‰	$\pm$*1.1* ‰	373	$\pm$*1.8*	34	360.4
	ol	55	-3.1 ‰	$\pm$*1.1* ‰	327.2	$\pm$*1.6*	35	371.7
	ol	54	-3.6 ‰	$\pm$*1.1* ‰	380.1	$\pm$*1.8*	33	408.5
	ol	59	-3.1 ‰	$\pm$*1.1* ‰	363.3	$\pm$*1.8*	38	416.2
	px	61	+6.9 ‰	$\pm$*1.1* ‰	214.3	$\pm$*1.0*	36	117.8

Major Elements

Table B.10: Major element analyses for all experiments. Note the high Al in experiments 4 and 11.

Experiment	phase	EMPA pit n^o	FeO	MgO	SiO_2	Na_2O	Al_2O_3	P_2O_5	CaO	TiO_2	Total
Exp 10	ol	28	0	58.6	43.0	0	0.01	0	0.019	0	101.7
	ol	27	0	58.3	43.2	0	0.02	0	0.024	0	101.6
	ol	30	0	58.1	43.2	0	0.01	0	0.023	0	101.3
	ol	31	0	58.1	43.1	0	0.01	0	0.019	0	101.3
	ol	29	0	58.5	43.3	0	0.01	0	0.020	0	101.8
	ol										
	ol										
	ol										
Exp 11	ol	21	0	58.1	43.4	0	0.01	0	0.018	0	101.4
	ol	24	0	57.5	42.4	0	0.02	0	0.009	0.003	99.8
	ol	22	0	58.2	43.3	0	0.02	0	0.000	0.004	101.6
	ol	25	0	58.3	42.7	0	0.03	0.010	0.014	0.004	101.1
	ol										
	ol										
	ol										
	ol	26	0	58.3	43.4	0	0.02	0	0.013	0	101.7

Experiment	phase	EMPA pit n^o	FeO	MgO	SiO_2	Na_2O	Al_2O_3	P_2O_5	CaO	TiO_2	Total
	px	23	0	36.6	54.9	0.012	9.26	0	0.070	0.014	100.9
	px										
	px										
Exp 4	ol	63	0	56.8	42.8	0	0.03	0.013	0.011	0	99.6
	ol	57	0	57.5	41.8	0	0.03	0	0	0	99.3
	ol	60	0	57.2	42.4	0	0.04	0	0.010	0	99.7
	ol	58	0	56.9	42.3	0	0.02	0	0.009	0.003	99.3
	ol	59	0	56.9	42.3	0	0.03	0.008	0.009	0	99.2
	ol	59	0	56.9	42.3	0	0.03	0.008	0.009	0	99.2
	ol										
	px	62	0	35.7	52.6	0.011	10.4	0	0.109	0.024	98.9
	px	61	0	36.5	53.9	0.017	7.9	0	0.118	0.015	98.4
Exp 5	ol	53	0	56.6	42.4	0	0.03	0.011	0.047	0.004	99.1
	ol	51	0	57.8	43.2	0	0.03	0.009	0.056	0	101.2
	ol	56	0	57.0	42.8	0	0.05	0	0.051	0	100.0
	ol	55	0	57.5	43.5	0	0.03	0	0.049	0	101.1
	ol	50	0	57.9	43.2	0	0.06	0	0.058	0	101.3
	px	52	0	39.3	60.1	0	0.09	0	0.211	0.004	99.7
	px	54	0	40.1	59.8	0.010	0.11	0	0.199	0.004	100.3

Experiment	phase	EMPA pit n^o	FeO	MgO	SiO_2	Na_2O	Al_2O_3	P_2O_5	CaO	TiO_2	Total
Exp 6	ol	66	0	56.8	42.2	0	0.04	0.009	0.045	0	99.1
	ol	68	0	56.9	42.7	0	0.05	0	0.040	0.005	99.7
	ol	67	0	57.2	41.8	0	0.03	0.009	0.019	0	99.0
	ol	65	0	56.9	43.0	0	0.03	0.008	0.021	0.004	99.9
	ol	64	0	56.8	42.7	0	0.04	0	0.044	0	99.7
	px	69	0	38.6	57.9	0	2.7	0	0.209	0.008	99.4
	px										
Exp 7	ol	72	0	56.2	42.5	0	0.09	0	0.023	0.003	98.8
	ol	70	0	57.0	42.9	0	0.03	0	0.028	0	100.0
	ol	71	0	56.8	42.7	0	0.03	0	0.025	0.005	99.7
	ol	73	0	56.7	42.6	0	0.03	0	0.020	0	99.4
Exp 8	ol	4	0	56.7	42.6	0	0.14	0.013	0.060	0.007	99.6
	ol										
	ol	10	0.09	57.0	42.6	0	0.06	0	0.091	0.003	99.8
	ol	1	0	57.5	43.0	0	0.15	0.009	0.062	0.008	100.7
	ol	9	0	57.5	42.0	0	0.06	0.011	0.089	0.004	99.8
	ol	3	0	57.2	42.1	0	0.16	0.017	0.063	0.006	99.6
	ol	2	0	57.0	42.5	0	0.13	0.014	0.060	0.005	99.7
	px	5	0	39.3	59.9	0.02	0.35	0	0.184	0.003	99.7

Experiment	phase	EMPA pit n^o	FeO	MgO	SiO_2	Na_2O	Al_2O_3	P_2O_5	CaO	TiO_2	Total
	px	11	0	38.5	59.5	0.05	1.5	0	0.448	0.010	100.0
	px	8	0	39.2	60.0	0.04	0.28	0	0.246	0.003	99.8
	px	16	0	39.7	60.4	0.01	0.07	0	0.254	0.004	100.4
	si	6	0	0	99.5	0	0.04	0	0	0	99.5
	si	7	0	0	99.7	0	0.06	0.010	0	0.006	99.8
Exp 9	ol	12	0	57.4	43.0	0	0.05	0.008	0.068	0	100.5
	ol	20	0	58.1	43.3	0	0.06	0.007	0.073	0	101.5
	ol	17	0	57.3	42.3	0	0.05	0	0.090	0.005	99.7
	ol	19	0	57.2	42.3	0	0.05	0.006	0.085	0	99.6
	ol	18	0	58.6	42.9	0	0.23	0.009	0.098	0.005	101.8
	ol	14	0	57.2	42.4	0	0.06	0.012	0.078	0.004	99.9
	px	15	0	39.2	60.7	0.02	0.15	0	0.456	0.005	100.5

B.3.3 Combined

Data for Chapter 5 was collected by all three analytical techniques (EMPA, 4f and 1270). Where data from different techniques is shown on the same graph (e.g. B vs Mg#), data was collected on or very near to the same spot (see Appendix B for spot locations). This enables us to tie together and directly compare major, trace and isotopic data for an individual crystal.]

Table B.11: A list of all the linked ion probe and electron probe pits. Pits were linked by matching phase ID and proximity. Most often linked pits are situated on the same crystal. Images of pit locations can be found in Appendix B.

Exp	**Phase**	**Pit n^o**		
		7f	**4f**	**EMPA**
Exp 10	ol	32	51	28
Exp 10	ol	30	50	27
Exp 10	ol	24	53	30
Exp 10	ol	23	54	31
Exp 10	ol	29	52	29
Exp 11	ol	17	55	21
Exp 11	ol	14	58	24
Exp 11	ol	16	56	22
Exp 11	ol	12	59	25
Exp 11	ol	13	60	26
Exp 11	px	15	57	23
Exp 4	ol	39	12	63
Exp 4	ol	35	13	57
Exp 4	ol	33	10	60
Exp 4	ol	36	14	58
Exp 4	ol	34	15	59
Exp 4	ol	41	11	59
Exp 4	px	38	17	62

Exp	Phase	Pit n^o		
		7f	**4f**	**EMPA**
Exp 4	px	37	16	61
Exp 5	ol	46	6	53
Exp 5	ol	44	4	51
Exp 5	ol	45	9	56
Exp 5	ol		8	55
Exp 5	ol	42	3	50
Exp 5	px	47	7	52
Exp 5	px	48	5	54
Exp 6	ol	10	22	66
Exp 6	ol	7	20	68
Exp 6	ol	8	21	67
Exp 6	ol	6	19	65
Exp 6	ol	5	18	64
Exp 6	px	9		69
Exp 7	ol	4	23	72
Exp 7	ol	3	24	70
Exp 7	ol	1	25	71
Exp 7	ol	2	26	73
Exp 8	ol		44	4
Exp 8	ol	53	48	10
Exp 8	ol	50	42	1
Exp 8	ol	52	47	9
Exp 8	ol	49	43	3
Exp 8	ol		41	2
Exp 8	px		45	5
Exp 8	px	51		11
Exp 8	si		46	6
Exp 9	ol	57	40	12

Exp	Phase	Pit n^o		
		7f	4f	EMPA
Exp 9	ol	58	39	20
Exp 9	ol	56	34	17
Exp 9	ol	55	35	19
Exp 9	ol	54	33	18
Exp 9	ol	59	38	14
Exp 9	px	61	36	15

B.3.4 Run conditions

Table B.12: Run conditions for all experiments performed and discussed in Chapter 5. There are two piston cylinder set ups in the labs at Edinburgh University, one reads directly in Celsius and the other reads in millivolts which have to be converted to Celsius, hence the extra mv column. V=voltage, T=temperature and P=pressure. All experiments completed in year 2019.

Exp	*Date*	Time	Power %	Amps	V	T$^\circ$C	P (Psi)	mv
4	*23/04*	13:31:00	11.6	-	20	124	3100	
		13:33:00	13.6	-	38	205	3400	
		13:35:00	16.2	-	40	293	4200	
		13:37:00	19.5	-	50	397	5500	
		13:39:00	24.4	-	60	556	5500	
		13:41:00	30.6	5	87	804	5500	
		13:43:00	34.8	6.5	92	1017	5500	
		13:45:00	41	8	100	1326	5500	
		13:47:00	44.8	9	118	1480	5500	
		13:50:00	48.1	10	121	1603	5500	
		13:58:00	48.8	10	121	1599	5400	
		14:12:00	49.1	10	122	1600	5400	
		14:47:00	49.7	10	125	1599	5300	

Exp	*Date*	Time	Power %	Amps	V	T°C	P (Psi)	mv
		15:30:00	50	10	125	1599	5500	
		15:41:00	36.2	7.1	90	1000	5300	
		17:57:00	36.4	7.1	90	1000	5400	
	24/04	09:41:00	36.4	7	90	1000	5250	
		17:05:00	36.5	7	90	1000	5300	
	25/04	09:16:00	36.5	7	90	1000	5250	
		15:30:00	36.3	7	90	1000	5250	
5	*09/05*	12:55:00	11.1	-	20	88	2000	
		12:57:00	15.9	-	40	244	3000	
		12:59:00	20.3	-	50	377	4000	
		13:01:00	24.4	-	60	514	5500	
		13:03:00	30.6	5	78	762	5500	
		13:05:00	34.8	6.2	85	979	5500	
		13:09:00	41	7.9	105	1288	5500	
		13:10:00	44.8	9	115	1448	5500	
		13:13:00	48.8	9.5	125	1593	5500	
		13:13:00	49	9.8	129	1604	5500	
		13:18:00	49.5	9.9	130	1605	5500	
		13:23:00	49.7	9.9	130	1605	5300	
		14:11:00	50.3	10	135	1600	5400	
		15:13:00	50.5	10	135	1592	5300	
		15:24:00	36.7	7	95	1002	5300	
		16:20:00	36.9	7	95	1000	5400	
	10/05	09:26:00	37.3	7	95	1000	5300	
		17:25:00	37.4	7	97	1000	5300	
	11/05	09:22:00	37.7	7	97	1000	5250	
		15:31:00	37.9	7	97	1000	5250	
6	*22/05*	12:01:00	11.2	-	25	162	2000	1.14

Exp	*Date*	Time	Power %	Amps	V	T°C	P (Psi)	mv
		12:04:00	17	-	40	289	3200	2.2
		12:06:00	21.8	-	45	416	4200	3.58
		12:08:00	26.9	5.8	60	563	5200	5.17
		12:10:00	31.3	6	65	731	5300	7.1
		12:12:00	37	6.8	80	981	5300	10.26
		12:14:00	40	7.5	85	1118	5300	12.1
		12:16:00	42.3	7.9	95	1222	5300	13.53
		12:17:00	47	8.8	105	1403	5300	16.08
		12:19:00	49.7	9.5	115	1494	6000	17.36
		12:20:00	53	10.2	121	1599	6000	18.84
		12:34:00	53.6	10.4	122	1601	5700	18.85
		13:21:00	54.2	9.4	125	1599	5600	18.84
		15:04:00	47.9	8.1	110	1364	5700	15.53
		15:07:00	41.5	8.1	92	1100	5750	11.84
		15:17:00	41.7	8.1	95	1100	5750	11.88
		17:54:00	41.7	8.1	95	1100	5500	11.88
	23/05	09:56:00	42.2	8.1	95	1100	5500	11.85
		16:05:00	42.1	8.1	95	1100	5500	11.85
	24/05	09:35:00	42.3	8.1	95	1100	5500	11.85
		15:34:00	42.3	8.1	95	1100	5500	11.85
7	*28/05*	14:48:00	11.6	-	22	118	2250	
		14:50:00	13.6	-	32	192	2850	
		14:51:00	16.2	-	40	271	3500	
		14:52:00	19.5	-	45	369	4250	
		14:54:00	24.4	-	60	520	4900	
		14:55:00	30.6	5	75	769	5300	
		14:57:00	34.8	6	85	983	5300	
		14:58:00	41	7.8	105	1281	5300	
		15:00:00	44.8	8.6	118	1444	5300	

Exp	*Date*	Time	Power %	Amps	V	T°C	P (Psi)	mv
		15:01:00	48.4	9.1	125	1575	5400	
		15:03:00	49.1	9.5	130	1600	5300	
		15:06:00	49.2	9.8	130	1600	5200	
		15:04:00	49.9	9.9	134	1600	5400	
		15:18:00	50.4	10	135	1600	5300	
		17:13:00	50.8	10	135	1571	5125	
		17:20:00	35.2	6.6	85	900	5400	
	29/05	08:49:00	35.4	6.6	85	900	5300	
		15:56:00	35.6	6.6	90	900	5300	
	30/05	09:32:00	35.7	6.6	90	900	5300	
		15:56:00	35.7	6.6	90	900	5300	
8	*29/05*	09:17:00	11.4	-	22	179	3000	1.24
		09:19:00	17.3	-	32	313	3500	2.53
		09:20:00	24	5	40	483	4000	4.28
		09:22:00	28.7	5.5	45	639	4500	6.01
		09:24:00	33.8	6.4	60	846	5300	8.51
		09:27:00	38	7	75	1039	5300	11.03
		09:28:00	40	7.5	85	1133	5300	12.3
		09:29:00	44.4	8.3	105	1311	5300	14.8
		09:31:00	49.7	9.3	118	1492	5300	17.35
		09:32:00	53.3	10	125	1601	5300	18.85
		10:04:00	57.6	10	130	1603	5500	18.88
		11:57:00	38.4	7	130	901	5500	9.21
		15:57:00	38.2	7	134	901	5500	9.21
	30/05	09:32:00	38.3	7	85	901	5400	9.21
		16:28:00	38.1	7	90	901	5400	9.21
	31/05	09:34:00	38.3	7	90	901	5300	9.21
		12:00:00	38.1	7	90	901	5300	9.21

Exp	*Date*	Time	Power %	Amps	V	T°C	P (Psi)	mv
9	*05/06*	10:51:00	11.5	-	21	102	2000	
		10:53:00	13.6	-	34	182	2800	
		10:54:00	16.2	-	40	260	3200	
		10:55:00	19.5	-	45	359	4100	
		10:56:00	24.4	-	60	513	4900	
		10:57:00	30.6	5	75	759	5200	
		10:58:00	34.8	6	95	959	5200	
		11:00:00	40.4	7.2	101	1263	5300	
		11:02:00	43.3	8	110	1387	5300	
		11:03:00	46.8	8.9	120	1529	5300	
		11:04:00	48.8	9.2	125	1606	5300	
		11:16:00	49.6	9.5	130	1603	5400	
		12:02:00	50.8	9.9	135	1603	5400	
		13:01:00	37.3	7	95	1000	5400	
		13:50:00	37.3	7	95	1000	5200	
		18:23:00	37.6	7	95	1000	5200	
	06/06	09:23:00	37.6	7	95	1000	5200	
		17:19:00	37.7	7	97	1000	5200	
	07/06	09:03:00	37.8	7	98	1000	5200	
		13:02:00						
10	*05/06*	13:34:00	10.6	-	25	157	2000	1.04
		13:37:00	17.3	-	40	300	3250	2.4
		13:39:00	24.4	5	55	487	4250	4.32
		13:41:00	28.7	5.5	62	625	5250	5.85
		13:42:00	33.1	6	70	792	5250	7.83
		13:43:00	37	6.7	81	956	5250	9.92
		13:45:00	42.3	7.8	95	1207	5250	13.33
		13:46:00	47	8.6	105	1389	5250	15.9
		13:48:00	53.3	10	121	1595	5250	18.77

Exp	*Date*	Time	Power %	Amps	V	T°C	P (Psi)	mv
		13:49:00	53.6	10	121	1604	5250	18.89
		14:00:00	55	10.1	125	1601	5400	18.85
		14:38:00	55.5	10.5	128	1601	5200	18.86
		15:46:00	55.9	10.5	128	1601	5200	18.85
		15:49:00	42	7.9	95	1100	5300	11.85
		18:24:00	42.2	7.9	95	1100	5200	11.85
	06/06	09:24:00	42.2	7.9	95	1100	5200	11.85
		17:20:00	42.3	7.9	96	1100	5200	11.85
	07/06	09:04:00	42.3	8	98	1100	5200	11.85
		15:54:00	42.3	8	98	1100	5200	11.85
11	*10/06*	10:07:00	12.6	-	28	156	2000	
		10:09:00	16.2	-	40	277	2800	
		10:11:00	19.5	-	49	380	4100	
		10:12:00	24.4	-	60	530	4500	
		10:14:00	30.6	5	78	780	5300	
		10:15:00	34.8	6.1	83	986	5300	
		10:16:00	40.4	7.6	102	1275	5300	
		10:17:00	43.3	8.1	112	1398	5300	
		10:19:00	46.6	9	120	1515	5400	
		10:20:00	49	9.5	125	1604	5500	
		10:28:00	49.2	9.9	130	1601	5400	
		10:46:00	49.9	9.9	130	1602	5400	
		10:55:00	50	9.9	130	1600	5400	
		11:36:00	50.6	10	135	1602	5350	
		12:22:00	50.6	10	135	1590	5300	
		12:27:00	34.6	6.6	95	900	5400	
		12:40:00	34.7	6.6	95	901	5400	
		13:39:00	34.6	6.6	95	900	5450	
		16:28:00	34.7	6.6	95	900	5400	

Exp	*Date*	Time	Power %	Amps	V	T°C	P (Psi)	mv
	11/06	09:18:00	35	6.6	95	900	5350	
		16:23:00	35.1	6.6	95	900	5375	
	12/06	08:58:00	35.2	6.6	95	900	5300	
		12:38:00	35.3	6.6	95	900	5300	

Appendix C

Images

C.1 Sample images for Chapter 3: Alps and Baetic Cordillera

C.1.1 Main samples

These are the images and locations of each probe pit (numbered) used in Chapter 3 of the thesis. Unless otherwise stated, green colours indicate 1270 pits, blue numbers indicate 4f pits an white/black numbers indicate EMPA pits.

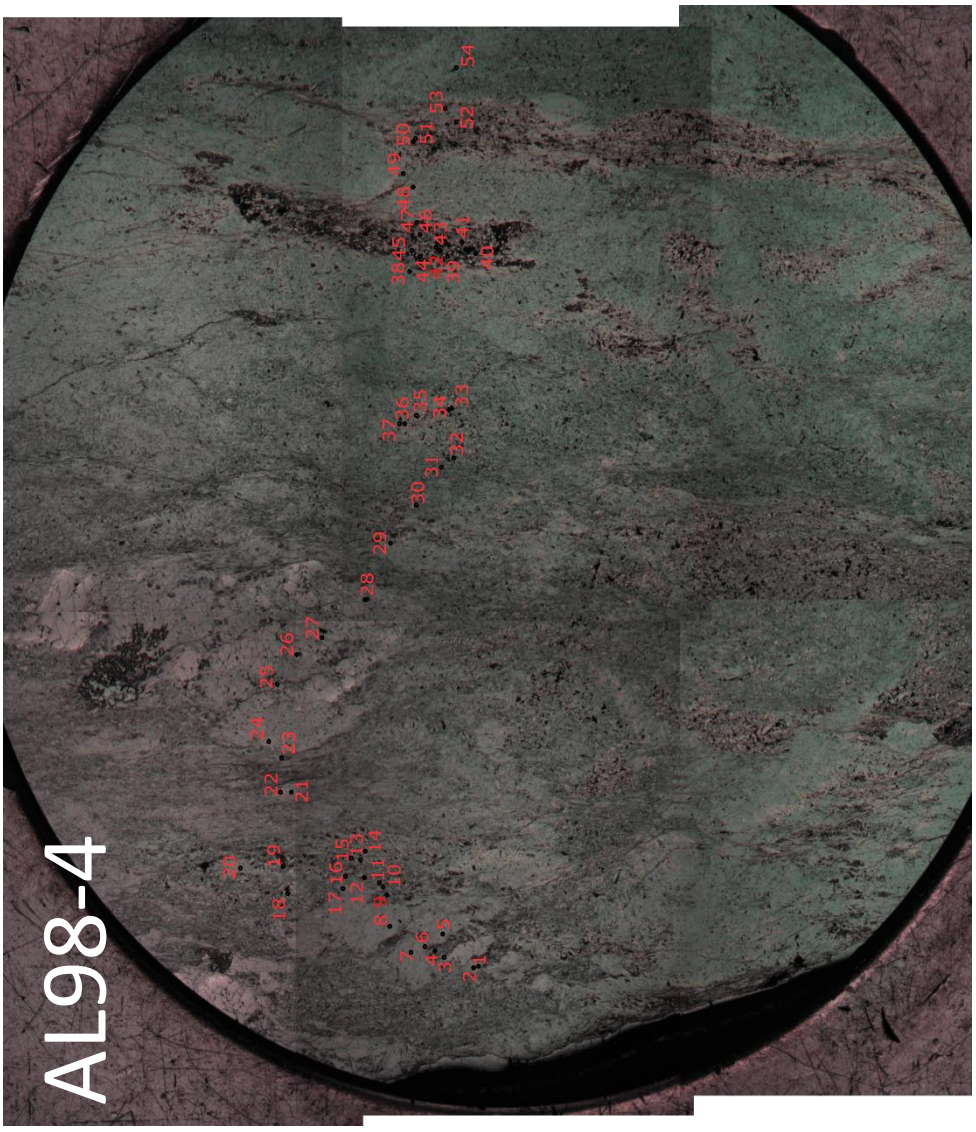
AL98-4
1
2
3
4
5
6
7
8
9
10
11
12
13
14
15
16
17
18
19
20
21
22
23
24
25
26
27
28
29
30
31
32
33
34
35
36
37
38
39
40
41
42
43
44
45
46
47
48
49
50
51
52
53
54

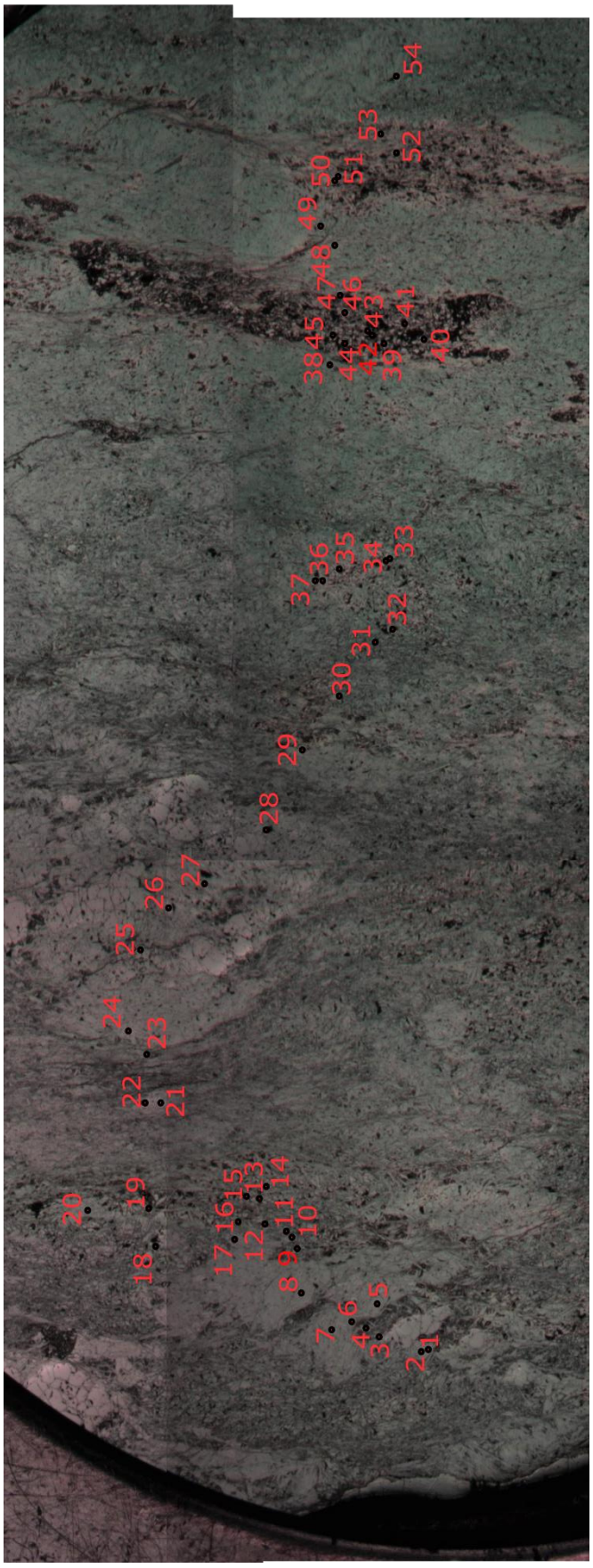

AL98-4 *closeup*

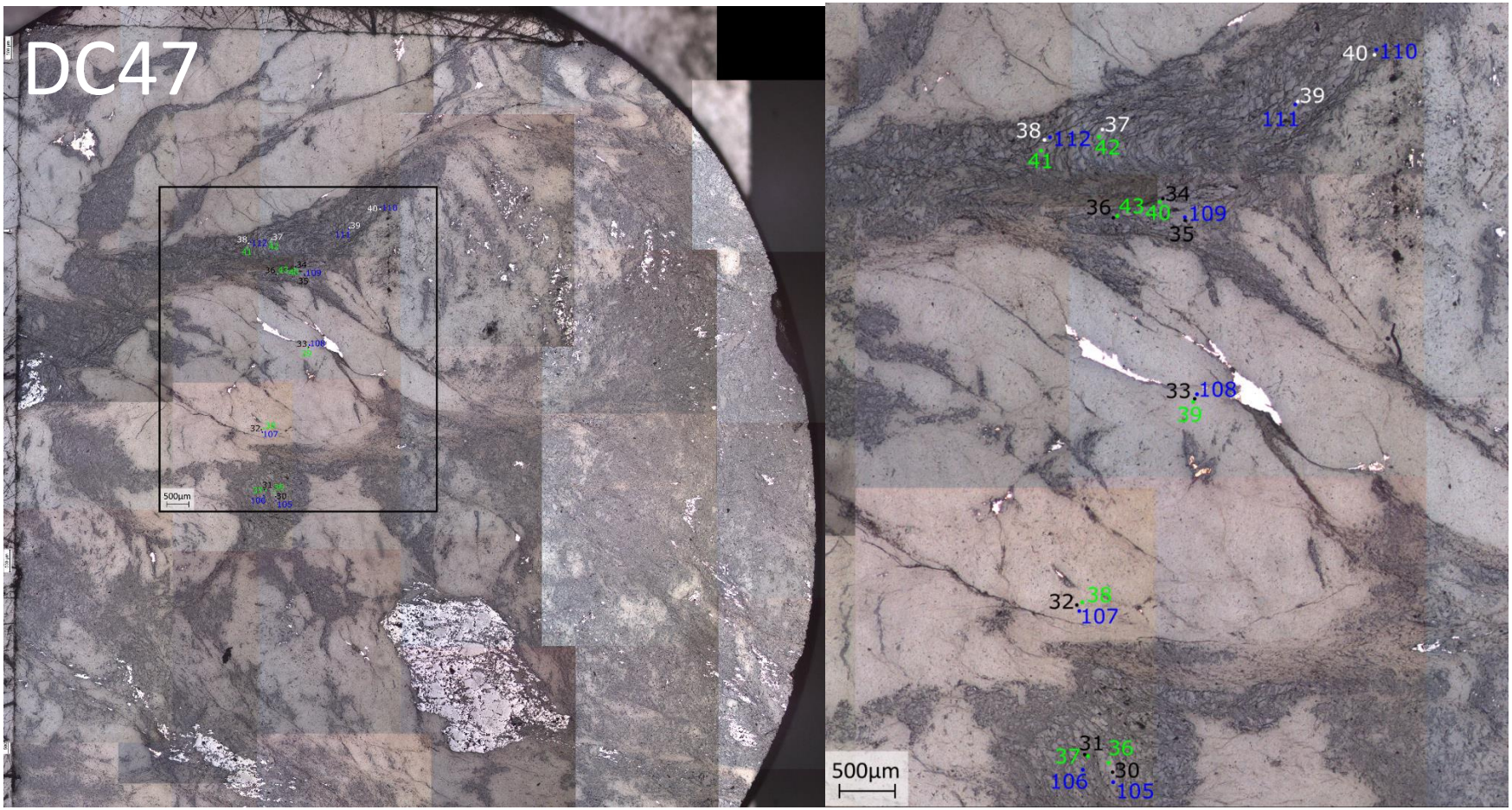

DC47 *closeup*

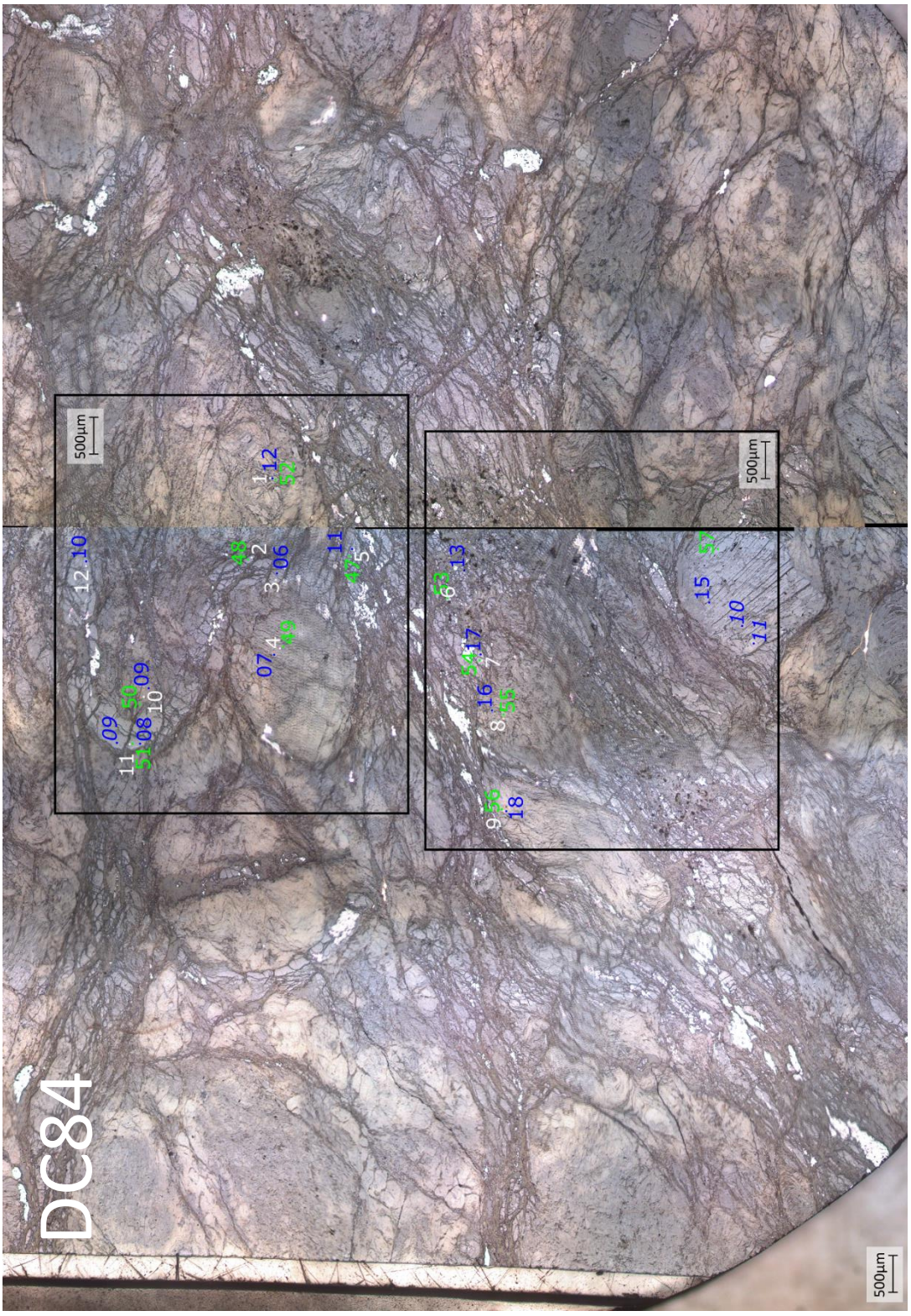
DC84
500µm
500µm
500µm

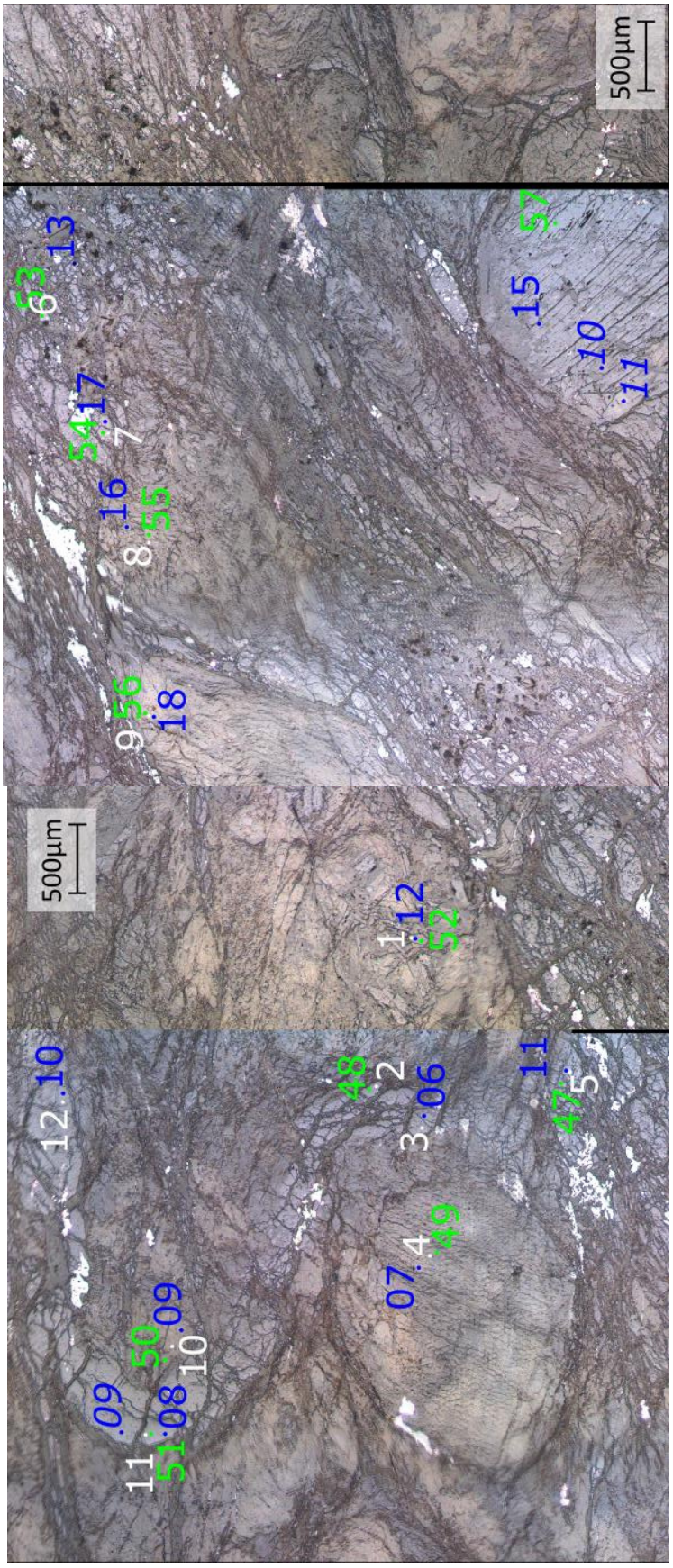

DC84 *closeups*

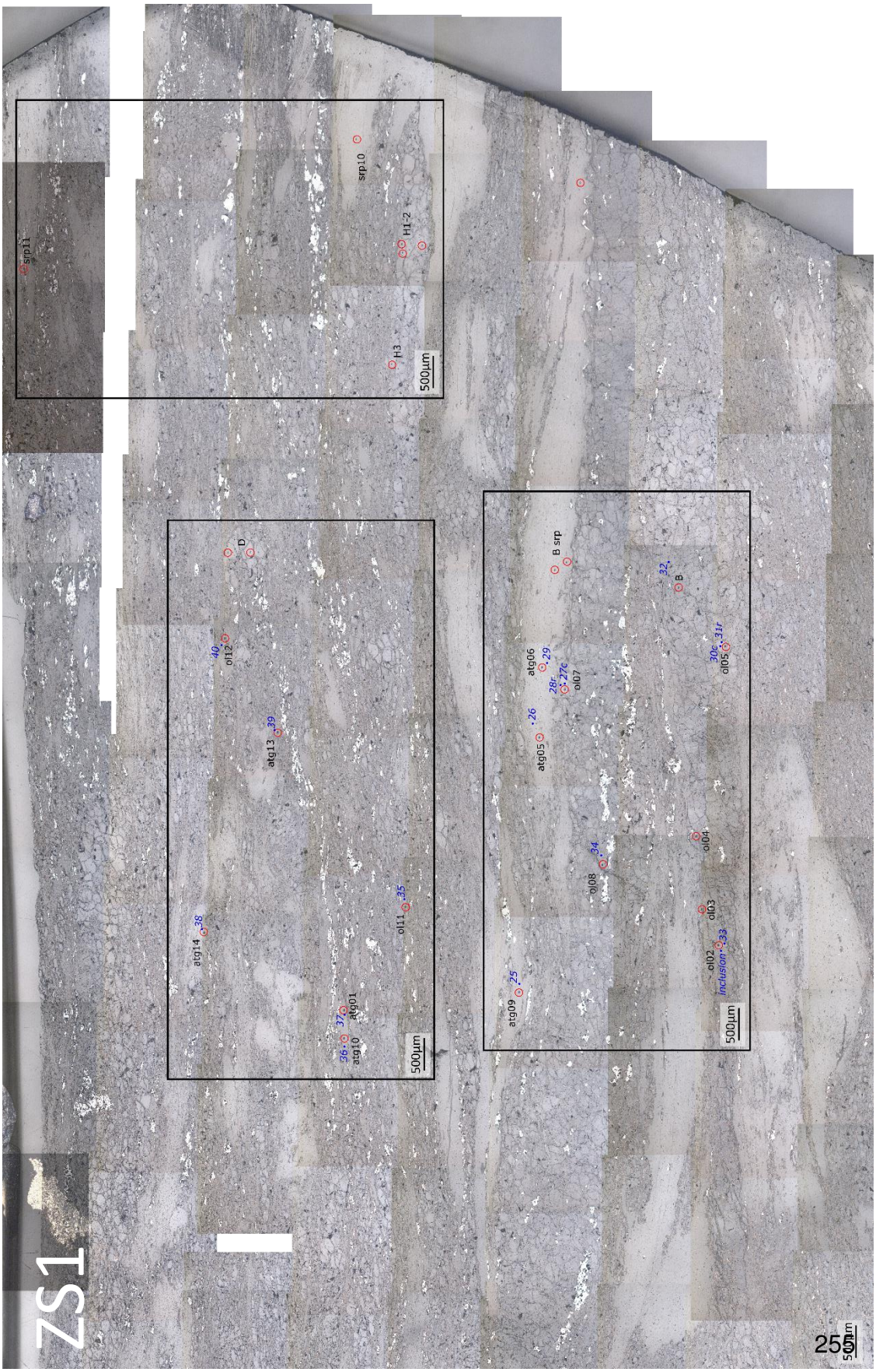
ZS1
srp11
srp10
H1-2
H3
500µm
D
40
olI12
39
atg13
38
atg14
olI1
35
37
atg01
36
atg10
500µm
B srp
32
B
atg06
29
28
27c
olI07
30c
olI05
31r
26
atg05
25
atg09
olI08
34
olI04
olI03
olI02
inclusion
33
500µm
500µm

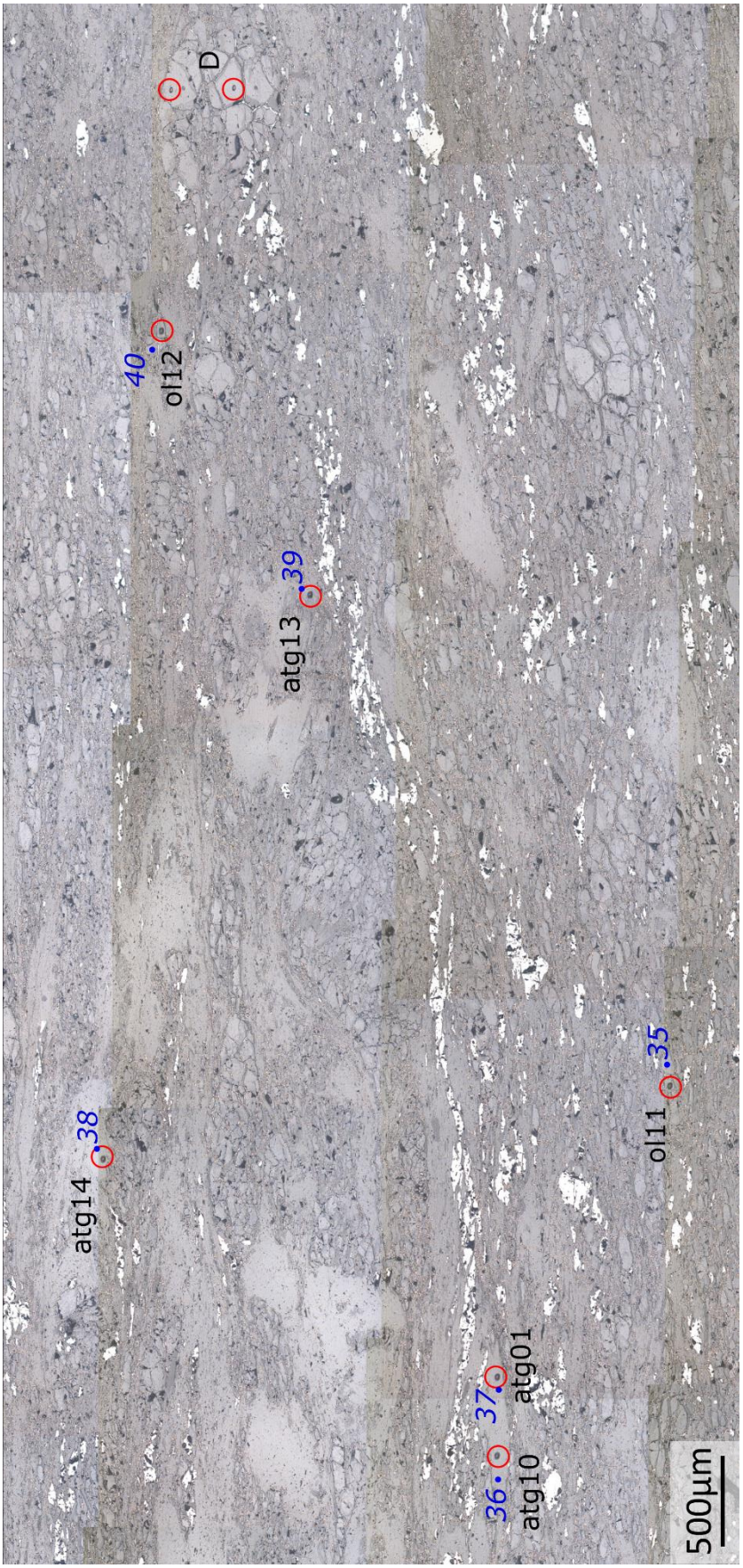

ZS1 *closeups*

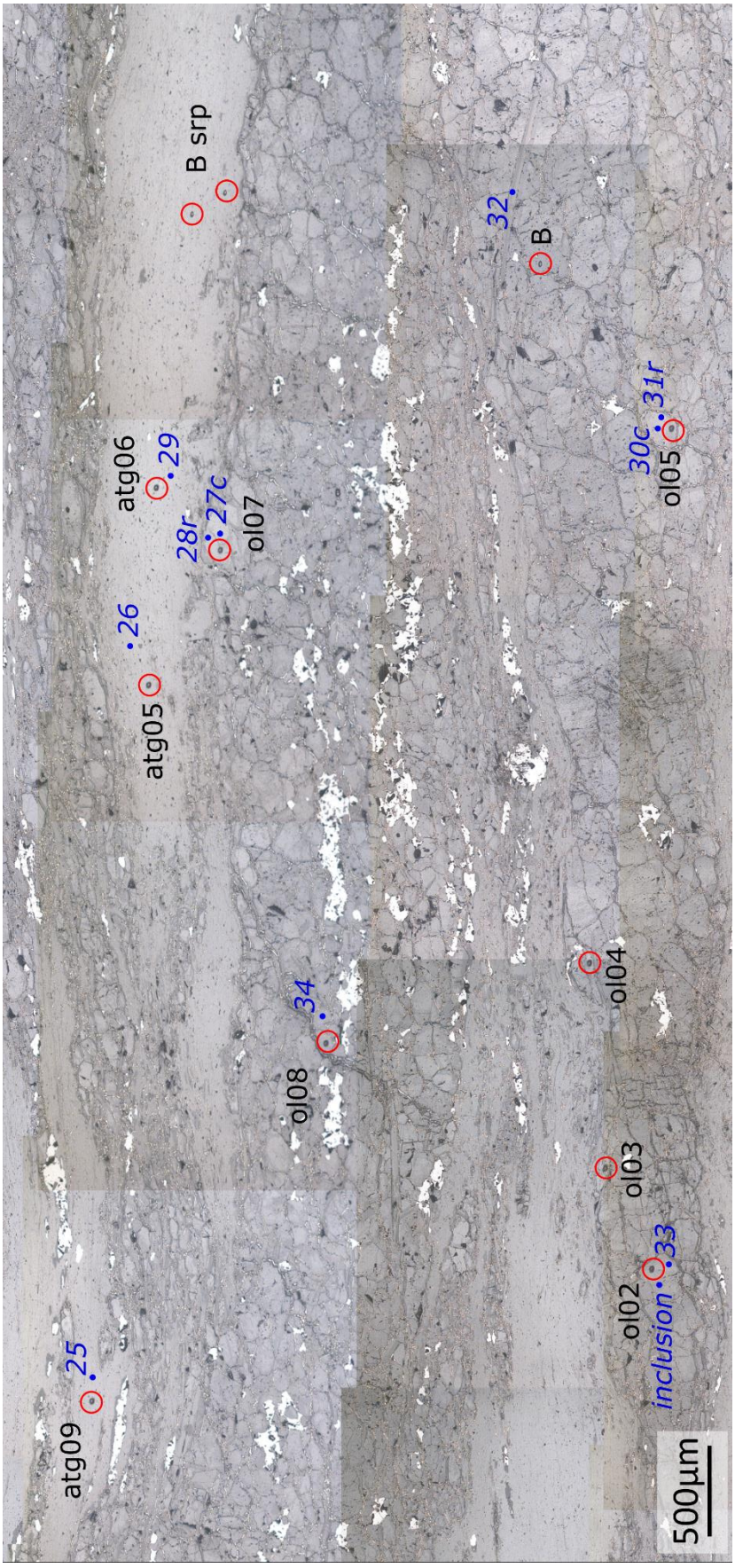

ZS1 *closeups*

ZS1 *closeups*

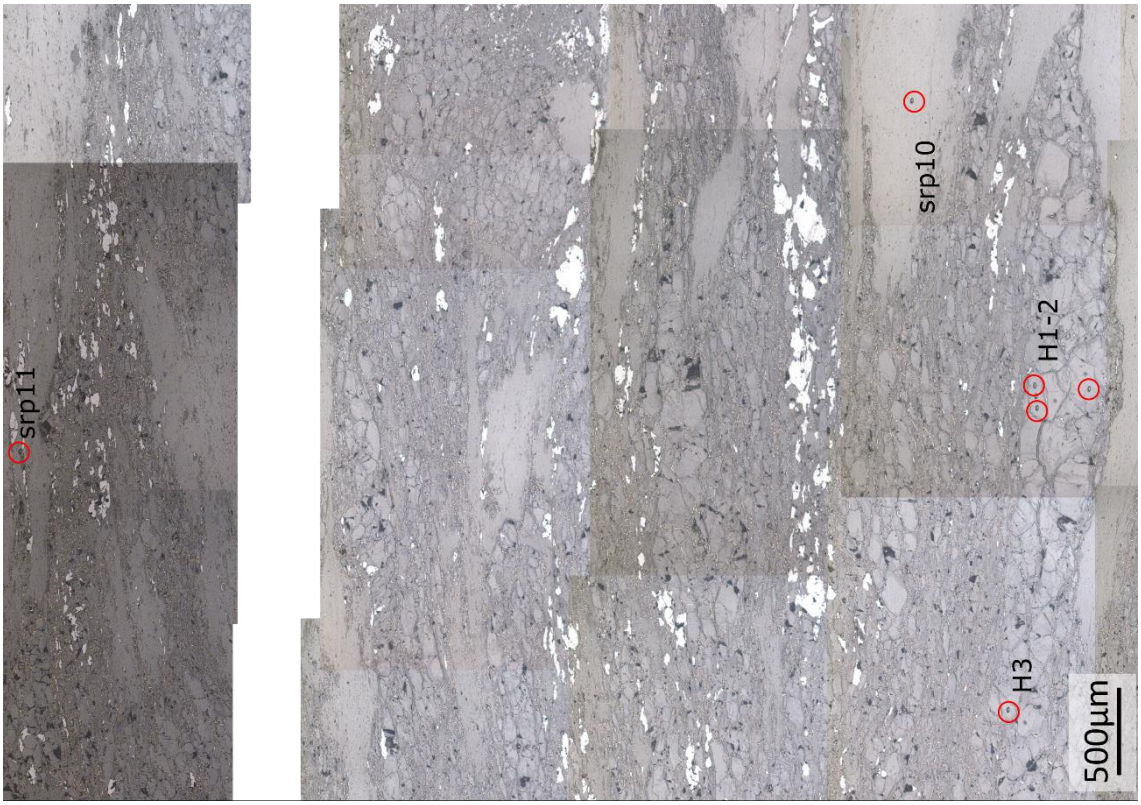

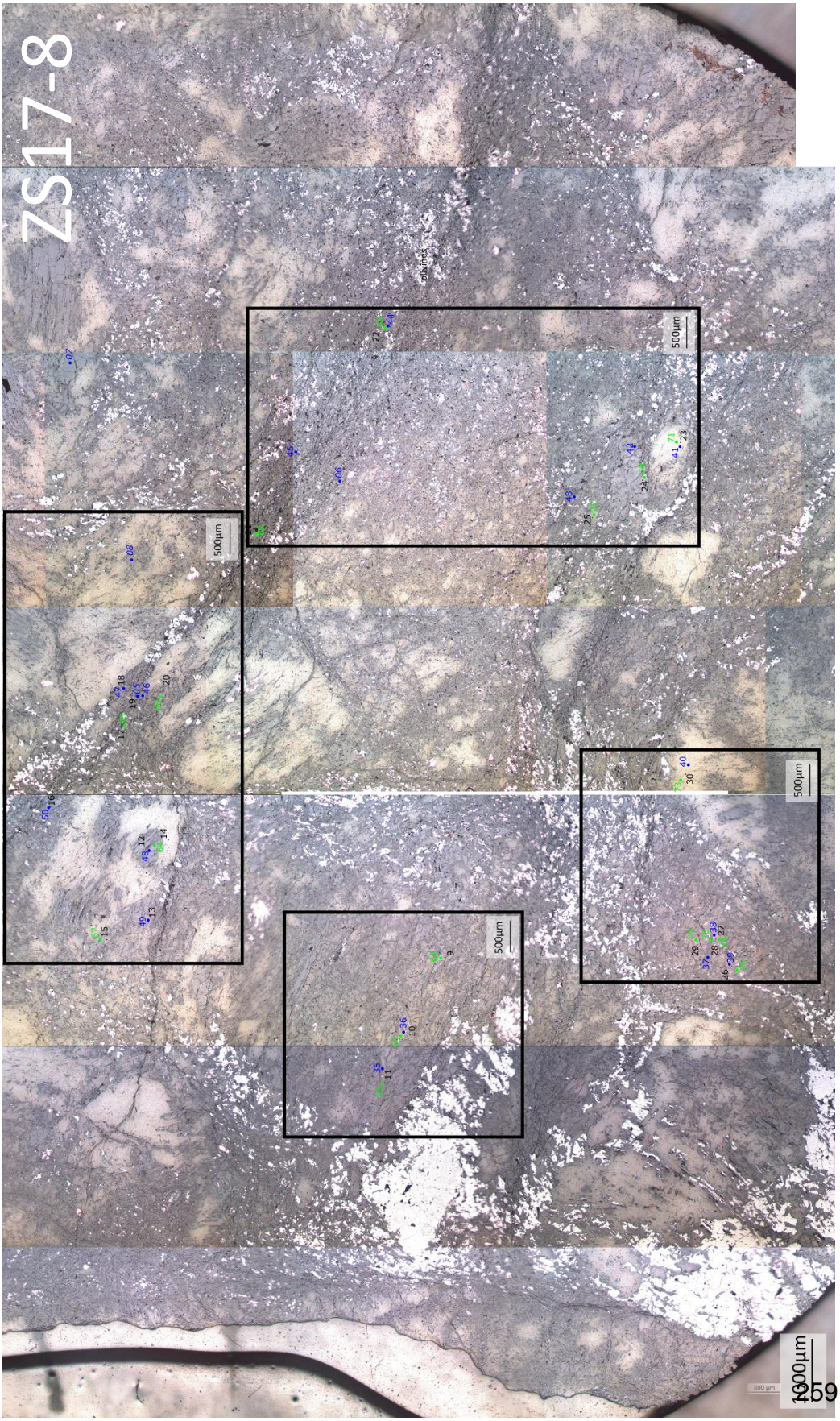
ZS17-8
1000µm
500µm
500µm
500µm
500µm

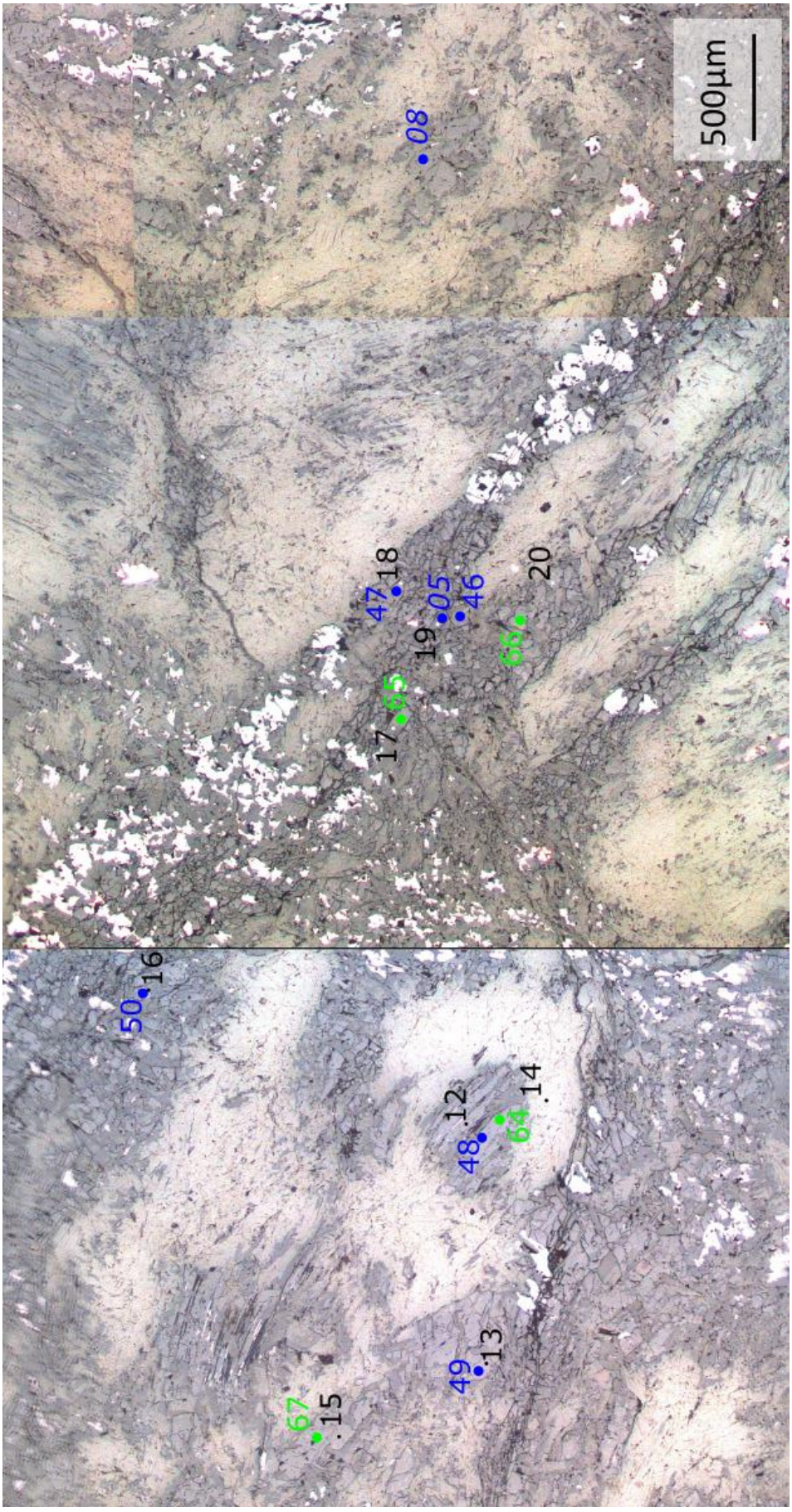

ZS17-8 *closeups*

ZS17-8 *closeups*

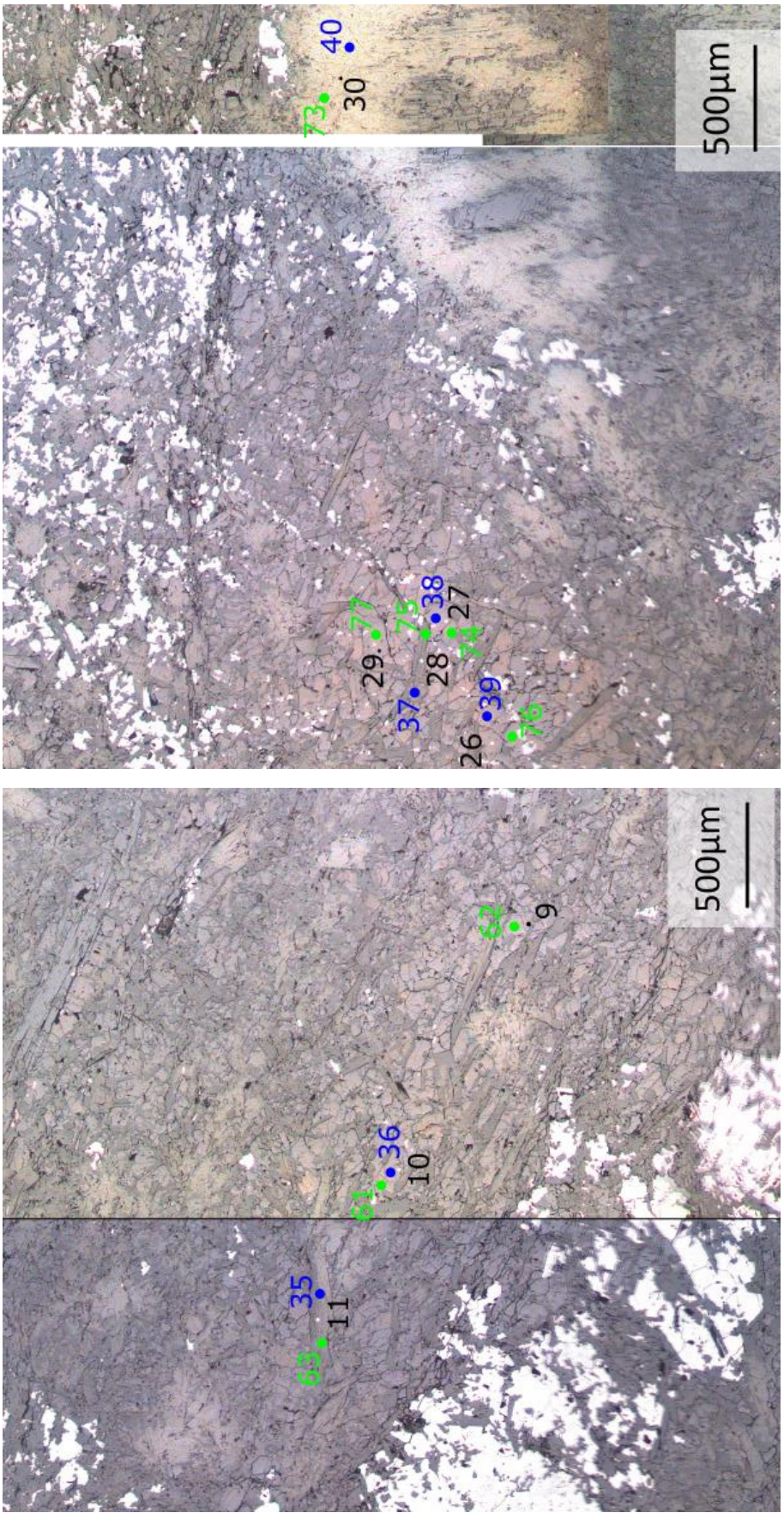

ZS17-8 *closeups*

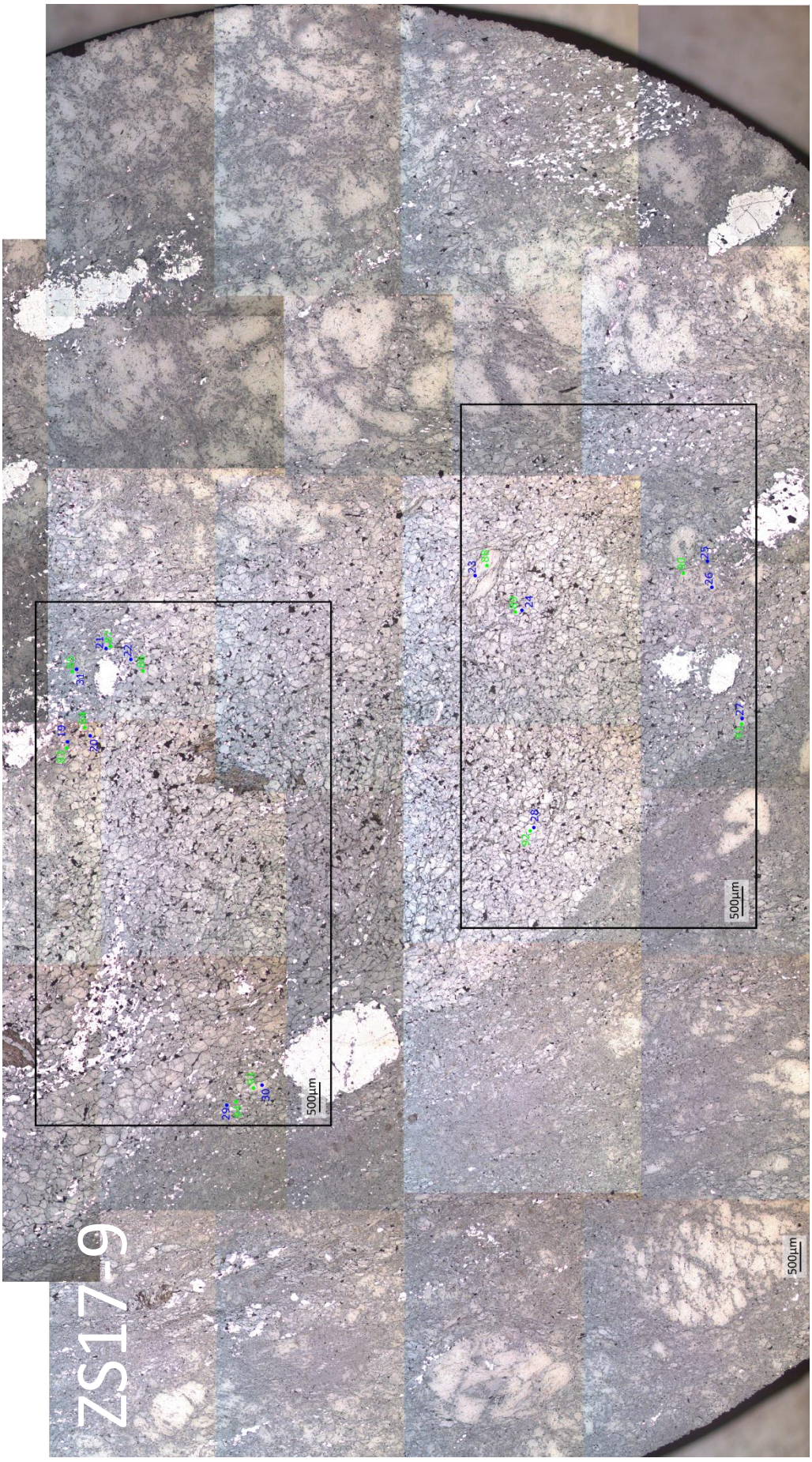
ZS17-9
500µm
500µm
500µm

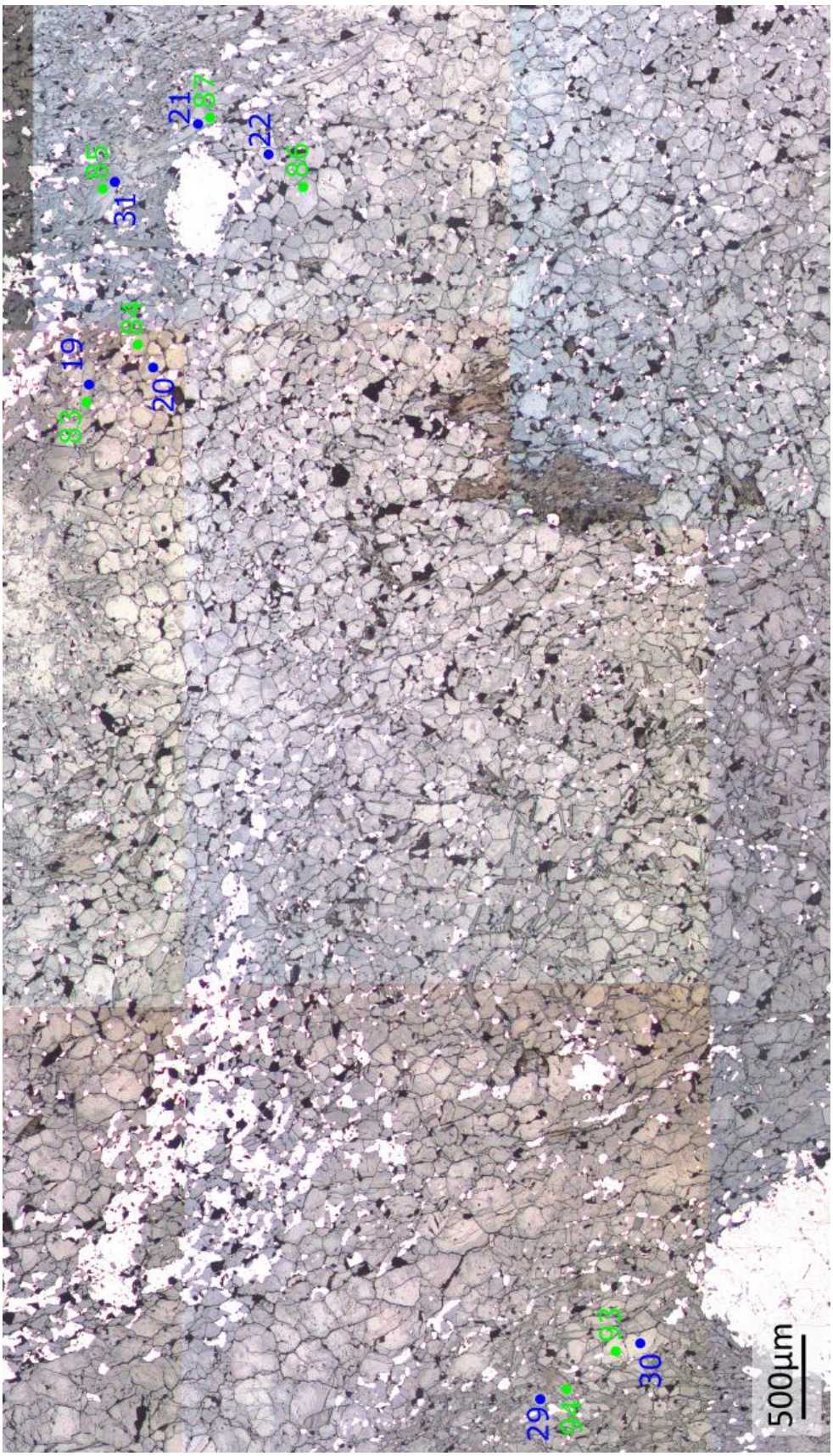

ZS17-9 *closeups*

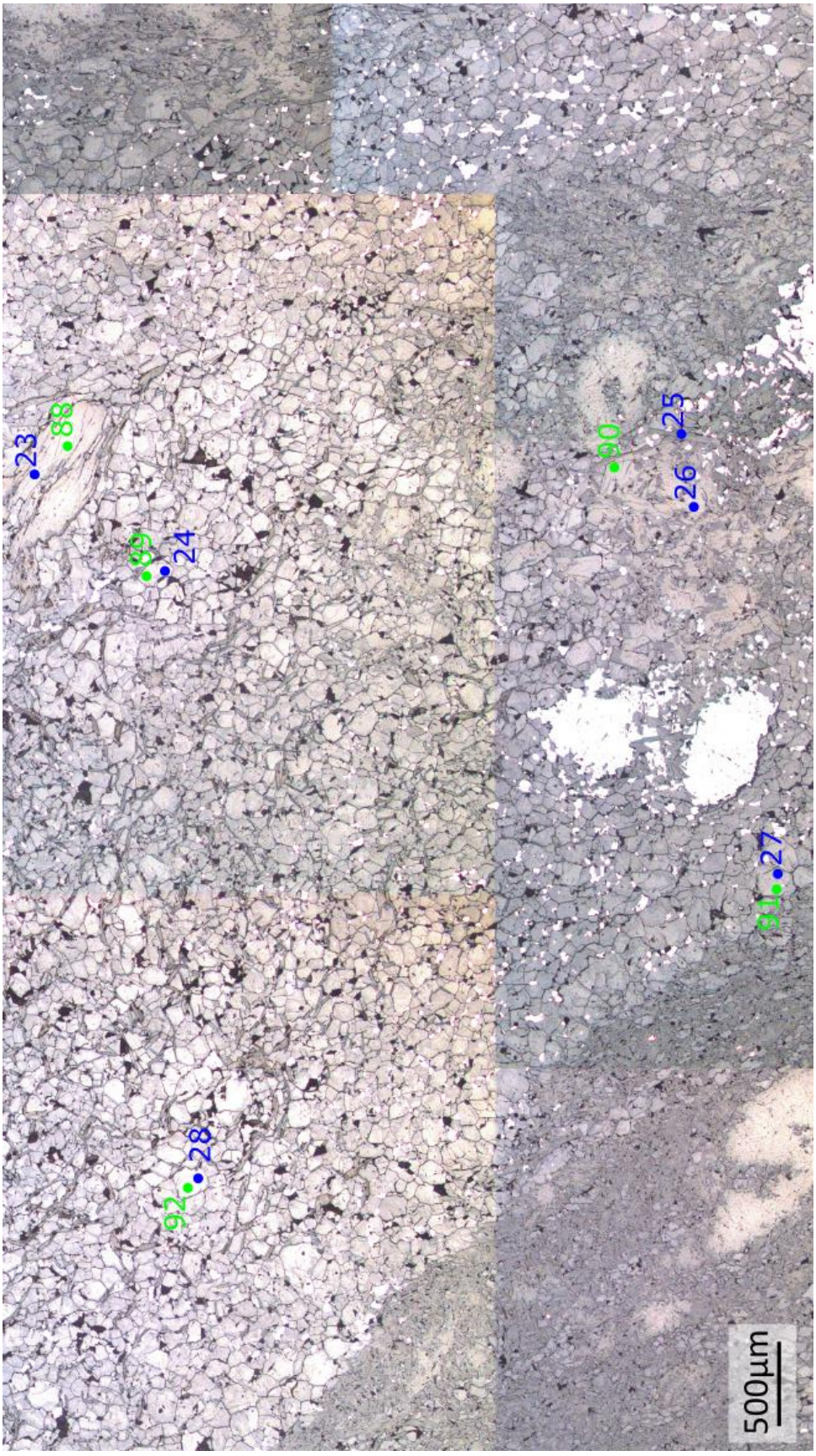

ZS17-9 *closeups*

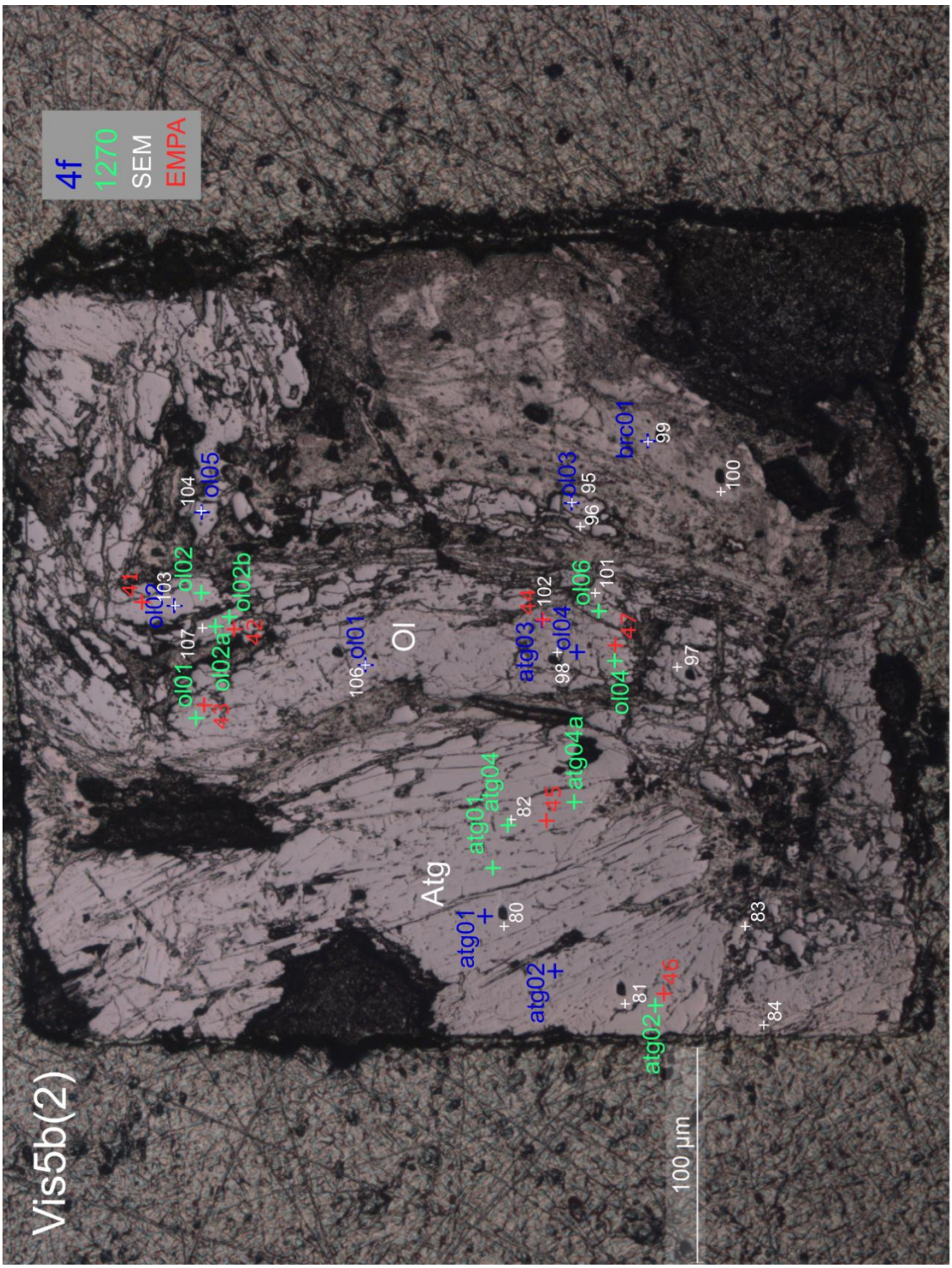
4f
1270
SEM
EMPA
Vis5b(2)
100 µm
Ol
Atg
ol01
ol02
ol02a
ol02b
ol03
ol04
ol05
ol06
atg01
atg02
atg03
atg04
atg04a
brc01
41
42
43
44
45
46
47

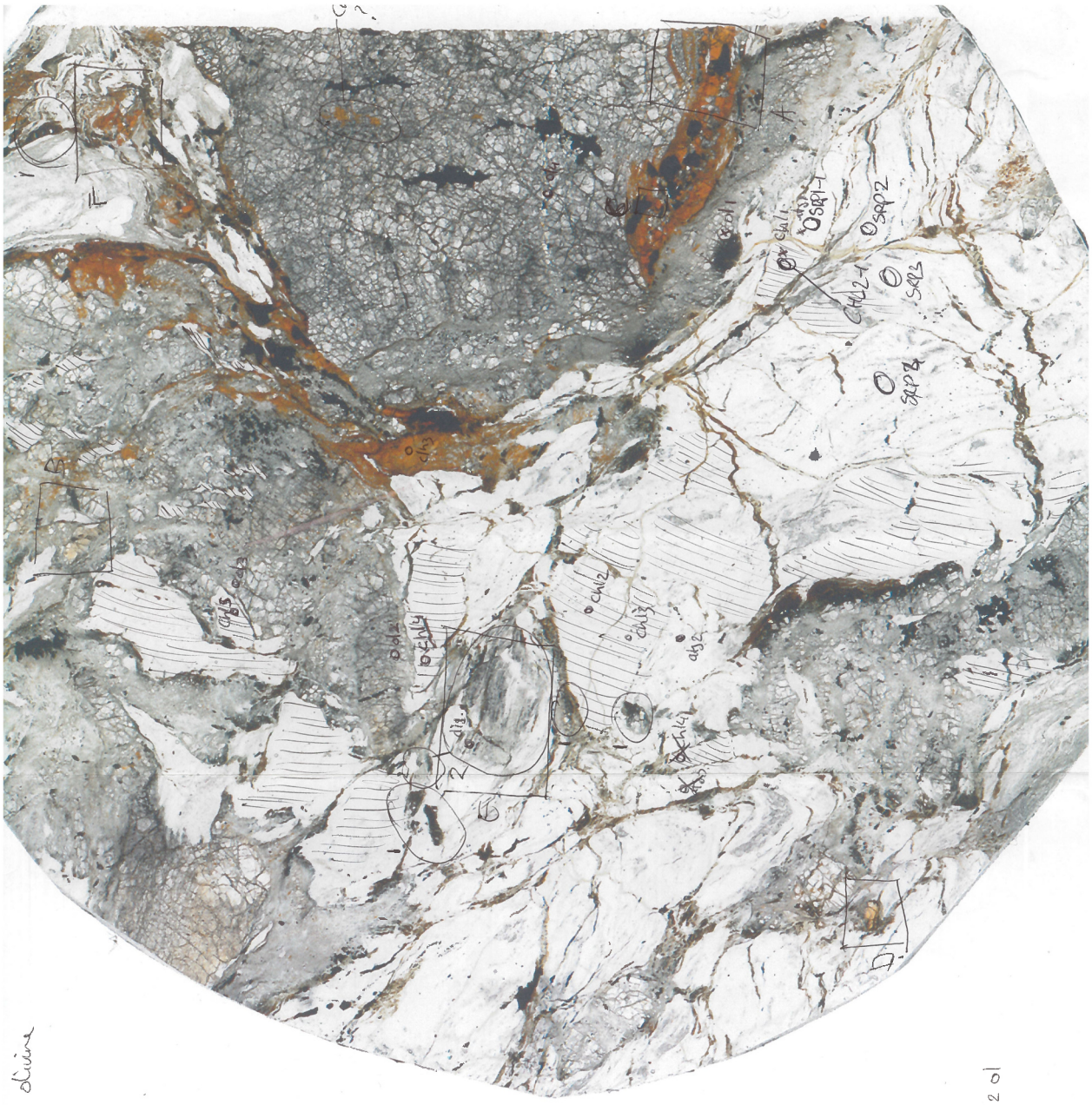
1 mesh-textured olivine
2 relic cpx
/// chlorite?
dark in xpol
Chm = Chm + 2 ol
n=4 n>2

C.1.2 Extra samples

These are the images and locations of each probe pit (numbered) collected in addition to the data collected for Chapter 3. These samples are not discussed in the thesis (except ODP6 and ODP7), but their data is presented in Appendix A. ZS17-1 to -7, DC-8 and DC27a1 images are only available in the digital appendix. Unless otherwise stated, green colours indicate 1270 pits, blue numbers indicate 4f pits an white/black numbers indicate EMPA pits.

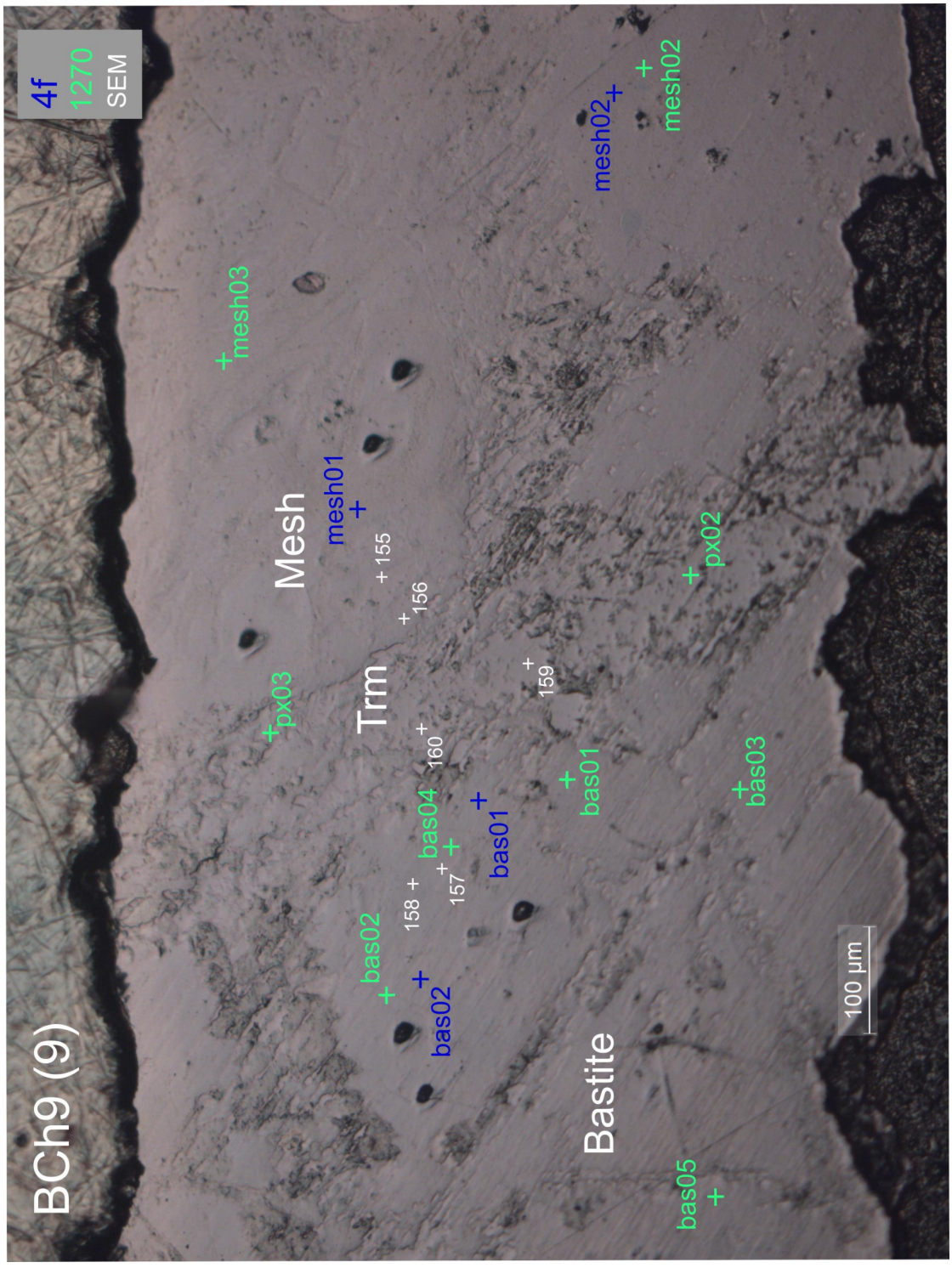
BCh9 (9)
4f
1270
SEM
Mesh
Trm
Bastite
mesh03
mesh01
mesh02
mesh02
px03
px02
bas01
bas01
bas02
bas02
bas03
bas04
bas05
155
156
157
158
159
160
100 µm

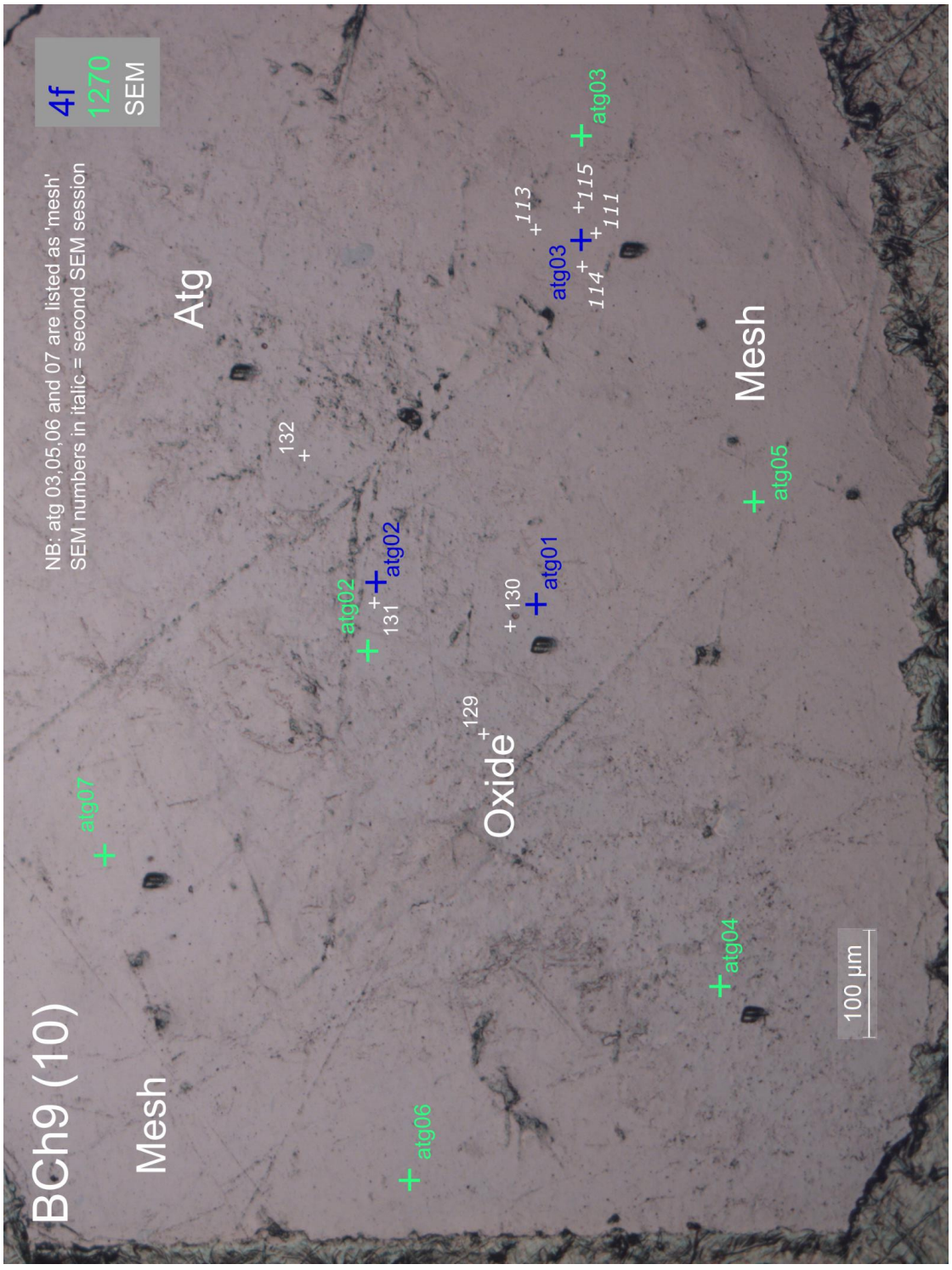
BCh9 (10)
4f
1270
SEM
NB: atg 03,05,06 and 07 are listed as 'mesh'
SEM numbers in italic = second SEM session
Mesh
Atg
Oxide
Mesh
atg07
atg06
atg02
atg02
atg01
atg03
atg03
atg04
atg05
129
130
131
132
113
114
115
111
100 µm

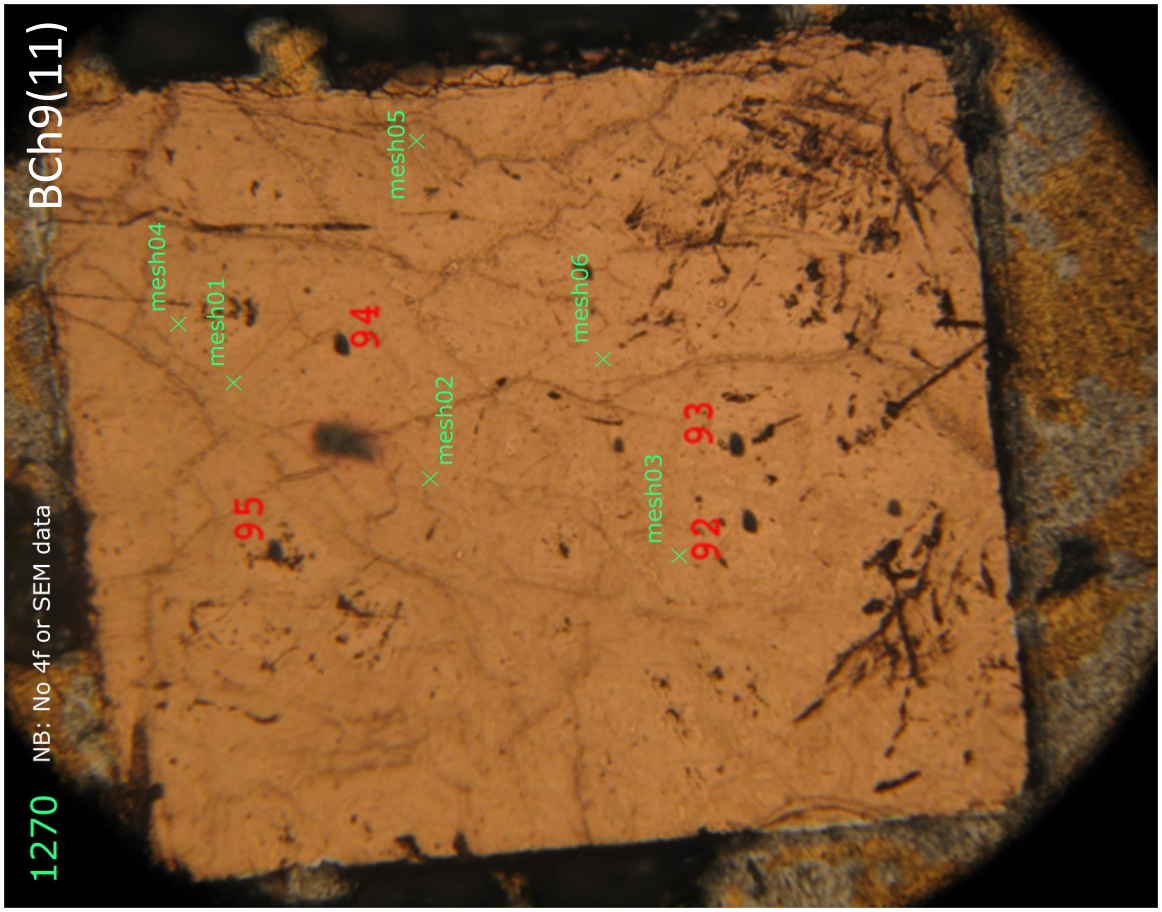
BCh9(11)
1270
NB: No 4f or SEM data
mesh04
mesh01
mesh05
mesh02
mesh06
mesh03
95
94
93
92

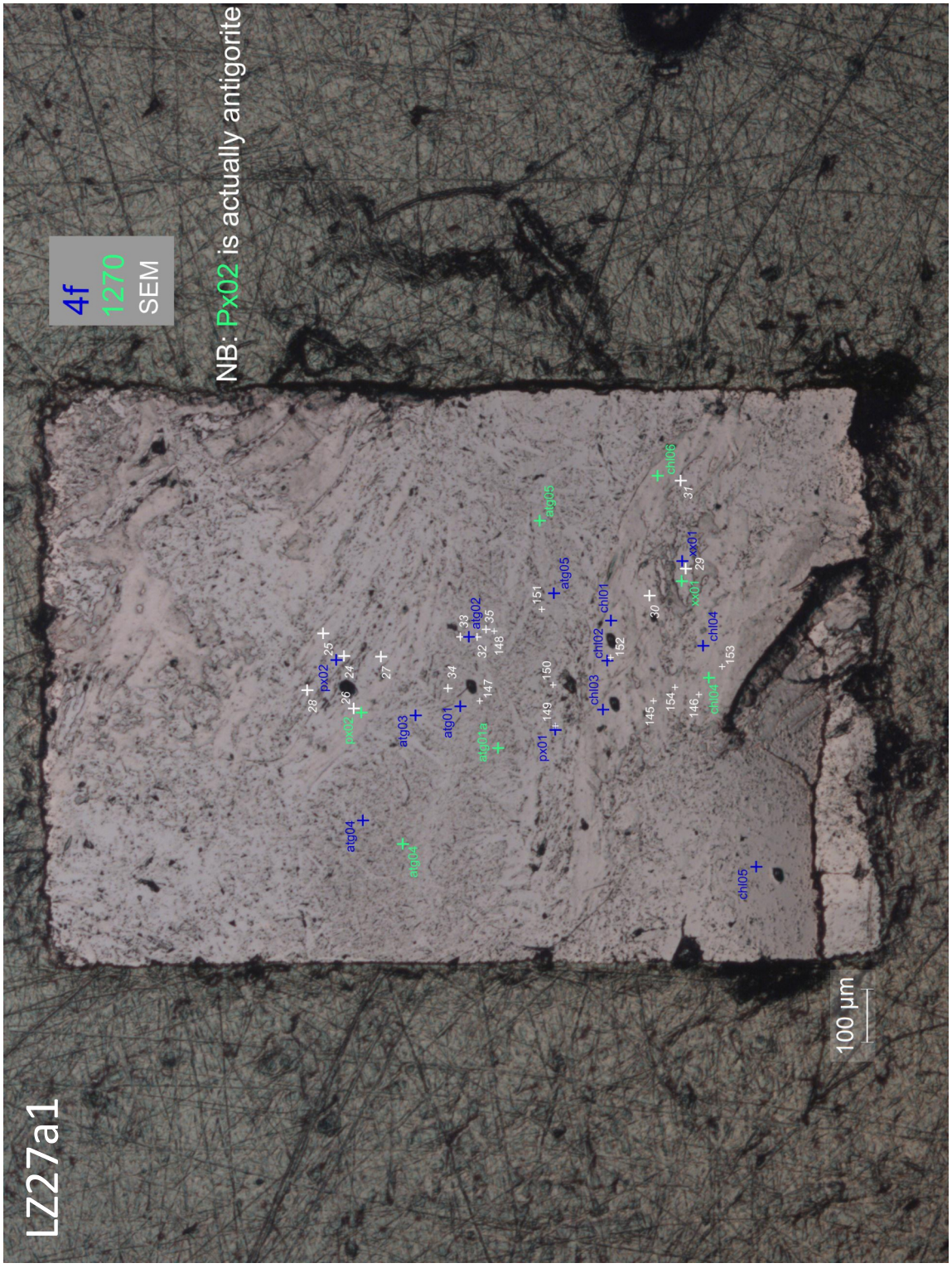
LZ27a1
4f
1270
SEM
NB: Px02 is actually antigorite
100 µm

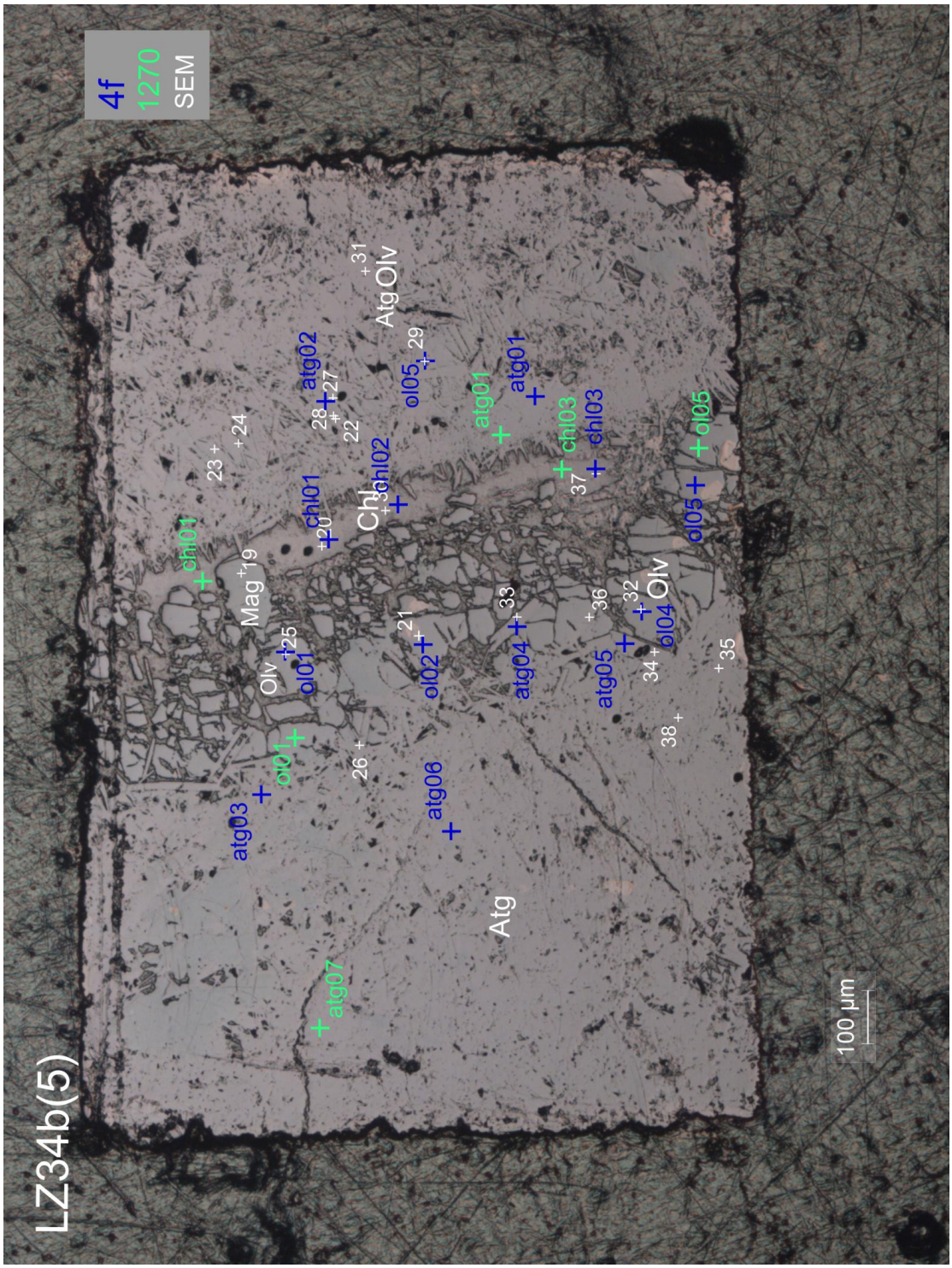
LZ34b(5)
4f
1270
SEM
100 µm
Atg
Olv
Mag
Chl
atg01
atg02
atg03
atg04
atg05
atg06
atg07
chl01
chl02
chl03
ol01
ol02
ol04
ol05

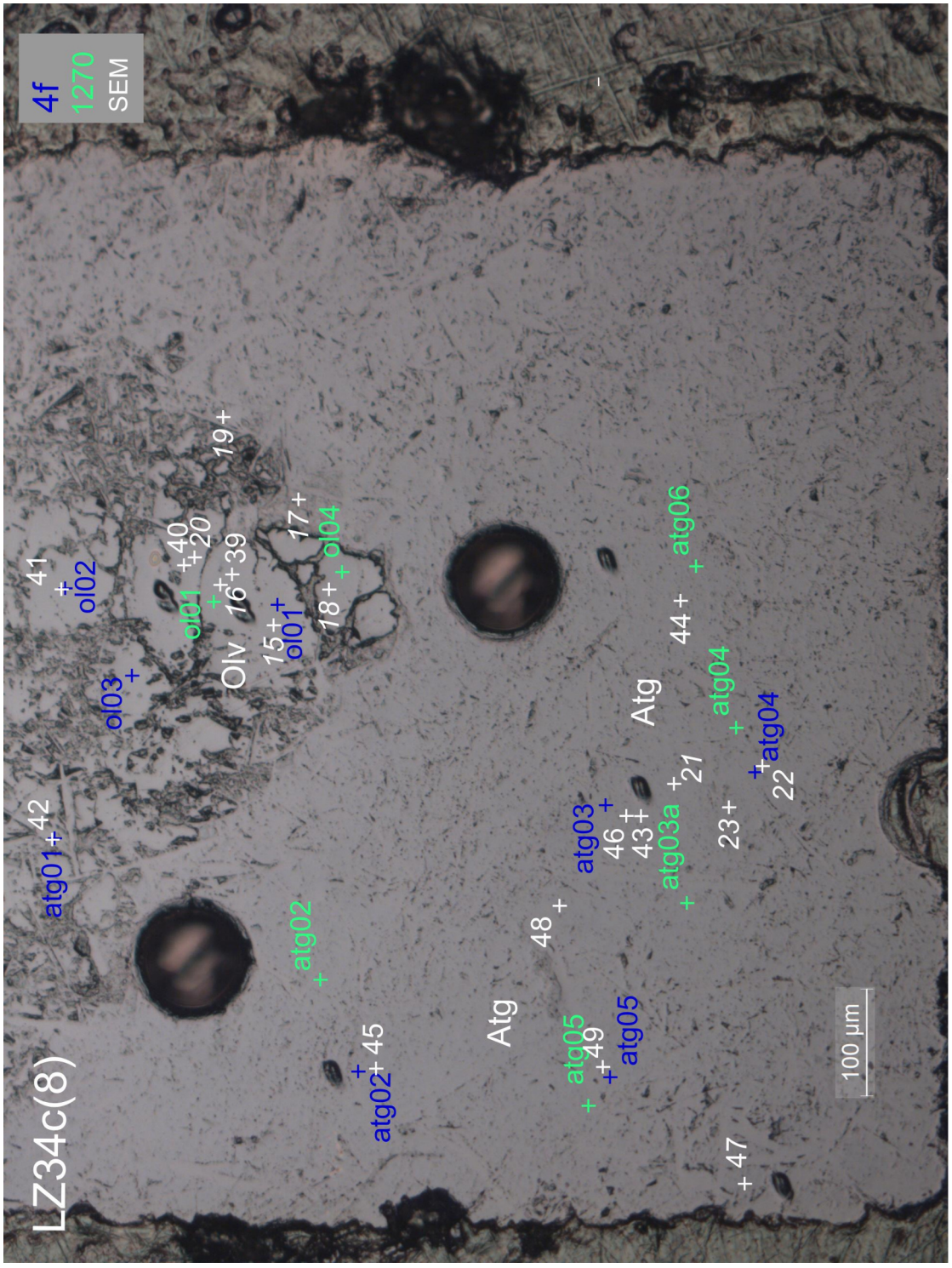
4f
1270
SEM
LZ34c(8)
atg01
42
41
ol02
ol03
ol01
40
20
Olv
16
39
19
15
ol01
17
18
ol04
atg02
atg02
45
Atg
48
atg05
49
atg05
atg03
46
43
atg03a
Atg
21
44
atg06
atg04
23
atg04
22
47
100 µm

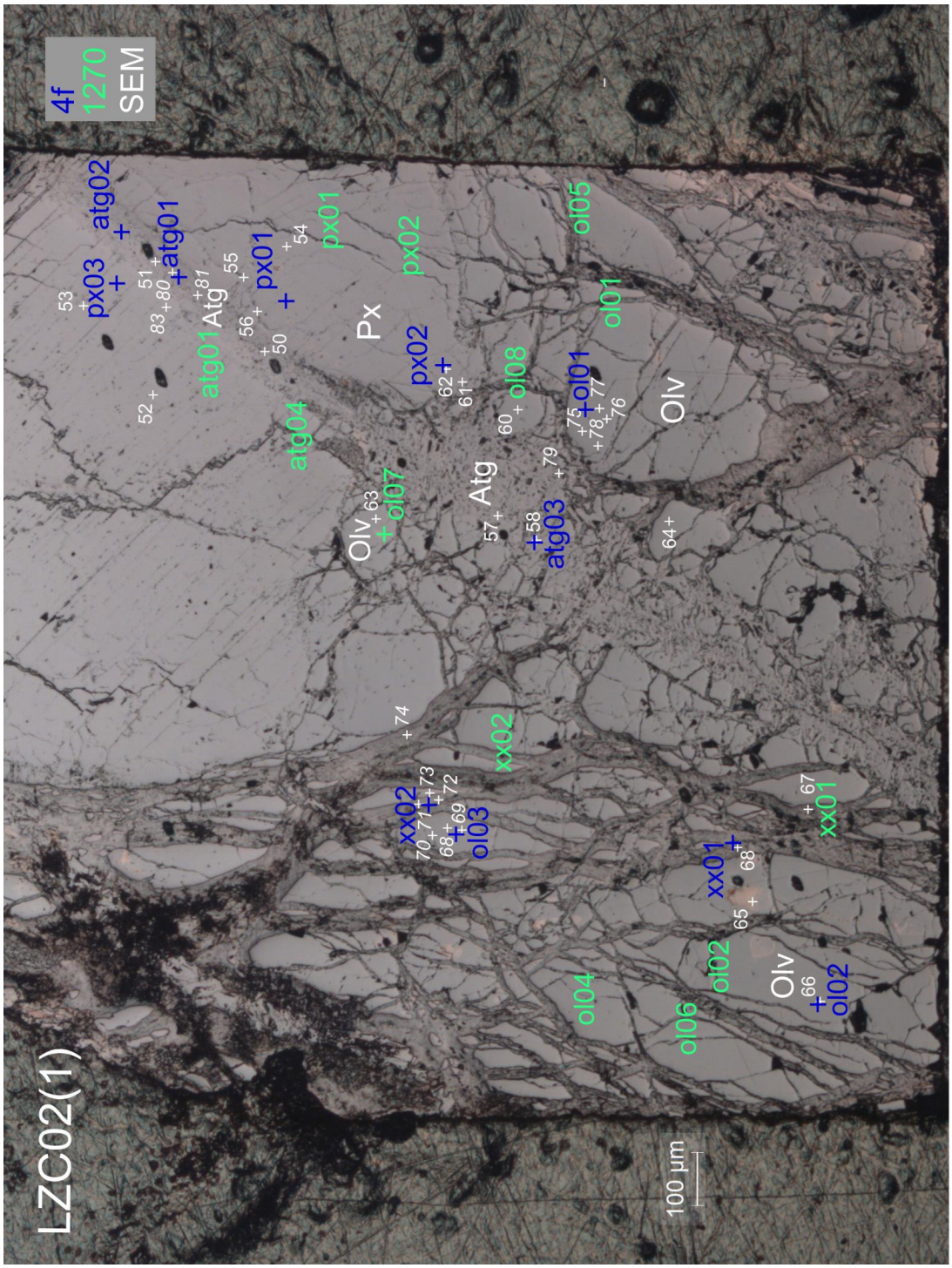
LZC02(1)
4f
1270
SEM
100 µm
px03
atg02
atg01
Atg
px01
atg04
Px
px02
ol07
Olv
Atg
ol08
ol01
ol05
atg03
xx02
ol03
xx01
ol04
ol06
ol02
xx01
Olv
ol02

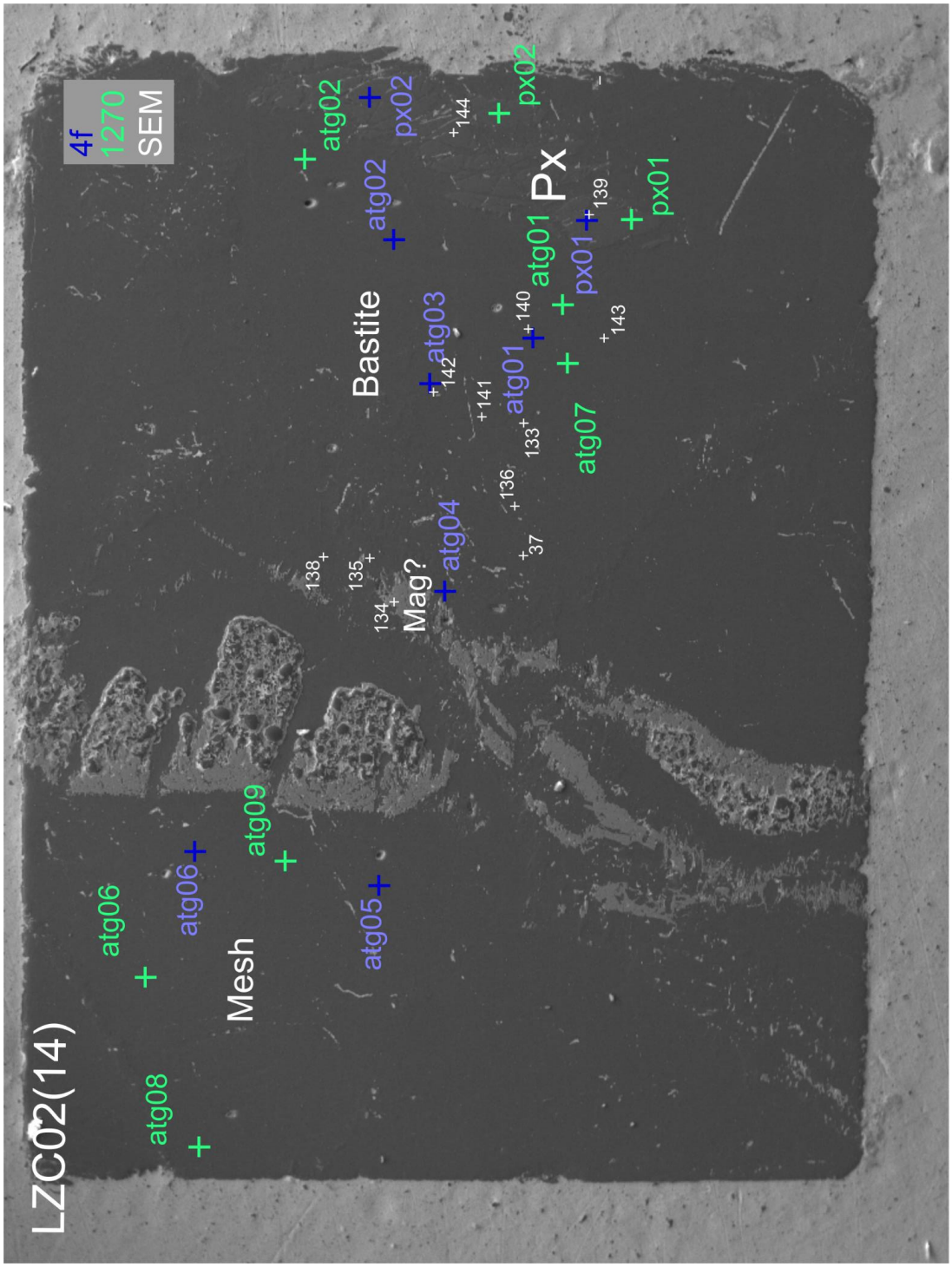
LZC02(14)
4f
1270
SEM
atg08
atg06
atg06
Mesh
atg09
atg05
atg02
px02
atg02
Bastite
px02
atg03
atg04
Mag?
atg01
atg01
Px
atg07
px01
px01
atg02
138
135
134
136
37
133
141
142
140
143
139
144

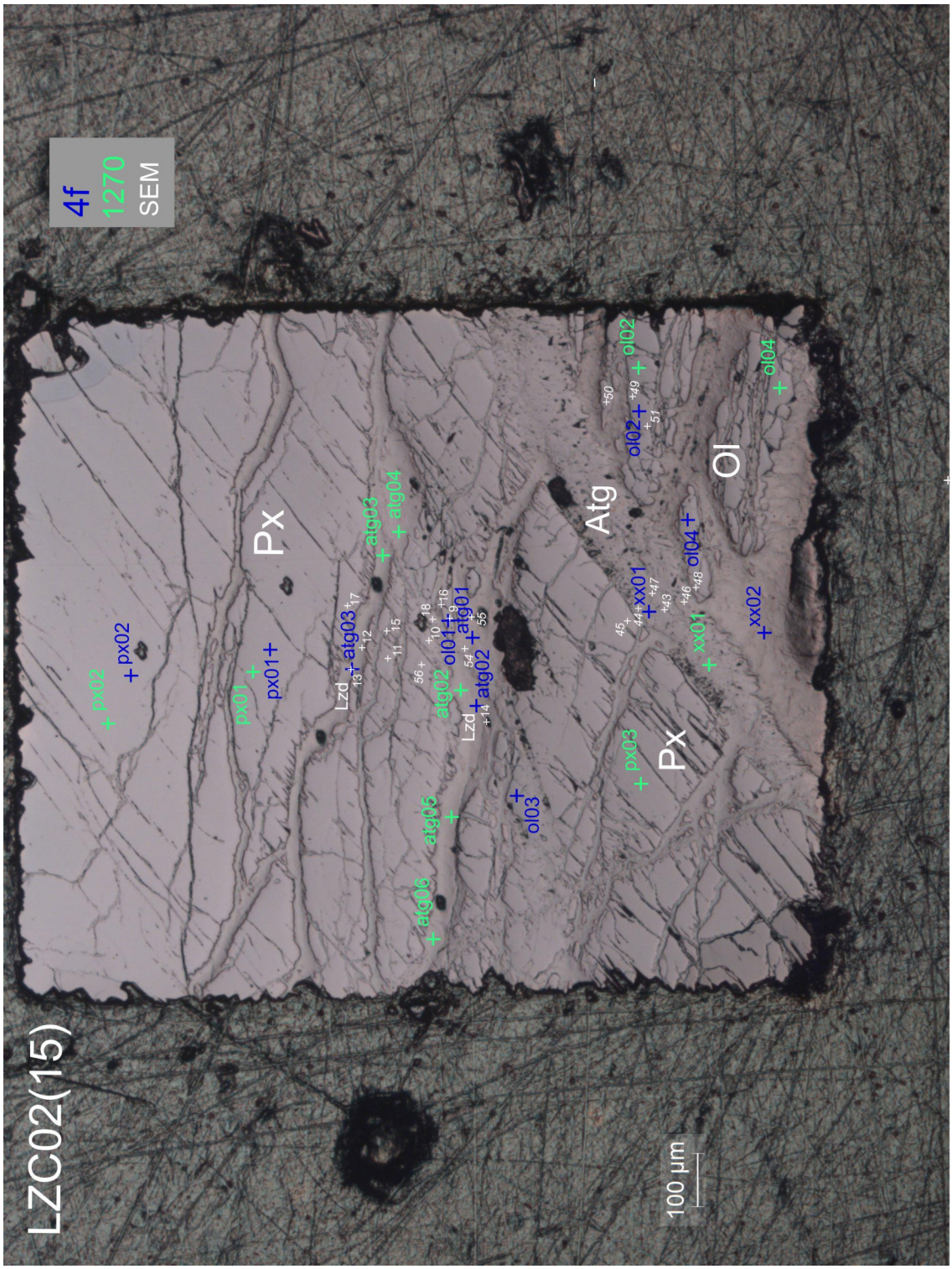
LZC02(15)
4f
1270
SEM
Px
Atg
Ol
Px
px02
px02
px01
px01
Lzd
atg03
atg03
atg04
atg02
ol01
atg01
Lzd
atg02
atg05
atg06
ol03
px03
ol02
ol02
xx01
xx01
ol04
ol04
xx02
100 µm

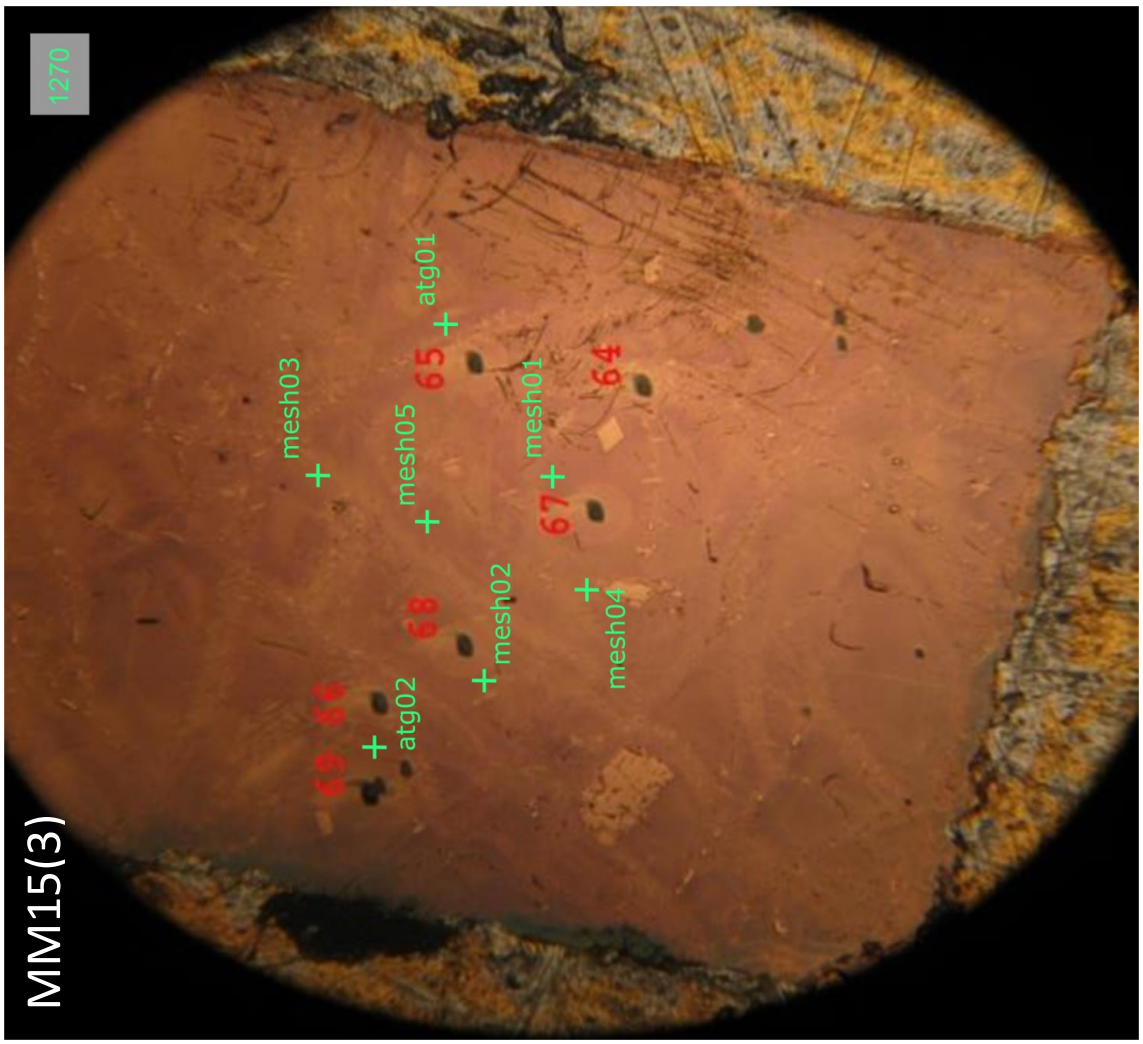
1270
MM15(3)
mesh03
atg01
mesh05
65
64
mesh01
67
mesh02
68
mesh04
66
69
atg02

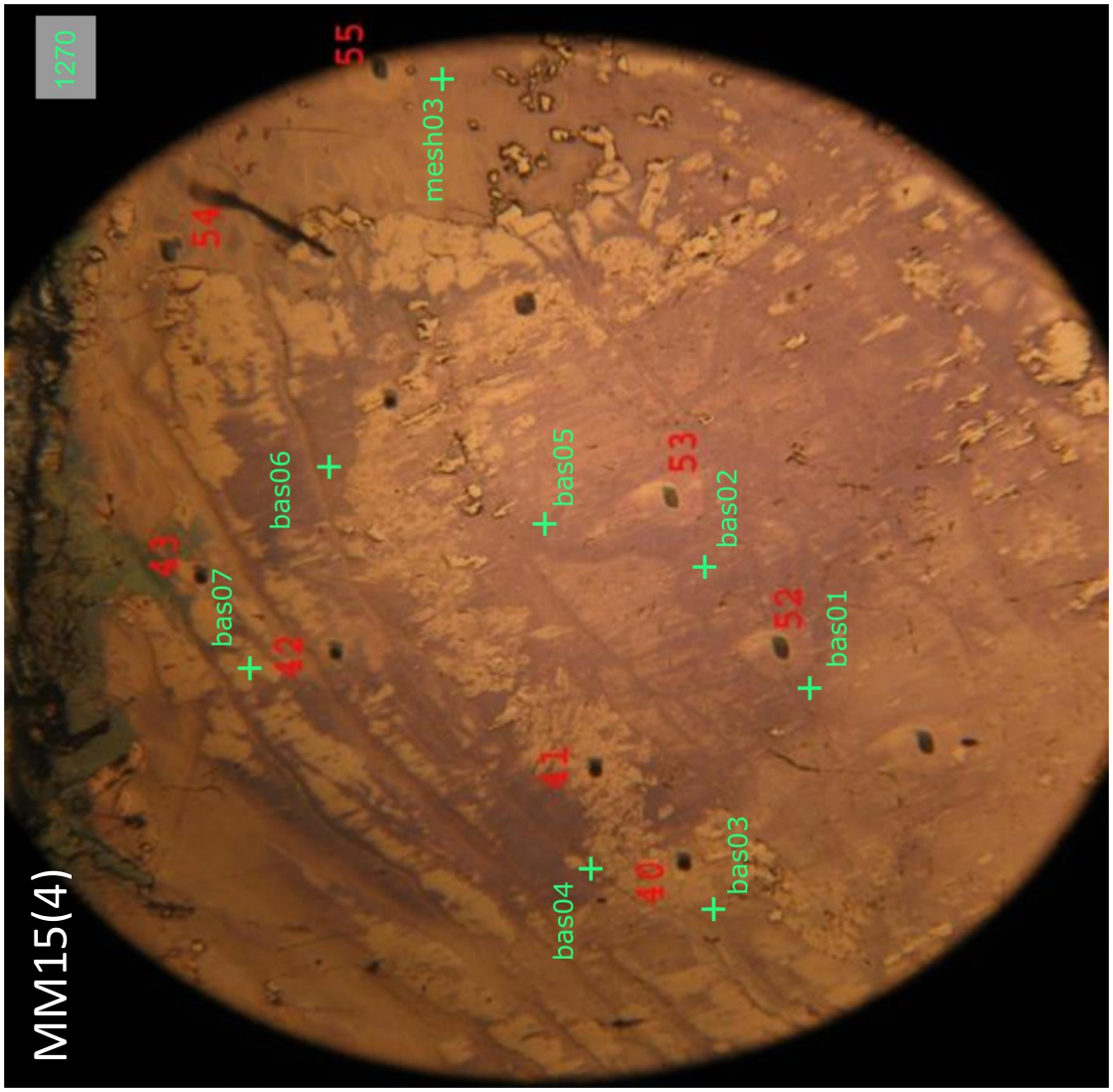
MM15(4)
1270
55
mesh03
54
43
bas07
42
bas06
bas05
53
bas02
52
bas01
41
bas04
40
bas03

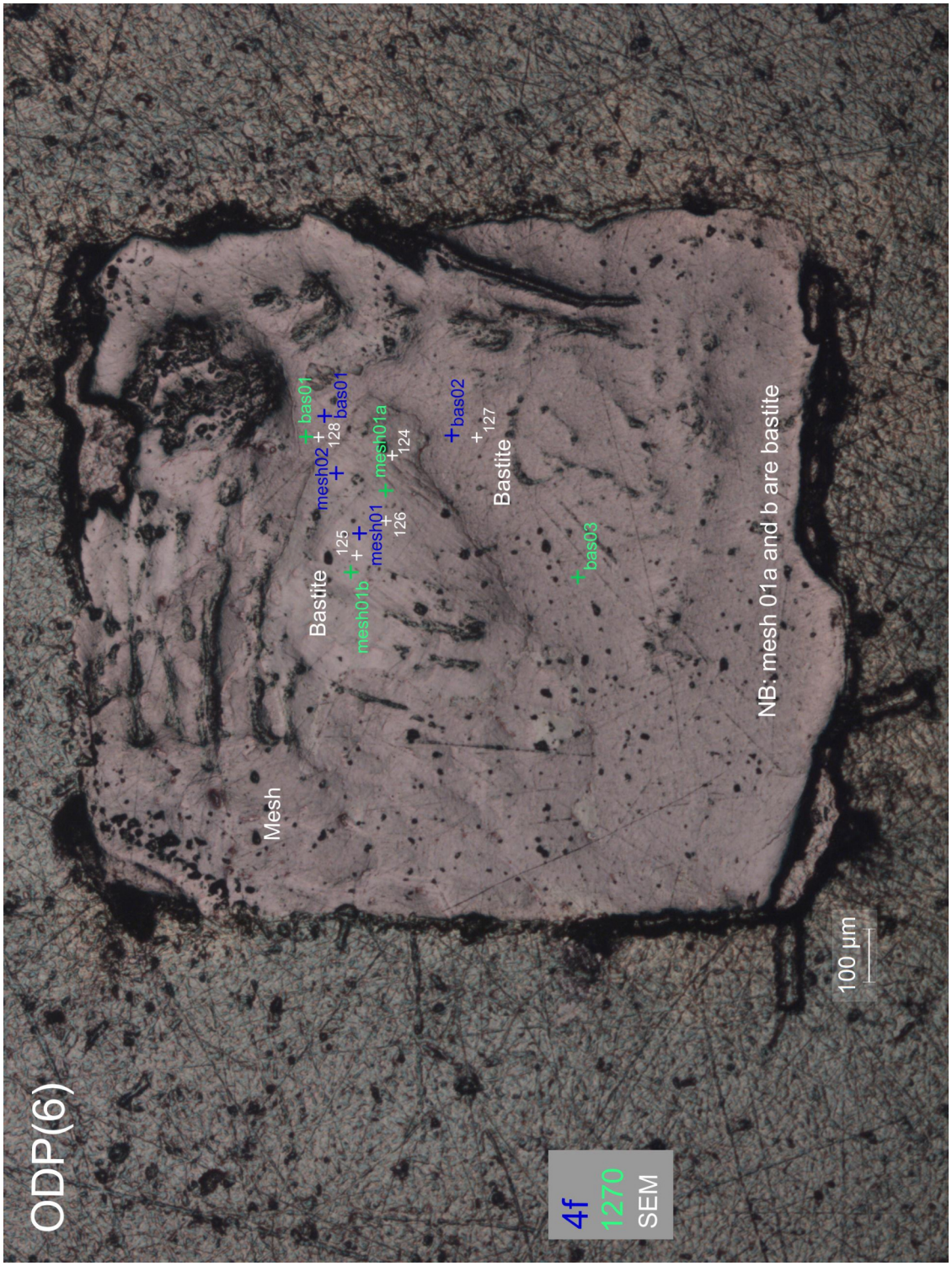
ODP(6)
4f
1270
SEM
Mesh
Bastite
Bastite
mesh01b
125
mesh01
126
mesh02
128
mesh01a
124
bas01
bas01
bas02
127
bas03
NB: mesh 01a and b are bastite
100 µm

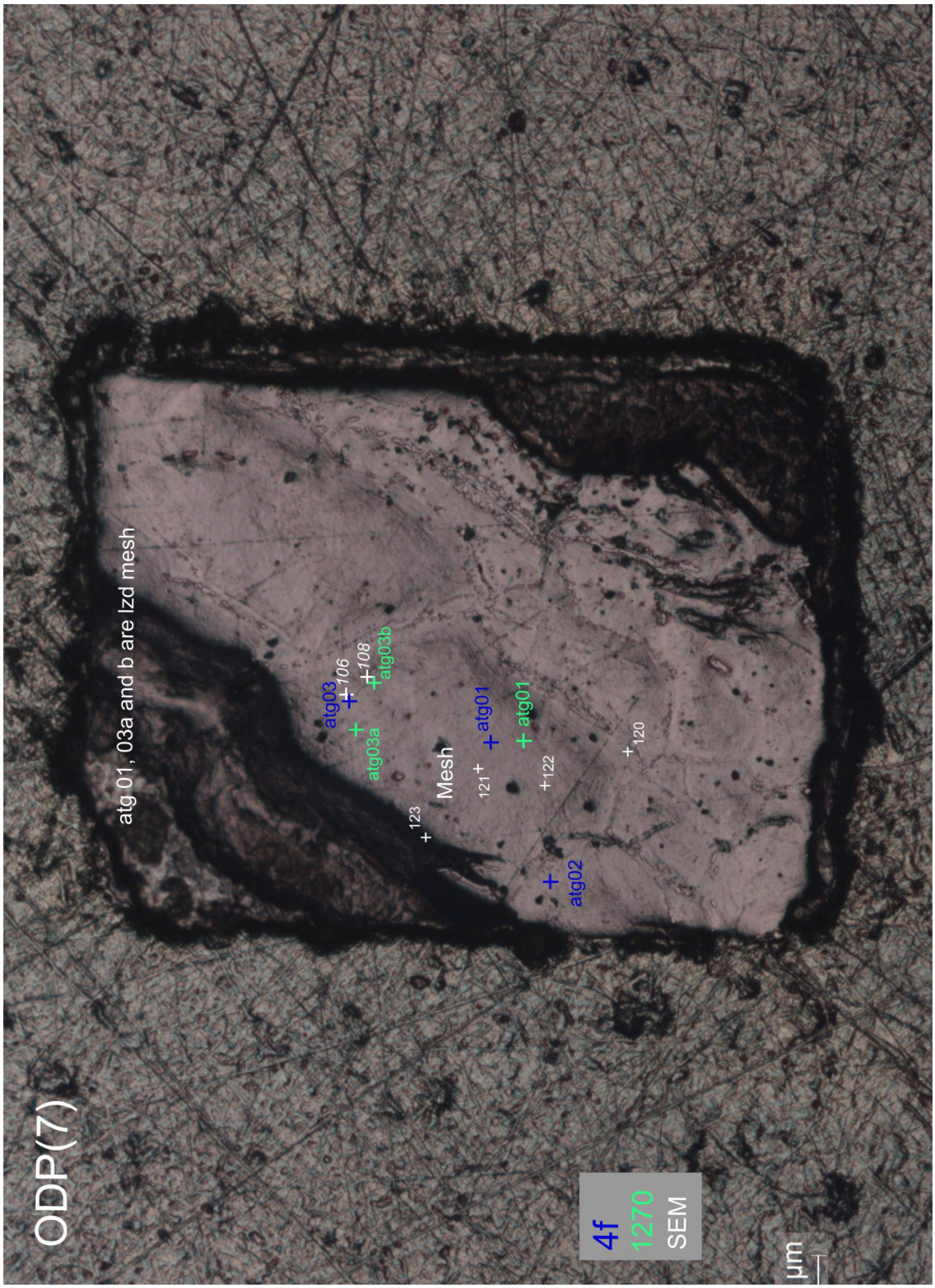
ODP(7)
atg 01, 03a and b are lzd mesh
atg03
106
108
atg03b
atg03a
Mesh
123
121
atg01
atg01
122
120
atg02
4f
1270
SEM
µm

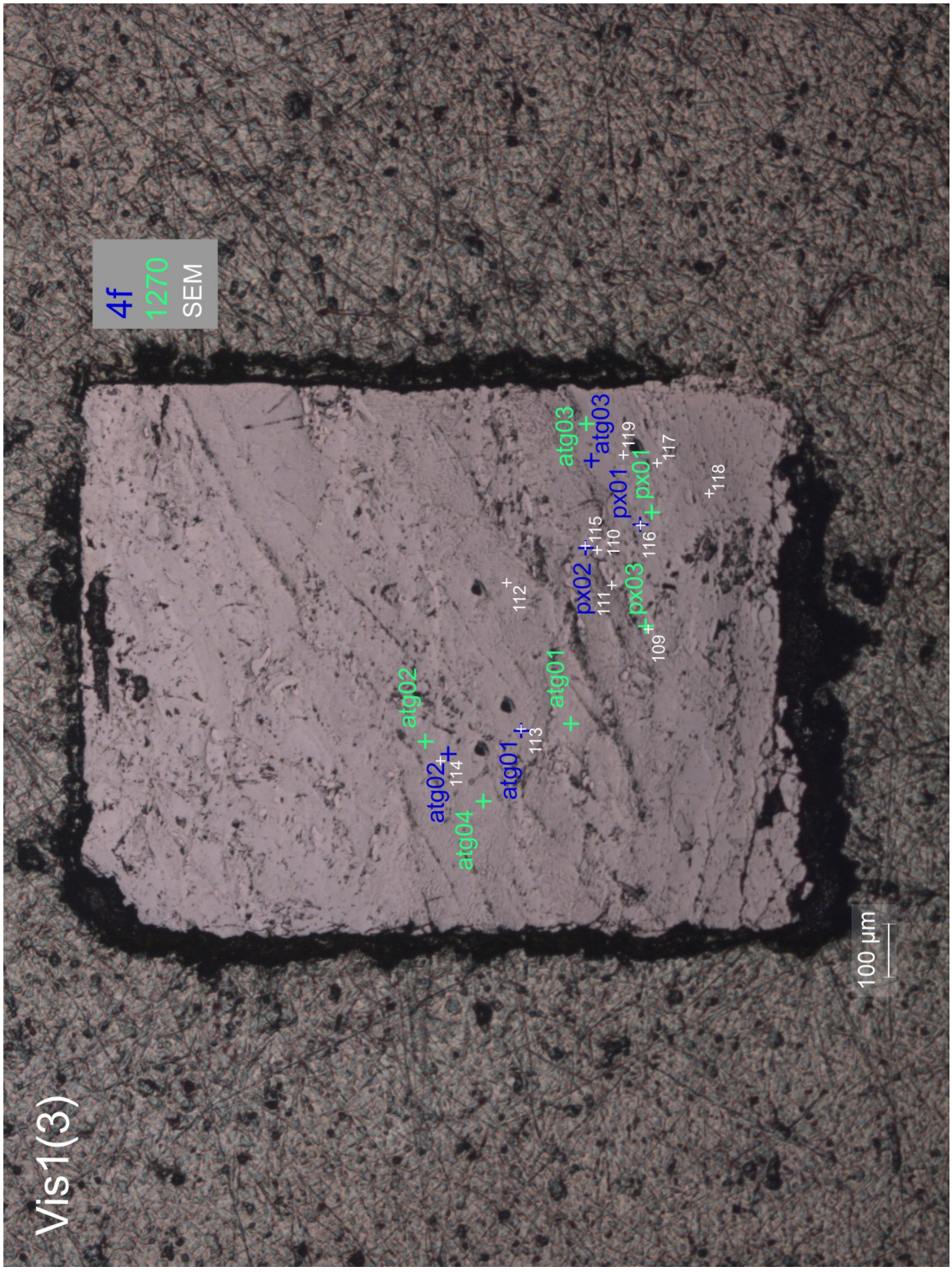
Vis1(3)
4f
1270
SEM
atg02
atg02
atg04
atg01
atg01
atg03
atg03
px02
px01
px03
px01
109
110
111
112
113
114
115
116
117
118
119
100 µm

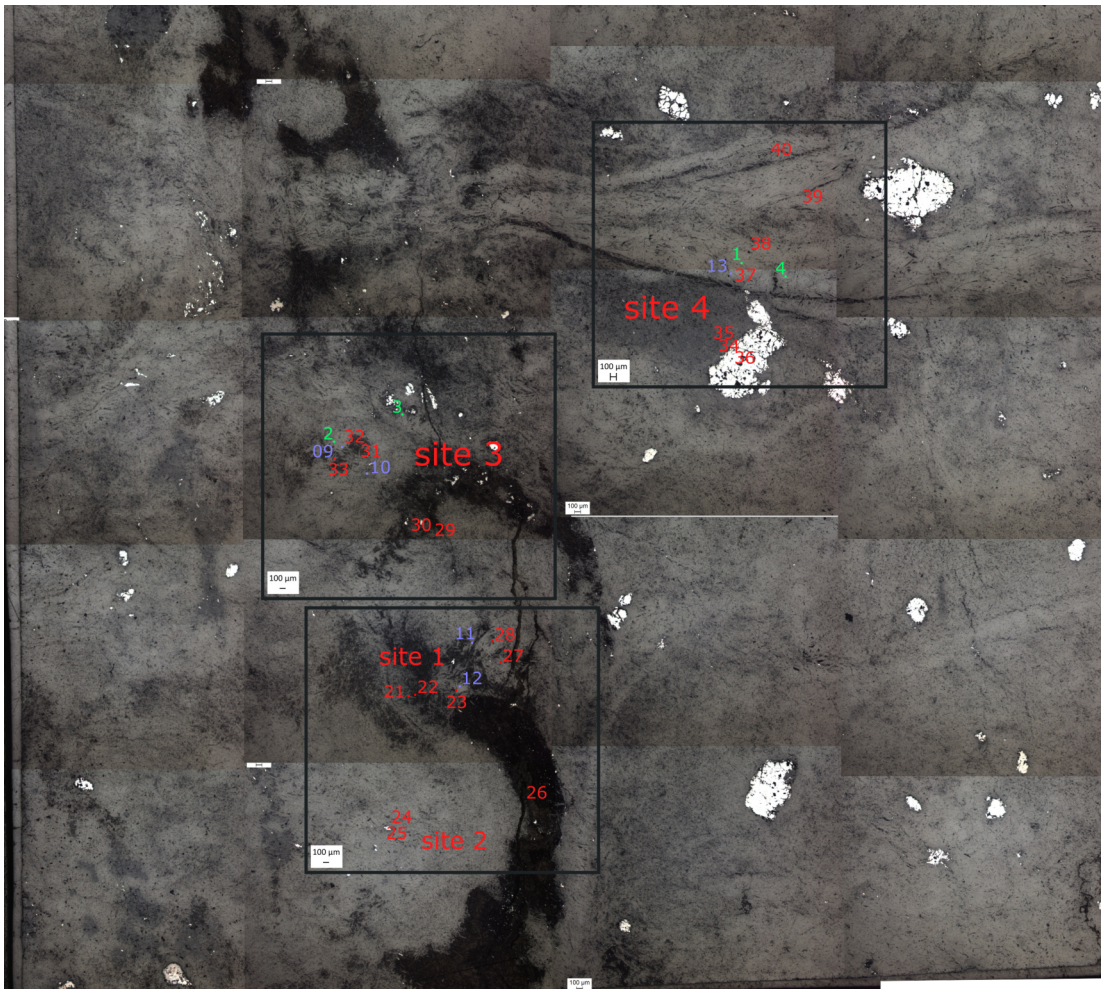

Figure C.1: Whole image of sample AZO-13-S with pit locations.

C.2 Sample images for Chapter 4: Serpentinites of Valmalenco

These are the images and locations of each probe pit (numbered) collected in addition to the data collected for Chapter 4. Unless otherwise stated, green colours indicate 1270 pits, blue numbers indicate 4f pits an white/black numbers indicate EMPA pits.

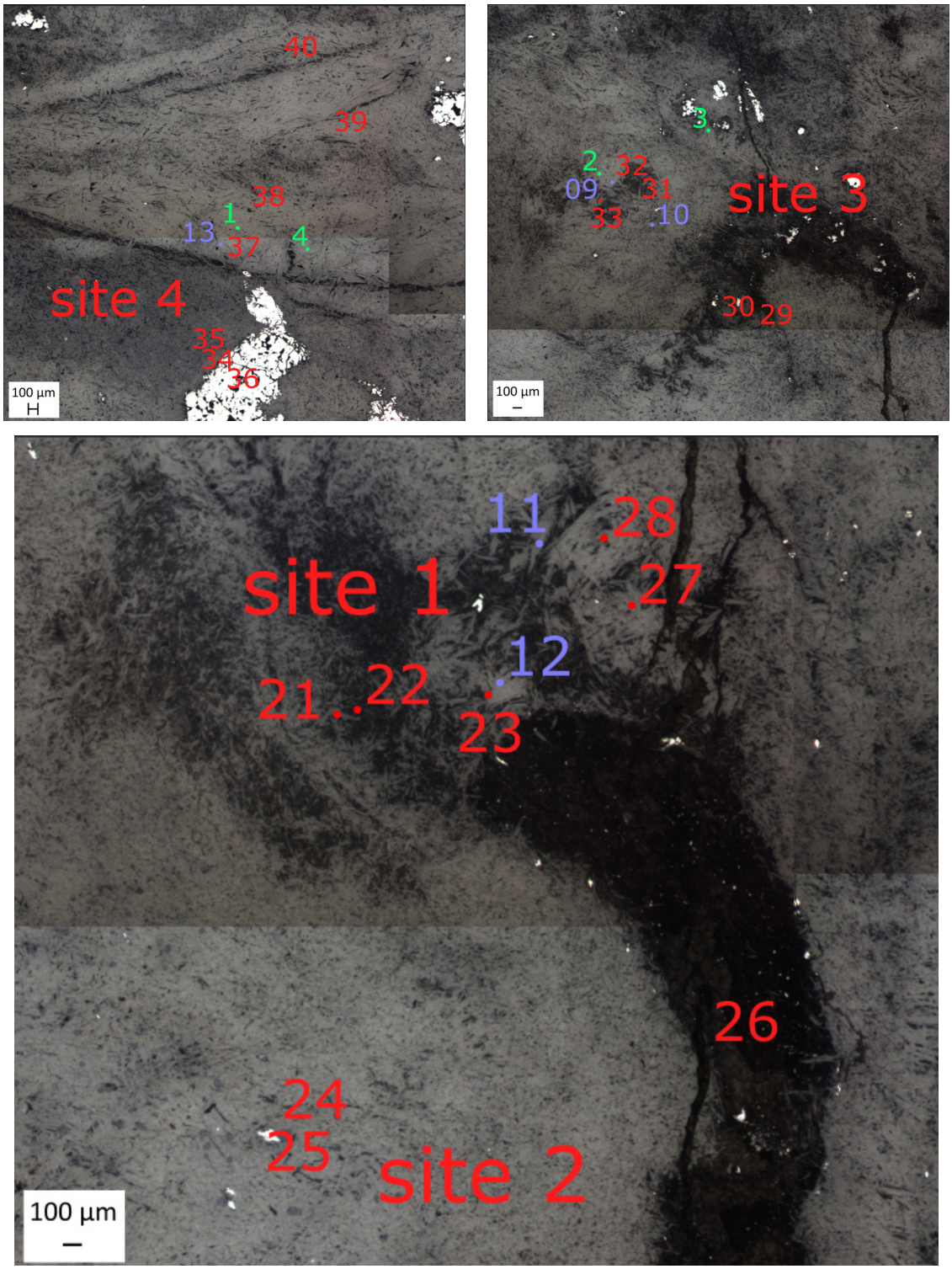

Figure C.2: Close up images of the ion probe and EMPA analytical pit locations with pit numbers that can be used to link to the data collected at that point.

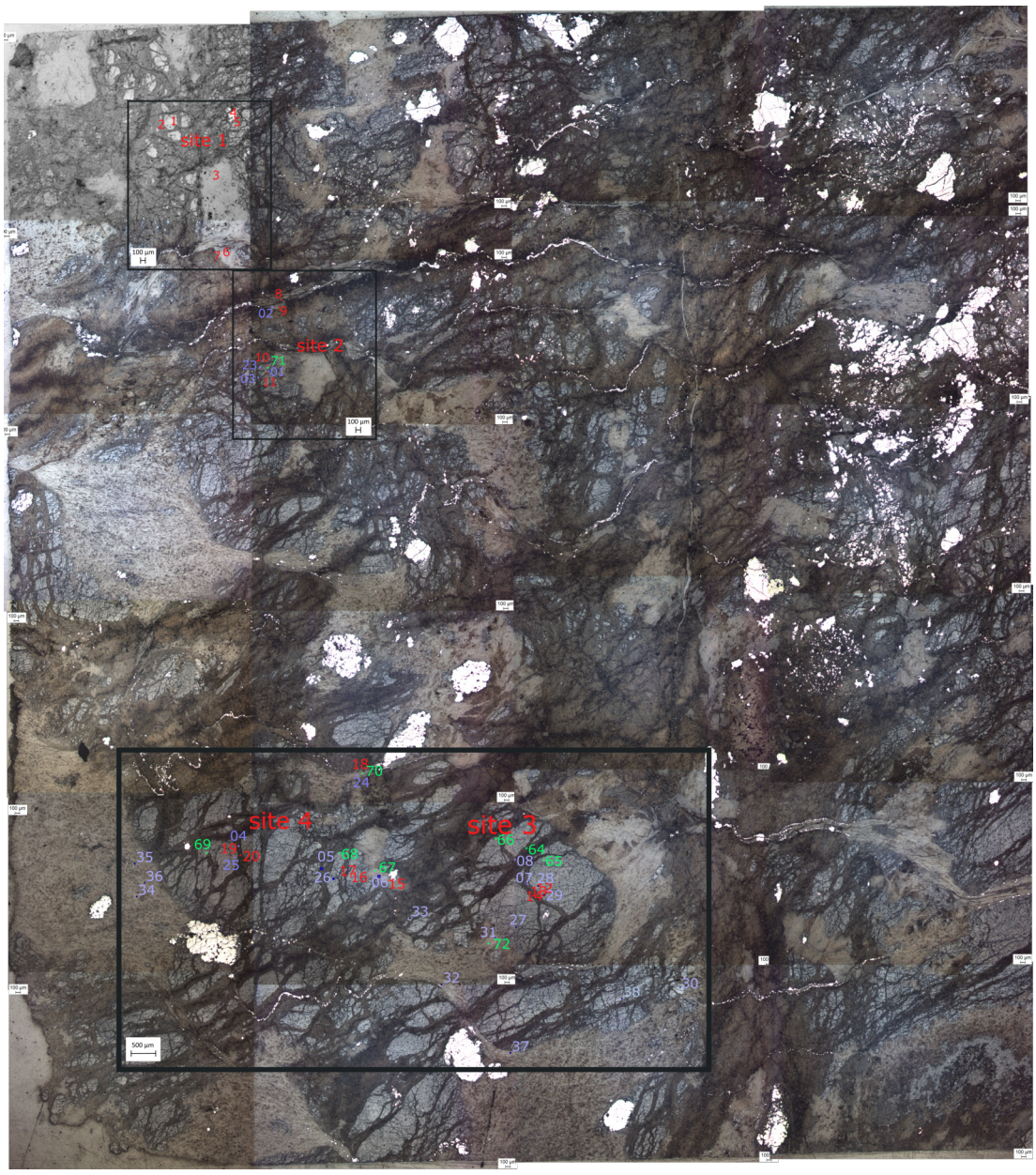

Figure C.3: Whole image of sample AZO-13 with pit locations.

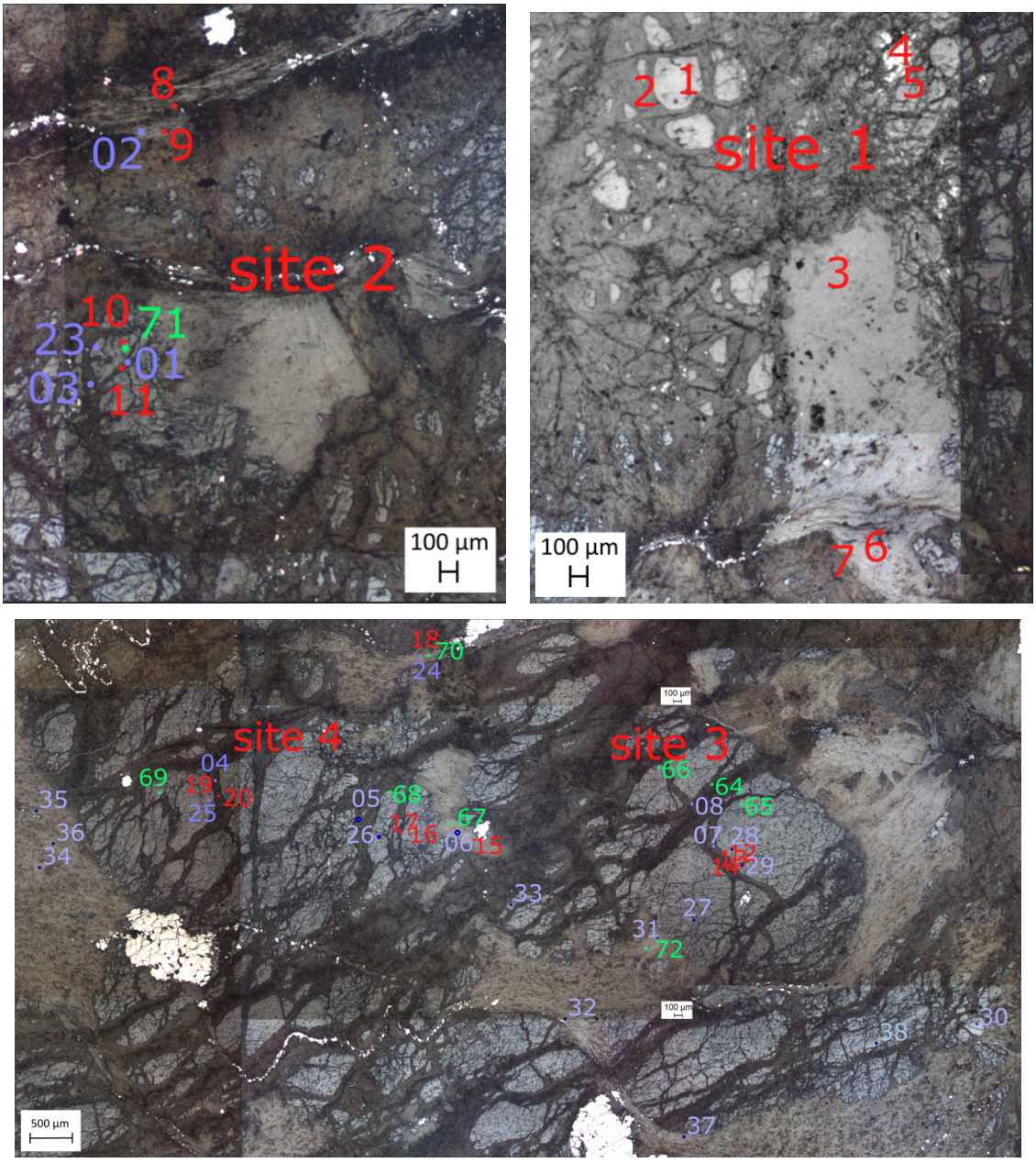

Figure C.4: Close up images of the ion probe and EMPA analytical pit locations with pit numbers that can be used to link to the data collected at that point.

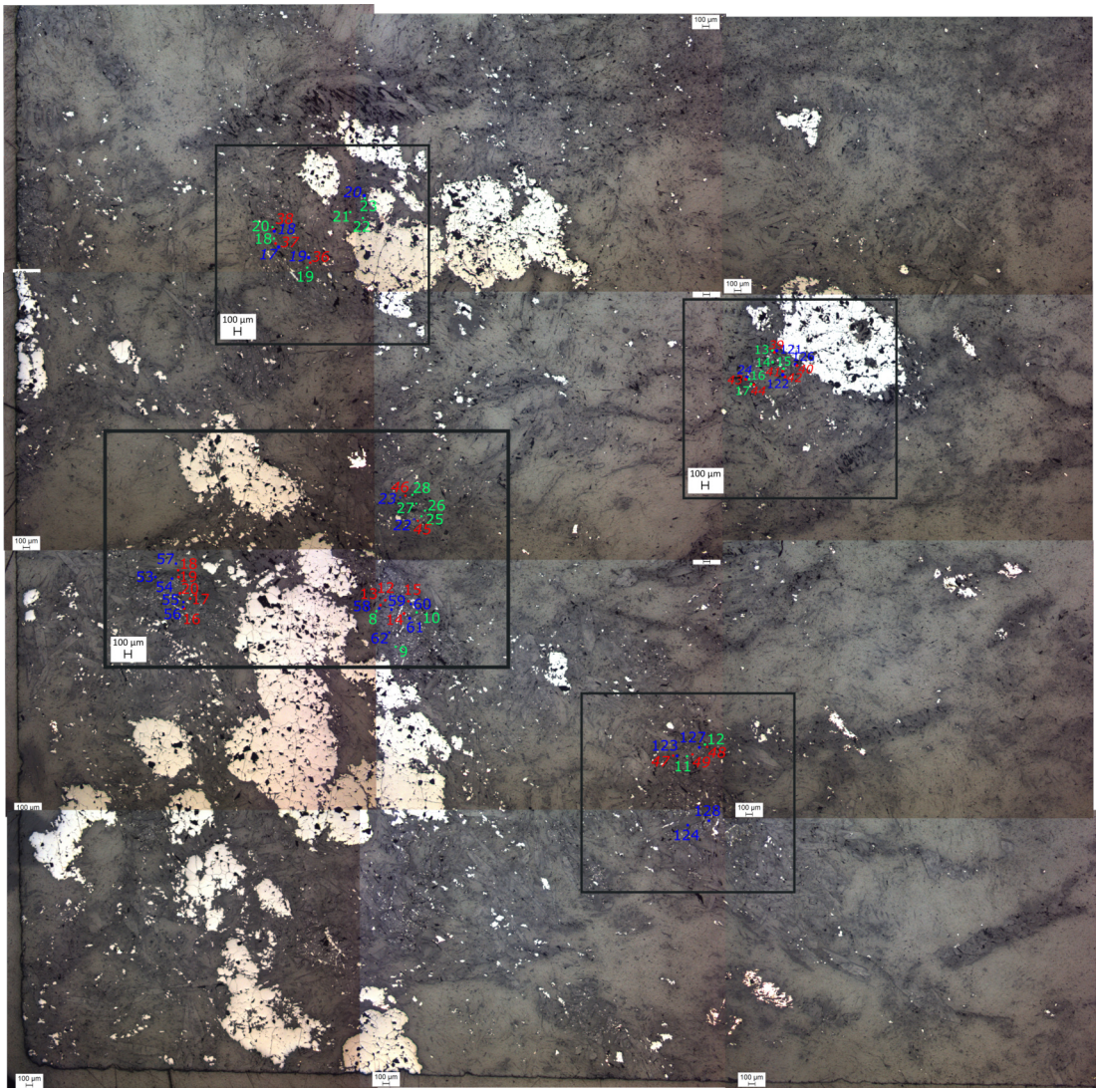

Figure C.5: Whole image of sample AZO-16 with pit locations.

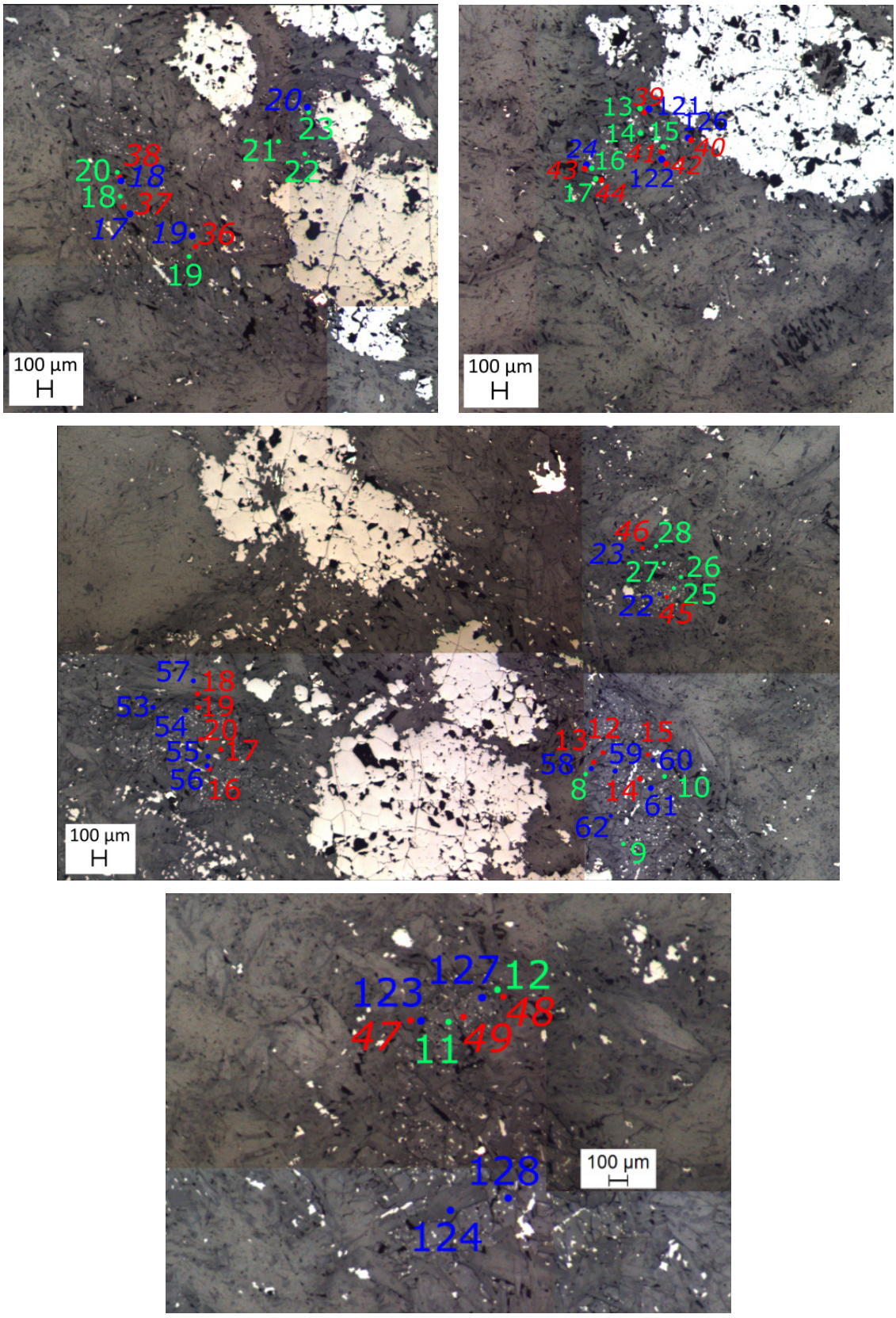

Figure C.6: Close up images of the ion probe and EMPA analytical pit locations with pit numbers that can be used to link to the data collected at that point.

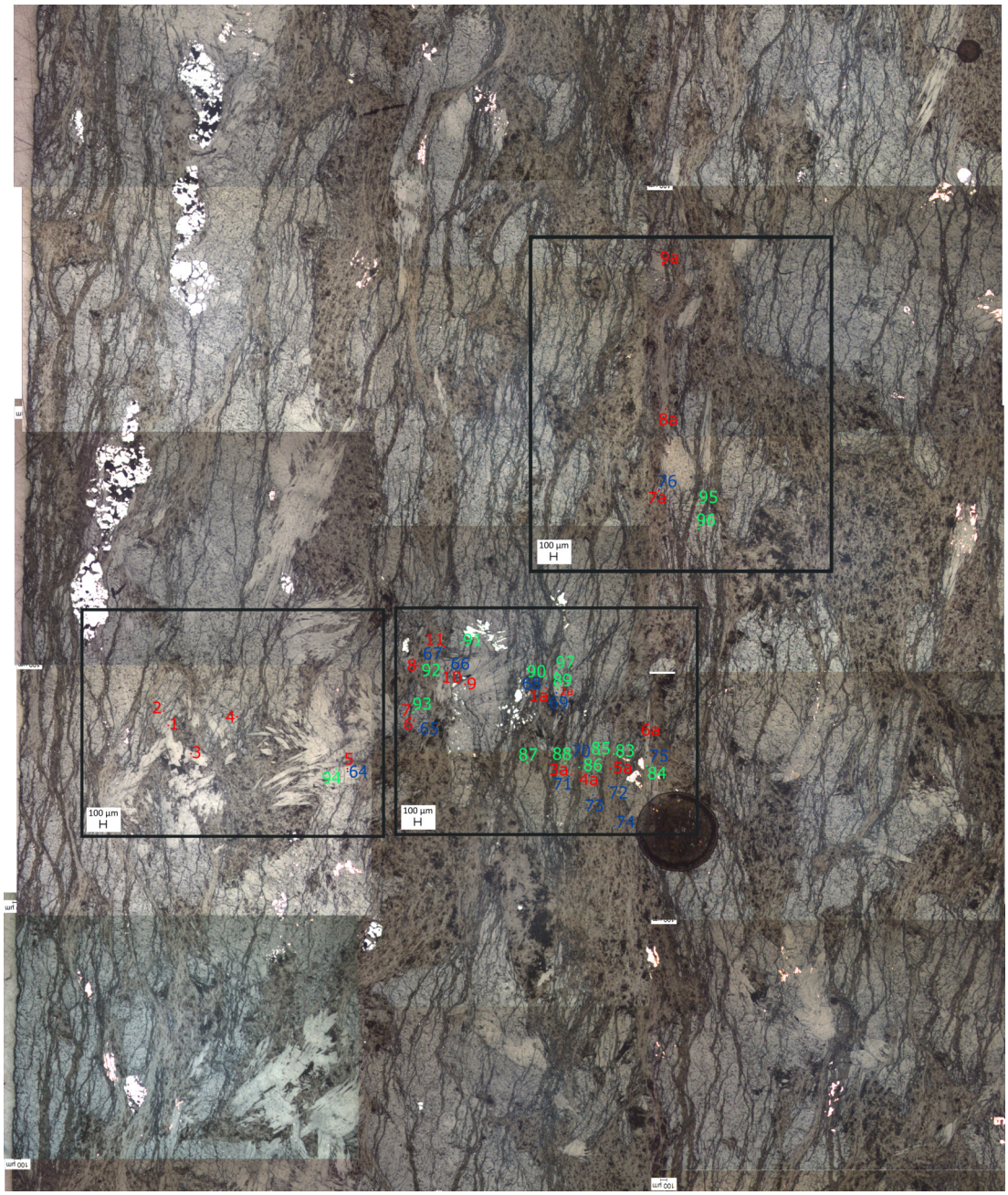

Figure C.7: Whole image of sample AZO-18 with pit locations.

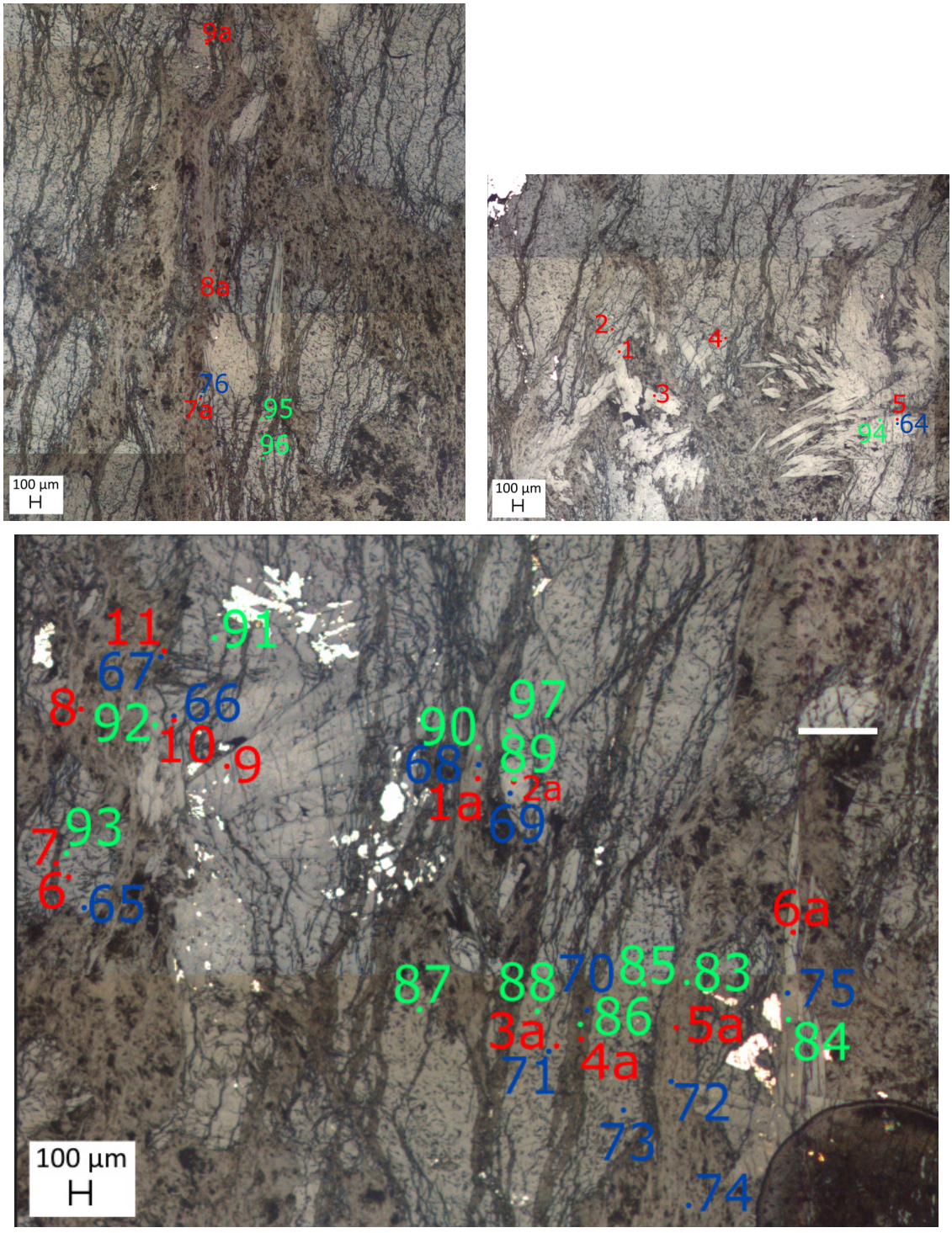

Figure C.8: Close up images of the ion probe and EMPA analytical pit locations with pit numbers that can be used to link to the data collected at that point.

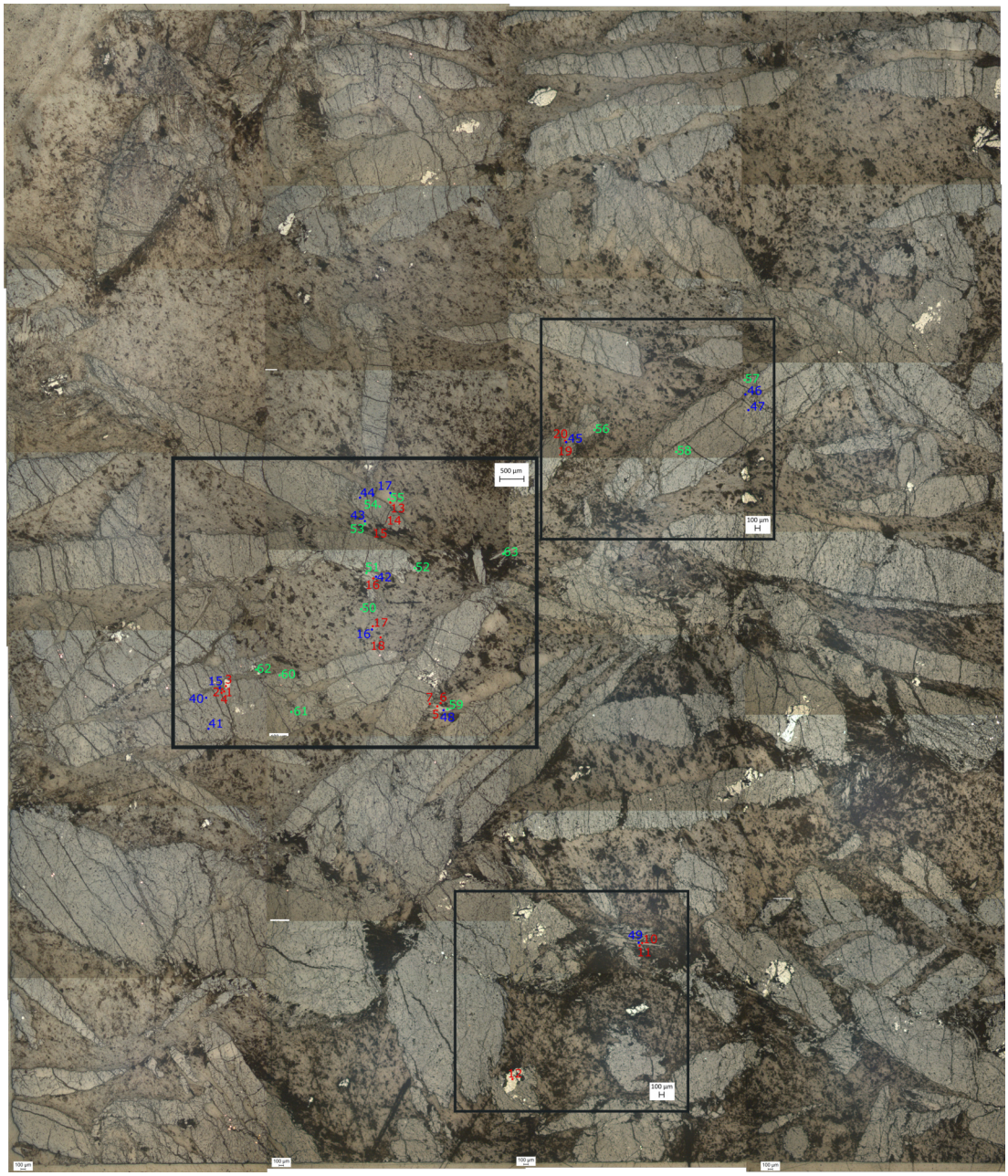

Figure C.9: Whole image of sample AZO-26 with pit locations.

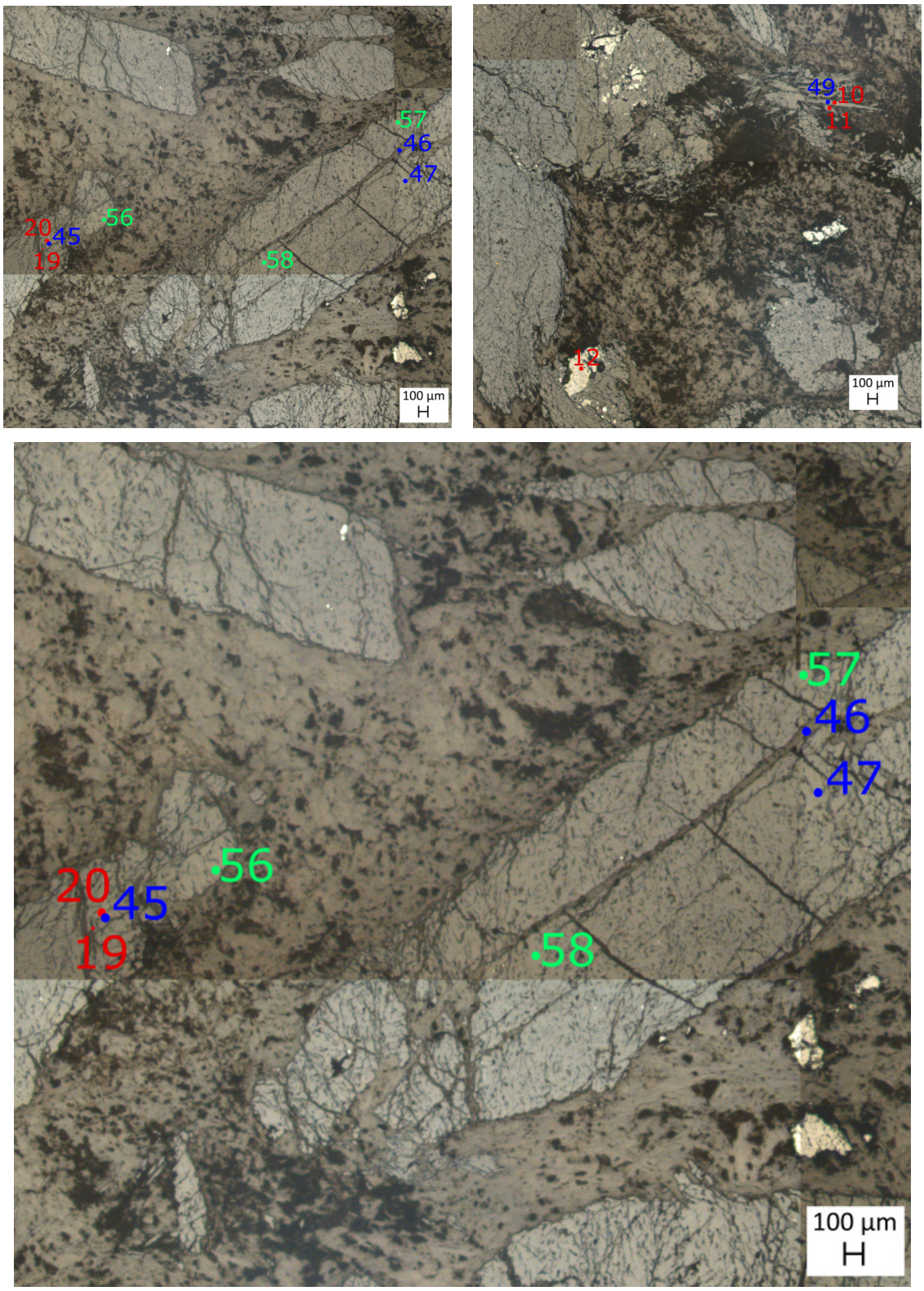

Figure C.10: Close up images of the ion probe and EMPA analytical pit locations with pit numbers that can be used to link to the data collected at that point.

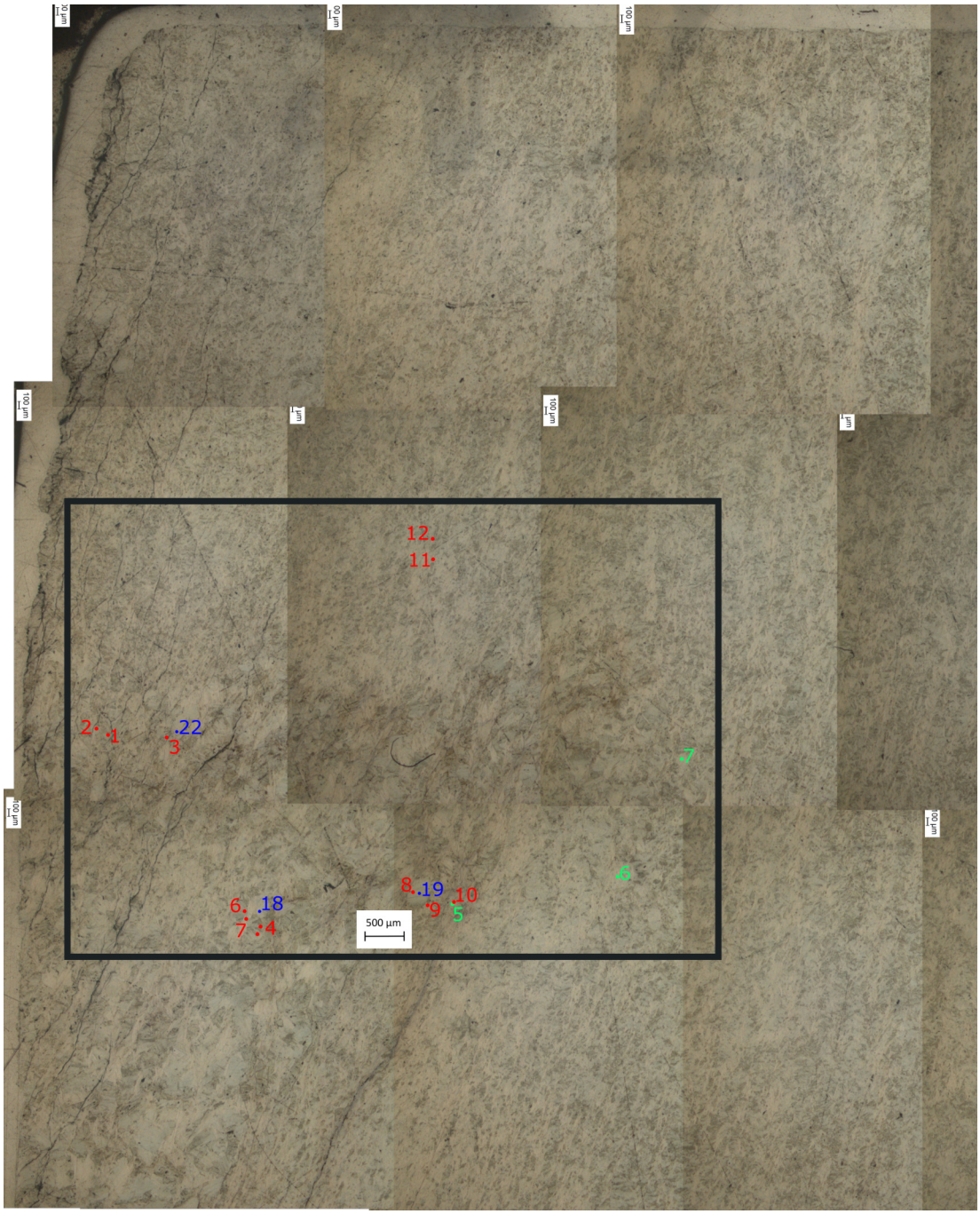

Figure C.11: Whole image of sample AZO-26-S with pit locations.

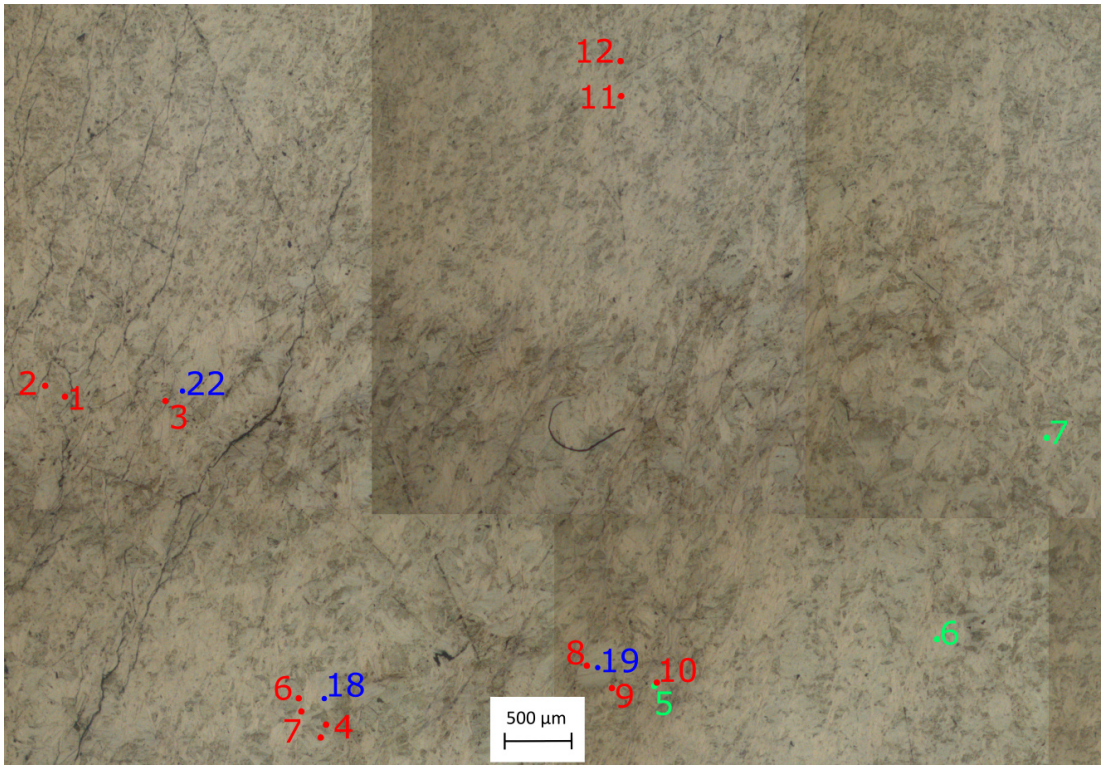

Figure C.12: Close up images of the ion probe and EMPA analytical pit locations with pit numbers that can be used to link to the data collected at that point.

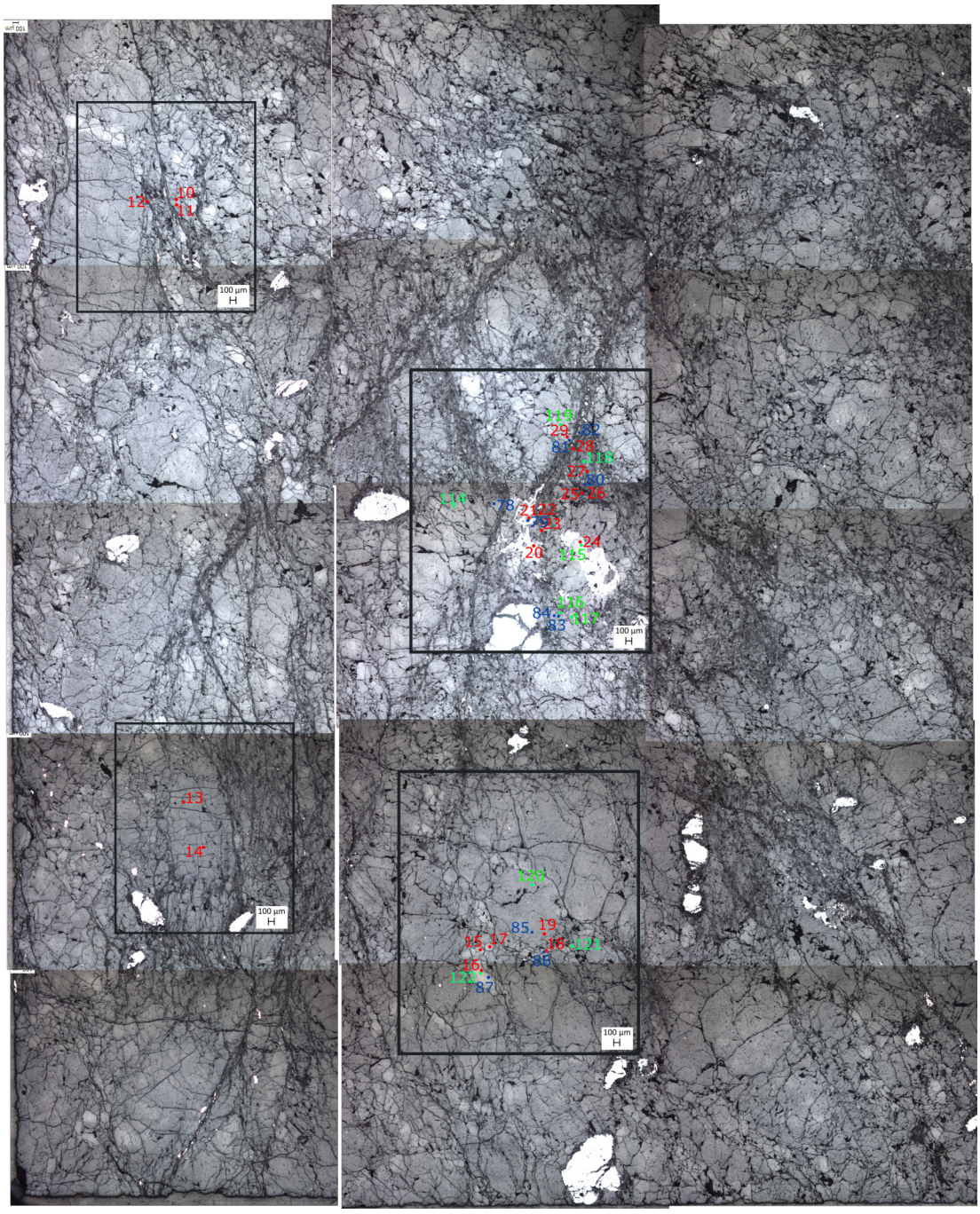

Figure C.13: Whole image of sample PR01 with pit locations.

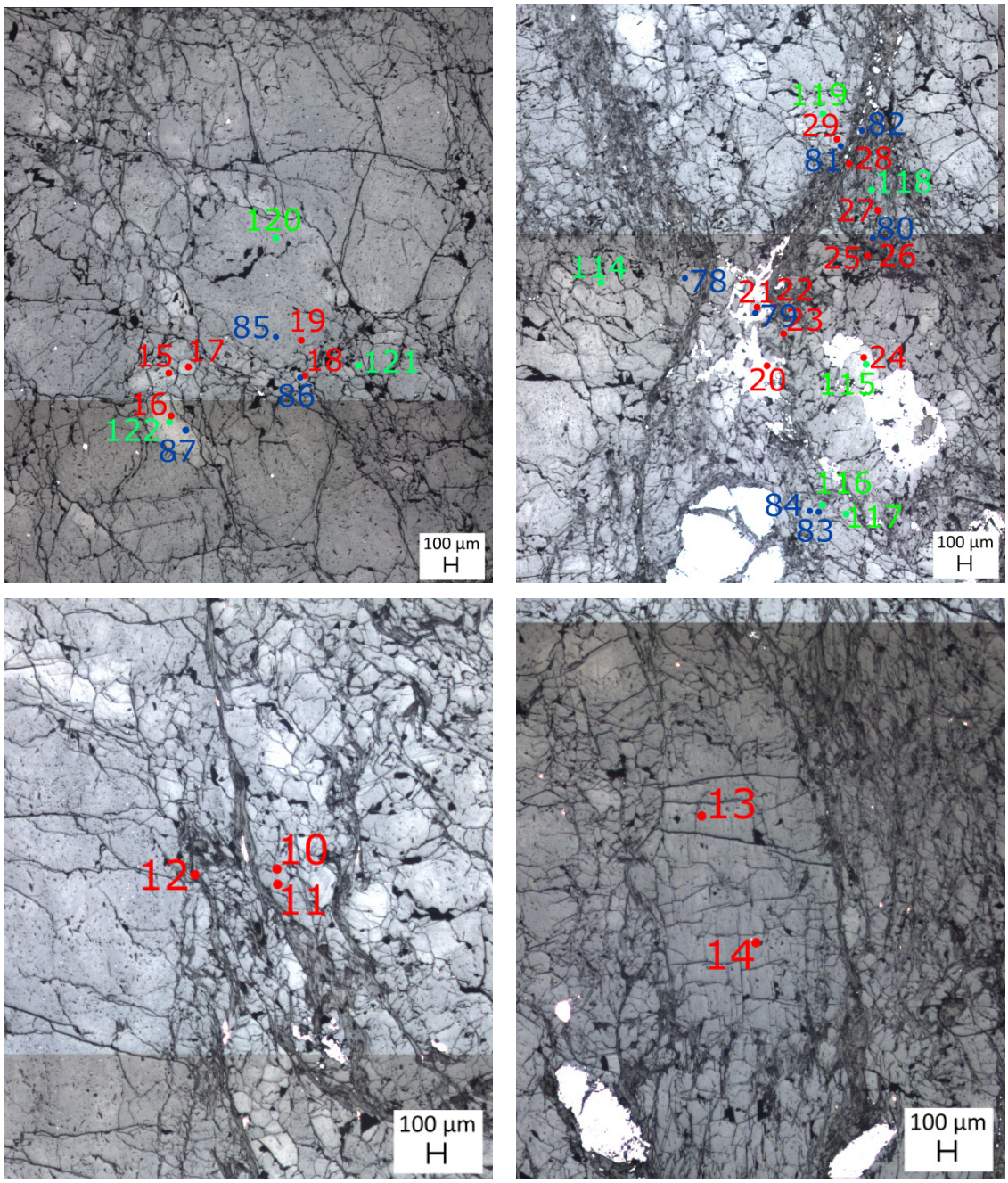

Figure C.14: Close up images of the ion probe and EMPA analytical pit locations with pit numbers that can be used to link to the data collected at that point.

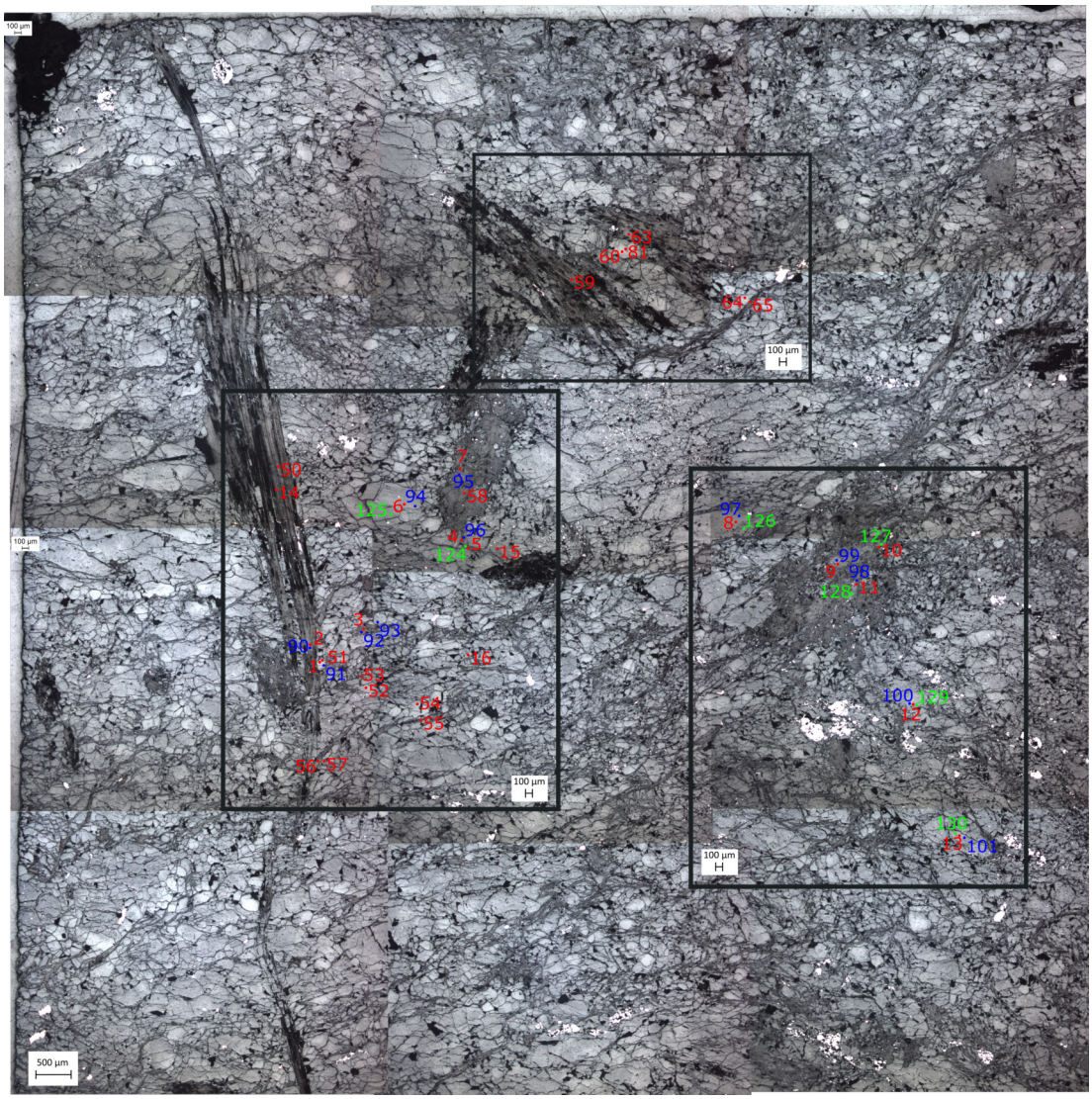

Figure C.15: Whole image of sample PR02 with pit locations.

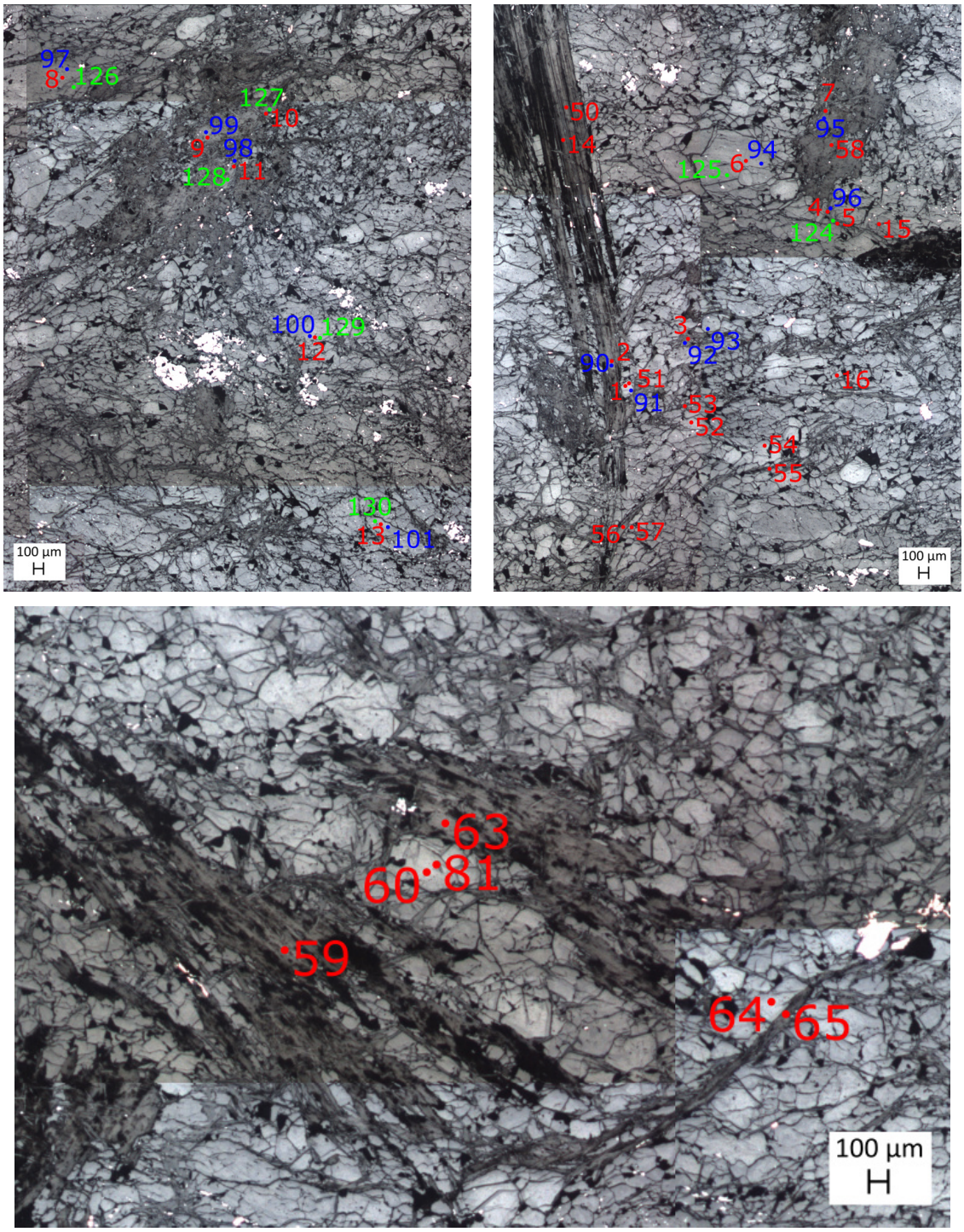

Figure C.16: Close up images of the ion probe and EMPA analytical pit locations with pit numbers that can be used to link to the data collected at that point.

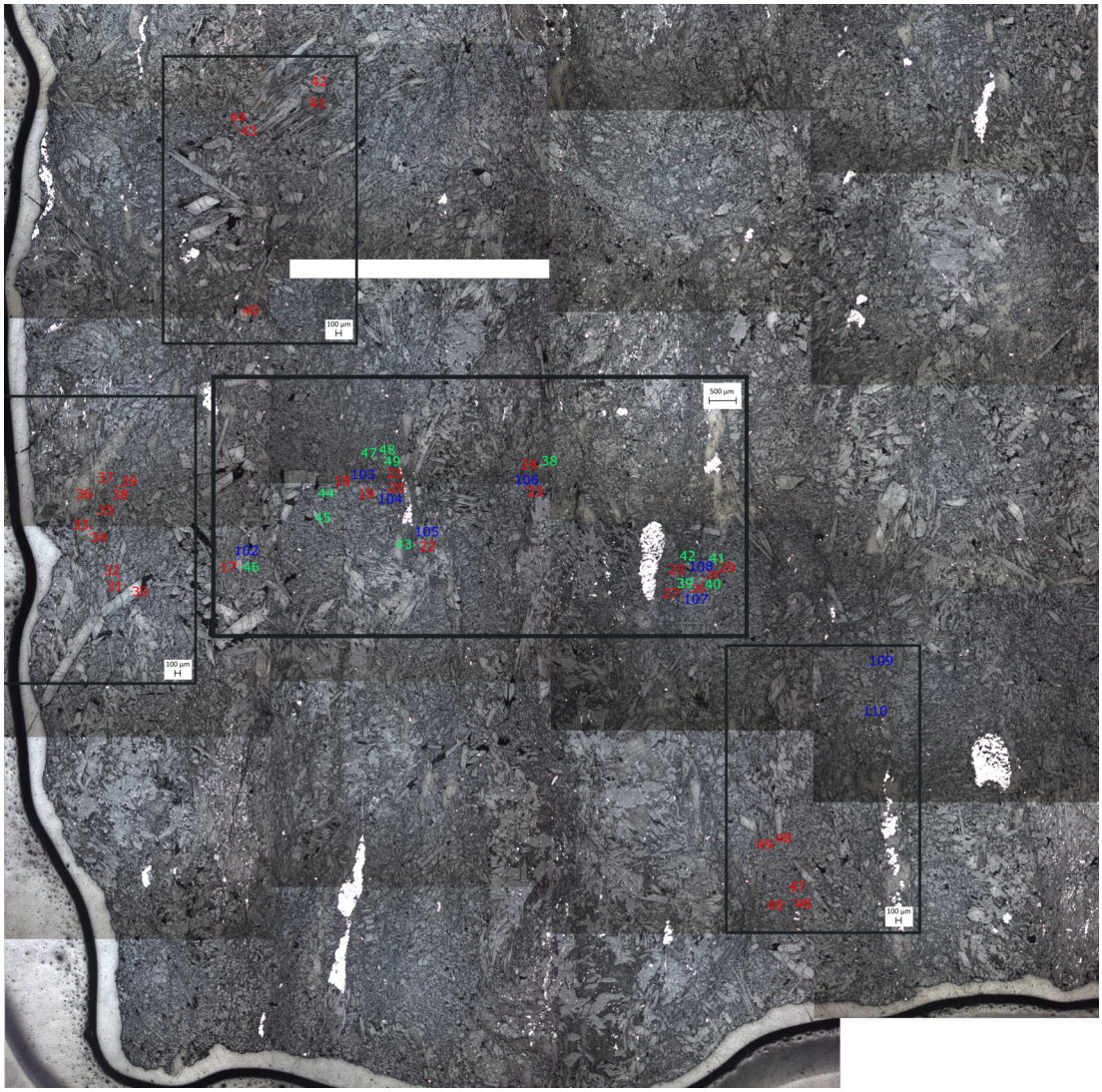

Figure C.17: Whole image of sample PR08 with pit locations.

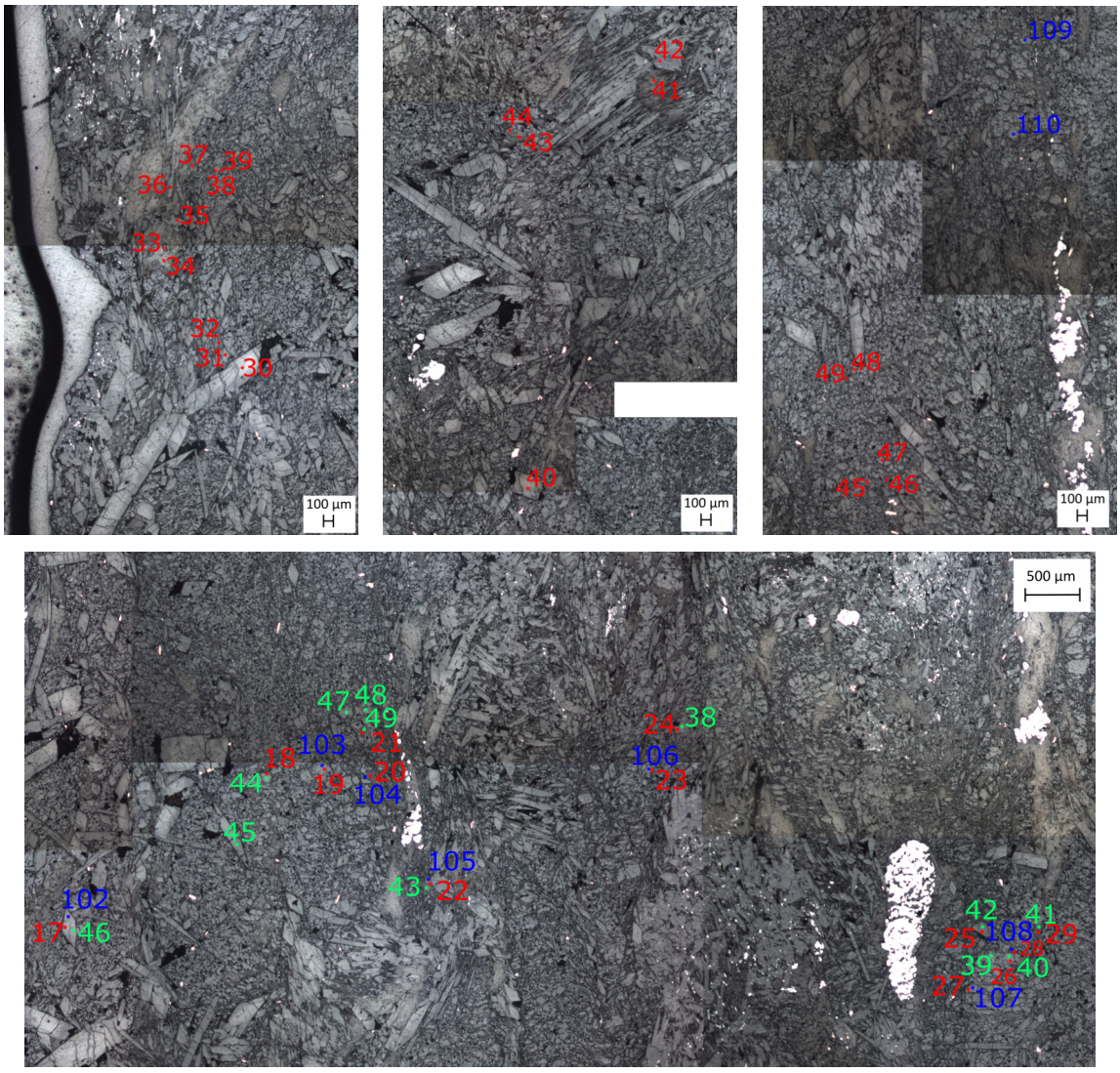

Figure C.18: Close up images of the ion probe and EMPA analytical pit locations with pit numbers that can be used to link to the data collected at that point.

C.3 Sample images for Chapter 5: Experiments

These are the images with probe pit locations for experiments 4 to 11. Unless otherwise stated, green colours indicate 1270 pits, blue numbers indicate 4f pits an white or black numbers indicate EMPA pits.

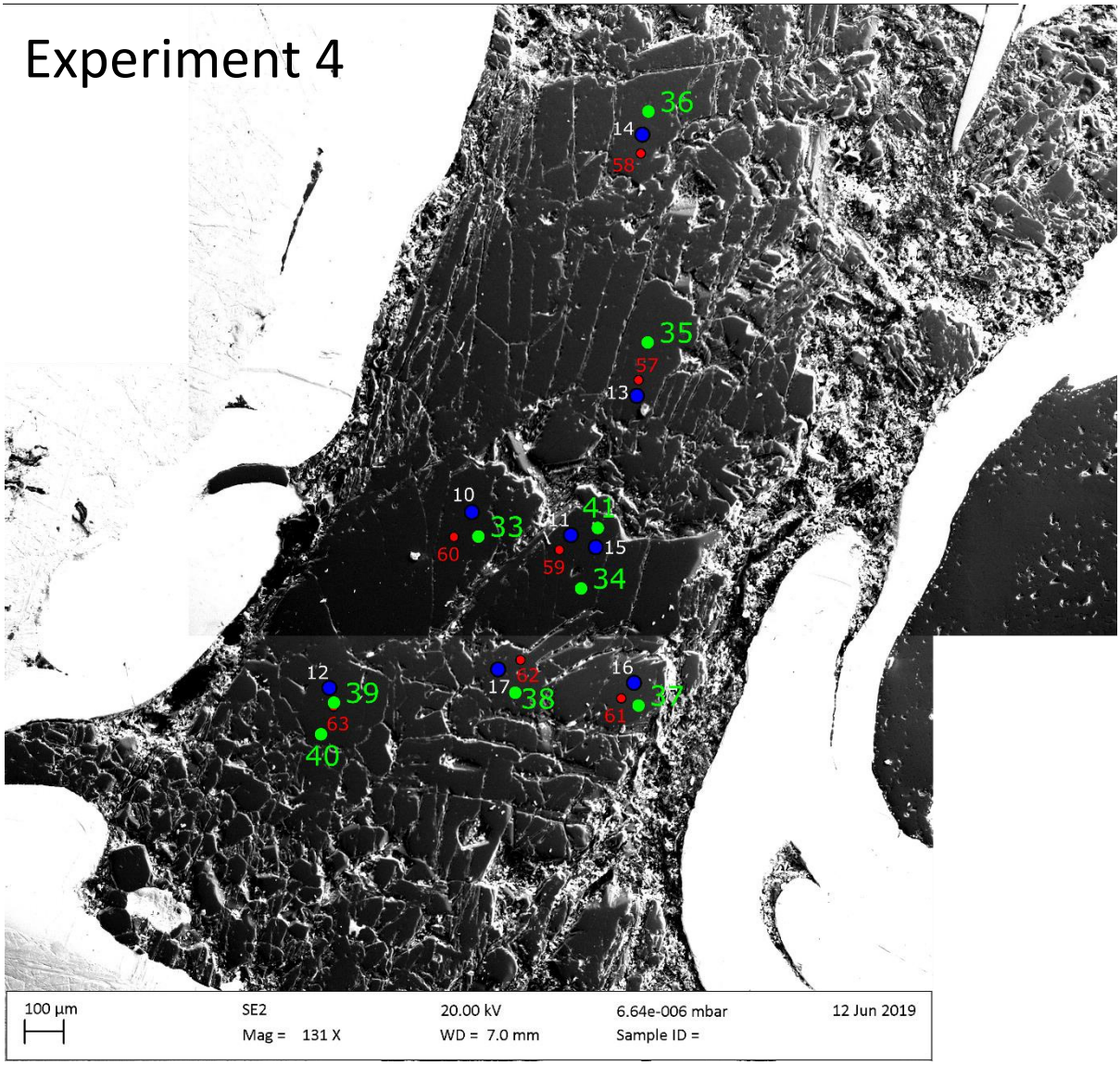
Experiment 4
36
14
58
35
57
13
10
33
60
11
41
15
59
34
12
39
63
40
17
62
38
16
37
61
100 µm
SE2
Mag = 131 X
20.00 kV
WD = 7.0 mm
6.64e-006 mbar
Sample ID =
12 Jun 2019

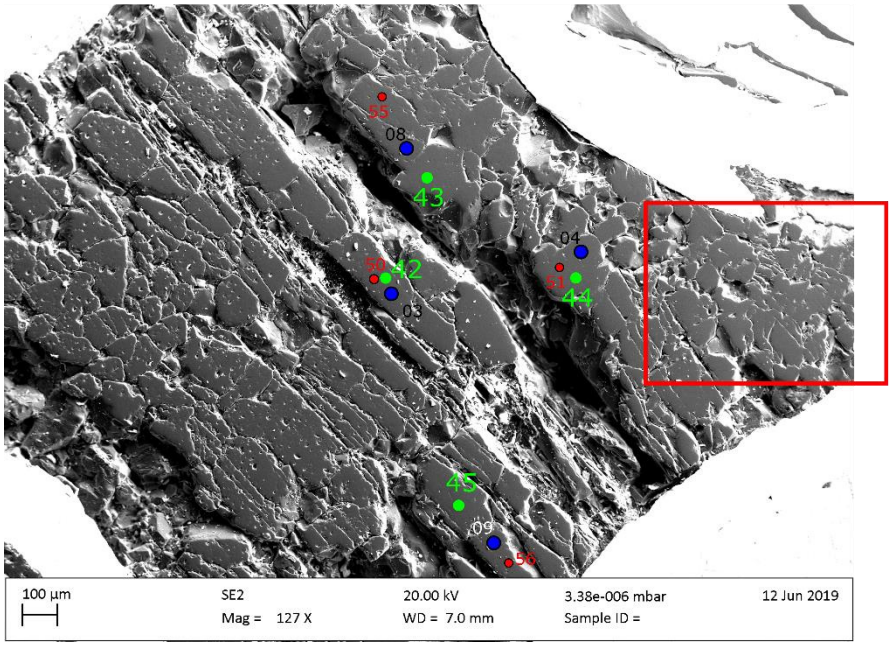

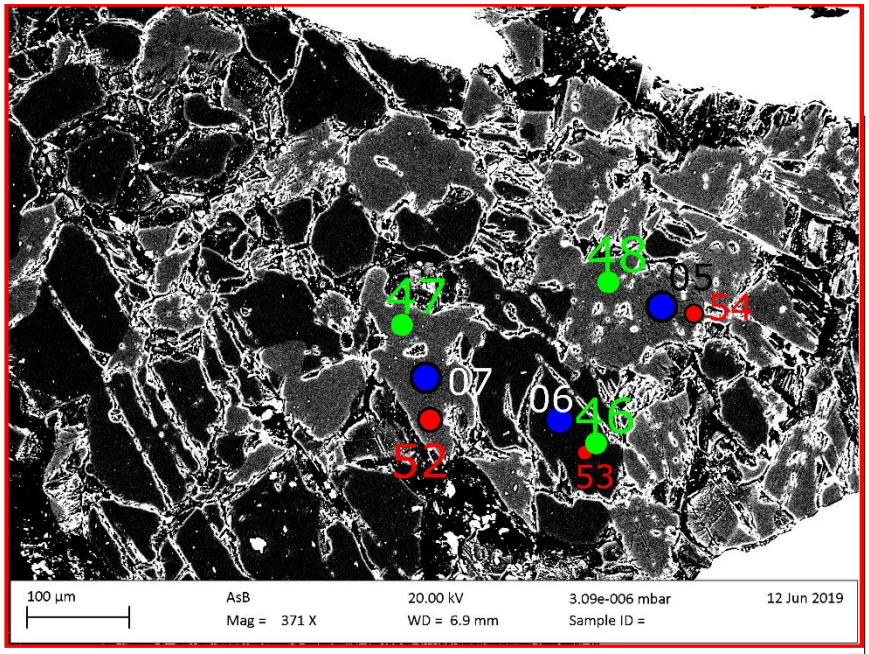

Experiment 5

Experiment 6

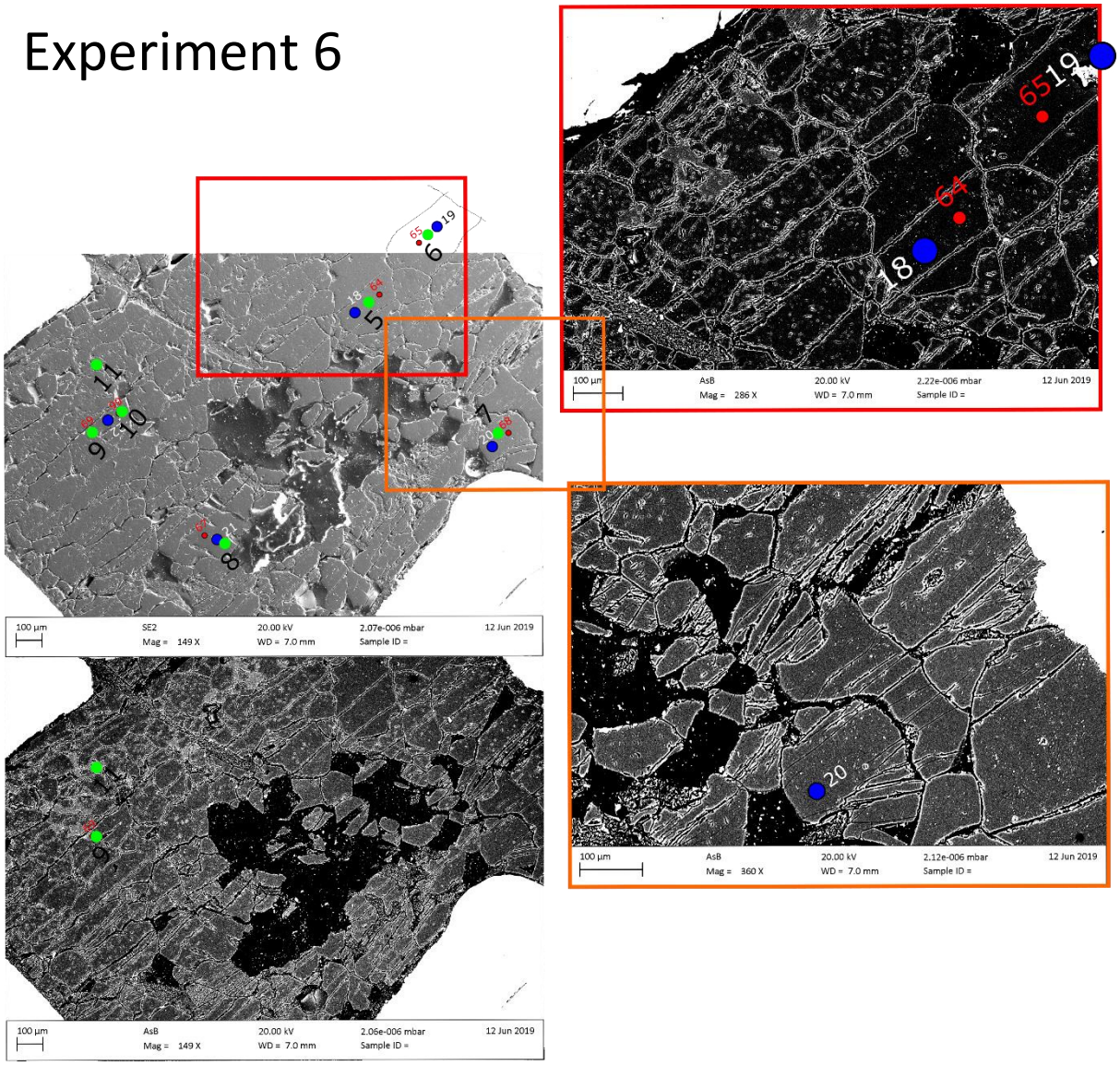

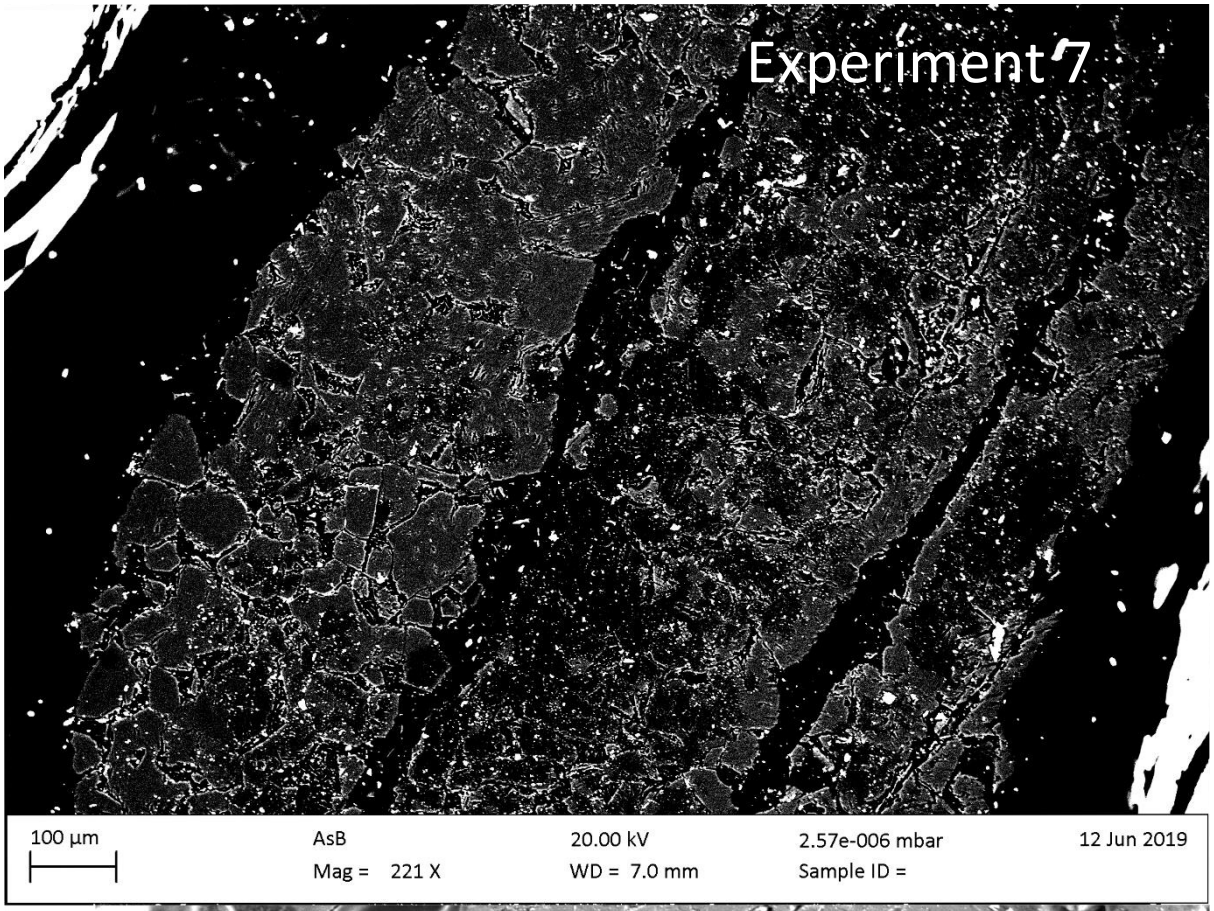
Experiment 7
100 µm
AsB
Mag = 221 X
20.00 kV
WD = 7.0 mm
2.57e-006 mbar
Sample ID =
12 Jun 2019

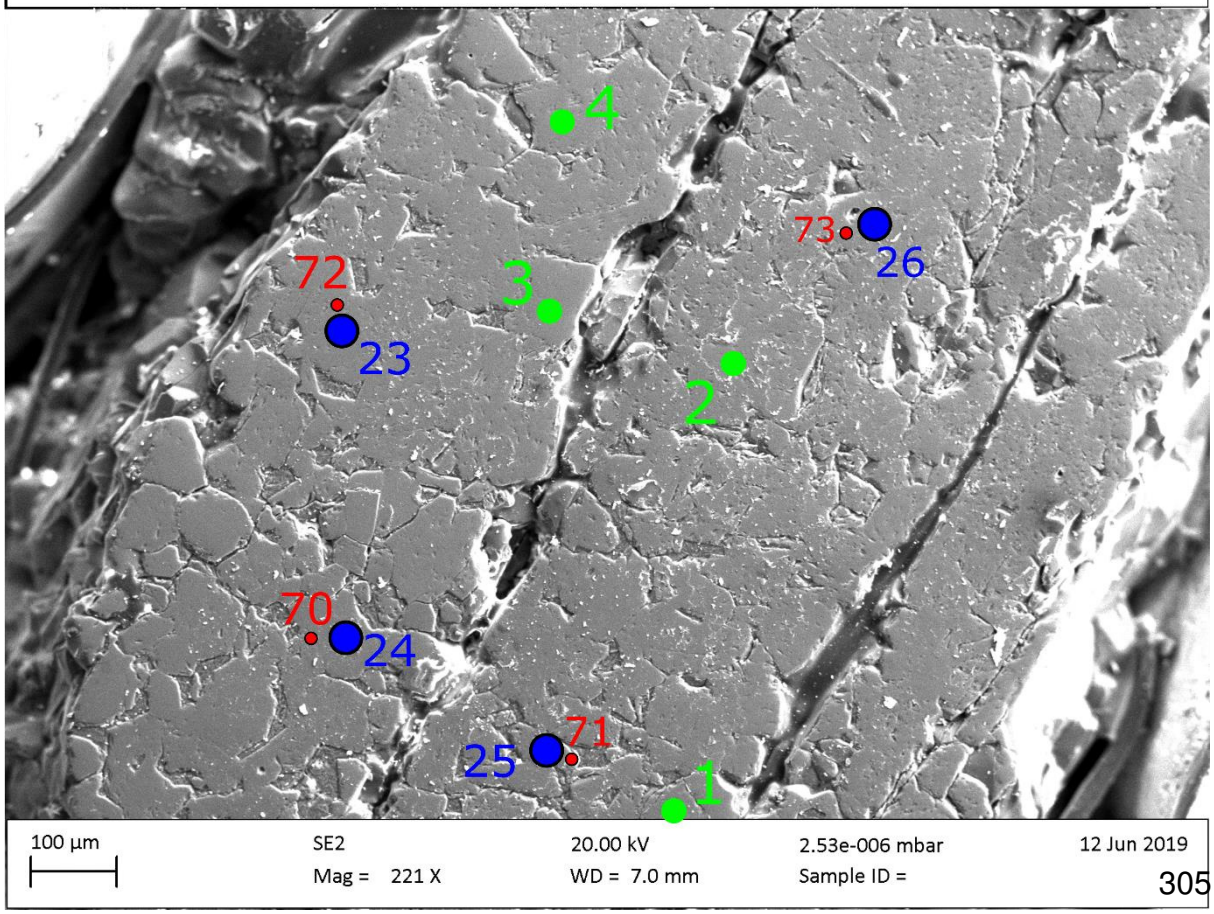
4
73
26
72
3
23
2
70
24
71
25
1
100 µm
SE2
Mag = 221 X
20.00 kV
WD = 7.0 mm
2.53e-006 mbar
Sample ID =
12 Jun 2019

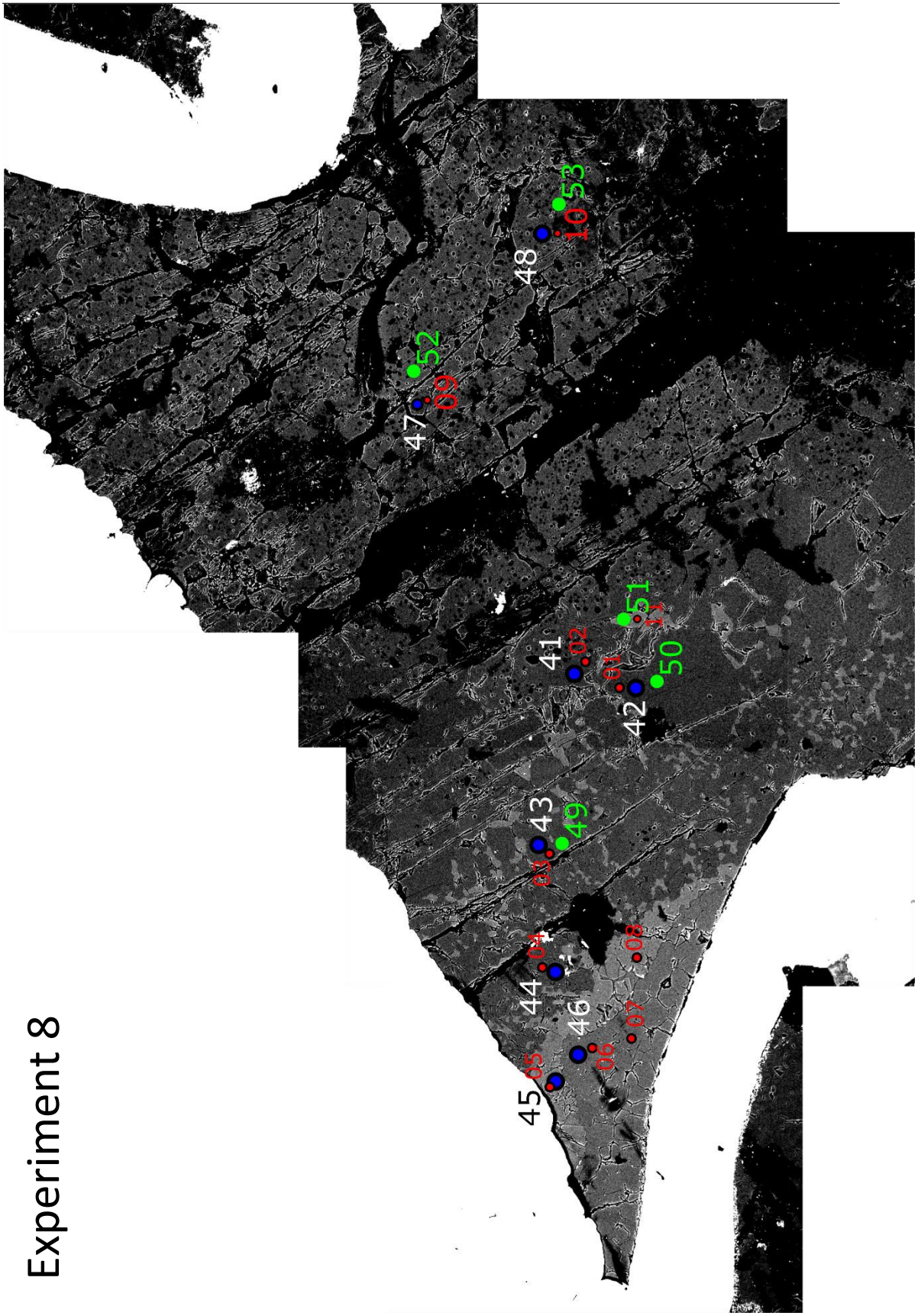
Experiment 8
41
42
43
44
45
46
47
48
49
50
51
52
53
01
02
03
04
05
06
07
08
09
10
11

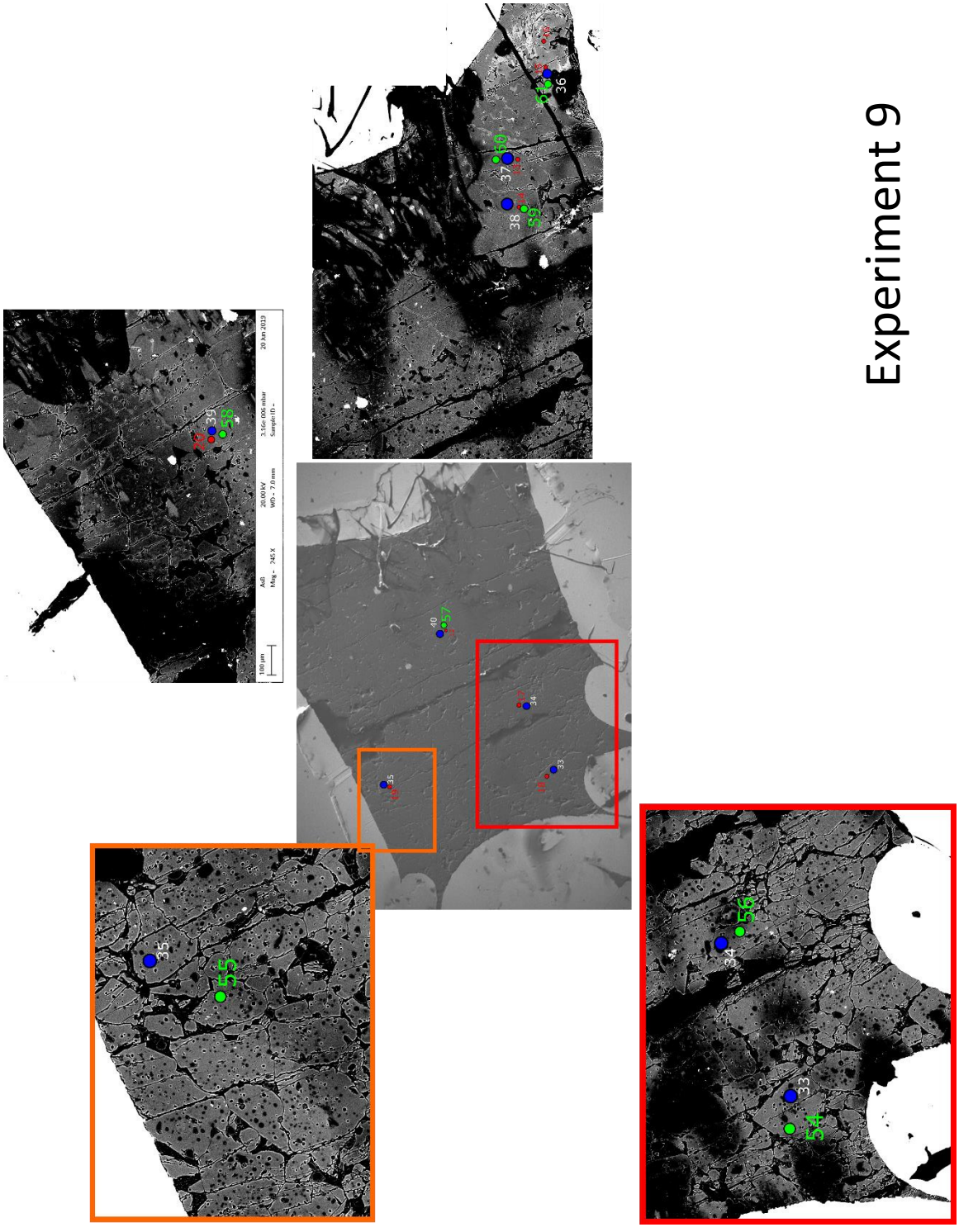
Experiment 9

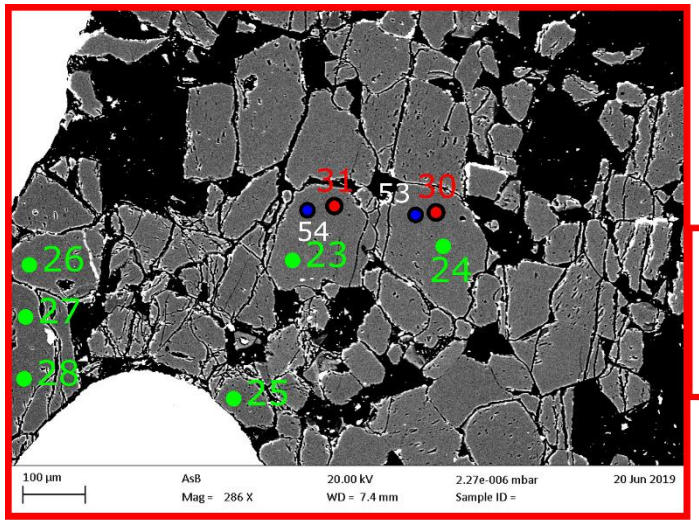

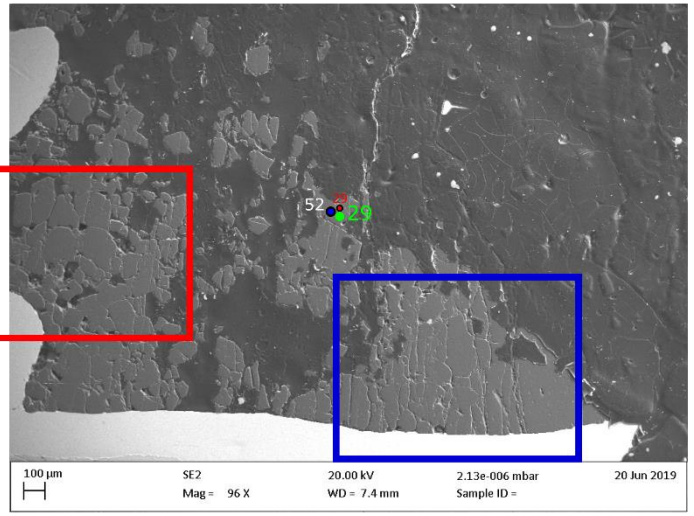

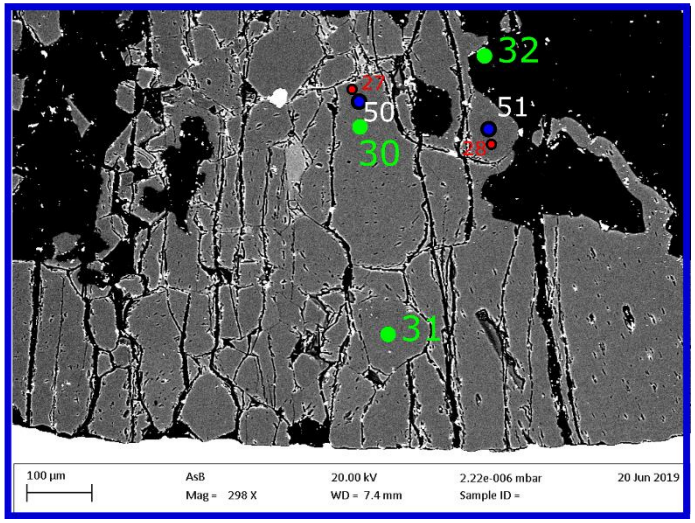

Experiment 10

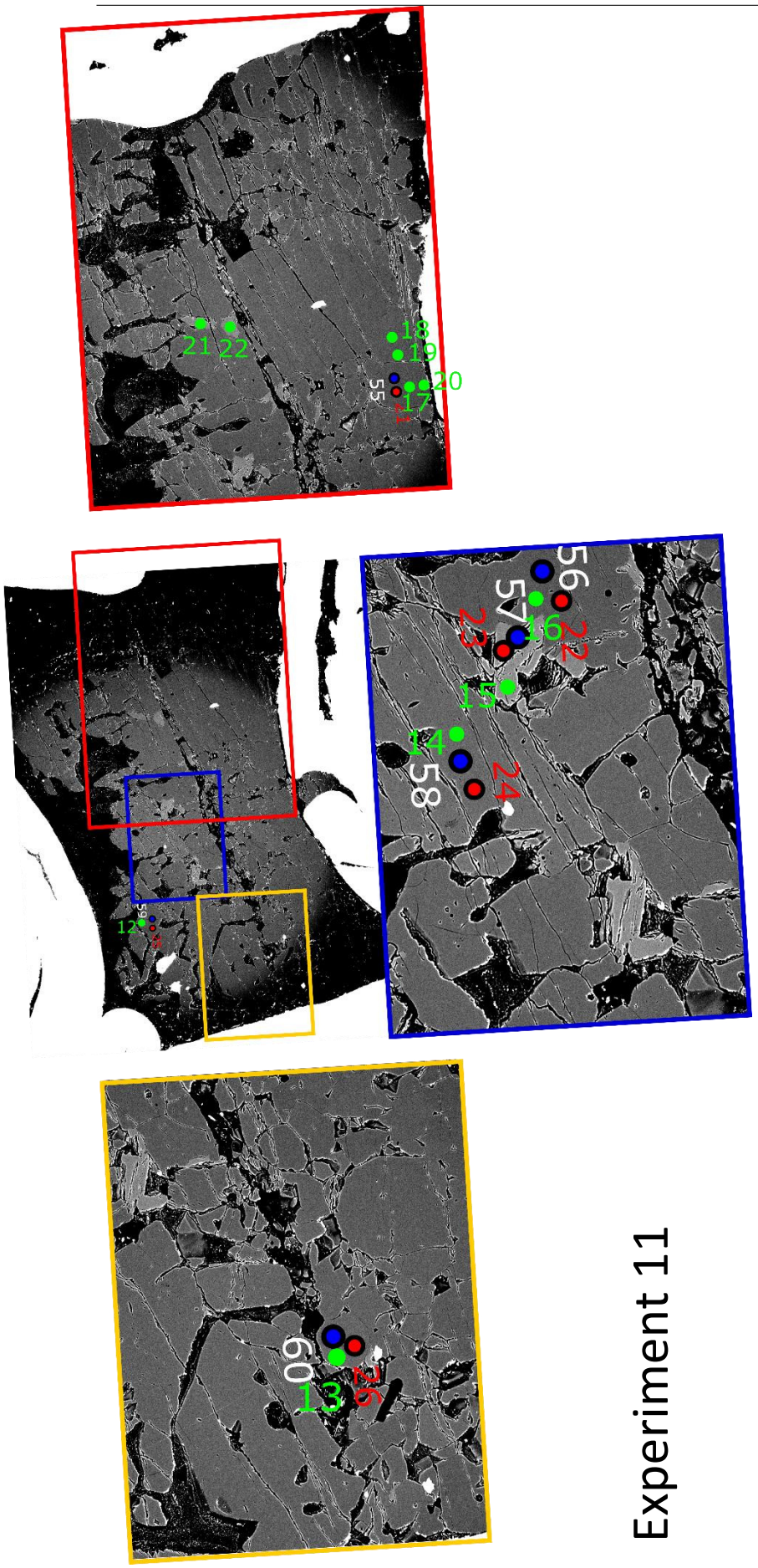

Experiment 11

Bibliography

Agrinier, P. and Cannat, M. (1997). Oxygen-isotope constraints on serpentinization processes in ultramafic rocks from the Mid-Atlantic Ridge (23°N). *Proceedings of the Ocean Drilling Program, Scientific Results*, 153.

Alt, J. C., Bernasconi, S. M., Shanks, W. C., Schwarzenbach, E. M., Crispini, L., Früh-Green, G. L., Padrón-Navarta, J. A., Marchesi, C., Gaggero, L., and Garrido, C. J. (2013). The role of serpentinites in cycling of carbon and sulfur: Seafloor serpentinization and subduction metamorphism. *Lithos*, 178:40–54.

Amato, J. M., Johnson, C. M., Baumgartner, L. P., and Beard, B. L. (1999). Rapid exhumation of the Zermatt-Saas ophiolite deduced from high-precision Sm-Nd and Rb-Sr geochronology. *Earth and Planetary Science Letters*, 171:425–438.

Andreani, M., Muñoz, M., Marcaillou, C., and Delacour, A. (2013). μXANES study of iron redox state in serpentine during oceanic serpentinization. *Lithos*, 178:70–83.

Angiboust, S., Agard, P., Jolivet, L., and Beyssac, O. (2009). The Zermatt-Saas ophiolite: The largest (60-km wide) and deepest (c. 70-80km) continuous slice of oceanic lithosphere detached from a subduction zone? *Terra Nova*, 21(3):171–180.

Angiboust, S., Pettke, T., De Hoog, J. C. M., Caron, B., and Oncken, O. (2014). Channelized Fluid Flow and Eclogite-facies Metasomatism along the Subduction Shear Zone. *Journal of Petrology*, 55(5):883–916.

Bakke, S. and Korneliussen, A. (1986). Jack-straw-textured olivines in some Norwegian metaperidotites. *Norsk Geologisk Tidsskrift*, 66(4):271–276.

Barnicoat, A. C. and Fry, N. (1986). High-pressure metamorphism of the Zermatt-Saas ophiolite zone , Switzerland. *Journal of the Geological Society*, 143(1980):607–618.

Benton, L. D., Ryan, G., and Tera, F. (2001). Boron isotope systematics of slab fluids as inferred from a serpentine seamount , Mariana forearc. *Earth and Planetary Science Letters*, 187:273–282.

Berger, A. and Gieré, R. (1995). Structural observations at the eastern contact of the Bergell Pluton. *Schweizerische Mineralogische Und Petrographische Mitteilungen*, 75:241–258.

Berger, A., Rosenberg, C., and Schmid, Stefan, M. (1996). Ascent, emplacement and exhumation of the Bergell pluton within the Southern Steep Belt of the Central Alps. *Schweizerische Mineralogische Und Petrographische Mitteilungen*, 76:357–382.

Boschi, C., Dini, A., Früh-Green, G. L., and Kelley, D. S. (2008). Isotopic and element exchange during serpentinization and metasomatism at the Atlantis Massif (MAR 30°N): Insights from B and Sr isotope data. *Geochimica et Cosmochimica Acta*, 72(7):1801–1823.

Bousquet, R., Oberhansli, R., Schmid, Stefan, M., Berger, A., Wiederkehr, M., Robert, C., Möller, A., Rosenberg, C., Zeilinger, G., Molli, G., and Koller, F. (2012). Metamorphic framework of the Alps.

Boutelier, D. A. and Chemenda, A. I. (2008). Exhumation of UHP/LT rocks due to the local reduction of the interplate pressure: Thermo-mechanical physical modelling. *Earth and Planetary Science Letters*, 271(1-4):226–232.

Bromiley, G. D. and Pawley, A. R. (2003). The stability of antigorite in the systems MgO-SiO2-H2O (MSH) and MgO-Al2O3-SiO2-H2O (MASH): The effects of Al3+ substitution on high-pressure stability. *American Mineralogist*, 88(1987):99–108.

Brooker, R. (1998). Reduction in piston-cylinder experiments: The detection of carbon infiltration into platinum capsules. *American Mineralogist*, 83(9-10):985–994.

Burkhard, D. J. M. and O'Neil, J. R. (1988). Contrasting serpentinization processes in the eastern Central Alps. *Contributions to Mineralogy and Petrology*, 99(4):498–506.

Burov, E., Francois, T., Yamato, P., and Wolf, S. (2014). Mechanisms of continental subduction and exhumation of HP and UHP rocks. *Gondwana Research*, 25(2):464–493.

Cannaó, E., Agostini, S., Scambelluri, M., Tonarini, S., and Godard, M. (2015). B , Sr and Pb isotope geochemistry of high-pressure Alpine metaperidotites monitors fluid-mediated element recycling during serpentinite dehydration in subduction melange (Cima di Gagnone, Swiss Central Alps). *Geochimica et Cosmochimica Acta*, 163:80–100.

Cannaò, E., Scambelluri, M., Agostini, S., Tonarini, S., and Godard, M. (2016). Linking serpentinite geochemistry with tectonic evolution at the subduction plate-interface: The Voltri Massif case study (Ligurian Western Alps, Italy). *Geochimica et Cosmochimica Acta*, 190:115–133.

Capponi, G. and Crispini, L. (2002). Structural and metamorphic signature of alpine tectonics in the Voltri Massif (Ligurian Alps, North - Western Italy). *Eclogae Geologicae Helvetiae*, 95(1):31–42.

Catanzaro, E., Champion, C., Garner, E., Marinenko, G., Sappenfield, K., and Shields, W. (1970). Standard Reference Materials: Boric Acid; Isotopic, and Assay Standard Reference Materials. *NBS (US) Spec. Publ.*, 260:1–70.

Chaussidon, M. and Albarède, F. (1991). Secular d11B variations of the continental crust: an ion microprobe study. *European Union of Geoscience EUG VI*, Terra Abst:494.

Chaussidon, M. and Marty, B. (1995). Primitive boron isotope composition of the mantle. *Science*, 269(5222):383–386.

Chiba, H., Chacko, T., Clayton, R. N., and Goldsmith, J. R. (1989). Oxygen isotope

fractionations involving diopside, forsterite, magnetite, and calcite: Application to geothermometry. *Geochimica et Cosmochimica Acta*, 53:1–11.

Connolly, J. A. D. (2010). The mechanics of metamorphic fluid expulsion. *Elements*, 6(3):165–172.

Contreras-Reyes, E., Grevemeyer, I., Flueh, E. R., Scherwath, M., and Heesemann, M. (2007). Alteration of the subducting oceanic lithosphere at the southern central Chile trench-outer rise. *Geochemistry, Geophysics, Geosystems*, 8(7):1–19.

Cui, X., Nabelek, P. I., and Liu, M. (2001). Heat and fluid flow in contact metamorphic aureoles with layered and transient permeability, with application to the Notch Peak aureole, Utah. *Journal of Geophysical Research: Solid Earth*, 106(B4):6477–6491.

De Hoog, J. C. M., Hattori, K., and Jung, H. (2014). Titanium- and water-rich metamorphic olivine in high-pressure serpentinites from the Voltri Massif (Ligurian Alps, Italy): Evidence for deep subduction of high-field strength and fluid-mobile elements. *Contributions to Mineralogy and Petrology*, 167(3):1–15.

De Hoog, J. C. M. and Savov, I. P. (2018). Boron Isotopes as a Tracer of Subduction Zone Processes. In *Boron Isotopes. Advances in Isotope Geochemistry*, pages 217–247. Springer.

Debret, B., Koga, K. T., Nicollet, C., Andreani, M., and Schwartz, S. (2013). F, Cl and S input via serpentinite in subduction zones: implications for the nature of the fluid released at depth. *Terra Nova*, 26(2):96–101.

Deschamps, F., Guillot, S., Godard, M., Chauvel, C., Andreani, M., and Hattori, K. (2010). In situ characterization of serpentinites from forearc mantle wedges: Timing of serpentinization and behavior of fluid-mobile elements in subduction zones. *Chemical Geology*, 269(3-4):262–277.

Domanik, K. and Holloway, J. R. (1996). The stability and composition of phengitic muscovite and associated phases from 5.5 to 11 GPa: Implications for deeply subducted sediments. *Geochimica et Cosmochimica Acta*, 60(21):4133–4150.

Eiler, J. M., McInnes, B., Valley, J., Graham, C., and Stopler, E. (1998). Oxygen isotope evidence for slab-derived fluids in the sub-arc mantle. *Nature*, 393:777–781.

Evans, B. W. (2004). The Serpentinite Multisystem Revisited : Chrysotile Is Metastable. *Internatioanl geology review*, 46(6):479–506.

Evans, B. W. (2008). Control of the Products of Serpentinization by the Fe Mg Exchange Potential of Olivine and Orthopyroxene. *Journal of Petrology*, 49(10):1873–1887.

Evans, B. W. (2010). Lizardite versus antigorite serpentinite: Magnetite, hydrogen, and life(?). *Geology*, 38(10):879–882.

Foster, G. L., Pogge Von Strandmann, P. A., and Rae, J. W. (2010). Boron and magnesium isotopic composition of seawater. *Geochemistry, Geophysics, Geosystems*, 11(8):1–10.

Fruh-Green, G., Plas, A., and Lecuyer, C. (1996). Petrologic and Stable Isotope Constraints on Hydrothermal Alteration and Serpentinization of the EPR Shallow Mantle at Hess Deep (Site 895). *Proceedings of the Ocean Drilling Program, Scientific Results*, 147.

Fumagalli, P. and Poli, S. (2005). Experimentally Determined Phase Relations in Hydrous Peridotites to 6.5 GPa and their Consequences on the Dynamics of Subduction Zones. *Journal of Petrology*, 46(3):555–578.

Galvez, M. E., Connolly, J. A., and Manning, C. E. (2016). Implications for metal and volatile cycles from the pH of subduction zone fluids. *Nature*, 539(7629):420–424.

Gilio, M., Scambelluri, M., Agostini, S., Godard, M., Peters, D., and Pettke, T. (2019). Petrology and geochemistry of serpentinites associated with the UHP Lago di Cignana Unit (Italian Western Alps). *Journal of Petrology - submitted*.

Gregory, C. J., McFarlane, C. R., Hermann, J., and Rubatto, D. (2009). Tracing the evolution of calc-alkaline magmas: In-situ Sm-Nd isotope studies of accessory minerals in the Bergell Igneous Complex, Italy. *Chemical Geology*, 260(1-2):73–86.

Groppo, C. and Castelli, D. (2010). Prograde P - T Evolution of a Lawsonite Eclogite from the Monviso Meta-ophiolite (Western Alps): Dehydration and Redox Reactions during Subduction of Oceanic FeTi-oxide Gabbro. *Journal of Petrology*, 51(12):2489–2514.

Guillot, S., Hattori, K., Agard, P., Schwartz, S., and Vidal, O. (2009). *Exhumation Processes in Oceanic and Continental Subduction Contexts : A Review*.

Guillot, S., Schwartz, S., Hattori, K., Auzende, A., and Lardeaux, J. (2004). The Monviso ophiolitic massif (Western Alps), a section through a serpentinite subduction channel. *Journal of the Virtual Explorer*, 16(17):<hal–00103165>.

Guillot, S., Schwartz, S., Reynard, B., Agard, P., and Prigent, C. (2015). Tectonic significance of serpentinites. *Tectonophysics*, 646:1–19.

Hacker, B. R., Abers, G. A., Peacock, S. M., and Johnston, S. (2003). Subduction factory: 1. Theoretical mineralogy, densities, seismic wave speeds and H2O contents. *Journal of Geophysical Research*, 108:2029.

Hålenius, U., Skogby, H., Edén, M., Nazzareni, S., Kristiansson, P., and Resmark, J. (2010). Coordination of boron in nominally boron-free rock forming silicates: Evidence for incorporation of BO3 groups in clinopyroxene. *Geochimica et Cosmochimica Acta*, 74(19):5672–5679.

Harvey, J., Clarke, E., Garrido, C. J., Hoog, C.-J. d., Padrón-Navarta, J. A., Marchesi, C., Sánchez-Vizcaíno, V. L., and Gómez-Pugnaire, M. T. (2019). Mineralogical controls on boron isotope systematics at the antigorite-out isograd: implications for subduction-related dehydration.

Harvey, J., Garrido, C. J., Savov, I., Agostini, S., Padrón-Navarta, J. A., Marchesi, C., López Sánchez-Vizcaíno, V., and Gómez-Pugnaire, M. T. (2014). 11B-rich fluids in subduction zones: The role of antigorite dehydration in subducting slabs and boron isotope heterogeneity in the mantle. *Chemical Geology*, 376:20–30.

Hattori, K. H. and Guillot, S. (2003). Volcanic fronts form as a consequence of serpentinite dehydration in the forearc mantle wedge. *Geology*, 31(6):525–528.

Healy, D., Reddy, S. M., Gray, E. M., Brovarone, A. V., and Timms, N. E. (2009). Trench-parallel fast axes of seismic anisotropy due to fluid-filled cracks in subducting slabs. *Earth and Planetary Science Letters*, 283(1-4):75–86.

Hermann, J., Muntener, O., and Scambelluri, M. (2000). The importance of serpentinite mylonites for subduction and exhumation of oceanic crust. *Tectonophysics*, 327:225–238.

Hervig, R. L., Moore, G. M., Williams, L. B., Peacock, S. M., Holloway, J. R., and Roggensack, K. (2002). Isotopic and elemental partitioning of boron between hydrous fluid and silicate melt. *American Mineralogist*, 87(5-6):769–774.

Hyndman, R. D. and Peacock, S. M. (2003). Serpentinization of the forearc mantle. *Earth and Planetary Science Letters*, 212(3-4):417–432.

Ingrin, J., Kovacs, I., Deloule, E., Balan, E., Blanchard, M., Kkohn, S. C., and Hermann, J. (2014). Identification of hydrogen defects linked to boron substitution in synthetic forsterite and natural olivine. *American Mineralogist*, 99:2138–2141.

Ishikawa, T. and Nakamura, E. (1994). Origin of the slab component in arc lavas from across-arc variation of B and Pb isotopes.

Jochum, K., Wilson, S., Abouchami, W., Amini, M., Chmeleff, J., Eisenhauer, A., Hegner, E., Iaccheri, L., Kieffer, B., Krause, J., McDonough, W., Mertz-Kraus, R., Raczek, I., Rudnick, R., Scholz, D., Steinhoefel, G., Stoll, B., Stracke, A., Tonarini, S., and D. Woodhead, J. (2010). GSD-1G and MPI-DING reference glasses for in situ and bulk isotopic analysis. *Geostandards and Geoanalytical Research*, 35:193–226.

Kakihana, H., Kotaka, M., Satoh, S., Nomura, M., and Okamoto, M. (1977). Fundamental Studies on the Ion-Exchange Separation of Boron Isotopes.

Kawamoto, T. (2006). Hydrous Phases and Water Transport in the Subducting Slab. *Reviews in Mineralogy and Geochemistry*, 62(1):273–289.

Klochko, K., Kaufman, A. J., Yao, W., Byrne, R. H., and Tossell, J. A. (2006). Experimental measurement of boron isotope fractionation in seawater. *Earth and Planetary Science Letters*, 248:276–285.

Konrad-Schmolke, M., Halama, R., and Manea, V. C. (2016). Slab mantle dehydrates beneath Kamchatka—Yet recycles water into the deep mantle. *Geochemistry Geophysics Geosystems*, 17:2987–3007.

Kretz, R. (1983). Symbols for rock-forming minerals. *American Mineralogist*, 68:277–279.

Lafay, R., Baumgartner, L. P., Putlitz, B., and Siron, G. (2019). Oxygen isotope disequilibrium during serpentinite dehydration. *Terra Nova*, 31(2):94–101.

Leeman, W. P. and Sisson, V. (2002). Geochemistry of Boron and Its Implications for Crustal and Mantle Processes. In *Volume 33: Boron: Mineralogy, Petrology, and Geochemistry*, pages 645–708.

Leeman, W. P., Tonarini, S., and Turner, S. (2017). Boron isotope variations in Tonga-Kermadec-New Zealand arc lavas: Implications for the origin of subduction components andmantle influences. *Geochemistry Geophysics Geosystems*, 18(3):1126–1162.

Lesne, P., Kohn, S. C., Blundy, J., Witham, F., Botcharnikov, R. E., and Behrens, H. (2011). Experimental simulation of closed-system degassing in the system basalt-H 2 O-CO 2 -S-Cl. *Journal of Petrology*, 52(9):1737–1762.

Li, X., Rahn, M., and Bucher, K. (2004). Serpentinites of the Zermatt-Saas ophiolite complex and their texture evolution. *Journal of Metamorphic Geology*, 22:159–177.

Liu, Y. and Tossell, J. A. (2005). Ab initio molecular orbital calculations for boron isotope fractionations on boric acids and borates. *Geochimica et Cosmochimica Acta*, 69(16):3995–4006.

López Sánchez-Vizcaíno, V., Gómez-Pugnaire, M. T., Garrido, C. J., Padrón-Navarta, J. A., and Mellini, M. (2009). Breakdown mechanisms of titanclinohumite in antig-

orite serpentinite (Cerro del Almirez massif, S. Spain): A petrological and TEM study. *Lithos*, 107(3-4):216–226.

Luffi, P., Horodyskyj, U., and Lee, C.-T. A. (2009). Geochemical evidence for exhumation of eclogite via serpentinite channels in ocean-continent subduction zonesGeochemical signatures of Franciscan eclogite exhumation. *Geosphere*, 5(5):426–438.

Marschall, H. R. (2018). Boron Isotopes in the Ocean Floor Realm and the Mantle. pages 189–215.

Marschall, H. R. and Monteleone, B. D. (2014). Boron isotope analysis of silicate glass with very low boron concentrations by secondary ion mass spectrometry. *Geostandards and Geoanalytical Research*, 39(1):31–46.

Marschall, H. R., Wanless, V. D., Shimizu, N., Pogge von Strandmann, P. A., Elliott, T., and Monteleone, B. D. (2017). *The boron and lithium isotopic composition of mid-ocean ridge basalts and the mantle*, volume 207. Elsevier Ltd.

Martin, C., Flores, K. E., and Harlow, G. E. (2016). Boron isotopic discrimination for subduction-related serpentinites. *Geology*, 44(11):899–902.

McCaig, A. M., Titarenko, S. S., Savov, I. P., Cliff, R. A., Banks, D., Boyce, A., and Agostini, S. (2018). No significant boron in the hydrated mantle of most subducting slabs. *Nature Communications*, 9(4602):1–10.

Meyer, C., Wunder, B., Meixner, A., Romer, R. L., and Heinrich, W. (2008). Boron-isotope fractionation between tourmaline and fluid: An experimental re-investigation. *Contributions to Mineralogy and Petrology*, 156(2):259–267.

Moody, J. B. (1976). Serpentinization : a review. *Lithos*, 9:125–138.

Mottl, M. J., Komor, S. C., Fryer, P., and Moyer, C. L. (2003). Deep-slab fluids fuel extremophilic Archaea on a Mariana forearc serpentinite mud volcano: Ocean drilling program leg 195. *Geochemistry, Geophysics, Geosystems*, 4(11).

Padrón-Navarta, J. A., Sánchez-Vizcaí, V. L., Garrido, C. J., and Gómez-Pugnaire, M. T. (2011). Metamorphic record of high-pressure dehydration of antigorite serpentinite to chlorite harzburgite in a subduction setting (Cerro del Almirez, Nevado-Filábride complex, Southern Spain). *Journal of Petrology*, 52(10):2047–2078.

Pagé, L., Hattori, K., and Guillot, S. (2018). Mantle wedge serpentinites : A transient reservoir of halogens , boron , and nitrogen for the deeper mantle. *Geology*, 46(10):883–886.

Palmer, M. (1991). Boron-isotope systematics of Halmahera arc (Indonesia) lavas: evidence for involvement of the subducted slab. *Geology*, 19:215–217.

Peacock, S. M. (1993). The importance of blueschist - eclogite dehydration reactions in subducting oceanic crust. *Geological Society Of America Bulletin*, 2(May):684–694.

Pearson, D. G., Brenker, F. E., Nestola, F., McNeill, J., Nasdala, L., Hutchison, M. T., Matveev, S., Mather, K., Silversmit, G., Schmitz, S., Vekemans, B., and Vincze, L. (2014). Hydrous mantle transition zone indicated by ringwoodite included within diamond. *Nature*, 507:221.

Peretti, A., Dubessy, J., Mullis, J., Frost, B. R., and Trommsdorff, V. (1992). Highly reducing conditions during Alpine metamorphism of the Malenco peridotite (Sondrio, northern Italy) indicated by mineral paragenesis and H2 in fluid inclusions. *Contributions to Mineralogy and Petrology*, 112(2-3):329–340.

Plank, T. and Langmuir, C. H. (1993). Tracing trace elements from sediment input to volcanic output at subduction zones. *Nature*, 362(6422):739–743.

Plümper, O., John, T., Podladchikov, Y. Y., Vrijmoed, J. C., and Scambelluri, M. (2017). Fluid escape from subduction zones controlled by channel-forming reactive porosity. *Nature Geoscience*, 10(2):150–156.

Poli, S. and Schmidt, M. W. (2002). Petrology of Subducted Slabs. *Annual Review of Earth and Planetary Sciences*, 30(1):207–235.

Prigent, C., Guillot, S., Agard, P., Lemarchand, D., Soret, M., and Ulrich, M. (2018). Transfer of subduction fluids into the deforming mantle wedge during nascent subduction: Evidence from trace elements and boron isotopes (Semail ophiolite, Oman). *Earth and Planetary Science Letters*, 484:213–228.

Puga, E., Nieto, J. M., Díaz De Federico, A., Bodinier, J. L., and Morten, L. (1999). Petrology and metamorphic evolution of ultramafic rocks and dolerite dykes of the Betic Ophiolitic Association (Mulhacen Complex, SE Spain): Evidence of eo-Alpine subduction following an ocean-floor metasomatic process. *Lithos*, 49(1-4):23–56.

Ranero, C. R., Morgan, J. P., McIntosh, K., and Reichert, C. (2003). Bending-related faulting and mantle serpentinization at the Middle America trench. *Nature*, 425(6956):367–373.

Reynard, B. (2013). Serpentine in active subduction zones. *Lithos*, 178:171–185.

Richter, F. M. . and McKenzie, D. (1984). Dynamical Models for Melt Segregation from a Deformable Matrix. *Journal of Geology*, 92(6):729–740.

Rosenberg, C. L., Berger, A., and Schmid, S. M. (1995). Observations from the floor of a granitoid pluton: inferences on the driving force of final emplacement. *Geology*, 23(5):443–446.

Rosner, M. and Meixner, A. (2004). Boron isotopic composition and concentration of ten geological reference materials. *Geostandards and Geoanalytical Research*, 28(3):431–441.

Rosner, M., Wiedenbeck, M., and Ludwig, T. (2008). Composition-Induced Variations in SIMS Instrumental Mass Fractionation during Boron Isotope Ratio Measurements of Silicate Glasses. *Geostandards and Geoanalytical Research*, 32(1):27–38.

Rouméjon, S. and Cannat, M. (2014). Geochemistry, Geophysics, Geosystems. *Geochemistry, Geophysics, Geosystems*, 15:4692–4711.

Rouméjon, S., Williams, M. J., and Früh-Green, G. L. (2018). In-situ oxygen isotope analyses in serpentine minerals: Constraints on serpentinization during tectonic exhumation at slow- and ultraslow-spreading ridges. *Lithos*, 323:156–173.

Rubatto, D. and Angiboust, S. (2015). Oxygen isotope record of oceanic and high - pressure metasomatism : a P – T – time – fluid path for the Monviso eclogites (Italy). *Contributions to Mineralogy and Petrology*, 170(5):1–16.

Rubatto, D. and Herman, J. (2003). Zircon formation during fluid circulation in eclogites (Monviso , Western Alps): Implications for Zr and Hf budget in subduction zones. *Geochimica et Cosmochimica Acta*, 67(12):2173–2187.

Scambelluri, M., Hoogerduijn Strating, E. H., Piccardo, G. B., Vissers, R. L., and Rampone, E. (1991). Alpine olivine- and titanian clinohumite-bearing assemblages in the Erro-Tobbio peridotite (Voltri Massif, NW Italy). *Journal of Metamorphic Geology*, 9(1):79–91.

Scambelluri, M., Muntener, O., Hermann, J., Piccardo, G. B., and Trommsdorff, V. (1995). Subduction of water into the mantle - history of an alpine peridotite. *Geology*, 23(5):459–462.

Scambelluri, M., Muntener, O., Ottolini, L., Pettke, T. T., and Vannucci, R. (2004). The fate of B , Cl and Li in the subducted oceanic mantle and in the antigorite breakdown fluids. *Earth and Planetary Science Letters*, 222:217–234.

Scambelluri, M. and Tonarini, S. (2012). Boron isotope evidence for shallow fluid transfer across subduction zones by serpentinized mantle. *Geology*, 40(10):907–910.

Schenk, O. and Urai, J. L. (2005). The migration of fluid-filled grain boundaries in recrystallizing synthetic bischofite: First results of in-situ high-pressure, high-temperature deformation experiments in transmitted light. *Journal of Metamorphic Geology*, 23(8):695–709.

Schmidt, M. W. and Poli, S. (1998). Experimentally based water budgets for dehydrating slabs and consequences for arc magma generation. *Earth and Planetary Science Letters*, 163(1-4):361–379.

Schwartz, S., Guillot, S., Reynard, B., Lafay, R., Debret, B., Nicollet, C., Lanari, P.,

and Line, A. (2013). Pressure – temperature estimates of the lizardite / antigorite transition in high pressure serpentinites. *LITHOS*, 178:197–210.

Skelton, A. D. L. and Valley, J. W. (2000). The relative timing of serpentinisation and mantle exhumation at the ocean-continent transition, Iberia: Constraints from oxygen isotopes. *Earth and Planetary Science Letters*, 178(3-4):327–338.

Slack, J. F., Palmer, M. R., and Stevens, B. P. (1989). Boron isotope evidence for the involvement of non-marine evaporites in the origin of the Broken Hill ore deposits. *Nature*, 342(6252):913–916.

Smith, E. M., Shirey, S. B., Richardson, S. H., Nestola, F., Bullock, E. S., Wang, J., and Wang, W. (2018). Blue boron-bearing diamonds from Earth's lower mantle. *Nature*, 560(7716):84–87.

Spandler, C., Pettke, T., and Hermann, J. (2014). Experimental study of trace element release during ultrahigh-pressure serpentinite dehydration. *Earth and Planetary Science Letters*, 391:296–306.

Syracuse, E. M., van Keken, P. E., Abers, G. A., Suetsugu, D., Bina, C., Inoue, T., Wiens, D., and Jellinek, M. (2010). The global range of subduction zone thermal models. *Physics of the Earth and Planetary Interiors*, 183(1-2):73–90.

Tatsumi, Y. (1986). FORMATION OF THE VOLCANIC FRONT IN SUBDUCTION ZONES. *Geophysical Research Letters*, 13(8):717–729.

Tenthorey, E. and Cox, S. F. (2003). Reaction-enhanced permeability during serpentinite dehydration. *Geology*, 31(10):921–924.

Tenthorey, E. and Herman, J. (2004). Composition of fluids during serpentinite breakdown in subduction zones : Evidence for limited boron mobility. *Geology*, 32(10):865–868.

Tonarini, S., Agostini, S., Doglioni, C., Innocenti, F., and Manetti, P. (2007). Evidence for serpentinite fluid in convergent margin systems: The example of El Salvador (Central America) arc lavas. *Geochemistry Geophysics Geosystems*, 8(9).

Tonarini, S., Leeman, W. P., and Leat, P. T. (2011). Subduction erosion of forearc mantle wedge implicated in the genesis of the South Sandwich Island (SSI) arc: Evidence from boron isotope systematics. *Earth and Planetary Science Letters*, 301(1-2):275–284.

Trommsdorff, V. and Connolly, J. (1996). The ultramafic contact aureole about the Bregaglia (Bergell) tonalite: Isograds and a thermal model. *Schweizerische Mineralogische Und Petrographische Mitteilungen*, 76(3):537–547.

Trommsdorff, V. and Connolly, J. A. D. (1990). Constraints on phase diagram topology for the system CaO-MgO-SiO2-CO2-H2O. *Contributions to Mineralogy and Petrology*, 104(1):1–7.

Trommsdorff, V. and Evans, B. W. (1972). Progressive metamorphism of antigorite schist in the bergell tonalite aureole (Italy). *American Journal of Science*, 272:425–437.

Trommsdorff, V., López Sánchez-Vizcaíno, V., Gómez-Pugnaire, M. T., and Müntener, O. (1998). High pressure breakdown of antigorite to spinifex-textured olivine and orthopyroxene, SE Spain. *Contributions to Mineralogy and Petrology*, 132(2):139–148.

Trommsdorff, V., Montrasio, A., Hermann, J., Müntener, O., Spillmann, P., and Gieré, R. (2005). The Geological Map of Valmalenco. *Schweizerische Mineralogische Und Petrographische Mitteilungen*, 85:1–13.

Ulmer, P. and Trommsdorff, V. (1995). Serpentine Stability to Mantle Depths and Subduction-Related Magmatism. *Science*, 268(5212):858–861.

Ulmer, P. and Trommsdorff, V. (1999). Phase relations of hydrous mantle subducting to 300 km. *Mantle Petrology: Field Observations and High-Pressure Experimentation. Spec. Publ. Geochem. Soc. No. 6*, (6):259–281.

Van Keken, P. E., Hacker, B. R., Syracuse, E. M., and Abers, G. A. (2011). Subduction factory : 4 . Depth - dependent flux of H 2 O from subducting slabs worldwide. *Journal of Geophysical Research*, 116(January):1–15.

Vils, F., Tonarini, S., Kalt, A., and Seitz, H.-m. (2009). Boron , lithium and strontium isotopes as tracers of seawater – serpentinite interaction at Mid-Atlantic ridge , ODP Leg 209. *Earth and Planetary Science Letters*, 286(3-4):414–425.

Viti, C. and Hirose, T. (2008). Dehydration reactions and micro / nanostructures in experimentally-deformed serpentinites. *Contributions to Mineralogy and Petrology*, 157:327–338.

Viti, C. and Mellini, M. (1998). Mesh textures and bastites in the Elba retrograde serpentinites. *European Journal of Mineralogy*, 10:1341–1359.

Walowski, K. J., Kirstein, L. A., De Hoog, J. C., Elliott, T. R., Savov, I. P., and Jones, R. E. (2019). Investigating ocean island mantle source heterogeneity with boron isotopes in melt inclusions. *Earth and Planetary Science Letters*, 508:97–108.

Weijermars, R. (1991). Geology and tectonics of the Betic Zone, SE Spain. *Earth Science Reviews*, 31(3-4).

Williams, L. B. and Hervig, R. L. (2004). Boron isotope composition of coals: A potential tracer of organic contaminated fluidsEditorial handling by R.S. Harmon. *Applied Geochemistry*, 19(10):1625–1636.

Williams, L. B., Hervig, R. L., Holloway, J. R., and Hutcheon, I. (2001). Boron isotope geochemistry during diagenesis . Part I . Experimental determination of fractionation during illitization of smectite. *Geochimica et Cosmochimica Acta*, 65(11):1769–1782.

Wunder, B., Deschamps, F., Watenphul, A., Guillot, S., Meixner, A., Romer, R. L., and Wirth, R. (2009). The effect of chrysotile nanotubes on the serpentine-fluid Li-isotopic fractionation. *Contributions to Mineralogy and Petrology*, 159:781–790.